Technical Report
TR-21-09
November 2021

Evaluation report of Task 9C based on comparisons and analyses of modelling results for the ONKALO REPRO-TDE experiment

Task 9 of SKB Task Force GWFTS – Increasing the realism in solute transport modelling based on the field experiments REPRO and LTDE-SD

Josep M Soler
Pekka Kekäläinen
Veli-Matti Pulkkanen
Luis Moreno
Aitor Iraola
Paolo Trinchero
Milan Hokr
Jakub Říha
Václava Havlová
Dagmar Trpkošová
Aleš Vetešník
Dan Reimitz
Jakub Višňák
Dušan Vopálka
Libor Gvoždík
Martin Milický
Michal Polák
Yuta Fukatsu
Tsuyoshi Ito
Yukio Tachi
Urban Svensson
Dong Kyu Park
Sung-Hoon Ji
Björn Gylling
G William Lanyon

SVENSK KÄRNBRÄNSLEHANTERING AB

SWEDISH NUCLEAR FUEL
AND WASTE MANAGEMENT CO

Box 3091, SE-169 03 Solna
Phone +46 8 459 84 00
skb.se

SVENSK KÄRNBRÄNSLEHANTERING

ISSN 1404-0344
SKB TR-21-09
ID 1943425

November 2021

Evaluation report of Task 9C based on comparisons and analyses of modelling results for the ONKALO REPRO-TDE experiment

Task 9 of SKB Task Force GWFTS – Increasing the realism in solute transport modelling based on the field experiments REPRO and LTDE-SD

Josep M Soler[1], Pekka Kekäläinen[2], Veli-Matti Pulkkanen[3], Luis Moreno[4], Aitor Iraola[5], Paolo Trinchero[5], Milan Hokr[6], Jakub Říha[6], Václava Havlová[7], Dagmar Trpkošová[7], Aleš Vetešník[8], Dan Reimitz[8], Jakub Višňák[8], Dušan Vopálka[8], Libor Gvoždík[9], Martin Milický[9], Michal Polák[9], Yuta Fukatsu[10], Tsuyoshi Ito[10], Yukio Tachi[10], Urban Svensson[11], Dong Kyu Park[12], Sung-Hoon Ji[12], Björn Gylling[13], G William Lanyon[14]

1 Institute of Environmental Assessment and Water Research, IDAEA-CSIC
2 University of Helsinki
3 VTT Technical Research Centre of Finland Ltd
4 Royal Institute of Technology, KTH
5 Amphos 21
6 Technical University of Liberec
7 ÚJV Řež
8 Czech Technical University in Prague
9 PROGEO
10 Japan Atomic Energy Agency, JAEA
11 Computer-aided Fluid Engineering AB
12 Korea Atomic Energy Research Institute, KAERI
13 Gylling GeoSolutions
14 Fracture Systems Ltd

Abstract

Task 9C of the SKB Task Force on Modelling of Groundwater Flow and Transport of Solutes (Task Force GWFTS) was the third subtask within Task 9 and focused on (1) predictive and (2) back-analysis modelling of experimental results from the REPRO-TDE in situ diffusion experiment. The test was performed at a depth of about 400 m in the ONKALO underground research facility in Finland. Synthetic groundwater containing radionuclide tracers (HTO, Cl-36, Na-22, Ba-133, Cs-134) was circulated for about four years in a packed-off interval of the so-called injection borehole. Tracer activities were additionally monitored in two observation boreholes arranged as a right-angled triangle and located at about 0.1 m wall-to-wall from the injection borehole.

Eleven modelling teams participated in the modelling exercise, using different model concepts and approaches. Three main types of models were applied: (1) An analytical solution to the diffusion-retention equations, (2) continuum-porous-medium-type numerical models, and (3) microstructure-based models. The predictive model calculations were based on laboratory-based information concerning porosities, diffusion coefficients and sorption partition coefficients available in the task description. Microstructural characterisation of rock samples was also available and used by the teams using microstructure-based models.

After the experimental results were made available, the modelling teams were able to revise their models to reproduce the observations. Some of the general conclusions from these back-analysis calculations are the need for reduced effective diffusion coefficients for Cl-36 compared to those applicable to HTO (anion exclusion), the need to implement weaker sorption for Na-22, compared to results from laboratory batch-sorption experiments, and the large differences between the theoretical initial concentrations for the strongly-sorbing Ba-133 and Cs-134 and the first measured values a few hours after tracer injection. The assumptions regarding the initial concentrations used in the different models greatly affected the results.

Different teams applied different concepts, concerning mainly the implementation of isotropic versus anisotropic diffusion, or the possible existence of a Borehole Disturbed Zone (BDZ) around the different boreholes. The role of microstructure was also included in two of the models. Results from the back-analysis modelling stage can be considered to have successfully reproduced the experimental results to different extents, but it is not clear from the results which concepts best represented the observed behaviour. Overcoring of the experimental section was not performed. The study of rock samples from the overcore could have provided relevant information concerning tracer transport distances in different directions (anisotropy) and potential increased sorption near the borehole walls (Borehole Disturbed Zones), thus improving the in situ characterisation of the transport and retention processes and the relevance of the different concepts.

Sammanfattning

Modelleringsuppgift 9C inom SKBs internationella arbetsgrupp för modellering av grundvattenflöde och transport av lösta ämnen (Task Force GWFTS) var den tredje deluppgiften inom Task 9 och fokuserade på (1) prediktiv samt (2) analyserande modellering av experimentella resultat från in situ diffusionsexperimentet REPRO-TDE. Den analyserande modelleringen utfördes när de experimentella resultaten var kända. REPRO-TDE utfördes på cirka 400 m djup i den underjordiska forskningsanläggningen ONKALO i Finland. Syntetiskt grundvatten innehållande radionukliderna (HTO, Cl-36, Na-22, Ba-133, Cs-134) cirkulerades i ungefär fyra år i en avpackad borrhålssektion av det så kallade injektionsborrhålet. Aktiviteterna av radionuklider övervakades och mättes dessutom i två observationsborrhål anordnade som i en rätvinklig triangel och belägna vid cirka 0,1 m vägg till vägg från injektionsborrhålet.

Elva modelleringsteam deltog i modelleringsövningen genom användande av olika modellkoncept och tillvägagångssätt. Tre huvudtyper av modeller användes: (1) En analytisk lösning av diffusions-retentionsekvationerna, (2) numeriska modeller baserade på kontinuerliga porösa medium och (3) mikrostrukturbaserade modeller. De prediktiva modellberäkningarna baserades på laboratoriebestämd information såsom porositeter, diffusionskoefficienter och sorptionsfördelningskoefficienter som finns tillgängliga i uppgiftsbeskrivningen. Mikrostrukturell karakterisering av bergprover fanns också tillgänglig och användes av teamen som använde mikrostrukturbaserade modeller.

Efter att de experimentella resultaten gjordes tillgängliga, fick modelleringsgrupperna uppdatera sina modelleringskoncept för att simulera de uppdaterade resultaten. Några av de allmänna slutsatserna från beräkningarna i denna efteranalys är behovet av att reducera den effektiva diffusionskoefficienten för Cl-36 jämfört med den som är tillämplig för HTO (anjon-uteslutning), behovet av att applicera svagare sorption för Na-22, jämfört med resultat från laboratoriemätningar av batch-absorptionsexperiment, samt de stora skillnaderna mellan de teoretiska initialkoncentrationerna, för de starkt sorberande ämnena Ba-133 och Cs-134, och de första uppmätta värdena några timmar efter spårinjektion. Antagandena om de initiala koncentrationerna för de olika modellerna påverkade resultatet mycket.

Huvudsakligen tillämpade de olika teamen olika koncept, då det gäller implementeringen av isotropisk kontra anisotrop diffusion och den möjliga närvaron av en störd zon runt de olika borrhålen. Mikrostrukturens roll ingick också i två av modellerna. Resultat från efter-analysmodelleringssteget kan anses ha framgångsrikt reproducerat experimentresultaten i olika omfattning, men det framgår inte helt klart från resultaten vilka koncept som är bättre på att representera de experimentella observationerna. Överborrning av experimentområdet utfördes inte i detta experiment. Det är möjligt att studier av bergprover från en överborrning kunde ha gett relevant information om transportavstånden för radionukliderna i olika riktningar (anisotropi) och potentiellt ökad kännedom om sorptionen på borrhålsväggarna (borrhålsstörda zoner) och därmed förbättrat karakteriseringen av transport- och retentionsprocesser samt relevansen av olika koncept.

Contents

1 Introduction

The SKB Task Force on Modelling of Groundwater Flow and Transport of Solutes (Task Force GWFTS) is an international forum in the area of conceptual and numerical modelling of groundwater flow and solute transport in fractured rock. Task 9 focuses on the fractured crystalline host rock surrounding present and future repositories for spent fuel and other radioactive waste. Task 9C was the third subtask within Task 9 and focused on predictive and inverse modelling of experimental results from the REPRO Through-Diffusion Experiment (TDE). The experiment was carried out by Geosigma AB and the University of Helsinki (Department of Chemistry), on assignment from Posiva Oy. The aim of the experiment was to quantify the diffusivity and connected porosity of the unaltered rock matrix under the stress conditions expected in the repository and the sorption properties of radionuclides in intact rock (Aalto et al. 2009, Rahkola et al. 2020). It involved the use of radioactive tracers at a depth of about 400 m at the ONKALO underground rock research facility in Olkiluoto, Finland. Details of the experimental setup and procedures are reported in the task description (Andersson et al. 2020), together with references to relevant rock-characterisation data (mineralogy, macro- and micro-structure; Toropainen 2012, Ikonen et al. 2015) and laboratory-based experimental results for porosities, permeabilities, diffusion coefficients and sorption parameters (Kuva et al. 2015, Muuri et al. 2017, Voutilainen et al. 2018).

1.1 Overview of the TDE experiment

The experiment started in November 2015 and lasted until December 2019. It was performed between three parallel boreholes arranged as a right-angled triangle. Borehole ONK-PP326 was used as the injection hole and boreholes ONK-PP324 and ONK-PP327 as observation holes (Figure 1-1). In this fashion, transport along foliation (PP326–PP324) and normal to foliation (PP326–PP327) could be monitored. The experiment was carried out in 1-m-long packed-off intervals, at about 12 m from the tunnel wall. The distances between the borehole walls were slightly longer than one decimetre (Table 1-1). Any advective flow between the boreholes was foreseen to be insignificant at the stage of initiation of the experiment, as the pressures in the test intervals and surrounding guard intervals were kept constant and equal in all three boreholes. However, due to unforeseen experimental conditions, after three months the control of the experimental pressures had to be abandoned and pressure gradients developed between the intervals.

The REPRO site contains very impermeable rock, locally lacking water-bearing fractures, representative of the host rock for a future repository for radioactive waste. This condition turned out to cause rather large pressure differences between the circulation intervals, even though the distances between them were only about 0.1 m. Figure 1-2 shows the pressures measured in the different circulation intervals at the times when pumps were switched off. Figure 1-3 shows the corresponding gradients between boreholes. Pressures changed significantly, partly due to experimental artefacts and sampling, and especially during a leakage in PP327 in late 2017. A general decrease in pressures over time can also be observed. Figure 1-3 shows that both the magnitude and direction of the hydraulic gradient between the boreholes changed significantly over time. Hydraulic gradients in the order of 100 m/m (0.1 MPa/0.1 m) or more seemed to prevail during long periods of time. Hydraulic conductivities calculated from field observations (inflow into the boreholes prior to the experiment, with the intervals open to the atmosphere) ranged from 10^{-15} to 2×10^{-14} m/s, which would be consistent with the observed large hydraulic gradients between boreholes during the experiment. Hydraulic conductivities measured in laboratory core tests were significantly higher, in the range from 2×10^{-13} to 10^{-11} m/s. However, the core samples were small and likely to have undergone sample disturbance (stress relief).

The bedrock surrounding the boreholes was veined gneiss (VGN), which shows a locally irregular weak to moderate banded foliation. The general orientation of the foliation was almost parallel to the drilling direction. Boreholes ONK-PP321 and ONK-PP322 were located very close to the three experimental drillholes (about 0.1 m from PP324; Figure 1-1). These holes were therefore plugged with packers in order to avoid a hydraulic sink. All holes were also equipped with an extra guard packer close to the borehole mouth to diminish the hydraulic gradient towards the REPRO niche.

Tracers HTO (198 MBq), Na-22 (22.4 MBq), Cl-36 (5.5 MBq), Ba-133 (1.92 MBq) and Cs-134 (2.09 MBq) were injected into the source interval in ONK-PP326, which was filled with synthetic groundwater (Cl-Na-dominated, pH 7, ionic strength 0.16 M), and recirculated. Temperature was 10 °C to 11 °C. The decreasing tracer concentrations in the injection interval and increasing tracer concentrations in the observation boreholes were analysed. This was done on extracted water samples in the laboratory; for HTO and Cl-36 by liquid scintillation counting and for Na-22, Ba-133 and Cs-134 by High-Resolution GXRS (gamma measurements), in most cases after chemical separation. When sampling, the extracted volumes were replaced with the same volumes of tracer-free synthetic groundwater. Furthermore, online measurements of Na-22, Ba-133 and Cs-134 were performed from the start for the injection interval and simultaneously for the two observation boreholes using a High-Performance Germanium detector and a Na(Tl)I-scintillation detector, respectively. Tracer concentrations in the injection interval were measured at a higher frequency during the first part of the experiment. In February 2017, focus was shifted towards analysing breakthrough concentrations in the observation boreholes. The High-Performance Germanium detector was then used for ONK-PP324 and the Na(Tl)I-scintillation detector for ONK-PP327. From February 2017, only sample collection and subsequent analysis were performed for the injection borehole ONK-PP326. Tracer concentrations were not measured in the adjacent boreholes ONK-PP321 and ONK-PP322 (Figure 1-1).

Overcoring and measurement of tracer distribution profiles in the rock was not originally defined as a priority in the design of the experiment. It was left as an option that was finally not implemented.

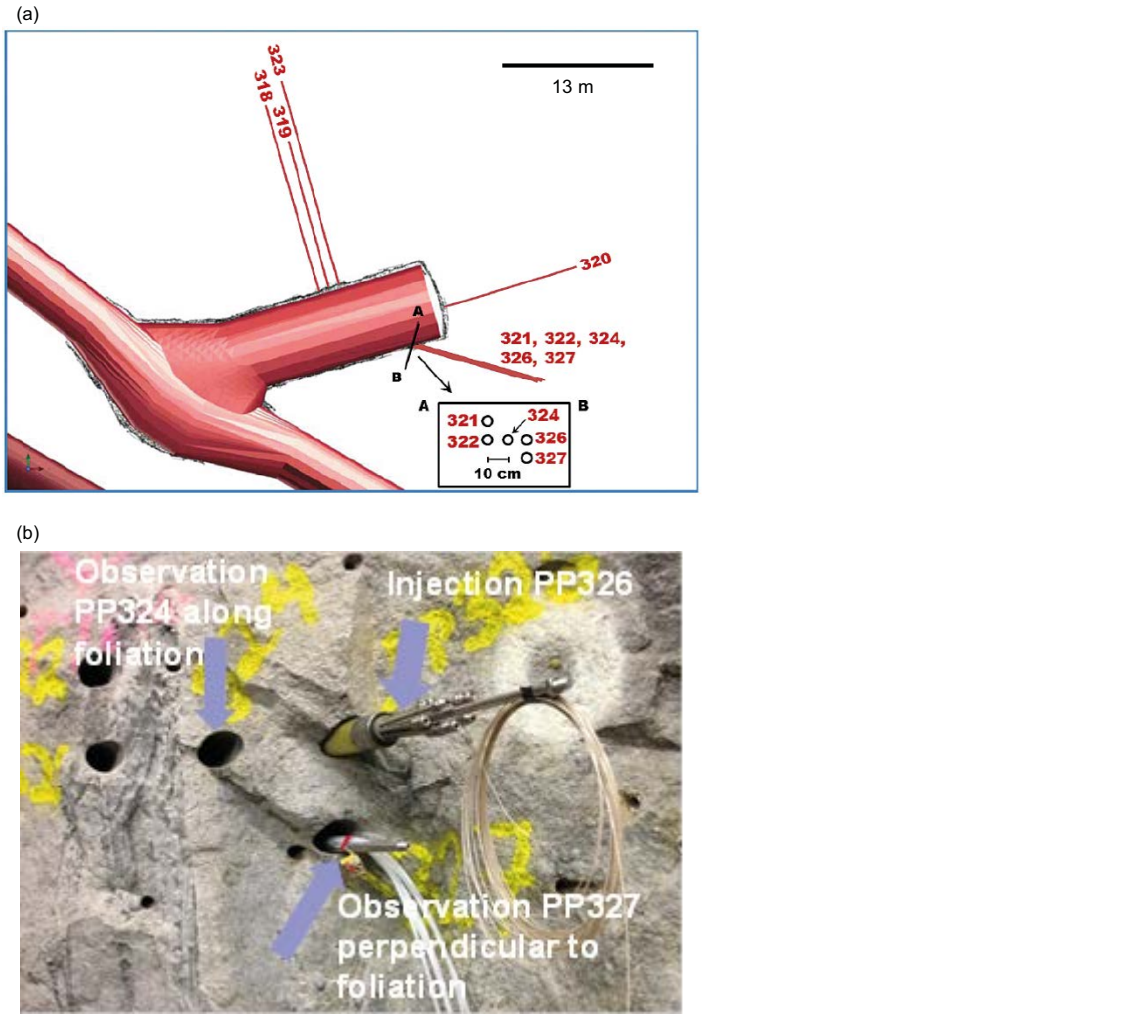

Figure 1-1. *(a) Location of REPRO boreholes in the investigation niche ONK-TKU-4219 (modified after Ikonen et al. 2015). (b) Photograph of the boreholes (see inset in (a)).*

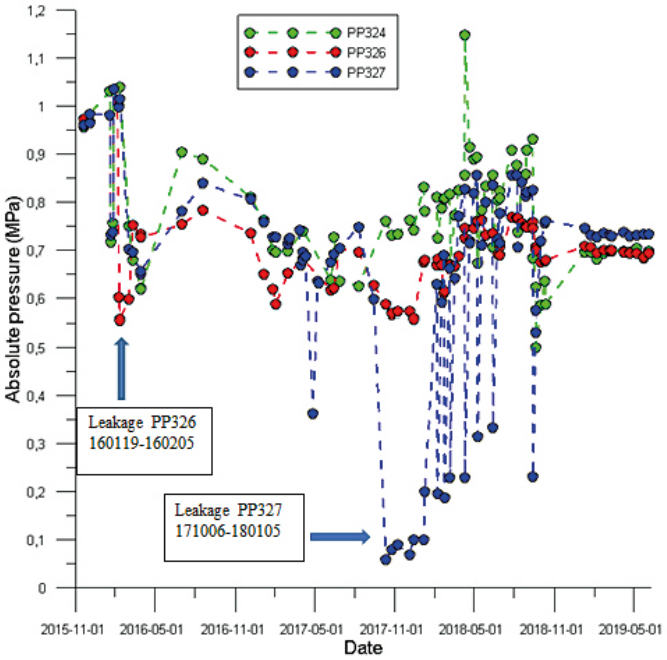

Figure 1-2. *Pressures in the three experimental intervals as measured from 2015-11-15 to 2019-05-16. The dots represent actual measurements and lines in between are interpolations. After Andersson et al. (2020).*

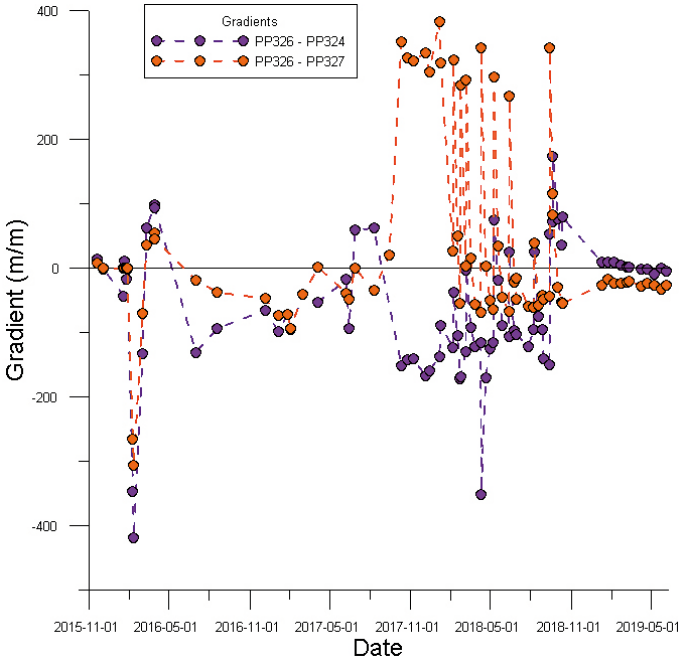

Figure 1-3. *Hydraulic gradients between PP326 and the PP324 and PP327 observation boreholes. The two leakages shown in Figure 1-2 are clearly visible as extremes. The dots represent actual measurements and lines in between are interpolations. After Andersson et al. (2020).*

Table 1-1 shows the geometric parameters and total volumes of water in the circulation systems of the three experimental boreholes. Notice that the total volumes of water reported in an early version of the task description were slightly smaller than those finally reported. Those early values were used in some of the model calculations. Likewise, distances between borehole intervals in the early version of the task description were slightly larger than those finally reported. Tables 1-2 to 1-6 show some of the information concerning porosities, diffusion coefficients and sorption partition coefficients available to the modelling teams in the task description (Andersson et al. 2020).

Table 1-1. Geometries and volumes for the three experimental boreholes.

Description	Measure	Units
Borehole diameter of 1 m experiment section in ONK-PP324 (± 2 σ)	56.76 ± 0.07	mm
Borehole diameter of 1 m experiment section in ONK-PP326 (± 2 σ)	56.92 ± 0.14	mm
Borehole diameter of 1 m experiment section in ONK-PP327 (± 2 σ)	57.00 ± 0.16	mm
Outer diameter of dummy in ONK-PP324, 326, and 327	54.0	mm
Length of annular slot in ONK-PP324, 326, and 327 (also distance between inlet and outlet)	1.00	m
PEEK tubing – inner diameter	1.02	mm
PEEK tubing – inner diameter in ONK-PP324 from 2018-09-12	2.03	mm
Distance of intact rock between test intervals ONK-PP326 to ONK-PP324*	0.115	m
Distance of intact rock between test intervals ONK-PP326 to ONK-PP327*	0.15	m
Total length of PEEK tubing ONK-PP324 (including 9 m detector tubing, 1 mm)	63.4	m
Total length of PEEK tubing ONK-PP326	43.4	m
Total length of PEEK tubing ONK-PP327	63.4	m
Volume of water in test interval ONK-PP324	240	mL
Volume of water in test interval ONK-PP326	254	mL
Volume of water in test interval ONK-PP327	262	mL
Total volume of water in ONK-PP324 test interval (including tubing)**	291	mL
Total volume of water in ONK-PP324 test interval (including tubing from 2018-09-12)	424	mL
Total volume of water in ONK-PP326 test interval (including tubing)**	290	mL
Total volume of water in ONK-PP327 test interval (including tubing)**	313	mL

* Distances between test intervals in an early version of the report were 0.119 m (PP326–PP324) and 0.153 m (PP326–PP327).

** Total volumes of water reported in an early version of the task description were 268 mL (PP324), 252 mL (PP326) and 268 mL (PP327).

Table 1-2. Rock matrix porosities obtained in the REPRO laboratory campaign. Data are reproduced from Ikonen et al. (2015, Tables 2, 3 and 4) and, where noted, from Kuva et al. (2015).

Borehole	Drillhole lengths (m)	Porosity (%)	Method
ONK-PP324	11.39–11.42	0.61 ± 0.15 0.50 ± 0.05	Water gravimetry Autoradiography
ONK-PP324	11.44–11.49	0.48 ± 0.14	Water gravimetry
ONK-PP324	11.49–11.51	1.02 ± 0.05	Ar-pycnometry
ONK-PP326	11.32–11.35	1.05 ± 0.22 1.40 ± 0.14	Water gravimetry Autoradiography
ONK-PP326	11.37–11.42	1.08 ± 0.29	Water gravimetry
ONK-PP326	11.42–11.44	2.9 ± 0.1	Ar-pycnometry
ONK-PP326	11.72–11.74	0.68 ± 0.08	Ar-pycnometry (Kuva et al. 2015)
ONK-PP327	11.92–11.95	0.67 ± 0.16 0.80 ± 0.08	Water gravimetry Autoradiography
ONK-PP327	12.00–12.05	0.81 ± 0.22	Water gravimetry
ONK-PP327	12.05–12.07	0.7 ± 0.1	Ar-pycnometry

Table 1-3. Effective diffusion coefficients (D_e) determined in water phase (through-diffusion) using HTO and Cl-36 as tracers. Uncertainties are given as ± 1 σ. The determinations were performed parallel to the foliation. Reproduced from Voutilainen et al. (2018).

Sample	HTO D_e (m^2/s)	Cl D_e (m^2/s)
ONK-PP324 11.42–11.44	$(3.4 \pm 0.6) \times 10^{-13}$	$(3.4 \pm 0.8) \times 10^{-13}$
ONK-PP326 11.35–11.37	$(4.8 \pm 0.6) \times 10^{-13}$	$(3.4 \pm 0.7) \times 10^{-13}$
ONK-PP327 11.95–11.97	$(3.5 \pm 0.6) \times 10^{-13}$	$(3.4 \pm 0.7) \times 10^{-13}$

Table 1-4. Effective diffusion coefficients (D_e) determined in water phase (in-diffusion) using Cs-134 as tracer. Uncertainties are not given, but large, since the values were derived as side results. Reproduced from Muuri et al. (2017, Table 3).

Rock type	Cs D_e (m^2/s)
Veined gneiss	3.0×10^{-13}
Pegmatitic rock (not present in TDE)	4.0×10^{-13}

Table 1-5. Formation factor (F_f) and surface conductivity (κ_s) obtained for TDE samples from electromigration measurements. Based on Voutilainen et al. (2018). Ff corresponds to the ratio between De and the diffusion coefficient in free water. The determinations were performed parallel to the foliation.

Sample	F_f	κ_s (S/m)
ONK-PP324 11.44–11.49	2.2×10^{-4}	8.5×10^{-5}
ONK-PP326 11.37–11.42	5.9×10^{-4}	9.1×10^{-4}
ONK-PP327 12.00–12.05	4.0×10^{-4}	2.4×10^{-4}

Table 1-6. Sorption partitioning coefficients obtained in batch experiments on crushed rock of different size fractions or intact rock cubes (1 cm × 1 cm × 1 cm) at Helsinki University. Uncertainty estimates, if available, represent one standard deviation.

Radionuclide	Rock type	Sorption partitioning coefficients (m^3/kg)	Source
Na-22	Veined gneiss Pegmatitic granite	0.0013 ± 0.0003 0.0008 ± 0.0003	Unpublished data
Ba-133	Veined gneiss Pegmatitic granite	0.06 ± 0.02 0.08 ± 0.02	Unpublished data
Cs-134 (cube)	Veined gneiss Pegmatitic rock	0.031 0.0041	(Muuri et al. 2017, Table 3)
Cs-134 (batch)	Veined gneiss Pegmatitic rock	0.092 0.033	(Muuri et al. 2017, Table 3)

1.2 Objectives of Task 9C

In Task 9C, the different teams were asked first to predict the evolution of the activities of the five tracers in the injection (ONK-PP326) and observation (ONK-PP324, ONK-PP327) boreholes. Decay-corrected activities (Bq/g water) should be reported, simulating a (hypothetical) experimental time period of 10 years. It was also encouraged to model alternative breakthrough curves and, where possible, to tie them to conceptual understanding or alternative supporting experimental data. A suggestion was made to start with relatively simple models, ignoring effects such as the loss of tracers during detected leakage events or the dilution of the solutions induced by sampling. These effects, together with potential advection in response to large pressure gradients, or uncertainty in the calculated distances between boreholes, could be addressed in a second stage. Finally, as the measured experimental activities were made available, the teams were asked to model those results (back-analysis).

Modelling teams were also asked to keep track of the tracer mass balances in the system, as tracers may

- remain in the tracer cocktail in the injection borehole and associated tubing,
- be within the rock matrix of the local rock volume,
- be in the water volume of the observation boreholes and associated tubing,
- have been removed from the system by sampling,
- have been removed from the system through leakages and other artefacts,
- have been removed from the local rock volume through advective flow (although less likely), electromigration, or other processes.

The TDE experiment was terminated on December 31st, 2019, and the last sample collections took place on October 9th and 17th, for the observation and injection intervals, respectively. Pressures were monitored until March 3rd, 2020. Pressures dropped considerably in the three boreholes at the beginning of February 2020, in connection with the calibration of pressure transducers. Additional final water samples were collected on March 3rd, 2020, and they showed somewhat increased tracer activities in all three boreholes, diverging from the well-defined trends observed until the end of 2019. The modelling teams did not include these last samples in their back-analysis calculations; modelling had already been finalised when these last analyses were made available. Therefore, and due also to the potential effect of the pressure drop in February 2020 (large local pressure gradients between the borehole intervals and the rock matrix), these last samples have not been included in this evaluation report.

Also, a significant fraction of the injected HTO activity (6 to 12 MBq of the injected 198 MBq) was detected in a section of the ONK-PP326 injection borehole between the packed-off circulation interval and the REPRO niche. Other tracers were not detected. At the moment, the possible transport path from the source interval has not been identified.

2 Modelling teams and models

Eleven different modelling teams participated in Task 9C. Below is a summary of the models they used (Table 2-1 and Sections 2.1 to 2.11). Three main types of models have been applied: (1) analytical solution to the diffusion-retention equations, (2) continuum-porous-medium-type numerical models, based on the use of Representative Elementary Volumes (REVs), and (3) microstructure-based models, accounting for small-scale heterogeneity (i.e. mineral grains and porosities). Details of the models can be found in appendices of this report (except for KAERI; concept based on Park and Ji 2018, 2020). Not all teams performed both predictive and back-analysis calculations.

Unless otherwise specified, the initial tracer activities (Bq/g water) in the injection borehole used in the models were calculated from the initial tracer activities (Bq) and the total volume of water in the circulation system (Table 1-1).

Table 2-1. Summary of the modelling approaches by the different teams.

UNIVERSITY OF HELSINKI (HYRL)
Analytical solution (1D radial) including injection and observation boreholes. No predictive calculations; only back-analysis model.
VTT TECHNICAL RESEARCH CENTRE OF FINLAND LTD (VTT)
3D continuum models, including the three boreholes. No predictive calculations; only back-analysis model through a sensitivity analysis. COMSOL Multiphysics code (Li et al. 2009, Perko et al. 2009).
ROYAL INSTITUTE OF TECHNOLOGY (KTH)
3D (HTO) and 2D continuum models, including the three boreholes (only predictive modelling). COMSOL Multiphysics code (Li et al. 2009, Perko et al. 2009).
AMPHOS 21 (A21)
2D continuum model including the three boreholes. PFLOTRAN code (Hammond et al. 2014).
TECHNICAL UNIVERSITY OF LIBEREC (TUL)
2D continuum model including the three boreholes. Flow123d code (Březina et al. 2018). In addition, a simple analytical solution for the breakthrough of HTO in the observation boreholes was also performed.
ÚJV Řež (UJV)
2D continuum models including either the three boreholes (HTO, Cl-36, Na-22) or only the injection borehole (Ba-133, Cs-134). GoldSim code (GoldSim Technology Group 2018).
CZECH TECHNICAL UNIVERSITY IN PRAGUE (CTU)
Continuum models, 2D for HTO and Cl-36, including the three boreholes, and 1D radial for Na-22, Ba-133 and Cs-134 (only injection borehole included). GoldSim code (GoldSim Technology Group 2018).
PROGEO
2D continuum model including the three boreholes. No predictive calculations; only back-analysis for HTO. MT3DMS code (Zheng and Wang 1999, Zheng 2010, Bedekar et al. 2016a, b).
JAPAN ATOMIC ENERGY AGENCY (JAEA)
2D continuum model including the three boreholes. Only predictive calculations. GoldSim code (GoldSim Technology Group 2018).
COMPUTER-AIDED FLUID ENGINEERING AB (CFE)
3D microstructure-based model domain; thin rock layer including one (injection) or two (injection + observation) boreholes. Solute transport by particle tracking. DarcyTools code (Svensson and Ferry 2014).
KOREA ATOMIC ENERGY RESEARCH INSTITUTE (KAERI)
Microstructure-based models (2D, rectangular sections). A given model includes the injection borehole and one of the observation boreholes. Only predictive calculations. COMSOL Multiphysics code (Li et al. 2009, Perko et al. 2009).

Model details and results from TUL, UJV, CTU and PROGEO are also available in Hokr et al. (2020, 2021).

2.1 University of Helsinki (HYRL)

The experimental results were modelled (back-analysis only) using an analytical solution to the diffusion problem (isotropic medium), assuming a 1D radial geometry (axisymmetric with respect to the injection borehole; Figure 2-1). Importantly, the initial model tracer concentrations in the injection borehole were the result of the fitting of the model to the measured borehole data. The initial theoretical values, from the initial tracer activities (Bq) and solution volume (mL), were not taken into account. For HTO and Cl-36, the model domain considered the injection borehole and an observation borehole. Separate model fittings were performed for (a) the injection borehole and (b) the two observation boreholes, due to the poor fit to the observation-borehole data when using the transport and retention parameters deduced from the injection borehole. For sorbing tracers, only the injection borehole was considered. No-flux conditions were used for all the external boundaries. The effect of tracer dilution induced by sampling in the different boreholes was included in the calculations.

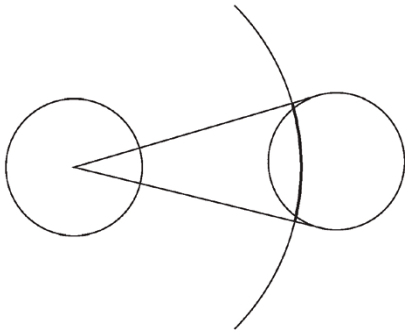

Figure 2-1. *Geometrical setup of the analytical model (HYRL). The injection borehole centre (left) is the origin of the radial coordinate system. The sector corresponding to the observation borehole is illustrated on the right.*

2.2 VTT Technical Research Centre of Finland Ltd (VTT)

3D numerical calculations (continuum model) including the three boreholes were performed using COMSOL Multiphysics (Li et al. 2009, Perko et al. 2009). Boreholes PP321 and PP322, located near PP324, were also included in the model domain. A series of sensitivity analyses with respect to different parameters was used to fit the models to the experimental results (back-analysis). The 3D model domain was a cylinder of 1 m in radius and 2.5 m in thickness (Figure 2-2). No-flux conditions were used at the external boundaries of the domain. For sorbing tracers, the initial theoretical concentrations (Bq/g water), calculated from the initial activities (Bq) of each tracer and the volume of water in the circulation system, were used as initial concentrations in the injection borehole. However, for non-sorbing tracers, the initial concentrations were calculated from the average activities in the first measured samples. The effects of sampling and also of a single large leakage event at t = 67 days, all inducing tracer dilution, were included in the calculations. The possible effects of advection and anisotropic diffusion due to foliation were also studied. Rock hydraulic conductivities up to 10^{-14} m/s would only result in small local variations in the results for the injection borehole (no effect on the observation boreholes).

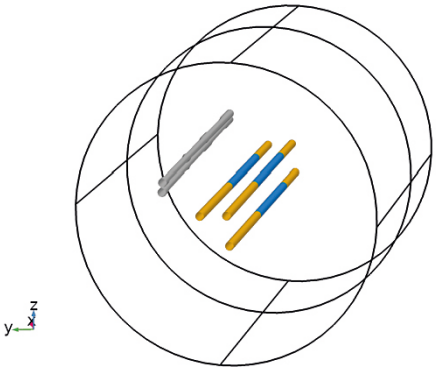

Figure 2-2. *Cylindrical model domain used by VTT. The radius of the cylinder is 1 m and the length 2.5 m. The experimental sections are coloured with blue; the rest of the boreholes PP324, PP326 and PP327 with yellow, and PP321 and PP322 with grey.*

2.3 Royal Institute of Technology (KTH)

KTH performed predictive calculations using 3D (HTO) and 2D continuum models. COMSOL Multiphysics (Li et al. 2009, Perko et al. 2009) was used for both types of models. The modelled system required in principle a 3D model, which needed a very large numerical mesh. Therefore, most of the predictions were performed using a 2D model (circular domain, radius 1 m; Figure 2-3), where the interval-end effects were neglected. No-flux conditions were used for all the external boundaries of the model domains. The two models were compared using the predictions for HTO and it was found that the differences were small. 2D simulations were performed for all the tracers. Moreover, sensitivity analyses were made concerning increased D_e values for Cs-134 due to surface-diffusion effects, reduced D_e values for Cl-36 due to potential anion exclusion, and the possibility of anisotropic diffusion due to foliation. No advection or sampling effects were included in the model calculations (reference case), but the effect of tracer dilution induced by sampling was evaluated for HTO.

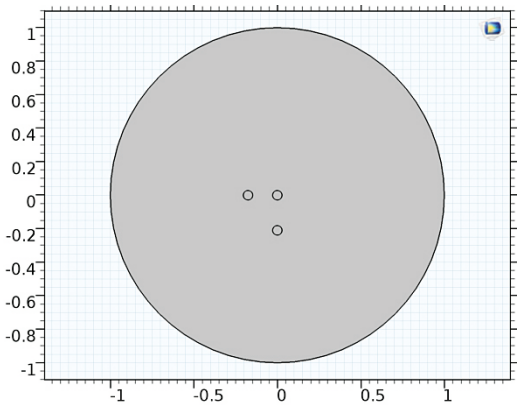

Figure 2-3. *Setup of the 2D system used by KTH. Borehole ONK-PP326 is located at the centre. Borehole ONK-PP324 is located to the left-hand side of the central borehole and ONK-PP327 is located below the central borehole. Dimensions are in metres.*

2.4 Amphos 21 (A21)

Two-dimensional modelling was performed using PFLOTRAN (Hammond et al. 2014). Tracers HTO, Na-22, Ba-133 and Cs-134 were considered in the first predictive modelling stage. A squared model domain (0.7 m × 0.7 m; Figure 2-4) included the three boreholes. All external boundaries of the domain were no-flux boundaries. Anisotropic diffusion due to the foliation was included using two approaches: (1) the implementation of the anisotropic 2D diffusion tensor, and (2) the implementation of statistically anisotropic heterogeneous diffusion fields. A homogeneous isotropic case was also included for reference.

Borehole Disturbed Zones (BDZ) were implemented in all three boreholes in the back-analysis stage of the modelling, together with homogeneous and isotropic diffusion. These calculations also included Cl-36. No advection or sampling effects were included in any of the calculations. Separate predictive calculations using the pressures measured in the different boreholes predicted no effect from advection if rock-matrix hydraulic conductivities were about 10^{-14} m/s.

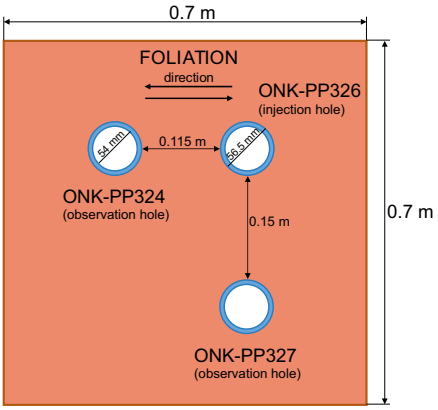

Figure 2-4. *Schematic layout of the geometry of the predictive model used by A21. The orange region represents the rock matrix while the blue rings represent the boreholes. Foliation direction is set on the x-axis.*

2.5 Technical University of Liberec (TUL)

Predictive and back-analysis calculations were performed using a 2D continuum model implemented in Flow123d (Březina et al. 2018)[1]. The same model domain and numerical mesh was used for all the tracers. A squared domain (0.75 m × 0.75 m) subject to isotropic diffusion included the three boreholes (Figure 2-5). No-flux conditions were used at the external boundaries. The dilution effect induced by sampling was included only in the back-analysis calculations. The effect of spatial discretisation was also analysed. The effects of leakages and complete replacement of water in PP324 were not considered for the prediction task. The potential effect of advection was studied in separate calculations, using a relatively large value of the rock hydraulic conductivity ($K = 2.9 \times 10^{-12}$ m/s), and resulting in a potential large effect.

For the back-analysis calculations a new mesh was implemented, with the same dimensions as the one previously used. Borehole Disturbed Zones (BDZ) around the three boreholes were also included, together with the effect of total replacement of water in PP324 at $t = 1\,028$ days.

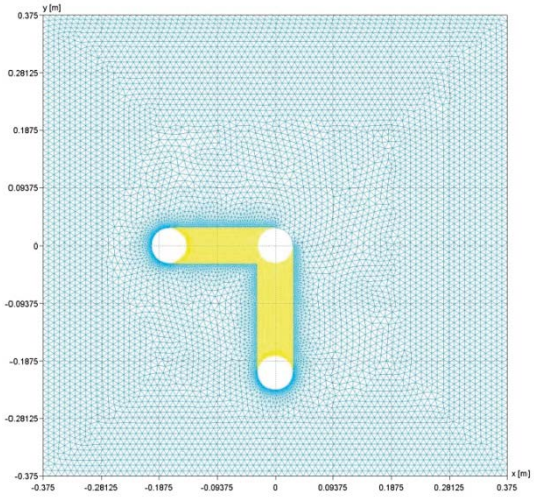

Figure 2-5. *Computational mesh used in the predictive calculations by TUL. The area in yellow corresponds to a zone with very fine spatial resolution (0.25 mm). Dimensions are in metres.*

[1] http://flow123d.github.io/

2.6 ÚJV Řež (UJV)

2D continuum models (Figure 2-6) subject to isotropic diffusion were used for predictive and back-analysis calculations using GoldSim (GoldSim Technology Group 2018). No-flux conditions were used in all the external boundaries of the model domains. The observation boreholes were not considered in the models for the strongly sorbing tracers (smaller model domains). Neither sampling nor potential advection effects were addressed in the calculations. The sensitivity with respect to spatial discretisation was analysed. For the back-analysis calculations, all model initial tracer concentrations in the injection borehole were recalibrated. The initial values for Ba-133 and Cs-134 were those from the first measured sample in the experiment. These values were significantly smaller than the theoretical values calculated from the initial activities of tracers (Bq) and solution volumes (mL). The initial value for HTO was also based on the first few measured samples. The initial concentrations for Cl-36 and Na-22 were adjusted to match the evolution of tracer concentrations in the injection borehole after about 100 days of experiment; the initial oscillations in concentrations were not considered in the fitting.

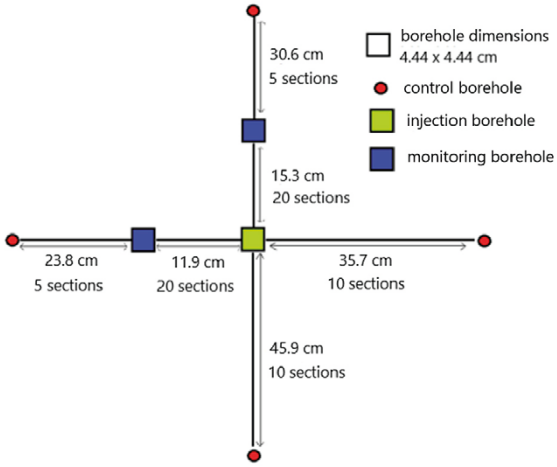

Figure 2-6. *Representation of the discretisation used for non-sorbing tracers by UJV (model with the finest discretisation).*

2.7 Czech Technical University in Prague (CTU)

CTU basically performed predictive model calculations using GoldSim (GoldSim Technology Group 2018). A 2D domain (0.45 m × 0.45 m; Figure 2-7) subject to isotropic diffusion and including the three boreholes was used for HTO and Cl-36. 1D-radial models were used for Na-22, Ba-133 and Cs-134 (observation boreholes not included). No-flux conditions were implemented in all the external boundaries and the effect of spatial discretisation was analysed.

Calibration (back-analysis) of the model was performed for HTO and Cl-36, fitting the model to the measurements at the PP324 observation borehole after total replacement of water (t = 1 028 d) and using the measured activities in the PP326 injection borehole during the whole experiment and in the PP324 observation borehole during the period before replacement of water as prescribed time-dependent boundary conditions.

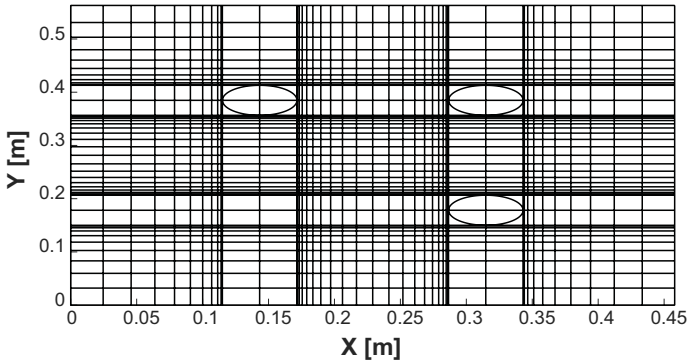

Figure 2-7. *2D grid used by CTU for HTO and Cl-36.*

2.8 PROGEO

PROGEO performed back-analysis calculations for HTO using the MT3DMS code (Zheng and Wang 1999, Zheng 2010, Bedekar et al. 2016a, b). The continuum model domain, subject to isotropic diffusion, consisted of a circular section (1/4 of a full circle) with a radius of 0.5 m and including the three boreholes (Figure 2-8). No-flux conditions were implemented in all the external boundaries. BDZ's were also included in the concept, although they resulted in a very small effect. The effects from sampling and from the leakage in the injection borehole about 60 days after the beginning of the experiment were also taken into account.

Three model variants were considered:

(1) Calibration to activities in PP326 (injection borehole).

(2) Calibration to activities in the two observation boreholes, resulting in very small porosities and diffusion coefficients.

(3) Implementation of a heterogeneous porosity distribution based on results from ^{14}C-PMMA autoradiography of a rock sample. Results led to the same conclusions as in variants 1 and 2.

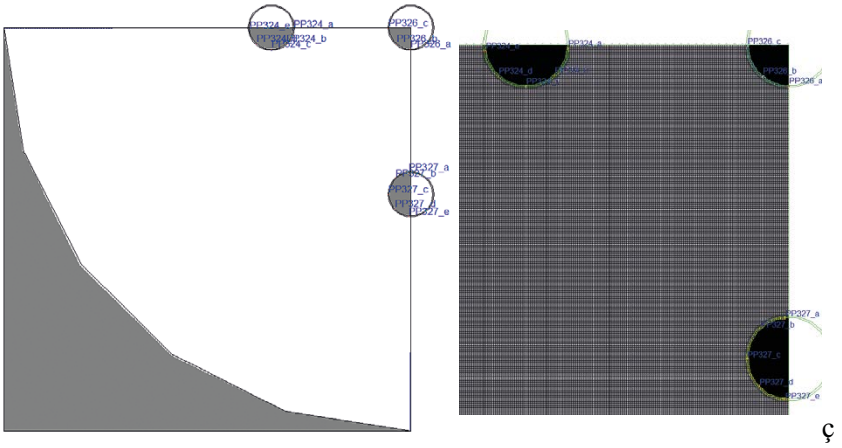

Figure 2-8. *Spatial discretisation used by PROGEO. The size of the domain is 0.5 m × 0.5 m (left). The image on the right corresponds to an enlargement of the area close to the boreholes. Grid size is 1 mm × 1 mm.*

2.9 Japan Atomic Energy Agency (JAEA)

Predictive model calculations were performed using a 2D continuum model including the three boreholes (Figure 2-9) using GoldSim (GoldSim Technology Group 2018). No-flux conditions were implemented in all the external boundaries. Sampling effects were not considered, but the effects of (a) a leakage event in the injection borehole at an early stage of the experiment, and of (b) the full replacement of solution in the PP324 observation borehole at about 1 000 days were taken into account. The implemented parameter values were based on a concept for upscaling from laboratory to in situ conditions. A BDZ was implemented in each of the boreholes, with higher ϕ, K_d and D_e values compared with those in the rock matrix. In the BDZ, ϕ and K_d decreased linearly with distance from the borehole wall. D_e was calculated as a function of ϕ (Archie's law). The effect of foliation (larger D_e parallel to foliation) was also included. The effects of cation excess and anion exclusion on D_e were also taken into account (D_e values for cations larger than those for anions).

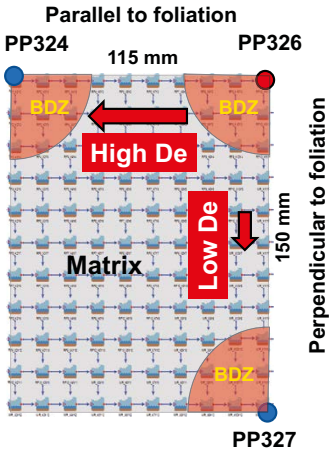

Figure 2-9. *Schematic representation of the model setup used by JAEA.*

2.10 Computer-Aided Fluid Engineering AB (CFE)

The model was based on the implementation of a Discrete Fracture Network at the microscopic scale, corresponding to the intergranular porosity. Modelling considered diffusion through this intergranular porosity, using the DarcyTools code (Svensson and Ferry 2014), with solute transport calculated by particle tracking. Sorption was implemented by setting three parameters (P_s, T_s, T_d). When a particle is close to a reactive mineral surface it has a certain probability P_s to sorb within a certain time T_s. If sorbed, it will remain so during and average time T_d before desorption. This concept is equivalent to equilibrium linear sorption. However, K_d values corresponding to the implemented P_s, T_s and T_d parameters were not reported.

The intergranular porosity network was defined based on measurements by micro X-ray computed tomography of a centimetric sample of the veined gneiss at the REPRO site. These measurements were made available to the modelling teams. The measured porosity map (cm scale) was repeated several times when defining the larger-scale domain for the in situ experiment. Anisotropic diffusion due to foliation was included in the calculations, assuming that D_e parallel to bedding was always twice that perpendicular to bedding.

For the predictive calculations, the 3D domain considered a thin (17.25 mm) rock domain. For conservative tracers (only HTO) the domain included the injection and one observation borehole (Figure 2-10). For sorbing tracers (Na-22, Ba-133, Cs-134) it only included the injection borehole. In the back-analysis stage, a new numerical grid was implemented, including only the injection borehole (even for conservative tracers). In all cases, no-flux conditions were applied to all external boundaries of the domains. No advection or sampling effects were taken into account.

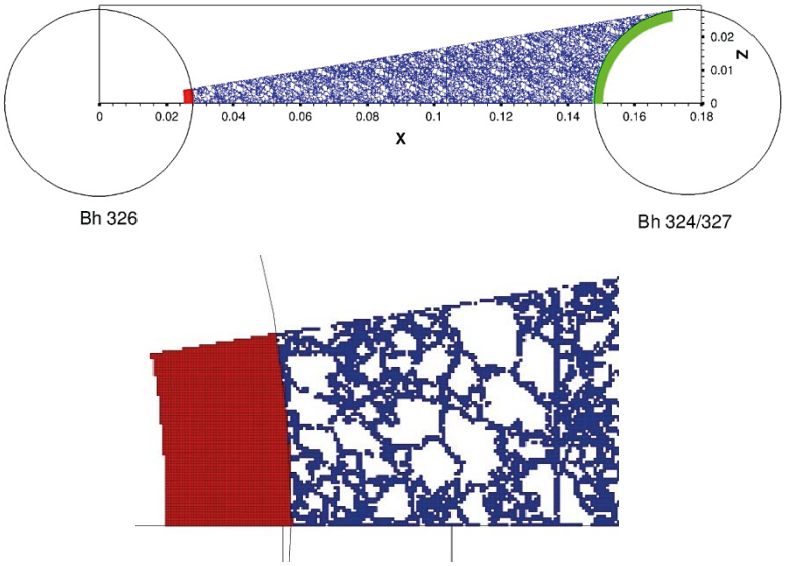

Figure 2-10. *The 3D X-ray based grid used by CFE in the predictive calculations. Computational grid in a 2D section (top) with an enlarged view close to borehole PP326 (bottom). Dimensions are in metres.*

2.11 Korea Atomic Energy Research Institute (KAERI)

2D microstructure-based models were used to make predictive calculation using COMSOL Multiphysics (Li et al. 2009, Perko et al. 2009). The concept was based on that reported in Park and Ji (2018, 2020) for the modelling of the LTDE-SD experiment at the Äspö Hard Rock Laboratory (Sweden). Only intragranular porosity was taken into account, based on microstructural characterisation (mineral staining and ^{14}C-PMMA autoradiography) of a rock sample performed at the University of Helsinki. Mineral-specific ϕ, D_e and K_d values were implemented for each of the minerals in the rock (K-feldspar, plagioclase, quartz, biotite). Sorption was only implemented in the biotite grains. The measured porosity and mineralogy map (cm scale) was repeated several times when defining the larger-scale domain for the in situ experiment. No-flux conditions were implemented in all the external boundaries of the domain. Sampling effects were not considered.

In each model run, only the injection borehole and one of the observation boreholes were taken into account. Separate models were considered for the two observation boreholes (Figure 2-11). Sensitivity analyses were performed concerning local porosity values from the ^{14}C-autoradiography (correspondence between gray-level and porosity), direction of diffusion (i.e. switching injection and observation boreholes in the domain; negligible effect), presence of a BDZ (increased porosity and K_d values in the BDZ, decreasing with distance from the borehole wall), and thickness of the BDZ. Additionally, the potential effect of anisotropic diffusion was studied for HTO.

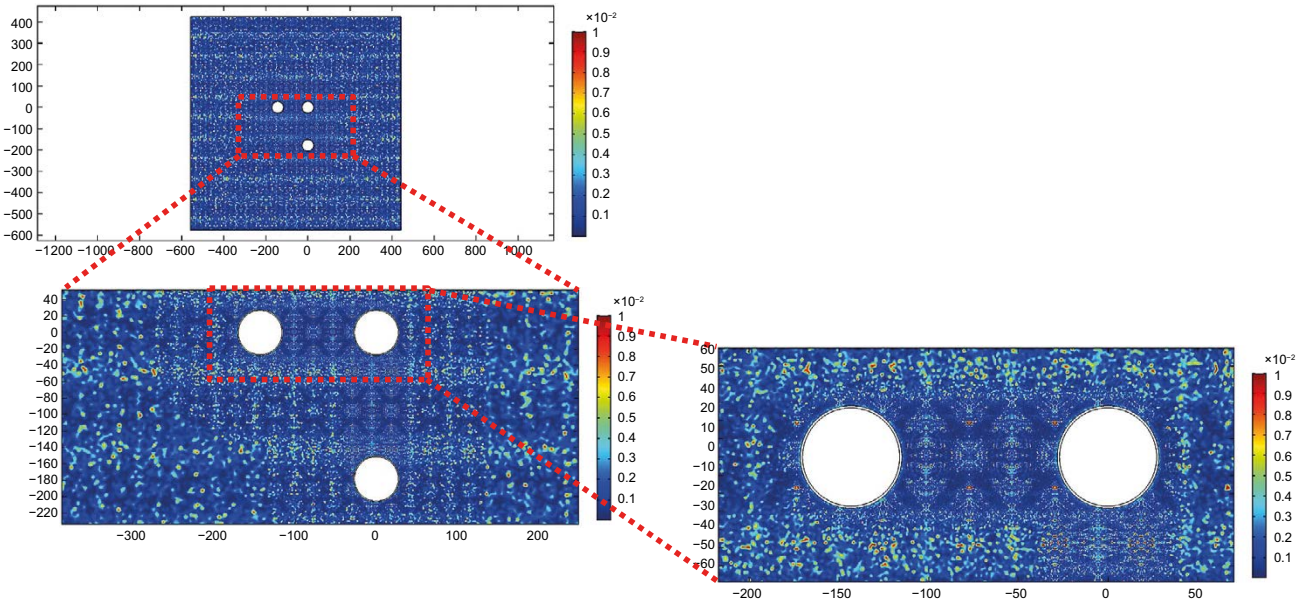

Figure 2-11. *Porosity map for the model domain including boreholes PP326 and PP324.*

3 Results and discussion

3.1 HTO

Figure 3-1 shows the results of the predictive model calculations from the different teams, together with the experimental measurements. Both raw measured concentrations and concentrations corrected for the dilution effect induced by sampling are shown. The model results for the injection borehole (ONK-PP326; Figure 3-1a,b) from all the teams are rather consistent, except for the inclusion by JAEA of the leakage event early in the experiment. Two groups of results can be observed, characterised by the different initial concentrations that were assumed. The larger values used by some teams were caused by the relatively smaller volumes of water in the borehole reported in an early version of the task description. Initial theoretical concentrations using the updated volumes are indicated with red numbers in Figure 3-1a,b. The porosity (ϕ) and D_e values assumed by the different teams were quite similar, (except for JAEA, Table 3-1), based on the reported supporting laboratory results. The parameter values assumed by JAEA were based on their concept for upscaling from laboratory to in situ conditions. KAERI did not report bulk ϕ and D_e values (parameters were specific for each different mineral). The trends shown by the different model results are mostly consistent with the measured data (not available when the predictions were made). The BDZ assumed in the JAEA model does not seem to have a large effect on the results, but the smaller D_e values in the rock matrix cause a slower drop in concentration (shallower slope of the curve).

Figure 3-1c,d shows the predictive model results and measurements for the two observation boreholes (ONK-PP324 and ONK-PP327). It is clear that all models overestimated the measured activities in those boreholes, although the results from JAEA for ONK-PP327 are closer to the measured values. Overestimation was particularly large in the results by KAERI. The effect of the anisotropy in diffusion assumed by A21, CFE and JAEA can be clearly observed in the results (retarded calculated breakthrough in ONK-PP327 compared to ONK-PP324). Notice also the large effect on the measurements induced by sampling (and especially by full replacement of water at t = 1 028 days, which was explicitly considered by JAEA) in borehole ONK-PP324. Sample volumes increased from 10 mL to 90 mL between December 2017 and August 2018 (between t = 746 d and t = 992 d).

Figure 3-2 shows the results of the back-analysis calculations by the different teams, together with the experimental data. In the back analysis, the choices of initial concentrations by the different teams were more uniform (Figure 3-2a,b). However, the ϕ and D_e values show larger differences (Table 3-2). Also, the curve from VTT clearly shows the effect of the leakage at t = 67 days (the other teams did not include it in the back-analysis models). The results from VTT and A21 show slower reductions in tracer concentrations when compared with the results from the other teams, consistent with the smaller D_e values for the rock matrix implemented in their models. CTU implemented an even smaller value of D_e, but only the activities in ONK-PP324 were taken into account in the fitting (Figure 3-2c; Section 2.7). This result also illustrates the apparently slower responses of the activities in the observation boreholes compared with those of the injection borehole (already seen in the analysis of the predictive calculations).

Figure 3-2c,d shows the back-analysis model and experimental results for the observation boreholes. The models that considered the full replacement of water in borehole ONK-PP324 at t = 1 028 days show clearly the effect in the evolution of concentrations. Overall, a better match was obtained by the teams that considered relatively small D_e values (VTT, A21, CTU, HYRL), although the fit is only approximate in most cases. The results from HYRL in the figure do not correspond to the parameters in Table 3-2. The curves correspond to a separate fit to the observation-borehole data using very small parameter values (see Section 2.1; $\phi = 3 \times 10^{-5}$, $D_e = 8.1 \times 10^{-16}$ m^2/s), showing the need for reduced transport parameters to match the activities in the observation boreholes; only the period after water replacement (t = 1 028 d) was considered for ONK-PP324. Also, as mentioned above (Section 2.7), the fit by CTU used the measured activities in the PP326 injection borehole during the whole experiment and in the PP324 observation borehole during the time before replacement of water (t = 1 028 d) as prescribed time-dependent boundary conditions.

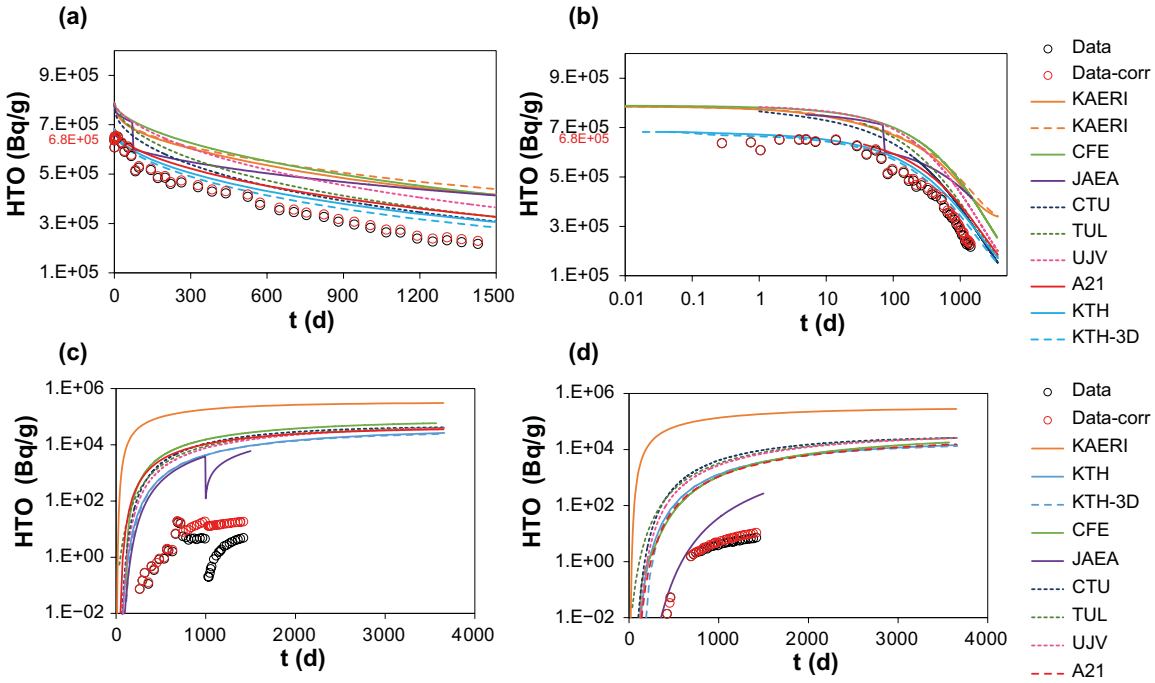

Figure 3-1. *Evolution of **HTO** activities (Bq/g_{water}) in the ONK-PP326 injection borehole (a,b) and in the ONK-PP324 (c) and ONK-PP327 (d) observation boreholes. Lines are **predictive** model results; black open circles are measured activities; red open circles are activities corrected for the dilution effect induced by sampling (and also by replacement of water in ONK-PP324 at t = 1 028 d). The red numbers on the vertical axis (a,b) indicate the theoretical initial activity. Analytical uncertainities are ca 1 % for ONK-PP326, less than 15 % for ONK-PP324, and 1 % to 2 % for ONK PP327, with somewhat larger uncertainties for the first few points in both ONK-PP324 and ONK-PP327.*

Table 3-1. Porosities and effective diffusion coefficients for HTO implemented in the predictive models by the different teams (central reference cases).

TEAM	ϕ	D_e ($\times 10^{-13}$ m^2/s)
KTH	0.01	3.9
A21	0.006	4.0 ‖
		2.0 ⊥
TUL	0.0094	3.9
UJV	0.0094	3.9
CTU	0.0094	3.9
JAEA matrix	0.0068	2.2 ‖
		1.1 ⊥
JAEA BDZ (1 mm)	0.05	52 ‖
		25 ⊥
CFE	0.006	4.0 ‖
		2.0 ⊥
KAERI	IGN	IGN

‖: Parallel to foliation.

⊥: Perpendicular to foliation.

IGN: Intragranular Network Model.

JAEA values in the BDZ are maximum values (linear decrease with distance from borehole wall).

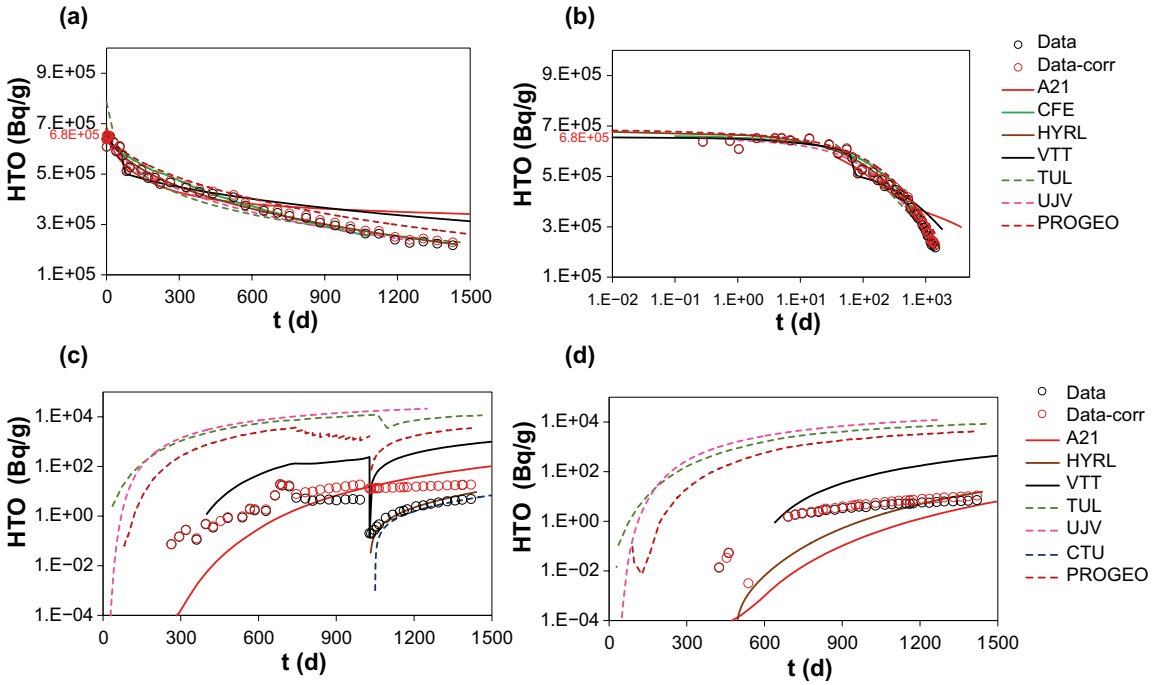

Figure 3-2. *Evolution of* ***HTO*** *activities (Bq/g_{water}) in the ONK-PP326 injection borehole (a,b) and in the ONK-PP324 (c) and ONK-PP327 (d) observation boreholes. Lines are* ***back-analysis*** *model results; black open circles are measured activities; red open circles are activities corrected for the dilution effect induced by sampling (and also by replacement of water in ONK-PP324 at t = 1 028 d). The red numbers on the vertical axis (a,b) indicate the theoretical initial activity. Analytical uncertainities are ca 1 % for ONK-PP326, less than 15 % for ONK-PP324, and 1 % to 2 % for ONK PP327, with somewhat larger uncertainties for the first few points in both ONK-PP324 and ONK-PP327.*

Table 3-2. Porosities and effective diffusion coefficients for HTO implemented in the back-analysis models by the different teams.

TEAM	ϕ	D_e ($\times 10^{-13}$ m^2/s)
HYRL	0.01	5.5
VTT	0.011	2.0
A21 matrix	0.006	0.36
A21 BDZ (21.75 mm)	0.03	3.0
TUL matrix	0.01	4.24
TUL BDZ (50 mm)	0.02	10.7
UJV	0.0094	7.0
CTU	0.0094	0.44
PROGEO matrix	0.009	4.17
PROGEO BDZ (1 mm)	0.002	9.2
CFE	0.0057	7.6 ||
		3.8 ⊥

||: Parallel to foliation.

⊥: Perpendicular to foliation.

TUL values in the BDZ are maximum values (decrease with distance from borehole wall).

The overall match of calculated results to both injection- and observation-borehole data (back-analysis) can be considered to be rather acceptable in the calculations by VTT ($\phi = 0.011$, $D_e = 2.0 \times 10^{-13}$ m^2/s) and A21 ($\phi = 0.006$, $D_e = 3.6 \times 10^{-14}$ m^2/s, BDZ with larger values), although they show a somewhat slow decrease in activities in the injection borehole.

3.2 Cl-36

Figure 3-3 shows the results of the predictive model calculations from the different teams, together with the experimental measurements. Both raw measured concentrations and concentrations corrected for the dilution effect induced by sampling are shown. The model results for the injection borehole (ONK-PP326; Figure 3-3a,b) show larger differences than in the case of HTO. Some teams also assumed relatively large initial concentrations in the injection borehole as a result of the relatively smaller volumes of water reported in an early version of the task description. But remarkably, the results from TUL and UJV show practically constant concentrations in the injection borehole, as a result of the very small ϕ and D_e values that were implemented (Table 3-3). These small values were based on the assumption of a strong anion-exclusion effect from data in Task 9A (predictive modelling of the REPRO WPDE experiments; Löfgren and Nilsson 2019, Soler et al. 2019). However, this almost constant tracer concentration is not consistent with the measurements (not available to the teams by the time of the predictive calculations). The results from JAEA, which also show a relatively slow decrease in concentration, reflect the small D_e value perpendicular to foliation that was implemented (anistropic diffusion, Table 3-3). JAEA also included the effect of a leakage early during the experiment. The combined effects of the leakage and the slower drop in concentrations result in a good match of the prediction with the measured data. KAERI did not report bulk ϕ and D_e values (parameters were specific for each different mineral).

Figure 3-3c,d shows the predictive model results and measurements for the two observation boreholes (ONK-PP324 and ONK-PP327). Like in the case of HTO, it is clear that most models overestimated the measured activities in those boreholes. However, the results from JAEA showed no breakthrough in ONK-PP327, due to the small D_e value perpendicular to foliation that was assumed (Table 3-3). The results by TUL and UJV are much closer to the observations. But again, these two teams implemented very small ϕ and D_e values (resulting in practically constant concentrations in the injection borehole). The small D_e value used by TUL and UJV (isotropic diffusion) was similar to that used by JAEA normal to foliation. However, the porosity implemented by JAEA was larger than the one assumed by TUL and CTU, resulting in a smaller pore diffusion coefficient ($D_p = D_e/\phi$) and smaller transport distances. Overestimation was particularly large in the results by KAERI. The effect of the anisotropic diffusion assumed by A21 and JAEA can be clearly observed in the results (retarded calculated breakthrough in ONK-PP327 compared to ONK-PP324).

Table 3-3. Porosities and effective diffusion coefficients for Cl-36 implemented in the predictive models by the different teams (central reference cases).

TEAM	ϕ	D_e ($\times 10^{-13}$ m^2/s)
KTH	0.01	3.4
A21	-	-
TUL	1.75×10^{-4}	0.05
UJV	1.75×10^{-4}	0.05
CTU	0.0094	3.4
JAEA matrix	0.0068	2.0 ||
		0.029 ⊥
JAEA BDZ (1 mm)	0.05	46 ||
		0.67 ⊥
CFE	-	-
KAERI	IGN	IGN

||: Parallel to foliation.

⊥: Perpendicular to foliation.

IGN: Intragranular Network Model.

JAEA values in the BDZ are maximum values (linear decrease with distance from borehole wall).

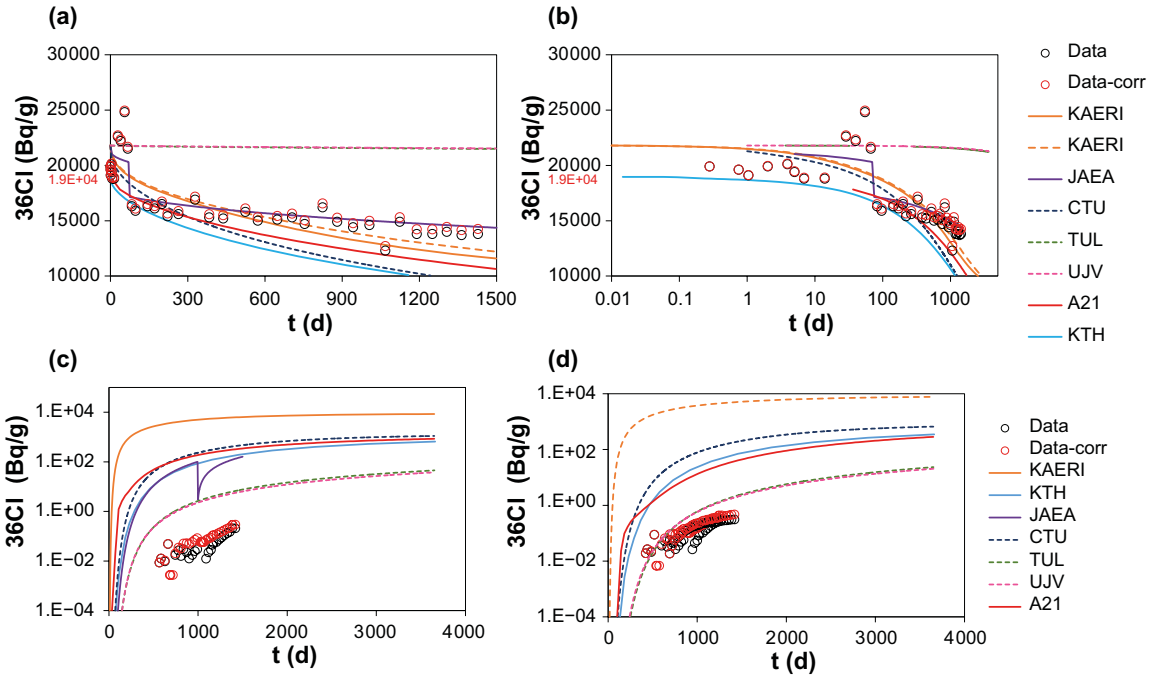

Figure 3-3. *Evolution of* ***Cl-36*** *activities (Bq/g_{water}) in the ONK-PP326 injection borehole (a,b) and in the ONK-PP324 (c) and ONK-PP327 (d) observation boreholes. Lines are* ***predictive*** *model results; black open circles are measured activities; red open circles are activities corrected for the dilution effect induced by sampling (and also by replacement of water in ONK-PP324 at t = 1 028 d). The red numbers on the vertical axis (a,b) indicate the theoretical initial activity. Analytical uncertainities are 2 % to 3 % for ONK-PP326, less than 50 % for ONK PP324, and less than 15 % for ONK PP327, with somewhat larger uncertainties for the first few points in both ONK-PP324 and ONK-PP327.*

Figure 3-4 shows the results of the back-analysis calculations by the different teams, together with the experimental data. The ϕ and D_e values implemented by the teams in the rock matrix are rather consistent (Table 3-4; in addition, A21 and TUL assumed the presence of a BDZ). Figure 3-4a,b shows the model and experimental results for the injection borehole. The curve from VTT clearly shows the effect of the leakage at t = 67 days (the other teams did not include it in the models), and reproduces well the observed decrease in concentrations (except for the observed transient increase at the time of the leakage). After about 600 days, the different curves are rather similar.

Concerning the observation boreholes, Figure 3-4c,d shows the back-analysis model and experimental results. The results from VTT clearly reflect the full replacement of water in ONK-PP324 at t = 1 028 days. The fits are approximate in all cases, but with a very good match to the ONK-PP324 data after water replacement by HYRL. This breakthrough curve corresponds to a separate fit to the observation-borehole data considering only the time after replacement of water (t = 1 028 d; ϕ = 0.01, $D_e = 5 \times 10^{-14}$ m^2/s).

The overall match of calculated results to both injection- and observation-borehole data (back-analysis) can be considered to be rather acceptable in the calculations by VTT (ϕ = 0.005, $D_e = 5.0 \times 10^{-14}$ m^2/s) and TUL (ϕ = 0.01, $D_e = 5.0 \times 10^{-14}$ m^2/s, BDZ with larger values), and reflecting an effect from anion exclusion, mainly on D_e. The results from A21 show a larger underestimation of activities in the observation boreholes, especially in ONK-PP327, perhaps related to a very strong BDZ effect assumed for those boreholes (ϕ = 0.03).

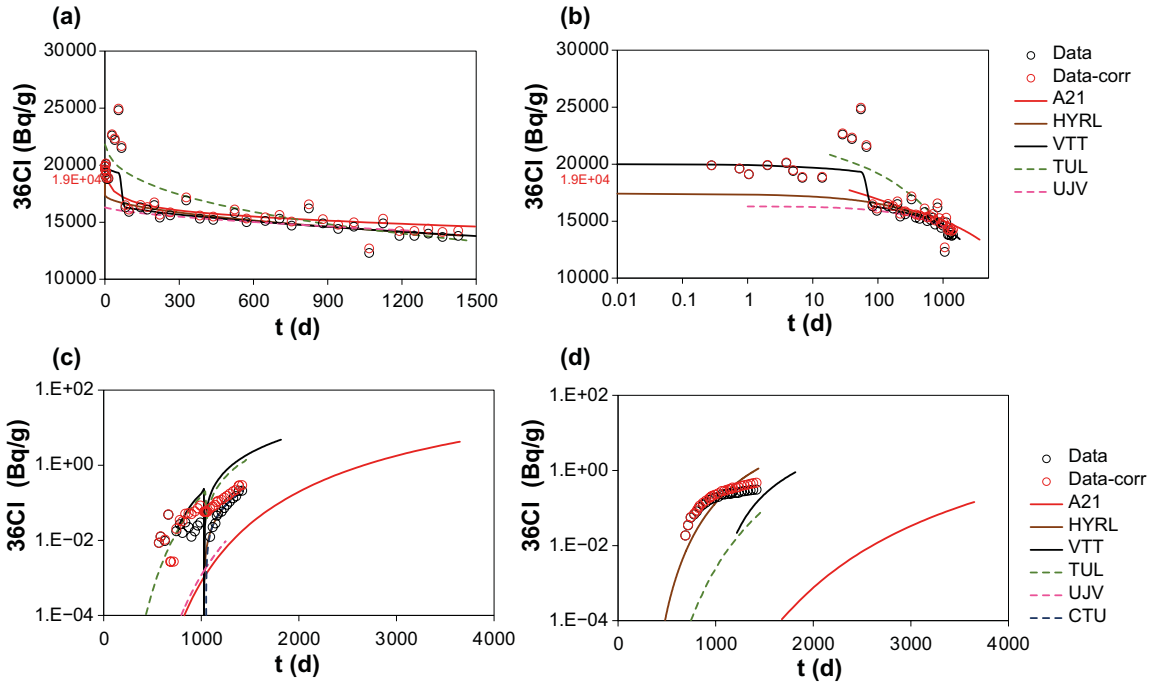

Figure 3-4. *Evolution of **Cl-36** activities (Bq/g_{water}) in the ONK-PP326 injection borehole (a,b) and in the ONK-PP324 (c) and ONK-PP327 (d) observation boreholes. Lines are **back-analysis** model results; black open circles are measured activities; red open circles are activities corrected for the dilution effect induced by sampling (and also by replacement of water in ONK-PP324 at t = 1 028 d). The red numbers on the vertical axis (a,b) indicate the theoretical initial activity. Analytical uncertainities are 2 % to 3 % for ONK-PP326, less than 50 % for ONK PP324, and less than 15 % for ONK PP327, with somewhat larger uncertainties for the first few points in both ONK-PP324 and ONK-PP327.*

Table 3-4. Porosities and effective diffusion coefficients for Cl-36 implemented in the back-analysis models by the different teams.

TEAM	ϕ	D_e ($\times 10^{-13}$ m^2/s)
HYRL	0.01	0.4
VTT	0.005	0.5
A21 matrix	0.006	0.25
A21 BDZ (21.75 mm)	0.03	2.1
TUL matrix	0.01	0.5
TUL BDZ (50 mm)	0.02	1.26
UJV	0.0094	0.35
CTU	0.0094	0.44
PROGEO	-	-
CFE	-	-

TUL values in the BDZ are maximum values (decrease with distance from borehole wall).

3.3 Na-22

Figure 3-5 shows the results of the predictive model calculations from the different teams, together with the experimental measurements (online measurements also included). The ϕ, D_e and K_d values implemented by the teams are reported in Table 3-5 (KAERI did not report bulk parameters; all parameters were mineral-specific). The values were rather consistent (except for JAEA), with differences given by the implementation of anisotropic diffusion or the presence of a BDZ assumed by some of the teams. As was the case with the conservative tracers, different initial concentration values were assumed by different teams. All the model results in the injection borehole, except for those from JAEA (ONK-PP326; Figure 3-5a,b), clearly underestimated the measured activities, suggesting that sorption of Na-22 in the rock was less than expected. This overestimation of sorption in the predictive calculations was already observed in Task 9A (predictive modelling of the REPRO WPDE experiments; Soler et al. 2019). JAEA used much smaller K_d values (in addition to the leakage event early during the experiment), which are clearly more consistent with the observations.

Not all the teams included the observation boreholes in the predictive calculations. Those who did showed no breakthrough of Na-22 in the observation boreholes (Figure 3-5c,d), which agrees well with the experimental observations. Only negligible activities were detected in the observation boreholes (< 0.05 Bq/g water), probably related to contamination. KAERI was the only team to report some breakthrough in late stages of the experiment and continuing during the extended 10-year calculation period.

Table 3-5. Porosities, effective diffusion coefficients and sorption distribution coefficients for Na-22 implemented in the predictive models by the different teams (central reference cases).

TEAM	ϕ	D_e (× 10^{-13} m^2/s)	K_d (× 10^{-3} m^3/kg)
KTH	0.01	2.5	1.3
A21	0.006	4.0 || 2.0 ⊥	1.3
TUL	0.0094	4.65	1.3
UJV	0.0094	4.65	1.3
CTU	0.0094	4.65	1.3
JAEA matrix	0.0068	1.7 || 0.81 ⊥	0.013
JAEA BDZ (1 mm)	0.05	40 || 19 ⊥	0.015
CFE	0.006	4.3 || 2.1 ⊥	P_s, T_s, T_d
KAERI	IGN	IGN	IGN

||: Parallel to foliation.

⊥: Perpendicular to foliation.

IGN: Intragranular Network Model.

P_s, T_s, T_d: Sorption implemented through these three parameters.

JAEA values in the BDZ are maximum values (linear decrease with distance from borehole wall).

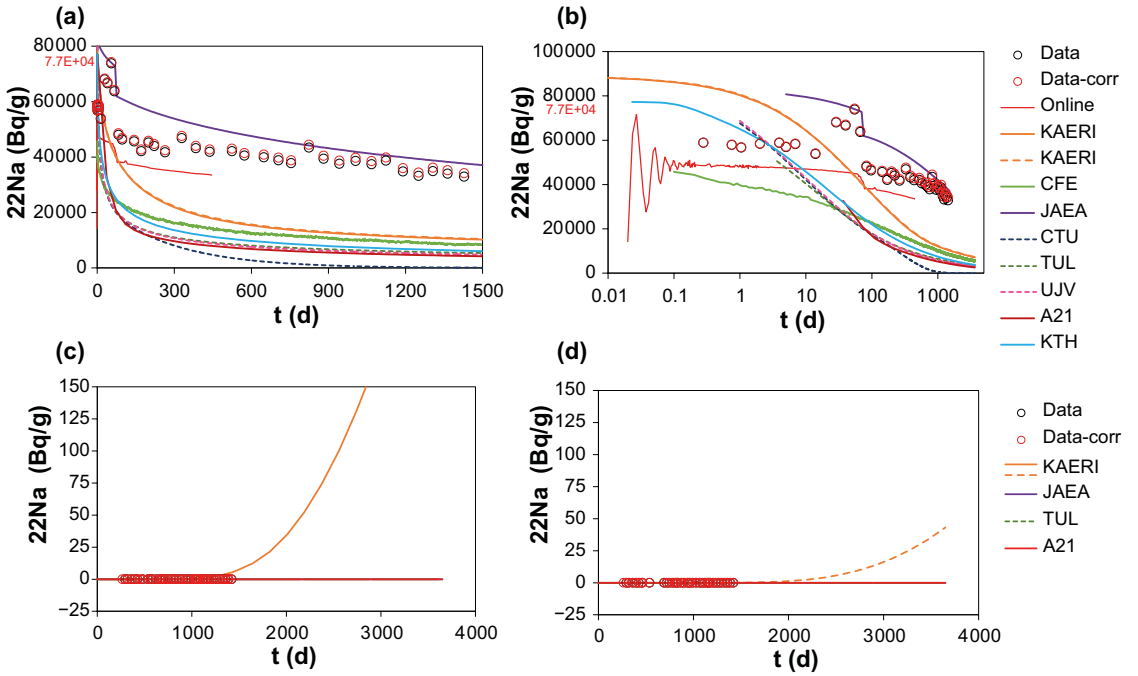

Figure 3-5. *Evolution of **Na-22** activities (Bq/g_{water}) in the ONK-PP326 injection borehole (a,b) and in the ONK-PP324 (c) and ONK-PP327 (d) observation boreholes. Lines are **predictive** model results; black open circles are measured activities; red open circles are activities corrected for the dilution effect induced by sampling (and also by replacement of water in ONK-PP324 at t = 1 028 d). The thin red line (a,b) corresponds to the online measurements. The red numbers on the vertical axis (a,b) indicate the theoretical initial activity. Analytical uncertainities are less than 1 % for ONK-PP326, with somewhat larger uncertainties for the early online measurements. Measured activities in both ONK-PP324 and ONK-PP327 are below or close to the detection limit (ca 0.001 Bq/g).*

Figure 3-6 shows the results of the back-analysis calculations by the different teams, together with the experimental data. Only two teams reported the results for the observation boreholes. The model fittings were in all the cases based on the sample measurements; the online data was not considered. The choices of initial concentrations in the injection borehole by different teams were still different (Figure 3-6a,b). All model results are much more consistent with the measured data than in the predictive calculations. To this end, K_d values had to be substantially reduced (orders of magnitude) compared to the values in the supporting laboratory data (Tables 1-6 and 3-6). Also, the curve from VTT clearly shows the effect of the leakage at $t = 67$ days (the other teams did not include it in the back-analysis models). The results from TUL, which used an initial concentration similar to that used by VTT, required the implementation of a BDZ with a large D_e value, together with another relatively large value in the rock matrix (Table 3-6). These parameter values translated into a somewhat fast drop in concentrations compared to the measurements (Figure 3-6a,b) and tracer breakthrough in the observation boreholes (Figure 3-6c,d). The results from all the other teams were rather consistent with the observations.

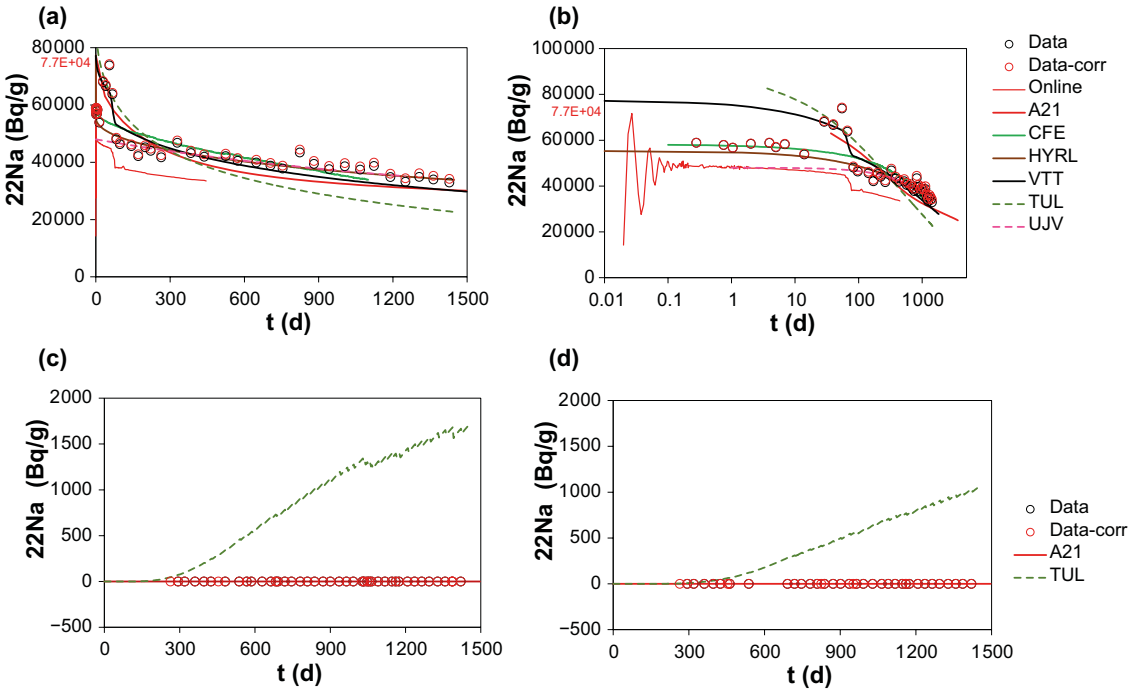

Figure 3-6. *Evolution of* ***Na-22*** *activities (Bq/g_{water}) in the ONK-PP326 injection borehole (a,b) and in the ONK-PP324 (c) and ONK-PP327 (d) observation boreholes. Lines are* ***back-analysis*** *model results; black open circles are measured activities; red open circles are activities corrected for the dilution effect induced by sampling (and also by replacement of water in ONK-PP324 at t = 1028 d). The thin red line (a,b) corresponds to the online measurements. The red numbers on the vertical axis (a,b) indicate the theoretical initial activity. Analytical uncertainities are less than 1 % for ONK-PP326, with somewhat larger uncertainties for the early online measurements. Measured activities in both ONK-PP324 and ONK-PP327 are below or close to the detection limit (ca 0.001 Bq/g).*

Table 3-6. Porosities, effective diffusion coefficients and sorption distribution coefficients for Na-22 implemented in the back-analysis models by the different teams.

TEAM	ϕ	D_e ($\times 10^{-13}$ m^2/s)	K_d ($\times 10^{-3}$ m^3/kg)
HYRL	0.01	0.45	0.024
VTT	0.009	0.5	0.1
A21 matrix	0.006	0.36	0.0065
A21 BDZ (21.75 mm)	0.03	3.0	0.0065
TUL matrix	0.01	5.05	0.0013
TUL BDZ (50 mm)	0.02	12.7	0.0013
UJV	0.0094	0.3	0.09
CTU	-	-	-
PROGEO	-	-	-
CFE	0.0057	7.6 $\parallel$ 3.8 $\perp$	0

$\parallel$: Parallel to foliation.

$\perp$: Perpendicular to foliation.

TUL values in the BDZ are maximum values (decrease with distance from borehole wall).

3.4 Ba-133

Figure 3-7 shows the results of the predictive model calculations from the different teams, together with the experimental measurements (online measurements also included). The ϕ, D_e and K_d values implemented by the teams are reported in Table 3-7 (KAERI did not report bulk parameters; CFE did not report the K_d values corresponding to their implementation of sorption). The values, except for the somewhat weaker sorption and smaller matrix D_e values implemented by JAEA, were all rather consistent. Some teams did consider anisotropic diffusion. In addition, JAEA assumed the presence of a BDZ with larger ϕ, D_e and K_d values.

All the model results for the injection borehole (ONK-PP326; Figure 3-7a,b,c) approximated relatively well the strong drop in concentrations (especially in the case of CFE). However, large differences are observed between models in the early part of the experiment (up to ca 200 days). Notice that TUL, CTU, and UJV implemented the same parameter values (Table 3-7), but the results are remarkably different in the early part of the experiment (Figure 3-7b). This observation is most probably due to differences in the spatial discretisations used in the models, which is expected to especially affect strongly-sorbing tracers. This effect had already been observed in Task 9A (predictive modelling of the REPRO WPDE experiments; Soler et al. 2019). This discretisation effect may also affect the results from other teams. Regarding the observation boreholes, all the teams that reported results for those boreholes showed no breakthrough of Ba-133 (Figure 3-7d,e).

Table 3-7. Porosities, effective diffusion coefficients and sorption distribution coefficients for Ba-133 implemented in the predictive models by the different teams (central reference cases).

TEAM	ϕ	D_e ($\times 10^{-13}$ m^2/s)	K_d ($\times 10^{-2}$ m^3/kg)
KTH	0.01	1.6	6.0
A21	0.006	4.0 || 2.0 ⊥	6.0
TUL	0.0094	3.0	6.0
UJV	0.0094	3.0	6.0
CTU	0.0094	3.0	6.0
JAEA matrix	0.0068	0.46 || 0.22 ⊥	1.7
JAEA BDZ (1 mm)	0.05	11 || 5.5 ⊥	2.6
CFE	0.006	4.3 || 2.1 ⊥	P_s, T_s, T_d
KAERI	IGN	IGN	IGN

||: Parallel to foliation.

⊥: Perpendicular to foliation.

IGN: Intragranular Network Model.

P_s, T_s, T_d: Sorption implemented through these three parameters.

JAEA values in the BDZ are maximum values (linear decrease with distance from borehole wall).

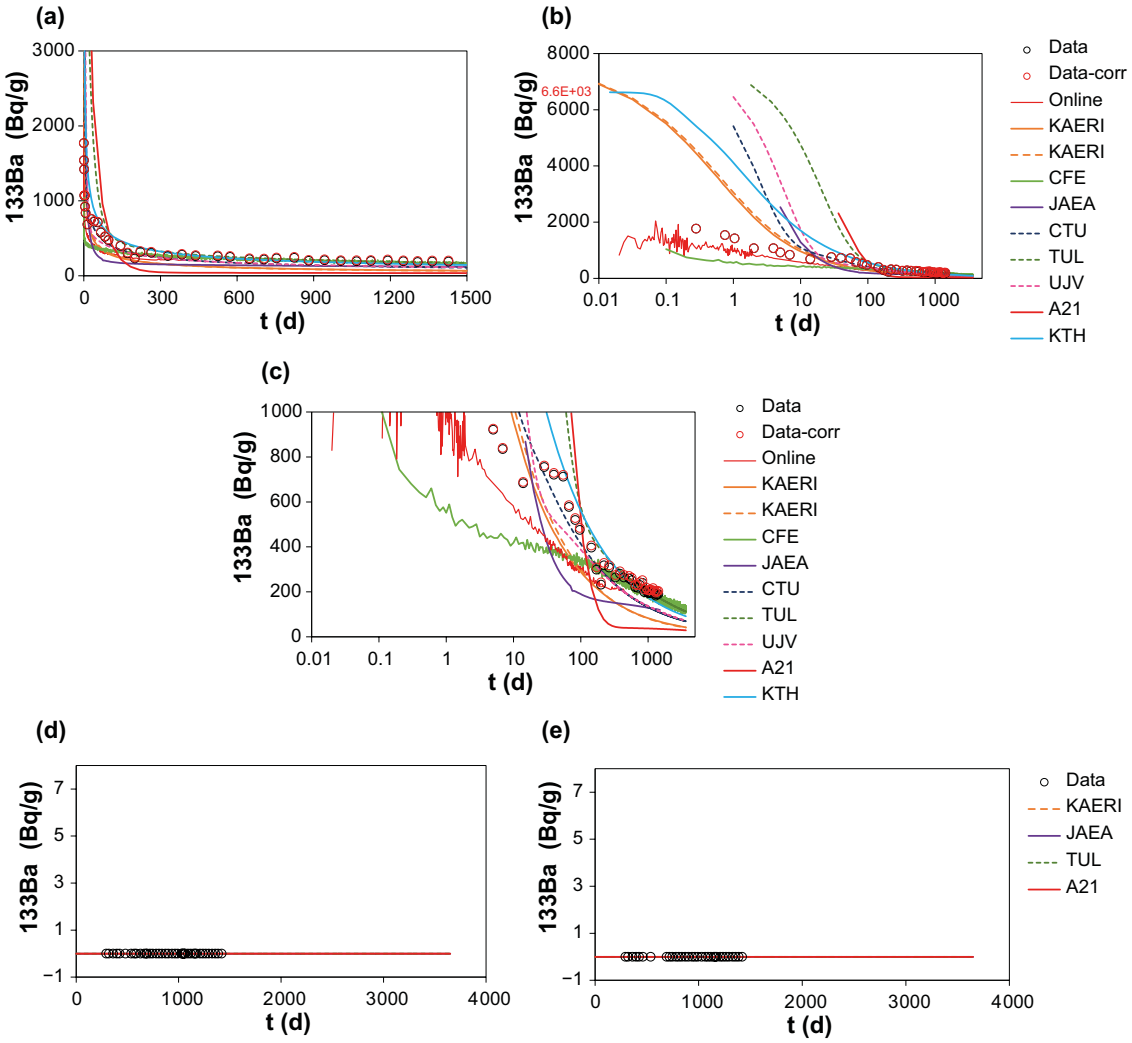

Figure 3-7. *Evolution of* ***Ba-133*** *activities (Bq/g_{water}) in the ONK-PP326 injection borehole (a,b,c) and in the ONK-PP324 (d) and ONK-PP327 (e) observation boreholes. Lines are* ***predictive*** *model results; black open circles are measured activities; red open circles are activities corrected for the dilution effect induced by sampling. The thin red line (a,b,c) corresponds to the online measurements. The red numbers on the vertical axis (b) indicate the theoretical initial activity. The two sets of results from KAERI correspond to two separate runs (one for each observation borehole). Analytical uncertainities are less than 5 % (samples) and less than 10 % (online) for ONK-PP326, with somewhat larger uncertainties for the early online measurements. Measured activities in both ONK-PP324 and ONK-PP327 are below the detection limit (ca 0.001 Bq/g).*

Figure 3-8 shows the results of the back-analysis calculations by the different teams, together with the experimental data. The model fittings were in all the cases based on the sample measurements; the online data was not considered. All model results match quite well the measured concentrations after ca 100 days. Most teams had to reduce the K_d values to different extents compared to values used in the predictive calculations (Tables 3-7 and 3-8). Model results in the early part of the experiment still show significant differences between models. An important factor is the different initial concentrations that were assumed by different teams. Some teams considered the theoretical initial concentrations calculated from the injected activity (Bq) and the volume of water in the borehole, while other teams assumed values based on the first measurements shortly after the start of the experiment (UJV). These first measured values were much smaller than the theoretical initial concentration, due to the strongly-sorbing nature of Ba-133. HYRL performed a fit based only on late data (t > 10 d) and did not consider the early data with higher concentrations (a very low initial concentration was assumed). The approaches from both UJV and HYRL, assuming small initial concentrations, resulted in rather small K_d values (Table 3-8).

In the case of CFE, very intense sorption right at the borehole wall caused a very fast drop in activity in the injection borehole. This issue is discussed in more detail in the corresponding report from CFE.

Only A21 reported results for the observation boreholes, showing no breakthrough of Ba-133 (Figure 3-8d,e).

Table 3-8. Porosities, effective diffusion coefficients and sorption distribution coefficients for Ba-133 implemented in the back-analysis models by the different teams.

TEAM	ϕ	D_e ($\times 10^{-13}$ m^2/s)	K_d ($\times 10^{-2}$ m^3/kg)
HYRL	0.01	0.45	0.23
VTT	0.009	2.0	5.0
A21 matrix	0.006	0.36	1.5
A21 BDZ (21.75 mm)	0.03	3.0	1.5
TUL matrix	0.01	3.25	3.07
TUL BDZ (50 mm)	0.02	8.20	61.45
UJV	0.0094	1.47	0.2
CTU	-	-	-
PROGEO	-	-	-
CFE	0.0057	7.6 || 3.8 $\perp$	× 0.17 compared to predictive case

||: Parallel to foliation.

$\perp$: Perpendicular to foliation.

TUL values in the BDZ are maximum values (decrease with distance from borehole wall).

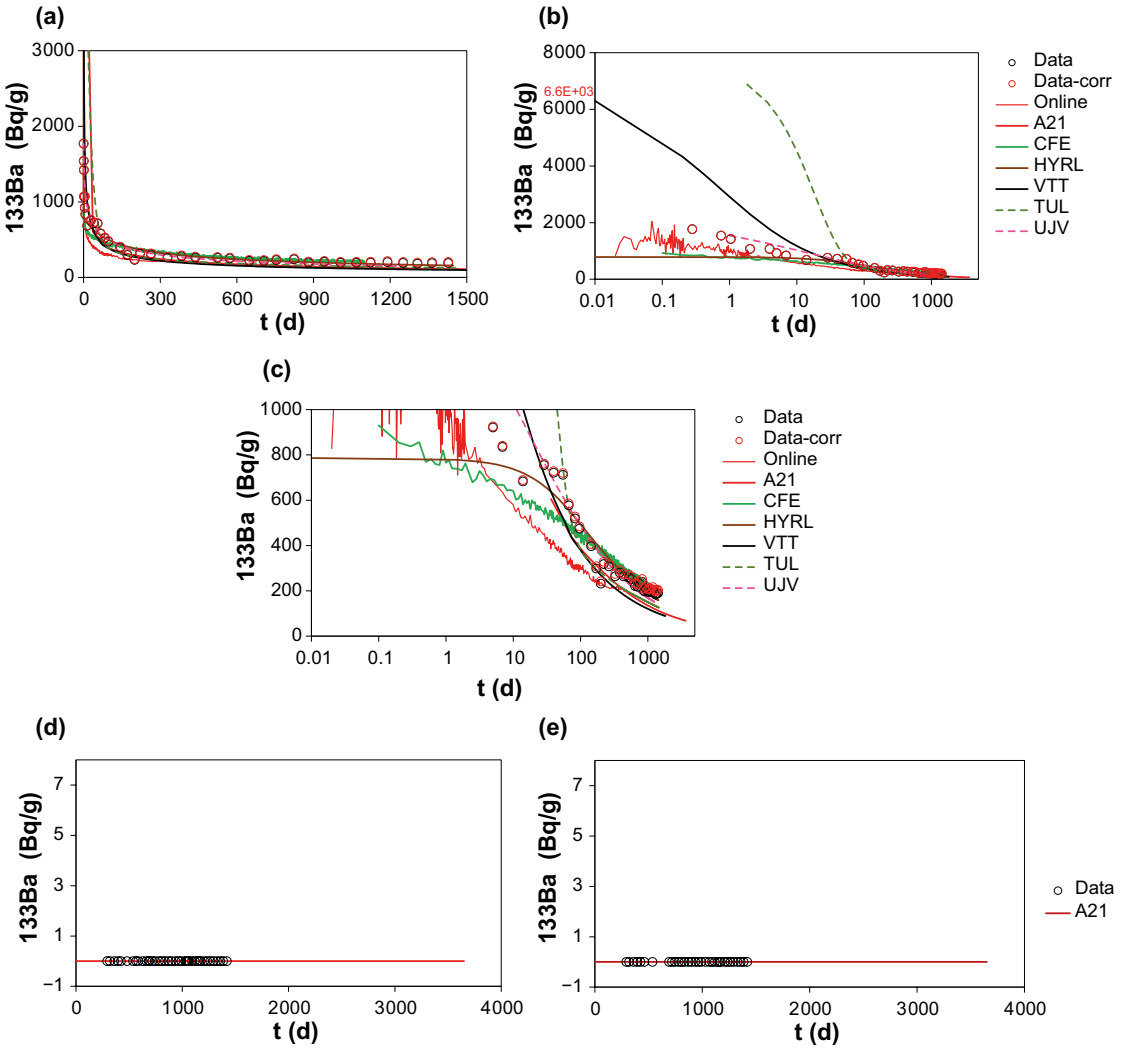

Figure 3-8. *Evolution of* ***Ba-133*** *activities (Bq/g_{water}) in the ONK-PP326 injection borehole (a,b,c) and in the ONK-PP324 (d) and ONK-PP327 (e) observation boreholes. Lines are* ***back-analysis*** *model results; black open circles are measured activities; red open circles are activities corrected for the dilution effect induced by sampling. The thin red line (a,b,c) corresponds to the online measurements. The red numbers on the vertical axis (b) indicate the theoretical initial activity. Analytical uncertainities are less than 5 % (samples) and less than 10 % (online) for ONK-PP326, with somewhat larger uncertainties for the early online measurements. Measured activities in both ONK-PP324 and ONK-PP327 are below the detection limit (ca 0.001 Bq/g).*

3.5 Cs-134

Figure 3-9 shows the results of the predictive model calculations from the different teams, together with the experimental measurements (online measurements also included). The ϕ, D_e and K_d values implemented by the teams are reported in Table 3-9 (KAERI did not report bulk parameters; CFE did not report the K_d values corresponding to their implementation of sorption). The values were rather consistent, although JAEA implemented somewhat smaller K_d and D_e values in the rock matrix. Some teams did consider anisotropic diffusion. In addition, JAEA assumed the presence of a BDZ with larger ϕ, D_e and K_d values.

Despite the rather consistent parameter values implemented by the different teams, the results for the injection borehole show significant differences (ONK-PP326; Figure 3-9a,b,c). Again, like in the case of Ba-133, spatial discretisation may play an important role (compare, e.g., the results from TUL, CTU and UJV; identical parameter values). Regarding the observation boreholes, all the teams that reported results for those boreholes showed no breakthrough of Cs-134 (Figure 3-10d,e).

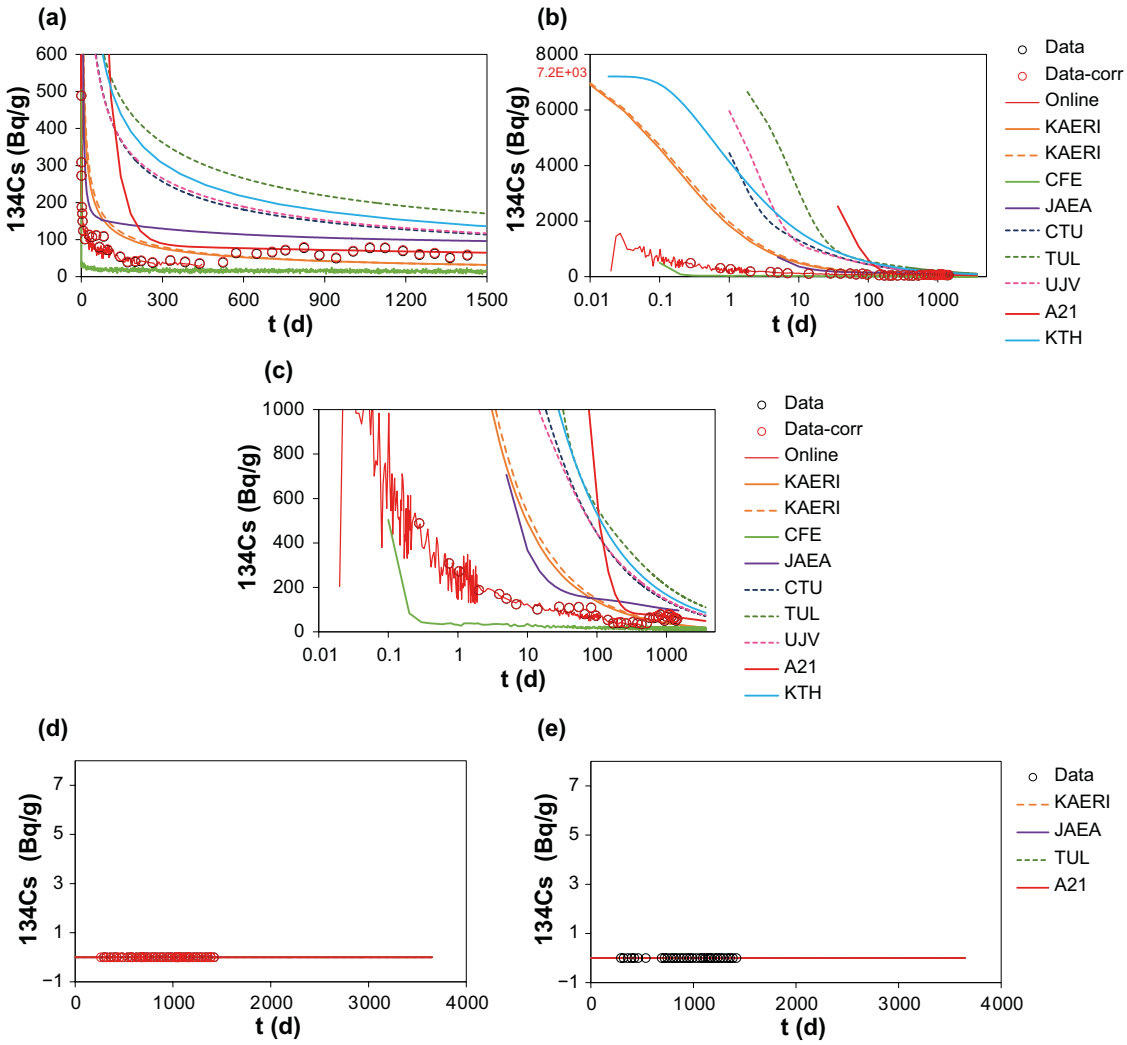

Figure 3-9. *Evolution of* ***Cs-134*** *activities (Bq/g_{water}) in the ONK-PP326 injection borehole (a,b,c) and in the ONK-PP324 (d) and ONK-PP327 (e) observation boreholes. Lines are* ***predictive*** *model results; black open circles are measured activities; red open circles are activities corrected for the dilution effect induced by sampling (and also by replacement of water in ONK-PP324 at t = 1 028 d). The thin red line (a,b,c) corresponds to the online measurements. The red number on the vertical axis (b) indicate the theoretical initial activity. Analytical uncertainities are less than 15 % (samples) and less than 100 % (online) for ONK-PP326. Measured activities in both ONK-PP324 and ONK-PP327 are below or very close to the detection limit (ca 0.001 Bq/g).*

Table 3-9. Porosities, effective diffusion coefficients and sorption distribution coefficients for Cs-134 implemented in the predictive models by the different teams (central reference cases).

TEAM	ϕ	D_e ($\times 10^{-13}$ m^2/s)	K_d ($\times 10^{-2}$ m^3/kg)
KTH	0.01	3.0	3.1
A21	0.006	4.0 || 2.0 ⊥	3.1
TUL	0.0094	3.0	3.1
UJV	0.0094	3.0	3.1
CTU	0.0094	3.0	3.1
JAEA matrix	0.0068	1.7 || 0.81 ⊥	1.6
JAEA BDZ (1 mm)	0.05	400 || 19 ⊥	3.0
CFE	0.006	4.3 || 2.1 ⊥	P_s, T_s, T_d
KAERI	IGN	IGN	IGN

||: Parallel to foliation.

⊥: Perpendicular to foliation.

IGN: Intragranular Network Model.

P_s, T_s, T_d: Sorption implemented through these three parameters

JAEA values in the BDZ are maximum values (linear decrease with distance from borehole wall).

Figure 3-10 shows the results of the back-analysis calculations by the different teams, together with the experimental data. Figure 3-10a,b,c shows the results for the injection borehole (ONK-PP326). Differences between teams are rather large. The results from A21 and CFE are consistent with the measurements. But note that the parameters implemented by these two teams were significantly different (Table 3-10). Again, an important factor is the different initial concentrations that were assumed by different teams. Like in the case of Ba-133, some teams considered the theoretical initial concentrations calculated from the injected activity (Bq) and the volume of water in the borehole, while other teams assumed values based on the first measurements shortly after the start of the experiment (UJV). These first measured values were much smaller than the theoretical initial concentration, due to the strongly-sorbing nature of Cs-134. HYRL performed a fit based only on late data (t > 10 d) and did not consider the early data with higher concentrations (a very low initial concentration was assumed). Again, the approaches from both UJV and HYRL, assuming small initial concentrations, resulted in rather small K_d values (Table 3-10).

Only A21 reported results for the observation boreholes, showing no breakthrough of Cs-134 (Figure 3-10d,e).

Table 3-10. Porosities, effective diffusion coefficients and sorption distribution coefficients for Cs-134 implemented in the back-analysis models by the different teams.

TEAM	ϕ	D_e ($\times 10^{-13}$ m^2/s)	K_d ($\times 10^{-2}$ m^3/kg)
HYRL	0.01	0.45	0.33
VTT	0.009	5.0	40.0
A21 matrix	0.006	0.36	9.0
A21 BDZ (21.75 mm)	0.03	3.0	9.0
TUL matrix	0.01	3.25	3.10
TUL BDZ (50 mm)	0.02	8.20	61.91
UJV	0.0094	3.0	0.5
CTU	-	-	-
PROGEO	-	-	-
CFE	0.0057	7.6 || 3.8 ⊥	× 0.06 compared to predictive case

||: Parallel to foliation.

⊥: Perpendicular to foliation.

TUL values in the BDZ are maximum values (decrease with distance from borehole wall).

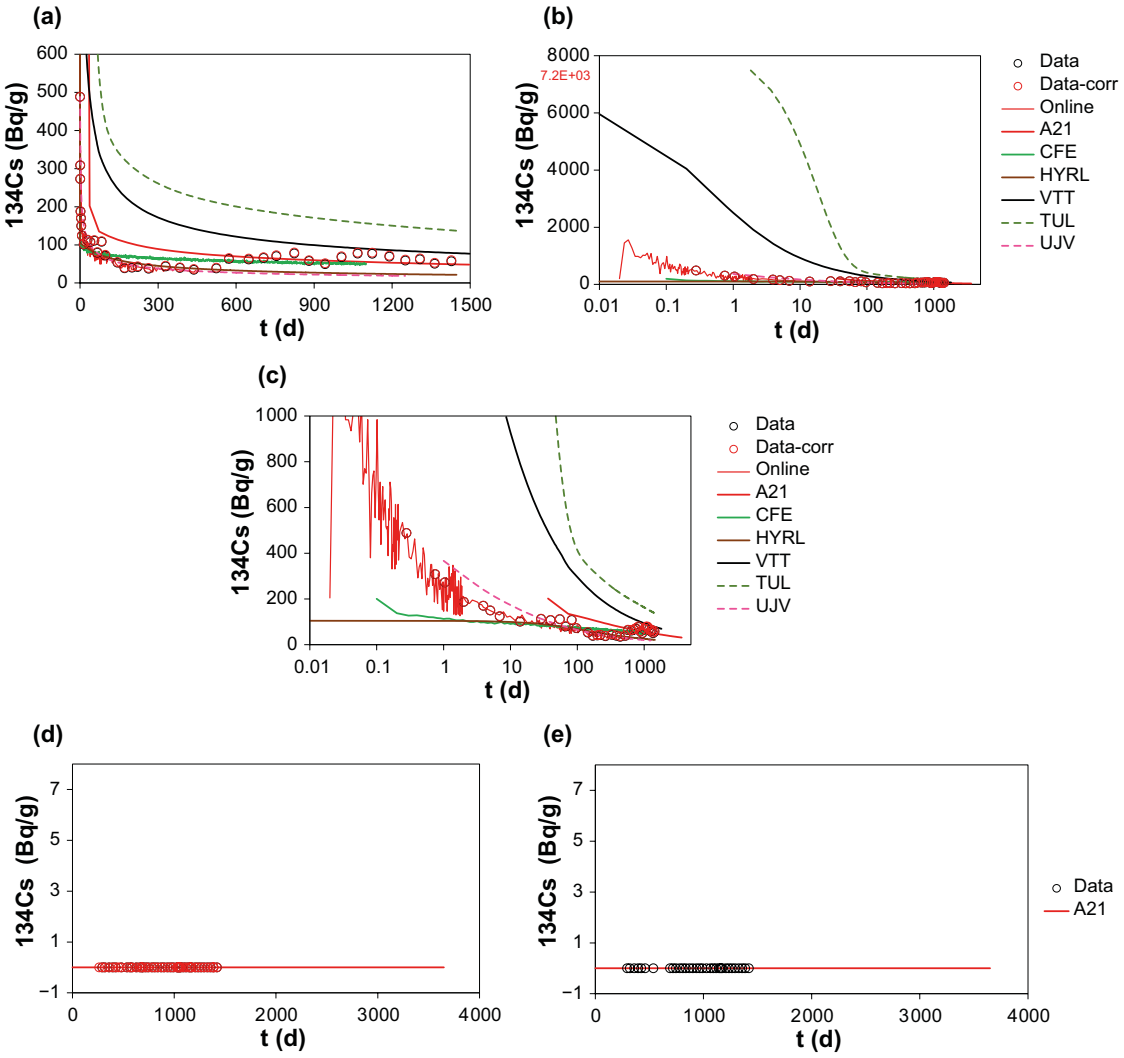

Figure 3-10. *Evolution of* ***Cs-134*** *activities (Bq/g_{water}) in the ONK-PP326 injection borehole (a,b,c) and in the ONK-PP324 (d) and ONK-PP327 (e) observation boreholes. Lines are* ***back-analysis*** *model results; black open circles are measured activities; red open circles are activities corrected for the dilution effect induced by sampling (and also by replacement of water in ONK-PP324 at t = 1 028 d). The thin red line (a,b,c) corresponds to the online measurements. The red number on the vertical axis (b) indicate the theoretical initial activity. Analytical uncertainities are less than 15 % (samples) and less than 100 % (online) for ONK-PP326. Measured activities in both ONK-PP324 and ONK-PP327 are below or very close to the detection limit (ca 0.001 Bq/g).*

4 Summary and conclusions

The REPRO-TDE in situ diffusion experiment was carried out between November 2015 and December 2019 at the ONKALO underground research facility by Geosigma AB and the University of Helsinki (Department of Chemistry), on assignment from Posiva Oy. Synthetic groundwater containing radionuclide tracers was circulated in a packed-off interval of the ONK-PP326 injection borehole. The evolution of tracer concentrations was monitored in the injection borehole and in packed-off intervals of the ONK-PP324 and ONK-PP327 observation boreholes. The distances between injection and observation borehole intervals were of the order of 0.1 m. The selected tracers were HTO (water tracer), Cl-36 (anion), Na-22 (weakly sorbing cation), Ba-133 and Cs-134 (strongly sorbing cations). In Task 9C of Task Force GWFTS the modelling teams were asked (1) to make predictions of the evolution of tracer concentrations in the different boreholes, and (2) to model the experimental results (borehole concentrations) after they were made available. Supporting laboratory-based information concerning porosities, diffusion coefficients and sorption partition coefficients was provided in the task description (Andersson et al. 2020).

Eleven modelling teams participated in Task 9C. Three main types of models were applied: (1) an analytical solution to the diffusion-retention equations, (2) continuum-porous-medium-type numerical models, and (3) microstructure-based models, accounting for small-scale heterogeneities (mineral grains and porosities). Models were mainly two-dimensional, although 3D model results were also presented. Direct comparison of two- and three-dimensional results for HTO by one of the teams (predictive modelling) showed only a very small effect from the different geometric setups.

The results of the predictive model calculations for the injection borehole showed some differences between teams due to different initial concentrations assumed in the calculations. An early version of the task description had reported total water volumes that were slightly smaller than the final values, resulting in higher initial tracer concentrations. However, this was not a significant factor in the overall calculated evolution of tracer concentrations.

For HTO, the predicted evolutions of tracer concentrations in ONK-PP326 were mostly consistent, reflecting also the similar parameter values (ϕ, D_e) used by the different models. The modelling results were also similar to the measured evolution of concentrations (not known by the teams at the time of the predictive calculations), except for the difference given by different initial concentrations assumed in different models. However, all model results greatly overestimated the measured concentrations in the observation boreholes. JAEA adopted model parameter values from their concept for upscaling from laboratory to in situ conditions, resulting in a somewhat different tracer evolution.

In the case of Cl-36, the predictive model results showed similar characteristics to those of HTO. However, two teams assumed very small ϕ and D_e values, resulting in practically constant concentrations in the injection borehole. These constant concentrations were not consistent with the measured evolution of tracer concentrations that was made available at a later time. In general, most model results also greatly overestimated the measured concentrations in the observation boreholes.

Concerning the weakly sorbing Na-22, most predictive models overestimated tracer sorption. Overestimation of Na-22 sorption had already been observed in the predictive calculations for Task 9A (predictive modelling of the REPRO WPDE experiments at ONKALO). However, JAEA assumed much smaller K_d values, resulting in better consistency with the experimental results. Basically, no breakthrough of Na-22 in the observation boreholes was predicted by any of the models during the experimental time (consistent with the observations), except for some limited breakthrough in the KAERI results.

For the case of the strongly sorbing Ba-133 and Cs-134, all results predicted strong drops in concentration at the injection borehole. However, large differences between different results were observed, especially in early stages of the experiment. Larger differences were observed for Cs-134, characterised by somewhat weaker sorption implemented by the teams compared to Ba-133. A significant issue here was the role played by spatial discretisation. Teams using identical ϕ, D_e and K_d values showed significantly different results, pointing to this effect. Discretisation had also been an issue for strongly-sorbing tracers in Task 9A. No breakthrough of these tracers in the observation boreholes was predicted (consistent with the observations).

In the second stage of the modelling exercise, the modelling teams tried to fit their models to the measured tracer concentrations in the different boreholes (back-analysis). Model results were clearly more consistent with the observations after this second modelling stage, but some differences remained. For instance, it was still difficult to simultaneously match the concentrations of the conservative HTO and Cl-36 in the injection and in the two observation boreholes. Approximate matches were achieved by VTT and A21 for HTO and by VTT for Cl-36. Some of the teams opted for separate fits to the observation-borehole data, either not considering a simultaneous poor fit to the injection-borehole data or using those concentrations as prescribed time-dependent boundary conditions. In the case of HTO, VTT used uniform porosities and effective diffusion coefficients in the rock ($\phi = 0.011$, $D_e = 2.0 \times 10^{-13}$ m^2/s), while A21 applied a BDZ in the three boreholes (Rock matrix: $\phi = 0.006$, $D_e = 3.6 \times 10^{-14}$ m^2/s; BDZ $\phi = 0.03$, $D_e = 3.0 \times 10^{-13}$ m^2/s). For Cl-36, the model results showed a general need for reduced D_e values (e.g. $D_e = 5 \times 10^{-14}$ m^2/s by VTT), probably related to anion-exclusion effects, compared to those applicable to HTO (values mainly in the 10^{-13} m^2/s range). Laboratory-based D_e values for HTO and Cl-36 in the task description (Andersson et al. 2020) were in the 10^{-13} m^2/s range (Table 1-3), with porosities between 0.5 % and 3 %, with most measurements about 1 % or less (Table 1-2). Laboratory results supplied in the task description for Task 9A (REPRO-WPDE; Löfgren and Nilsson 2019) had indicated smaller D_e values for Cl-36 (ca 5×10^{-15} m^2/s).

For Na-22, K_d values had to be substantially reduced (orders of magnitude; Tables 1-6 and 3-6) compared to the values in the supporting laboratory data to reproduce the injection-borehole data (no breakthrough in the observation borehes, except in the model results by one of the teams). Different concepts were applied (isotropic vs. anisotropic diffusion; homogeneous rock vs. implementation of a BDZ), resulting in similarly qualitatively good matches to the measured data. An additional issue was the difference between the theoretical initial tracer concentration (from the injected total activity and the volume of water in the borehole circulation system) and the first measurements during the experiment. Different teams assumed different values of the initial concentrations, affecting the parameter values needed to achieve a reasonable match to the data.

For the strongly-sorbing Ba-133 and Cs-134 all the back-analysis model results showed strong reductions in concentrations in the injection borehole. Better overall consistency between the teams and also with the experimental results was still achieved for Ba-133. However, in the back-analysis the K_d values implemented for Cs-134 were larger in general than those for Ba-133 (it was the other way around in the predictive models). A very important factor in controlling the model fits to the data was the choice of the initial tracer concentration. For both tracers, the differences between the theoretical initial concentration and the first measured values a few hours after tracer injection were very large. Also, the quality of the fits in early stages of the experiment for the teams that assumed initial concentrations based on the theoretical values was poor. There was great difficulty in reconciling those very different concentrations (the large value at $t = 0$ and much smaller values after only a few hours). This apparent discrepancy may point to processes not included in any of the models and causing a large initial loss of sorbing tracers. These processes could for instance be related to the activity of HTO that was detected in a section of the injection borehole between the packed-off circulation interval and the REPRO niche (unidentified transport paths). For Cs-134, the teams assuming the theoretical initial concentrations in their models required K_d values larger than those based on laboratory results, either in the whole rock matrix or in a BDZ around the injection borehole (Tables1-6 and 3-10). For Ba-133, which also experienced a very fast drop in concentrations, there was an overall general need towards slightly reduced K_d values compared to those reported in the task description (Tables 1-6 and 3-8).

Finally, different concepts concerning rock structure were applied in different models, mainly the implementation of isotropic vs. anisotropic diffusion, or the possible existence of a BDZ around the different boreholes. The role of microstructure was also included in two of the models. Modelling results have in many cases successfully reproduced the experimental observations, to different extents. However, it is not clear from the results which concepts best represent the observed behaviour. Overcoring of the experimental section had been contemplated as a possibility in early stages of the experiment, although it was finally not performed. Overcoring, and the measurement of tracer distribution profiles, could have provided important information concerning these issues, allowing the determination of tracer transport distances in different directions and potential increased sorption near the borehole walls (BDZ). In addition, even if the potential effect of advection has been shown to be very small if rock hydraulic conductivities are about 10^{-14} m/s or less, the analysis of tracer distribution profiles could have also provided evidence for or against possible advection.

From a modelling perspective, Task 9C allowed continuing with the development of models (e.g. the incorporation of microstructural information or the application of statistically anisotropic domains), and with the testing of different features, events and processes, such as isotropic versus anisotropic diffusion, the presence of borehole disturbed zones, or the explicit consideration of the dilution induced by sampling, leakages, or the replacement of solutions. The contact between the different teams and the use of the same experimental and supporting laboratory results was fundamental in the completion of the task.

Acknowledgements

The helpful comments from Kersti Nilsson and Johan Byegård and the constructive review by Lasse Koskinen are gratefully acknowledged. JAEA's modelling study was performed as a part of "The project for validating assessment methodology in geological disposal system" funded by the Ministry of Economy, Trade and Industry of Japan. The TF GWFTS Task 9 Evaluator Josep Soler is based at IDAEA-CSIC, which is a Centre of Excellence Severo Ochoa (Spanish Ministry of Science and Innovation, Project CEX2018-000794-S). Modelling studies of TUL, UJV, CTU, and PROGEO were performed as a part of the Radioactive Waste Repository Authority (SÚRAO, Czech Republic) project "Research support for the safety assessment of a deep geological repository".

In memory of Luis Moreno who contributed so much to the Task Force GWFTS and always took the time to help out and discuss scientific questions with his colleagues.

References

SKB's (Svensk Kärnbränslehantering AB) publications can be found at www.skb.com/publications.

Aalto P, Aaltonen I, Kemppainen K, Koskinen L, Lahti M, Lindgren S, Mustonen A, Ylä-Mella M, Ahokas H, Hellä P, Andersson J, Hakala M, Hudson J, Johansson E, Snellman M, Laaksoharju M, Pedersen K, Pitkänen P, Poteri A, 2009. Programme for repository host rock characterisation in the ONKALO (ReRoC). Posiva Working Report 2009-31, Posiva Oy, Finland.

Andersson P, Nilsson K, Löfgren M, 2020. Task description of Task 9C – Modeling of REPRO experiment TDE. Task 9 of SKB Task Force GWFTS – Increasing the realism in solute transport modelling based on the field experiments REPRO and LTDE-SD. SKB P-17-31, Svensk Kärnbränslehantering AB.

André M, Malmstrom M E, Neretnieks I, 2009. Specific surface area measurements on intact drillcores and evaluation of extrapolation methods for rock matrix surfaces. Journal of Contaminant Hydrology 110, 1–8.

Autio J, Siitari-Kauppi M, Timonen J, Hartikainen K, Hartikainen J, 1998. Determination of the porosity, permeability and diffusivity of rock in the excavation disturbed zone around full scale deposition holes using the ^{14}C-PMMA and He-gas methods. Journal of Contaminant Hydrology 35, 19–29.

Autio J, Hjerpe T, Siitari-Kauppi M K, 2003. Porosity, diffusivity and permeability of EDZ in crystalline rock and effect on migration in a KBS-3 type repository. In: Impact of the excavation disturbed or damaged zone (EDZ) on the performance of radioactive waste geological repositories: proceedings of a European Commission Cluster conference and workshop, Luxembourg, 3–5 November 2003, 149–155.

Bedekar V, Morway E D, Langevin C D, Tonkin M, 2016a. MT3D-USGS version 1: A U.S. Geological Survey release of MT3DMS updated with new and expanded transport capabilities for use with MODFLOW. Techniques and Methods 6-A53, U.S. Geological Survey.

Bedekar V, Morway E D, Langevin C D, Tonkin M, 2016b. MT3D-USGS version 1.0.0: Groundwater solute transport simulator for MODFLOW. U.S. Geological Survey Software Release, 30 September 2016.

Boving T B, Grathwohl P, 2001. Tracer diffusion coefficients in sedimentary rocks: correlation to porosity and hydraulic conductivity. Journal of Contaminant Hydrology 53, 85–100.

Březina J, Stebel J, Flanderka D, Exner P, Hybš J, 2018. Flow123d, Version 2.2.1, User guide and input reference. Technical university of Liberec, Faculty of Mechatronics, Informatics and Interdisciplinary Studies, Liberec, Czech Republic.

Buffle J, Zhang Z, Startchev K, 2007. Metal flux and dynamic speciation at (bio)interfaces. Part I: Critical evaluation and compilation of physico-chemical parameters for complexes with simple ligands and fulvic/humic substances. Environmental Science & Technology 41, 7609–7620.

Byegård J, Johansson H, Skålberg M, Tullborg E-L, 1998. The interaction of sorbing and non-sorbing tracers with different Äspö rock types. Sorption and diffusion experiments in the laboratory scale. SKB TR-98-18, Svensk Kärnbränslehantering AB.

CIMNE, 2009. GiD – The personal pre and post processor. International Centre for Numerical Methods in Engineering, Barcelona, Spain.

Crawford J, 2010. Bedrock K_d data and uncertainty assessment for application in SR-Site geosphere transport calculations. SKB R-10-48, Svensk Kärnbränslehantering AB.

GoldSim Technology Group, 2018. User's guide, GoldSim, Probabilistic Simulation Environment. GoldSim Technology Group, Issaquah, WA.

Gómez-Hernández J J, Journel A G, 1993. Joint sequential simulation of multiGaussian fields. Geostatistics Tróia 92, 85–94.

Hakanen M, Ervanne H, Puukko E, 2014. Safety case for the disposal of spent nuclear fuel at Olkiluoto – Radionuclide migration parameters for the geosphere. Posiva 2012-41, Posiva Oy, Finland.

Hammond G E, Lichtner P C, Mills R T, 2014. Evaluating the performance of parallel subsurface simulators: An illustrative example with PFLOTRAN. Water Resources Research 50, 208–228.

Havlová V, Zuna M, Večerník P, Brázda L, Kolomá K, Trpkošová D, Gvoždík L, Milický M, Sosna K, Svoboda J, Staš L, Souček K, 2017. Přenos hodnot migračních PArametrů granitických hornin z MIkroměřítka do REálného měřítka horninového masivu (PAMIRE) (Transfer of granitic rock migration parameters from microscale to real scale in the rock massive). Final Report, ÚJV Řež, ÚJV Z4932. (In Czech.)

Havlová V, Zuna M, Brázda L, Kolomá K, Galeková E, Rosendorf T, Jankovský F, 2019. Radionuclide migration processes in a crystalline rock environment and the migration parameters of rocks of the Bohemian Massif. Final report. SÚRAO TZ 333/2018/EN.

Hokr M, Havlová V, Vetešník A, Gvoždík L, Milický M, Polák M, Reimitz D, Říha J, Trpkošová D, Višňák J, Vopálka D, 2020. Testing of transport models using foreign in situ experiments. SÚRAO Report 481/2020/ENG, Prague, Czech Republic.

Hokr M, Havlová V, Vetešník A, Gvoždík L, Milický M, Polák M, Reimitz D, Říha J, Trpkošová D, Višňák J, Vopálka D, 2021. Testing of fracture-matrix transport models using in situ data and benchmark problems. SKB P-20-22, Svensk Kärnbränslehantering AB.

Huang I B, Yen S K, 2002. Diffusion in hollow cylinders for some boundary conditions: I. Mathematical treatment. Materials Chemistry and Physics 74, 289–299.

Ikonen J, Sammaljärvi J, Siitari-Kauppi M, Voutilainen M, Lindberg A, Kuva J, Timonen J, 2015. Investigation of rock matrix retention properties supporting laboratory studies I: Mineralogy, porosity, and pore structure. Posiva Working Report 2014-68, Posiva Oy, Finland.

Iraola A, 2015. Interface between GiD and PFLOTRAN (iGP): development and application. Universitat Autònoma de Barcelona (UAB), Catalonia, Spain.

Iraola A, Trinchero P, Voutilainen M, Gylling B, Selroos J-O, Molinero J, Svensson U, Bosbach D, Deissmann G, 2017. Microtomography-based Inter-Granular Network for the simulation of radionuclide diffusion and sorption in a granitic rock. Journal of Contaminant Hydrology 207, 8–16.

JAEA, 2015. Preliminary assessment of geological disposal system for spent fuel in Japan – First progress report on direct disposal. JAEA-Research 2015-016, Tokai-mura, Japan.

JAEA, 2020. Assessment methodology development on geological disposal system. H31 Report, Ministry of Economy, Trade and Industry, Tokyo, Japan.

JNC, 1999. H12 project to establish technical basis for HLW disposal in Japan. Supporting report 3: Safety assessment of the geological disposal system. JNC Technical Report TN1400 99-010, Tokai-mura, Japan.

Jokelainen L, Meski T, Lindberg A, Soler J M, Siitari-Kauppi M, Martin A, Eikenberg J, 2013. The determination of ^{134}Cs and ^{22}Na diffusion profiles in granodiorite using gamma spectroscopy. Journal of Radioanalytical and Nuclear Chemistry 295, 2153–2191.

Kuva J, Voutilainen M, Kekäläinen P, Siitari-Kauppi M, Timonen J, Koskinen L, 2015. Gas phase measurements of porosity, diffusion coefficient, and permeability in rock samples from Olkiluoto bedrock, Finland. Transport in Porous Media 107, 187–204.

Kuva J, Voutilainen M, Kekäläinen P, Siitari-Kauppi M, Sammaljärvi J, Timonen J, Koskinen L, 2016. Gas phase measurements of matrix diffusion in rock samples from Olkiluoto bedrock, Finland. Transport in Porous Media 115, 1–20.

Li Q, Ito K, Lowry C S, Loheide II S P, 2009. COMSOL Multiphysics: A novel approach to groundwater modeling. Groundwater 47, 480–487.

Löfgren M, Nilsson K, 2019. Task description of Task 9A – modelling of REPRO experiments WPDE-1 and WPDE-2. Task 9 of SKB Task Force GWFTS – Increasing the realism in solute transport modelling based on the field experiments REPRO and LTDE-SD. SKB P-17-18, Svensk Kärnbränslehantering AB.

Missana T, García-Gutiérrez M, Alonso U, Mingarro M, 2006. On radionuclide retention mechanisms in fractured geologic media. Journal of Iberian Geology 32, 55–77.

Muuri E, Siitari-Kauppi M, Matara-aho M, Ikonen J, Lindberg A, Qian L, Koskinen L, 2017. Cesium sorption and diffusion on crystalline rock: Olkiluoto case study. Journal of Radioanalytical and Nuclear Chemistry 311, 439–446.

Muuri E, Matara-aho M, Puhakka E, Ikonen J, Martin A, Koskinen L, Siitari-Kauppi M, 2018a. The sorption and diffusion of ^{133}Ba in crushed and intact granitic rocks from the Olkiluoto and Grimsel in situ test sites. Applied Geochemistry 89, 138–149.

Muuri E, Sorokina T, Garcia D, Grive M, Bruno J, Koskinen L, Martin A, Siitari-Kauppi M, 2018b. The diffusion of ^{133}Ba in granitic rock cubes from the Olkiluoto and Grimsel in situ test sites. Applied Geochemistry 92, 188–195.

Neretnieks I, 1980. Diffusion in the rock matrix: an important factor in radionuclide retardation. Journal of Geophysical Research 85, 4379–4397.

NUMO, 2013. Safety of the geological disposal project 2010. Safe geological disposal based on reliable technologies. English summary. NUMO TR-13-05, Nuclear Waste Management Organization of Japan.

Ohlsson Y, 2000. Studies of ionic diffusion in crystalline rock. PhD thesis. KTH Royal Institute of Technology, Sweden.

Ota K, Möri A, Alexander W R, Frieg B, Schild M, 2003. Influence of the mode of matrix porosity determination on matrix diffusion calculations. Journal of Contaminant Hydrology 61, 131–145.

Park D K, Ji S-H, 2018. Numerical simulation of anomalous observations from an in situ long-term sorption diffusion experiment in a rock matrix. Journal of Hydrology 565, 502–515.

Park D K, Ji S-H, 2020. Corrigendum to "Numerical simulation of anomalous observations from an in situ long-term sorption diffusion experiment in a rock matrix" [J. Hydrol.565 (2018) 502–515]. Journal of Hydrology 586, 124758. doi:10.1016/j.jhydrol.2020.124758

Perko J, Seetharam S C, Mallants D, 2009. Simulation tools used in long-term radiological safety assessments. Project Near Surface Disposal of Category A Waste at Dessel. NIROND-TR 2008-11 E, ONDRAF/NIRAS, Belgium.

Poteri A, Andersson P, Nilsson K, Byegård J, Skålberg M, Siitari-Kauppi M, Helariutta K, Voutilainen M, Kekäläinen P, Ikonen J, Sammaljärvi J, Lindberg A, Timonen J, Kuva J, Koskinen L, 2018a. The first matrix diffusion experiment in the water phase of the REPRO project: WPDE 1. Posiva Working Report 2017-23, Posiva Oy, Finland.

Poteri A, Andersson P, Nilsson K, Byegård J, Skålberg M, Siitari-Kauppi M, Helariutta K, Voutilainen M, Kekäläinen P, 2018b. The second matrix diffusion experiment in the water phase of the REPRO project: WPDE 2. Posiva Working Report 2017-24, Posiva Oy, Finland.

Rahkola K, Poteri A, Koskinen L, Andersson P, Nilsson K, Byegård J, Siitari-Kauppi M, Helariutta K, 2020. REPRO: Through Diffusion Experiment (TDE) – Diffusion and porosity properties of rock matrix in stress field of repository level. 22nd EGU General Assembly 2020, 4–8 May 2020. EGU2020-74.

Skagius K, Neretnieks I, 1986. Porosities and diffusivities of some nonsorbing species in crystalline rocks. Water Resources Research 22, 389–398.

Skagius K, Neretnieks I, 1988. Measurements of caesium and strontium diffusion in biotite gneiss. Water Resources Research 24, 75–84.

Soler J M, Landa J, Havlova V, Tachi Y, Ebina T, Sardini P, Siitari-Kauppi M, Eikenberg J, Martin A J, 2015. Comparative modeling of an in situ diffusion experiment in granite at the Grimsel Test Site. Journal of Contaminant Hydrology 179, 89–101.

Soler J M, Neretnieks I, Moreno L, Liu L, Meng S, Svensson U, Trinchero P, Iraola A, Ebrahimi H, Molinero J, Vidstrand P, Deissmann G, Říha J, Hokr M, Vetešník A, Vopálka D, Gvoždík L, Polák M, Trpkošová D, Havlová V, Park D-K, Ji S-H, Tachi Y, Ito T, 2019. Evaluation and modelling report of Task 9A based on comparisons and analyses of predictive modelling results for the REPRO WPDE experiments. Task 9 of SKB Task Force GWFTS – Increasing the realism in solute transport modelling based on the field experiments REPRO and LTDE-SD. SKB R-17-10, Svensk Kärnbränslehantering AB.

Svensson U, Ferry M, 2014. DarcyTools: a computer code for hydrogeological analysis of nuclear waste repositories in fractured rock. Journal of Applied Mathematics and Physics 2, 365–383.

Svensson U, Voutilainen M, Muuri E, Ferry M, Gylling B, 2019a. Modelling transport of reactive tracers in a heterogeneous crystalline rock matrix. Journal of Contaminant Hydrology 227, 103552. doi:10.1016/j.jconhyd.2019.103552

Svensson U, Trinchero P, Ferry M, Voutilainen M, Gylling B, Selroos J-O, 2019b. Grains, grids and mineral surfaces: Approaches to grain scale matrix modelling based on X-ray micro computed tomography data. SN Applied Sciences 1, 1277. doi:10.1007/s42452-019-1254-1

Tachi Y, Yotsuji K, 2014. Diffusion and sorption of Cs^+, Na^+, I^- and HTO in compacted montmorillonite as a function of porewater salinity: Integrated sorption and diffusion model. Geochimica et Cosmochimica Acta 132, 75–93.

Tachi Y, Yotsuji K, Seida Y, Yui M, 2011. Diffusion and sorption of Cs^+, I^- and HTO in samples of the argillaceous Wakkanai Formation from the Horonobe URL, Japan: Clay-based modeling. Geochimica et Cosmochimica Acta 75, 6742–6759.

Tachi Y, Ebina T, Takeda C, Saito T, Takahashi H, Ohuchi Y, Martin A J, 2015. Matrix diffusion and sorption of Cs^+, Na^+, I^- and HTO in granodiorite: Laboratory-scale results and their extrapolation to the in situ condition. Journal of Contaminant Hydrology 179, 10–24.

Tachi Y, Ito T, Akagi Y, Satoh H, Martin A, 2018. Effects of fine-scale surface alterations on tracer retention in a fractured crystalline rock from the Grimsel Test Site. Water Resources Research 54, 9287–9305.

Toropainen V, 2012. Core drilling of REPRO drillholes in ONKALO at Olkiluoto 2010–2011. Posiva Working Report 2012-26, Posiva Oy, Finland.

Tsukamoto M, Ohe T, 1993. Effects of biotite distribution on caesium diffusion in granite. Chemical Geology 107, 29–46.

Tullborg E-L, Larson S Å, 2006. Porosity in crystalline rocks – A matter of scale. Engineering Geology 84, 75–83.

Van Loon L R, Soler J M, Müller W, Bradbury M H, 2004. Anisotropic diffusion in layered argillaceous rocks: a case study with Opalinus Clay. Environmental Science & Technology 38, 5721–5728.

Van Loon L R, Glaus M A, Müller W, 2007. Anion exclusion effects in compacted bentonites: towards a better understanding of anion diffusion. Applied Geochemistry 22, 2536–2552.

Voutilainen M, Ikonen J, Sammaljärvi J, Siitari-Kauppi M, Lindberg A, Kuva J, Timonen J, Löfgren M, 2018. Investigation of rock matrix retention properties – Supporting laboratory studies II: Diffusion coefficient and permeability. Posiva Working Report 2017-39, Posiva Oy, Finland.

Widestrand H, Byegård J, Selnert E, Skålberg M, Höglund S, Gustafsson E, 2010. Long Term Sorption Diffusion Experiment (LTDE-SD) Supporting laboratory program – Sorption diffusion experiments and rock material characterization. With supplement of adsorption studies on intact rock samples from the Forsmark and Laxemar site investigations. SKB R-10-66, Svensk Kärnbränslehantering AB.

Witthüser K, Arnepalli D, Singh D N, 2006. Investigations on diffusion characteristics of granite and chalk rock mass. Geotechnical & Geological Engineering 24, 325–334.

Zheng C, 2010. MT3DMS v5.3 supplemental user's guide. Technical Report to the U.S. Army Engineer Research and Development Center, Department of Geological Sciences, University of Alabama.

Zheng C, Wang P P, 1999. MT3DMS: A modular three-dimensional multi-species transport model for simulation of advection, dispersion and chemical reactions of contaminants in groundwater systems: documentation and user's guide. Contract Report SERDP-99-1, University of Alabama.

Zuna M, Havlová V, Kolomá K, Jankovský F, Grecká M, Švagera O, Holeček J, Řihošek J, Sosna K, Gvoždík L, Milický M, Kryl J, Bukovská Z, Soejono I, Zelinková T, 2020. Výzkum puklinové konektivity v PVP Bukov – Průběžná zpráva č.1 (The research of fracture connectivity at the Bukov URF). Interim Report, SÚRAO, TZ 459/2020. (In Czech.)

Appendix A

University of Helsinki (HYRL), VTT Technical research centre of Finland Ltd (VTT), Finland

Pekka Kekäläinen (HYRL), Veli-Matti Pulkkanen (VTT)

A1 Introduction

The objective of the modelling study described in this chapter is to scope models and model parameters that could explain the decrease in the injection borehole tracer solution activities and the increase in observation boreholes tracer solutions activities in REPRO in situ through diffusion experiment (TDE). The aim of the modelling study is rather to find out 1) which model features could explain the experimental observed behaviour and 2) what is the effect of different phenomena than to find the best fit to the experimental data.

The simulated tracers are the ones used in TDE: H-3 and Cl-36 (which are a priori assumed non-sorbing), Na-22 (weakly sorbing), as well as Ba-133 and Cs-134 (strongly sorbing). The scoped models are

1) *Analytical* model: analytically solved linear, isotropic diffusion model with one-dimensional axisymmetric representation of bedrock,
2) *Linear* model: linear, isotropic diffusion model with three-dimensional representation of bedrock,
3) *Advection* model: linear, isotropic diffusion model including advection with three-dimensional representation of bedrock, and
4) *Foliation* model: linear, anisotropic foliation following diffusion model with three-dimensional representation of bedrock.

Linear sorption is assumed in all the models. The models combine batch tracer solutions with one dimensional axisymmetric (Analytical model) or three-dimensional spatial presentation (Linear, Advection and Foliation models) of the bedrock surrounding the experimental sections of the TDE drillholes. The concentration in the bedrock at the experimental section boundary is the batch solution concentration and the mass flux to bedrock decreases the batch solution concentration. The scoped parameters include the linear sorption distribution coefficient, K_d, the porosity, ε, the effective diffusion coefficient, D_e, the hydraulic conductivity, K, and the strength of foliation.

A2 Model description

A2.1 Tracers

The transport of the tracers in TDE (H-3, Cl-36, Na-22, Ba-133 and Cs-134) is considered in the models. Their half-lives, injected activities, and experimental results on their effective diffusion coefficients and linear sorption partitioning coefficients are presented in the task description (Andersson et al. 2020). Experimental results are also reported in Tables 1-2 to 1-6.

A2.2 Injection and observation solutions

The injection borehole (PP326) and the observation boreholes (PP324 and PP327) tracer solutions are considered in the model as well mixed batch solutions. The volumes of the solutions consist of the test interval (volume between the rock and dummy) and the PEEK tubing. The observation borehole PP324 solution volume increased during the experiment (at around 1 000 days) due to the equipment replacement and the increase is considered in the models. The tracer solution volumes (including the change in PP324 volume) used in the model are listed in Table 1-1.

A2.3 One-dimensional radially symmetric model geometry in Analytical model

Since the distance between the injection hole and the observation hole is small compared to their length, the model geometry is simplified to a one dimensional radially symmetric system in Analytical model (Figure A-1). Looking from the injection drillhole, a sector corresponding to the observation drillhole size represents the observation drillhole.

A2.4 Three-dimensional model geometry in *Linear*, *Advective* and *Foliation* models

TDE drillholes (PP324, PP326 and PP327) have been positioned in the model (Figure A-2a) according to the location survey data (Toropainen, 2012). The data specifies the starting points of the boreholes and the azimuth and dip angles at the measuring points (approximately every half a metre along the more than 12 m long drillholes). The drillholes PP321 and PP322 close to the TDE have been included in the model using only the initial point locations and directions. The drillhole diameters are listed in Table 1-1.

A cylindrical block (radius is 1 m and length is 2.5 m) of bedrock around the injection borehole PP326 experimental section at the end of the drillhole is considered in the model (Figure A-2b). The cylinder bottom is at the boundary of the inner guard and the top at the boundary of the outer guard. The metre long experimental section is located half a metre from the inner guard edge and a metre from the outer guard edge.

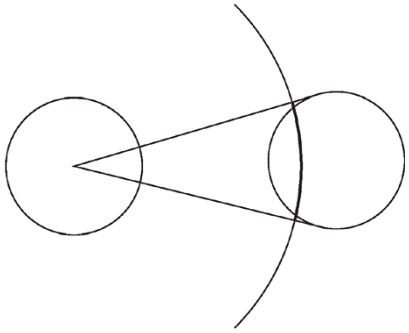

Figure A-1. *Geometrical setup of Analytical model. The injection drillhole (on left) centre is the origin of the radial coordinate system. The sector corresponding to the observation drillhole is illustrated on right.*

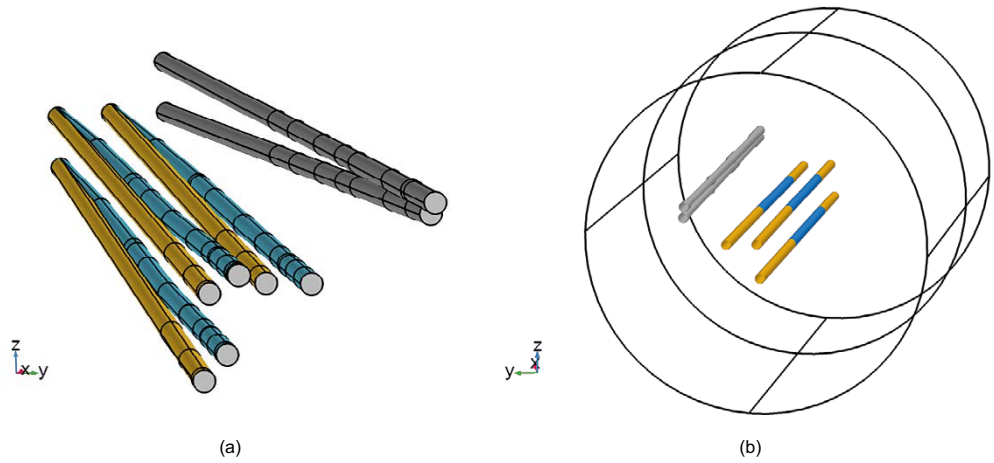

Figure A-2. *(a) TDE drillholes PP324, PP326 and PP327 locations according 1) to the initial point coordinates and directions (yellow) and 2) to the location survey data (cyan). The latter option has been chosen for modelling. The drillholes PP321 and PP322 are also illustrated (grey). (b) The modelled cylindrical block of rock around the experimental section of TDE. The radius of the cylinder is 1 m and the length 2.5 m. The experimental sections are coloured with blue, the rest of the drillholes PP324, PP326 and PP327 with yellow and PP321 and PP322 with grey.*

The bedrock in the cylinder is considered as a three-dimensional object, where the tracers can transport and where water can flow. The injection and observation borehole solutions are treated as well mixed batch solutions and, therefore, only the borehole boundaries are taken into account in the three-dimensional model geometry (that is, the inner parts of the boreholes are not considered in three dimensional model geometry).

A3 Mathematical model

The experimental results are decay corrected and, therefore, radioactive decay is not considered in the mathematical model. Consequently, instead of using specific activities directly, tracer concentrations in units kg/m^3 are used in the transport equations.

The mass balance equation of tracer i in the injection borehole batch solution is

$$V^{\text{inj}} \frac{\partial c_i^{\text{inj}}}{\partial t} = R_i^{\text{inj}}, \tag{A-1}$$

where V^{inj} is the injection borehole batch solution volume and c_i^{inj} the tracer i concentration (in units kg/m^3) in injection borehole batch solution. The supply term R_i^{inj} (kg/s) describes the decrease of concentration in the batch solution due to transport to bedrock and due to sampling. Mathematically, the supply term is

$$R_i^{\text{inj}} = -\int_{\partial\Omega_{\text{inj}}} \mathbf{j}_i \cdot \mathbf{n} dS - R_i^{\text{inj, sampling}}, \tag{A-2}$$

where $\mathbf{j}_i$ is the tracer i mass flux (in units kg/(m^{2}s)) through the drillhole boundary (with normal $\mathbf{n}$) to bedrock. Integration over the drillhole boundary $\partial\Omega_{\text{inj}}$ gives the flow rate in units kg/s from the batch solution to bedrock. $R_i^{\text{inj, sampling}}$ describes how sampling reduces the tracer concentration in the batch solution.

The mathematical models for the observation boreholes tracer concentrations are similar to the injection borehole model. Simply replacing superscript “inj” with an abbreviation for the observation drillhole PP324 (or PP327) in the previous equations yields the mathematical model.

The mass balance of tracer i in bedrock is

$$\varepsilon \frac{\partial c_i}{\partial t} + \rho_{rock} \frac{\partial c_i^s}{\partial t} + \nabla \cdot \mathbf{j}_i = \varepsilon R_i, \tag{A-3}$$

where ε is the porosity, c_i the tracer concentration in water in the bedrock porosity (kg/m^3), ρ_{rock} the rock apparent density ($\rho_{\text{rock}} = (1-\varepsilon)\rho_{\text{grain}}$ with the rock grain density ρ_{grain}), c_i^s the sorbed tracer i content (mass of tracer per mass of rock) in units (kg/kg), $\mathbf{j}_i$ the mass flux of tracer i and R_i the supply rate of tracer i in water.

The constitutive model for the sorbed content c_i^s is the linear sorption isotherm with the distribution coefficient $K_{\text{d},i}$:

$$c_i^{\text{s}} = K_{\text{d},i} c_i \,, \tag{A-4}$$

from which

$$\frac{\partial c_i^{\text{s}}}{\partial t} = K_{\text{d},i} \frac{\partial c_i}{\partial t} \,. \tag{A-5}$$

Radioactive decay or chemical reactions are not considered in model and, therefore, the supply term R_i is zero.

Resulting from the above constitutive equations, the mass balance equation for tracer i can be written in form

$$\left(\varepsilon + (1-\varepsilon)\rho_{grain} K_{d,i}\right) \frac{\partial c_i}{\partial t} + \nabla \cdot \mathbf{j}_i = 0 \,. \tag{A-6}$$

A3.1 Analytical model

In *Analytical* model, the tracers are assumed to move by linear, isotropic diffusion in bedrock meaning that the mass flux of tracer i is

$$\mathbf{j}_i = -D_e \nabla c_i \tag{A-7}$$

with the effective diffusion coefficient D_e. Consequently, the mass balance equation for tracer i in the injection reduces to form

$$V^{\text{inj}} \frac{\partial c_i^{\text{inj}}}{\partial t} = \int_{\partial\Omega_{\text{inj}}} D_e \nabla c_i \cdot \mathbf{n} dS - R_i^{\text{inj, sampling}}. \tag{A-8}$$

In one dimensional axisymmetric coordinates, the equation reduces to

$$V^{\text{inj}} \frac{\partial c_i^{\text{inj}}(t)}{\partial t} = A^{\text{inj}} D_e \frac{\partial c_i^{\text{inj}}(t)}{\partial r} - R_i^{\text{inj, sampling}}. \tag{A-9}$$

The dilution of the tracer concentration due the sampling is

$$R_i^{\text{inj, sampling}} = \frac{1}{\Delta t} \log\left(\frac{V^{\text{inj}}}{V^{\text{inj}} - \Delta V^{\text{inj}}} \right) V^{\text{inj}} c_i^{\text{inj}}, \tag{A-10}$$

where ΔV^{inj} is the volume of the samples and Δt time between them. The equations for the observation boreholes tracer concentrations are similar to the injection borehole ones (simply with a change of subscript $^{\text{inj}}$). In that case, the area A^{obs} corresponds to the sector of observation drillhole (Figure A-1).

With the diffusive mass flux in Equation (A-7), the tracer i mass balance in the bedrock, Equation (A-6), can be written as

$$\left(\varepsilon + (1-\varepsilon)\rho_{grain} K_{d,i}\right) \frac{\partial c_i}{\partial t} - \nabla \cdot (D_e \nabla c_i) = 0 \tag{A-11}$$

or alternatively (by dropping subscript i) as

$$\frac{\partial c}{\partial t} - \nabla \cdot \left(D \nabla c \right) = 0 \text{ in } \Omega \tag{A-12}$$

with the apparent diffusion coefficient

$$D = \frac{D_e}{\varepsilon + (1-\varepsilon)\rho_{grain} K_d}. \tag{A-13}$$

In one dimensional axisymmetric coordinates, the equation reduces to

$$\frac{\partial c}{\partial t} - D\left(\frac{\partial^2 c}{\partial r^2} + \frac{1}{r}\frac{\partial c}{\partial r} \right) = 0, \quad r > a, \tag{A-14}$$

where a is the radius of the injection hole.

At the beginning concentration of the tracer in the injection hole is constant c_0, and there is no tracer in the rock Ω, or in the observation drillhole, which gives us an initial condition

$$c = \begin{cases} c_0 \text{ in injection solution,} \\ 0, \text{ in bedrock and observation solution,} \end{cases} \quad \text{at } t = 0 \tag{A-15}$$

We are interested in the time evolution of the tracer concentration in the injection hole and in the observation hole.

For the injection tracer time evolution, we can eliminate the integral term on the right hand side of Equation (A-9) by rescaling the initial value c_0. Setting a boundary condition $C(t, b) = 0$ for some $b > a$ "large enough", we can solve our problem by separating the variables (see Appendix at the end of this chapter).

Consider next the observation hole. The flux into the observation hole is approximated by the flux into a sector corresponding to the observation hole at the distance $b = d - a/2$ from the center of the injection hole, here d is the distance between the centers of the injection hole (Figure A-1). We approximate the concentration the observation hole in the following way. The flux into the observation hole is computed from the flow generated by the solution of the radial diffusion equation, Equation (A-14), with boundary conditions

$$\begin{aligned} c(a,t) &= c^{\text{inj}}(t) \\ c(b,t) &= 0. \end{aligned} \tag{A-16}$$

In order to make computations simpler, the effect of dilution due the sampling in the injection hole is assumed negligible in the observation hole and we don't take it into account.

If we take into account dilution of the tracer concentration due the sampling in the observation hole, the time evolution of the concentration the observation hole, c^{obs}, can now be described with the equation

$$V^{\text{obs}} \frac{dc^{\text{obs}}}{dt}(t) = -A^{\text{obs}} D_e \frac{\partial c}{\partial r}(b,t) - R^{\text{obs, sampling}} \tag{A-17}$$

with

$$R^{\text{obs, sampling}} = \frac{1}{\Delta t} \log\left(\frac{V^{\text{obs}}}{V^{\text{obs}} - \Delta V^{\text{obs}}} \right) V^{\text{obs}} c(b,t), \tag{A-18}$$

where V^{obs} is the observation drillhole volume (either PP324 or PP327) and ΔV^{obs} the sample volume take during Δt. The solution of the model is constructed in the Appendix at the end of this chapter.

Summarizing *Analytical* model, the mathematical problem for the injection tracer solution time evolution is to find $c = c(r,t)$ and $c^{\text{inj}} = c^{\text{inj}}(t)$ such that

$$\begin{aligned} &\frac{\partial c}{\partial t} - D\left(\frac{\partial^2 c}{\partial r^2} + \frac{1}{r}\frac{\partial c}{\partial r} \right) = 0, \quad r > a, \\ &V^{\text{inj}} \frac{\partial c_i^{\text{inj}}}{\partial t}(t) = A^{\text{inj}} D_{\text{e}} \frac{\partial c}{\partial r}(a,t) - \frac{1}{\Delta t} \log\left(\frac{V^{\text{inj}}}{V^{\text{inj}} - \Delta V^{\text{inj}}} \right) V^{\text{inj}} c_i^{\text{inj}}, \end{aligned} \tag{A-19}$$

with initial values

$$c(r,0) = 0 \quad \text{and} \quad c^{\text{inj}}(0) = c_0 \tag{A-20}$$

and boundary conditions

$$c(a,t) = c^{\text{inj}} \quad \text{and} \quad c(b,t) = 0 \quad \text{for some large enough b}. \tag{A-21}$$

a is the injection drillhole radius. The value c_0 is rescaled in time to obtain the time dependence of the boundary conditions.

The mathematical problem for the observation drillhole tracer solution time evolution is

(a) to find $c = c(r,t)$ such that

$$\frac{\partial c}{\partial t} - D\left(\frac{\partial^2 c}{\partial r^2} + \frac{1}{r}\frac{\partial c}{\partial r} \right) = 0, \quad r > a, \tag{A-22}$$

with initial value $c(r,0) = 0$ and boundary conditions

$$c(a,t) = c_0 \quad \text{and} \quad c(b,t) = 0. \tag{A-23}$$

a is the injection drillhole radius, b the distance between injection and observation drillholes and c_0 is constant, and,

(b) to find $c^{obs} = c^{obs}(t)$ using solution $c = c(r,t)$ to (a) such that

$$V^{obs}\frac{dc^{obs}(t)}{dt} = -A^{obs}D_e\frac{\partial c(b,t)}{\partial r} - \frac{V^{obs}}{\Delta t}\log\left(\frac{V^{obs}}{V^{obs}-\Delta V^{obs}}\right)c(b,t) \tag{A-24}$$

with initial value $c^{obs}(0) = 0$.

A3.2 Linear model

In TDE, samples from the tracer solutions in the injection and observation drillholes have been taken according to the information provided by the Task Force. A volume of the tracer solution is extracted and the volume is replaced with a tracer free solution corresponding the chemical composition of the batch solution. In *Linear* model, instead of extracting a volume of tracer solution at certain time points, a continuous sampling rate has been used. Mathematically this is

$$R_i^{sampling} = rc_i, \tag{A-25}$$

where r is the sampling rate and c_i the tracer i concentration. The sampling rate function $r = r(t)$ has been constructed such that the sample volume V_k taken at time t_k is distributed over time period from the previous and next sampling time with a triangle distribution:

$$\frac{1}{2}(t_k - t_{k-1})r_k + \frac{1}{2}(t_{k+1} - t_k)r_k = V_k, \tag{A-26}$$

where r_k is the sampling rate at time t_k. The continuous sampling rate function $r = r(t)$ is the piecewise linear interpolation of the sampling rates r_k at times t_k. The function has been smoothened slightly to avoid sharp corners in the distribution. With the function, the volume extracted from the batch solutions in the model correspond over time to the volumes extracted from TDE.

The sampling rate functions for the injection and observation drillhole batch solutions are illustrated in Figure A-3. The sampling schedule at the beginning of TDE for the injection drillhole has been dense in comparison to later sampling schedule. To smoothen the sampling rate function, the first samples have been combined to one in the sampling rate function (green arrow in Figure A-3). The leak in the injection solution circulation (47.7 ml at 67th day of TDE) is represented with the highest peak (orange arrow). The large 90 ml samples taken from the drillhole PP324 solution can be noticed as the high plateau between approximately 700 and 1 000 days (black arrow).

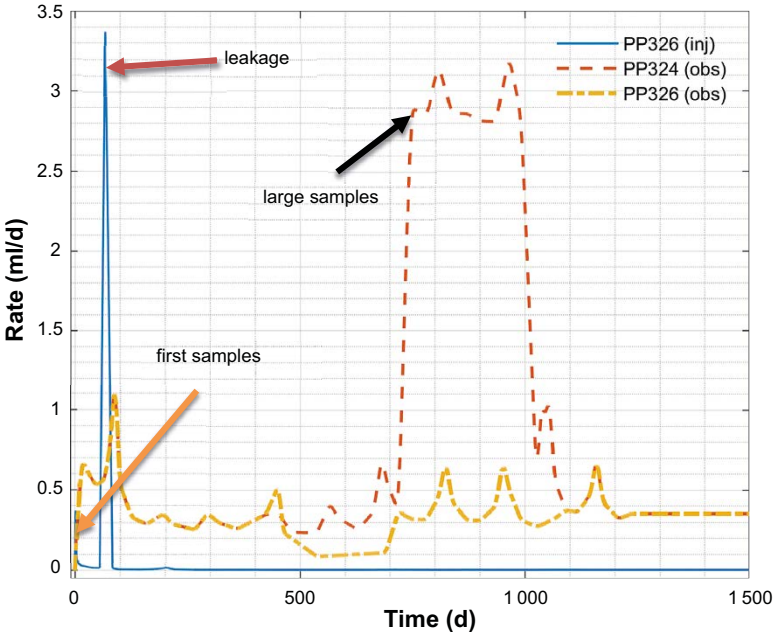

Figure A-3. *The sampling rate function for the tracer solution in the injection drillhole PP326 (blue line), the observation drillhole PP324 (red dashed line) and the observation drillhole (yellow dash-dot line).*

The tracer solution circulation equipment in drillhole PP324 was renewed at day 1 028 of TDE. The tracer solution was replaced with a new salt solution without radioactive tracers and the circulation equipment pipeline diameter was increased (from 1 mm to 2 mm). In the model, the new salt solution is taken into account by setting the PP324 solution tracer concentration to zero at the day of the equipment renewal and the new pipelines are considered by increasing the PP324 tracer solution volume (according to Table 1-1).

The constitutive model for the mass flux in *Linear* model is isotropic, linear diffusion model with effective diffusion coefficient $D_{e,i}$:

$$\mathbf{j}_i = \mathbf{j}_{d,i} = -D_{e,i}\nabla c_i . \tag{A-27}$$

The boundary conditions for tracer i concentration at the injection drillhole experimental section boundary ($\partial\Omega_{inj}$), at the observation drillhole PP324 experimental section boundary ($\partial\Omega_{obs324}$) and at the observation drillhole PP327 experimental section boundary ($\partial\Omega_{obs327}$) are

$$c_i = c_i^{inj} \text{ at } \partial\Omega_{inj}, \quad c_i = c_i^{obs324} \text{ at } \partial\Omega_{obs324} \quad \text{and} \quad c_i = c_i^{obs327} \text{ at } \partial\Omega_{obs327}, \tag{A-28}$$

where c_i^{inj}, c_i^{obs324} and c_i^{obs327} are the batch solution concentrations. For sorbing tracers, the initial values for the tracer concentrations in the injection borehole is calculated from their initial activities. For non-sorbing tracers, the initial values are calculated from the average of the first samples activities.

On outer bedrock boundaries in the model, no flux boundary is assumed:

$$\mathbf{j}_i \cdot \mathbf{n} = 0 . \tag{A-29}$$

The initial values for all the tracers in the bedrock is zero concentration.

Summarizing, the mathematical problem for *Linear* model is to find $c_i = c_i(\mathbf{x},t)$ in bedrock ($\mathbf{x} = (x,y,z)$) and $c_i^{inj} = c_i^{inj}(t)$, $c_i^{obs324} = c_i^{obs324}(t)$ as well as $c_i^{obs327} = c_i^{obs327}(t)$ such that

$$\left(\varepsilon + (1-\varepsilon)\rho_{grain}K_{d,i}\right)\frac{\partial c_i}{\partial t} + \nabla \cdot \mathbf{j}_i = 0 \tag{A-30}$$

$$V^{sol}\frac{\partial c_i^{sol}}{\partial t} = -\int_{\partial\Omega_{sol}} \mathbf{j}_i \cdot \mathbf{n} dS - rc_i, \quad \text{sol=inj, obs324, obs327} \tag{A-31}$$

$$\mathbf{j}_i = -D_{e,i}\nabla c_i \tag{A-32}$$

with initial values

$$c_i(\mathbf{x},0) = 0 \text{ in } \Omega_{bedrock} \quad c^{inj}(0) = c_0, \quad c^{obs324}(0) = 0 \text{and} \quad c^{obs327}(0) = 0$$

and boundary conditions

$$c_i = c_i^{inj} \text{ at } \partial\Omega_{inj}, \quad c_i = c_i^{obs324} \text{ at } \partial\Omega_{obs324} \quad \text{and} \quad c_i = c_i^{obs327} \text{ at } \partial\Omega_{obs327} .$$

r is the sampling rate function (Figure A-3 and Equation (A-25)).

A3.3 Advective model

In order to avoid water pressure gradients by pressure differences between drillholes, active control of water pressure was planned for TDE. Due to practical constraints, however, the pressure values were let to balance to natural values after the initial period of TDE. To estimate the effect of pressure differences between drillholes on the tracer transport, advective component is added to the tracer transport in *Linear* model.

For advective transport, a model for water flow in bedrock is needed. Here, quasistatic Darcy flow through the rock is assumed. The quasistatic assumption means that the water velocity field in the model is static at each time point and it is determined by the pressure values at the drillholes, but these pressure values may change in time.

The quasistatic mass balance equations for water is

$$\nabla \cdot \mathbf{l} = \varepsilon S \ , \tag{A-33}$$

where the water mass flux is $\mathbf{l} = \rho_{\text{water}}\mathbf{u}$, porosity ε and water supply term S. The constitutive equation for the infiltration velocity $\mathbf{u}$ is Darcy's law:

$$\mathbf{u} = -\frac{K}{\rho_{\text{water}} g}\nabla p \, . \tag{A-34}$$

Here, K is the hydraulic conductivity, ρ_{water} the water density, g the gravitational acceleration and p the water pressure. Gravitational effects are neglected due to relatively small model height (2 m).

In the model, the water pressure at experimental section boundaries of the drillholes PP324, PP326 and PP326 follow the experimentally measured values in TDE (Figure 1-2). Pressure values at the drillhole PP321 and PP322 boundaries are assumed constant (0.95 MPa) based on the somewhat constant measured pressure level. Similarly, the inner and outer guard edges (on the experimental section side) of the boreholes PP324, PP326 and PP327 are at constant pressure (0.97 MPa).

The temporal evolution of the pressure can be computed from the above water mass balance equation, Darcy's law and the time dependent boundary conditions. With the pressure, the temporally evolving Darcy velocity is obtained.

The mathematical model for the batch tracer solutions is similar to the *Linear* model.

The mathematical model for tracer transport in the bedrock is also similar to the *Linear* model with exception of the flux term definition. In the *Advective* model, the mass flux of tracer i is

$$\mathbf{j}_i = \mathbf{j}_{\text{d},i} + \mathbf{j}_{\text{a},i} \, , \tag{A-35}$$

where the diffusive flux $\mathbf{j}_{\text{d},i}$ is similar to the *Linear* model, Equation (A-27). The advective flux is

$$\mathbf{j}_{\text{a},i} = c_i \mathbf{u} \tag{A-36}$$

with the Darcy velocity $\mathbf{u}$ from the water flow model.

Summarizing, the mathematical problem for *Advective* model is

(a) first to find $p = p(\mathbf{x}, t)$ in bedrock such that

$$\nabla \cdot \left(-\rho_{\text{water}} \frac{K}{\rho_{\text{water}} g}\nabla p \right) = 0 \tag{A-37}$$

with boundary conditions

$$p = p_{\text{exp}}(t) \text{ on experimental sections,}$$
$$p = p_{\text{constant}} \text{ on other hole walls, and}$$
$$-\nabla \mathbf{p} \cdot \mathbf{n} = 0 \text{ on outer boundary}$$

and

(b) second, with $p = p(\mathbf{x}, t)$ from (a), to find $c_i = c_i(\mathbf{x}, t)$ in bedrock and $c_i^{\text{inj}} = c_i^{\text{inj}}(t)$, $c_i^{\text{obs324}} = c_i^{\text{obs324}}(t)$ as well as $c_i^{\text{obs327}} = c_i^{\text{obs327}}(t)$ such that

$$\varepsilon \frac{\partial c_i}{\partial t} + \nabla \cdot \mathbf{j}_i = 0 \tag{A-38}$$

$$V^{\text{sol}} \frac{\partial c_i^{\text{sol}}}{\partial t} = -\int_{\partial \Omega_{\text{sol}}} \mathbf{j}_i \cdot \mathbf{n} dS - r c_i, \quad \text{sol=inj, obs324, obs327} \tag{A-39}$$

$$\mathbf{j}_i = -D_{\mathrm{e},i}\nabla c_i + c_i\mathbf{u} \quad \text{and} \quad \mathbf{u} = -\frac{K}{\rho_{\mathrm{water}} g}\nabla p \tag{A-40}$$

with initial values

$$c_i(\mathbf{x},0) = 0 \text{ in } \Omega_{\mathrm{bedrock}} \quad c^{\mathrm{inj}}(0) = c_0, \quad c^{\mathrm{obs324}}(0) = 0 \text{and} \quad c^{\mathrm{obs327}}(0) = 0$$

and boundary conditions

$$c_i = c_i^{\mathrm{inj}} \text{ at } \partial\Omega_{\mathrm{inj}}, \quad c_i = c_i^{\mathrm{obs324}} \text{ at } \partial\Omega_{\mathrm{obs324}} \quad \text{and} \quad c_i = c_i^{\mathrm{obs327}} \text{ at } \partial\Omega_{\mathrm{obs327}}.$$

A3.4 Foliation model

In TDE, the directions from the injection drillhole to observation drillholes were chosen to be along (PP324) and perpendicular (PP327) to the rock foliation. At the experimental section depth of the drillholes (approximately 12 m from the tunnel wall), the foliation direction deviates from the tunnel wall foliation direction but is oriented rather towards PP324 than towards PP327. To estimate the effect of foliation, anisotropic diffusion model that takes into account the foliation direction has been developed.

The *Foliation* model follow the *Linear* model equations, but with an anisotropic diffusive mass flux. Instead of using the isotropic diffusion defined by Equation (A-27), an anisotropic diffusion flux is assumed

$$\mathbf{j}_{\mathrm{d},i} = -\mathbf{D}_{\mathrm{e}}\nabla c_i. \tag{A-41}$$

Here $\mathbf{D}_{\mathrm{e}}$ is the effective diffusion tensor. In a foliation coordinate system where *xz*-plane is the foliation direction in bedrock, the effective diffusion tensor can be expressed as a diagonal tensor:

$$\mathbf{D}_{\mathrm{e}}^{*} = \begin{pmatrix} fD_{\mathrm{e,\,ove}} & 0 & 0 \\ 0 & \frac{1}{f^2}D_{\mathrm{e,\,ove}} & 0 \\ 0 & 0 & fD_{\mathrm{e,\,ove}} \end{pmatrix} \tag{A-42}$$

with the foliation factor f and the volumetric overall effective diffusivity $D_{\mathrm{e,ove}}$ such that $\det \mathbf{D}_{\mathrm{e}}^{*} = D_{\mathrm{e,ove}}^3$, that is, the volumetric diffusion behaviour is preserved. In the direction of the foliation plane, the overall effective diffusion coefficient is increased by the foliation factor, whereas in the direction perpendicular to the foliation, the overall effective diffusion coefficient is decreased (by division with the square of the foliation factor). The relative difference in diffusion strengths to the perpendicular and along foliation is called the foliation strength:

$$F = \frac{f}{1/f^2} = f^3. \tag{A-43}$$

The effective diffusion tensor in the foliation coordinate system can be mapped to the Cartesian coordinate system as

$$\mathbf{D}_{\mathrm{e}} = \mathbf{Q}\mathbf{D}_{\mathrm{e}}^{*}\mathbf{Q}^{\mathsf{T}}, \tag{A-44}$$

if the mapping between the coordinate systems is $\mathbf{x}^{*} = \mathbf{y} + \mathbf{Q}\,(\mathbf{x} - \mathbf{o})$ with $\mathbf{x}$ the Cartesian system coordinate, $\mathbf{x}^{*}$ the foliation system coordinate, $\mathbf{y}$ a Cartesian point and $\mathbf{o}$ the origin. In the model, an orthogonal, curvilinear foliation coordinate system is defined according to the experimentally determined foliation directions from the drillcores (Toropainen 2012). Specifically, the foliation coordinates follow piecewise linear interpolations for foliation dip and dip directions that are constructed with the experimental data. The foliation coordinate system is illustrated in Figure A-4. The foliation dip and dip direction are approximately 30°/150° at the drillhole PP326 experimental section, 70°/170° at PP324 and 40°/170° at PP327, but vary by location according to the experimental data.

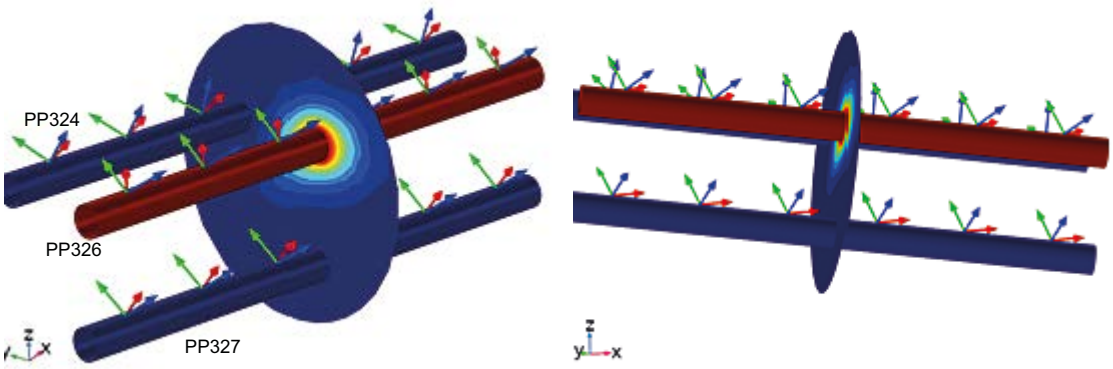

Figure A-4. *Foliation coordinate system (on PP326) with respect to the Cartesian coordinate system (lower left corner) close to the experimental sections of the drillholes. The direction of foliation is the plane spanned by x- and z-coordinates of the foliation system (red and blue arrows) and the direction perpendicular to foliation is pointed by the y-axis (green arrow). The effect of foliation on the diffusion profile is also illustrated (the coloured plane).*

Summarizing, the mathematical problem for *Foliation* model is to find $c_i = c_i(\mathbf{x}, t)$ in bedrock and $c_i^{\text{inj}} = c_i^{\text{inj}}(t)$, $c_i^{\text{obs324}} = c_i^{\text{obs324}}(t)$, as well as $c_i^{\text{obs327}} = c_i^{\text{obs327}}(t)$ such that

$$\varepsilon \frac{\partial c_i}{\partial t} + \nabla \cdot \mathbf{j}_i = 0 \tag{A-45}$$

$$V^{\text{sol}} \frac{\partial c_i^{\text{sol}}}{\partial t} = -\int_{\partial\Omega_{\text{sol}}} \mathbf{j}_i \cdot \mathbf{n} dS - r c_i, \quad \text{sol=inj, obs324, obs327} \tag{A-46}$$

$$\mathbf{j}_i = -\mathbf{D}_{\text{e},i} \nabla c_i \quad \text{and} \quad \mathbf{D}_{\text{e}} = \mathbf{Q}\mathbf{D}_{\text{e}}^{*}\mathbf{Q}^{\mathsf{T}}, \tag{A-47}$$

with initial values

$$c_i(\mathbf{x}, 0) = 0 \text{ in } \Omega_{\text{bedrock}} \quad c^{\text{inj}}(0) = c_0, \quad c^{\text{obs324}}(0) = 0 \text{and} \quad c^{\text{obs327}}(0) = 0$$

and boundary conditions

$$c_i = c_i^{\text{inj}} \text{ at } \partial\Omega_{\text{inj}}, \quad c_i = c_i^{\text{obs324}} \text{ at } \partial\Omega_{\text{obs324}} \quad \text{and} \quad c_i = c_i^{\text{obs327}} \text{ at } \partial\Omega_{\text{obs327}}.$$

$\mathbf{D}_{\text{e}}^{*}$ is the diagonal tensor in the foliation coordinate system, Equation (A-42).

A4 Simulation cases

The simulations with ***Analytical*** model aim to find parameter combinations that fit best to the experimental data. We treated HTO and chlorine as non-sorbing tracers. In the fittings we used the value e = 1 % for the porosity of the rock and used D_p and the initial tracer concentration as a fitting parameter. For sorbing tracers, we used D_p and D as fitting parameters (and also the initial tracer concentration), and K_d is computed using the value ρ_r = 2 700 kg/m^3 for the density of the rock. Model was fitted manually to follow the shape of the data curve.

In simulation set A with *Linear* model, the injection solution concentration decrease and the observation tracer solution increase is studied with five diffusion coefficients and five sorption distribution coefficients (Table A1). The distribution coefficients and effective diffusivities have been chosen such that they give reasonable injection solution concentration graphs for the simulated tracers.

Table A-1. Simulation set A. Linear model with all tracers.

K_d (m³/kg) \ D_e (m²/s)	1×10^{-14}	5×10^{-14}	1×10^{-13}	2×10^{-13}	5×10^{-13}
0	A11	A12	A13	A14	A15
1×10^{-4}	A21	A22	A23	A24	A25
1×10^{-3}	A31	A32	A33	A34	A35
5×10^{-2}	A41	A42	A43	A44	A45
4×10^{-1}	A51	A52	A53	A54	A55

In simulation set B with ***Linear*** model, the injection solution concentration decrease and the observation tracer solution increase is studied with five porosities and five effective diffusion coefficients (Table A-2). The tracers are assumed non-sorbing.

Table A-2. Simulation set B. Linear model with non-sorbing tracers.

ε (%) \ D_e (m²/s)	1×10^{-14}	5×10^{-14}	1×10^{-13}	2×10^{-13}	5×10^{-13}
0.5	B11	B12	B13	B14	B15
0.7	B21	B22	B23	B24	B25
0.9	B31	B32	B33	B34	B35
1.1	B41	B42	B43	B44	B45
1.3	B51	B52	B53	B54	B55

In simulation set C with ***Advection*** model, the effect of water flow in the rock matrix is studied with three hydraulic conductivities and five effective diffusion coefficients (Table A-3). The hydraulic conductivity values correspond to values for intact rock. Porosity of 0.9 % is used and no sorption is assumed in the simulations.

Table A-3. Simulation set C. Advection model.

K (m/s) \ D_e (m²/s)	1×10^{-14}	5×10^{-14}	1×10^{-13}	2×10^{-13}	5×10^{-13}
0	C11	C12	C13	C14	C15
5×10^{-15}	C21	C22	C23	C24	C25
1×10^{-14}	C31	C32	C33	C34	C35

In simulation set D with ***Foliation*** model, the effect of foliation is studied with five effective diffusion coefficients and four foliation strengths (Table A-4) Porosity of 0.9 % is used and no sorption is assumed in the simulations.

Table A-4. Simulation set D. Foliation model.

F \ $D_{d,ove}$ (m²/s)	1×10^{-14}	5×10^{-14}	1×10^{-13}	2×10^{-13}	5×10^{-13}
1	D11	D12	D13	D14	D15
2	D21	D22	D23	D24	D25
3	D31	D32	D33	D34	D35
5	D41	D42	D43	D44	D45

A5 Results and discussion

A5.1 Analytical model

With *Analytical* model, optimal values of the fitting parameters for injection drillhole data are listed in the Table A-5. For sorbing tracers the values of the fitting parameters cannot be determined quite uniquely.

The fitting curves of the tracers are plotted in Figure A-5. For Cs the simplified model did not work. The concentration of Cs in the injection hole begins to increase after 500 days which is not captured by the model.

For the observation holes, *Analytical* model worked quite poorly. In the observation hole PP324, we made fittings to the data after the restart of the measurements at approximately 1 000 days of TDE. For Cl we got a nice fitting with the values $\varepsilon = 1$ % and $D_p = 5 \times 10^{-12}$ m^2/s for the parameters, Figure A-5. For HTO the fitting looks also nice, the optimal value of the diffusion coefficient is reasonable ($D_p = 2.7 \times 10^{-11}$ m^2/s), but the value of the porosity $\varepsilon = 0.003$ % is extremely small. In the observation hole PP327 the data of Cl does not follow the shape of the prediction of our model, Figure A-6. The data of HTO can be followed with *Analytical* model but again the optimal value of the porosity is extremely small: $\varepsilon = 0.001$ %, $D_p = 2.7 \times 10^{-11}$ m^2/s.

Table A-5. The optimal values of the fitting parameters.

Tracer	D_p [m^2/s]	D_e [m^2/s]	ε	D [m^2/s]	K_d [m^3/kg]
HTO	5.5×10^{-11}	5.5×10^{-13}	0.01	5.5×10^{-11}	0
Cl	4.0×10^{-12}	4.0×10^{-14}	0.01	4.0×10^{-12}	0
Na	4.5×10^{-12}	4.5×10^{-14}	0.01	6.0×10^{-13}	2.4×10^{-5}
Ba	4.5×10^{-12}	4.5×10^{-14}	0.01	6.5×10^{-15}	2.3×10^{-3}
Cs	4.5×10^{-12}	4.5×10^{-14}	0.01	6.5×10^{-15}	3.3×10^{-3}

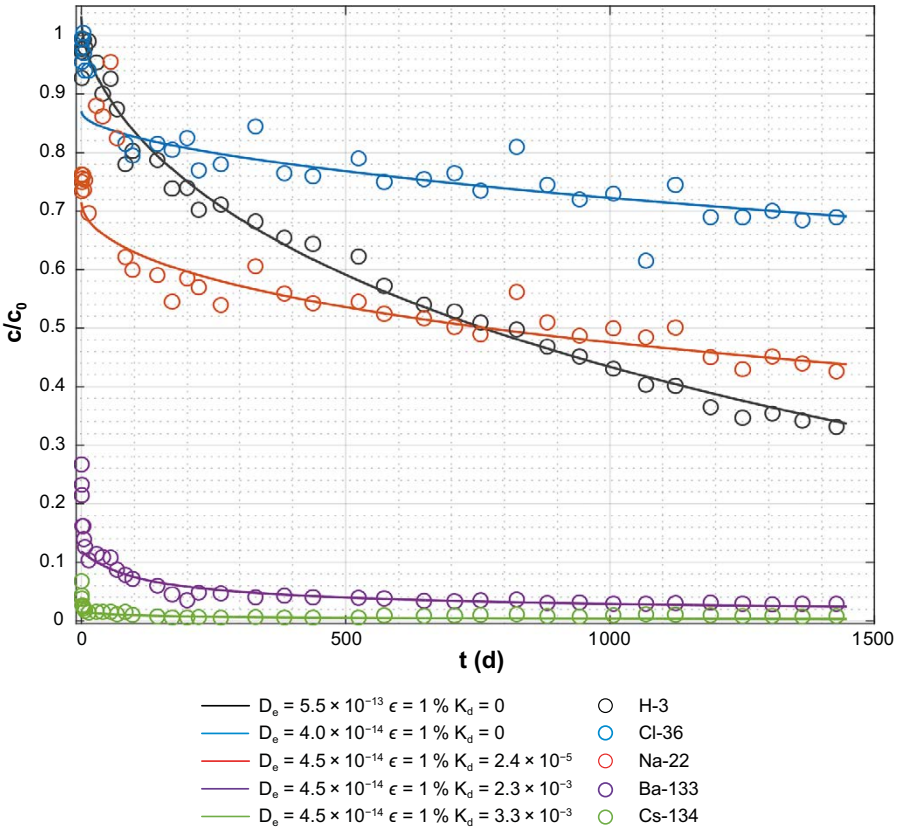

Figure A-5. *Fitting to the measured data of the injection hole.*

Near the injection hole, the concentration gradient of tracer is large and, therefore, the evolution of the tracer concentration in the dominated by the diffusion out of the hole and our model works quite well. Further away from the injection hole the diffusion is weaker and effects of details (inhomogeneity of the rock, flow of the pore water) become significant for the transport of tracers, and our simple diffusion model cannot describe the transport of the tracers there.

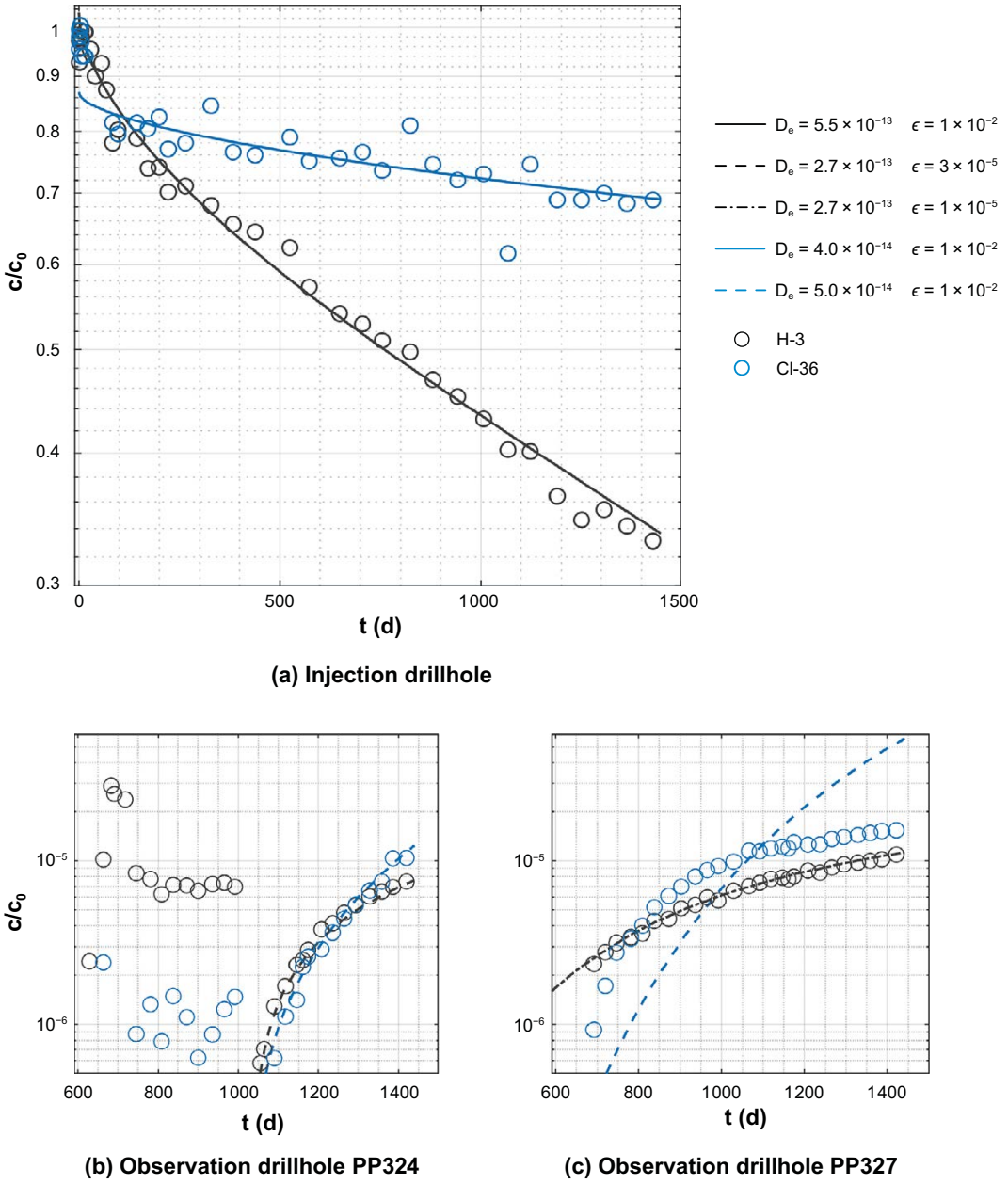

(a) Injection drillhole

(b) Observation drillhole PP324

(c) Observation drillhole PP327

Figure A-6. *Fittings to the measured data with Analytical model. (a) Injection drillhole tracer concentration temporal evolution with different D_es (m^2/s) and porosities (ε) for non-sorbing tracers H-3 and Cl-36, (b) the tracer breakthrough to observation drillhole PP324 and (c) to PP327. c/c_0 is the relative activity, that is, the drillhole specific activity divided by the injection drillhole initial specific activity.*

A5.2 Linear model

The general behaviour of TDE, that is, the tracer decrease in the injection drillhole and the breakthrough to observation drillholes can be captured with *Linear* model. In accordance with the experimental results, the simulations suggest that the sorbing tracers do not break through to the observation drillholes within the duration of TDE (even with the highest used D_e), whereas the non-sorbing tracers can be noticed in the observation drillholes within TDE. Given the uncertainties related to natural rock properties and to *in situ* experiments, the experimental injection activity trends for all the tracers somewhat follow the simulated diffusion graphs with parameter values reasonably close to those measured in laboratory.

The simulation results of set A with *Linear* model are compared to experimental results in Figure A-7. The graphs show that similar injection solution concentration decreases could be explained with different parameter pairs. For example, the graph with the parameter pair $D_e = 1 \times 10^{-14}$ m^2/s and $K_d = 4 \times 10^{-2}$ (purple thin line) practically coincides with the graph with the pair $D_e = 5 \times 10^{-13}$ m^2/s and $K_d = 1 \times 10^{-3}$ (yellow thin dot-dash line). The concentration drop before 100 days (arrows in Figure A-7) corresponds to the leak of the injection solution, which is presented in the model with the high peak in the sampling rate function.

For strongly sorbing Ba-133 and Cs-134, the steep experimental injection solution concentration decrease is difficult to capture with a linear volumetric sorption model even with high volumetric distribution coefficient values (approximately one order of magnitude higher K_ds than determined in laboratory). This suggests that the tracers sorb already on the experimental section rock wall (no sorption observed on experimental equipment) before entering the surrounding rock volume. Resulting from the uncertainties in determining the distribution coefficient values, the diffusion coefficients are also difficult to estimate for strongly sorbing tracers.

For weakly sorbing Na-22, the closest simulation graph to experimental results is obtained with $D_e = 5 \times 10^{-14}$ m^2/s and $K_d = 1 \times 10^{-4}$. The distribution coefficient value is one order of magnitude lower than the experimentally determined value (Table 1-6), but is the same order of magnitude as in REPRO WPDE simulations (Poteri et al. 2018a, b). The experimentally determined value corresponds to the yellow graphs in Figure A-7.

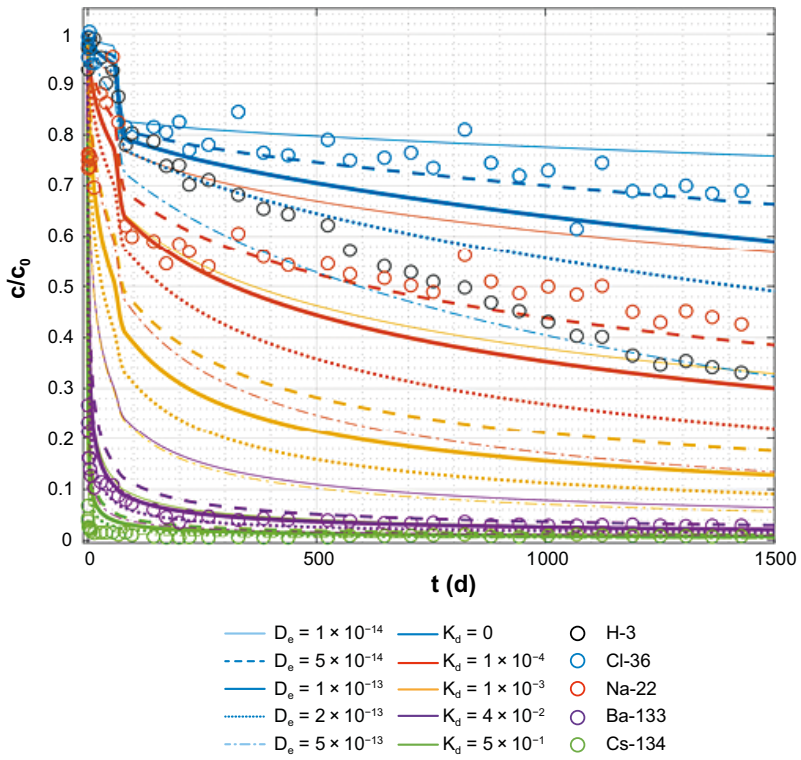

Figure A-7. *Simulated injection drillhole concentration decrease with different effective diffusion coefficients and distribution coefficients (lines) as well as experimental results for TDE tracers (circles).*

Since the sorbing tracers do not break through to the observation drillholes and the behaviour of non-sorbing tracers (H-3 and Cl-36) is further analysed with the simulation set B, the observation solution concentrations for simulation set A are not illustrated here.

The simulation results of set B with *Linear* model are compared to experimental non-sorbing tracer results in Figure A-8. The line colours correspond to different effective diffusion coefficients and line types to different porosities. No sorption is considered, meaning that porosity determines the capacity factor.

The injection borehole results (Figure A-8) suggest that the Cl-36 experimental results could be explained with the line with porosity of 0.7 % and $D_e = 5 \times 10^{-14}$ m^2/s. The effective diffusion coefficient corresponds to the one for Na-22, but the laboratory measurements with TDE samples give approximately six times higher values for Cl-36. H-3 experimental injection solution concentration profile drops faster than the simulated diffusion profiles after 500 days of TDE, but still the values lie between D_es $(2–5) \times 10^{-13}$ m^2/s, which are close to the laboratory measurements (on average $D_e = 3.4 \times 10^{-13}$ m^2/s for TDE samples). The non-diffusion behaviour seems to be H-3 and injection solution specific. Therefore, explanations that are not nuclide specific, such as advection and foliation, can be excluded.

The first breakthrough of H-3 to observation drillhole PP324 occurs at approximately 500 days of TDE according to experimental results (Figure A-8b). The first experimentally determined concentrations (up to equipment renewal at approximately 1 000 days) are, however, quite scattered. The breakthrough of Cl-36 occurs 100–200 days later and, again, the concentrations are quite scattered before equipment renewal. The scattered concentrations for H-3 and Cl-36 are also at different levels if compared to each other. After equipment renewal, H-3 and Cl-36 experimental graphs somewhat coincide and form a clear profile. In PP327, both H-3 and Cl-36 can be noticed at approximately 700 days of TDE and the concentration profiles almost coincide. The simulations results suggest that the first breakthrough to PP324 could be explained with the *Linear* model with $D_e = 1 \times 10^{-13}$ m^2/s and porosities ranging between 0.5–1.1 % (orange graphs in Figure A-8b). Similarly, the simulations results suggest that the first breakthrough to PP327 could be explained with $D_e = 1 \times 10^{-13}$ m^2/s and porosity 0.5 – 0.7 %, or alternatively with $D_e = 2 \times 10^{-13}$ m^2/s and porosity 1.1–1.3 %. These effective diffusion coefficients suggested by the first breakthrough lie between the diffusion coefficient suggested by the injection drillhole results ($D_e = 5 \times 10^{-14}$ m^2/s for Cl-36 and $D_e = (2–5) \times 10^{-13}$ m^2/s for H-3).

In PP324, the experimental results begin to form a clear profile after the equipment renewal at 1 028 days of TDE. Simulation parameters matching the profile are $D_e = 5 \times 10^{-14}$ and porosity 0.7 %. These correspond to the injection profile for Cl-36. In PP327, the profile shape is not captured by *Linear* model. The simulated profiles increase too fast in comparison to experimental results.

When the H-3 and Cl-36 injection and observation solution concentrations are plotted as relative concentrations (Figure A-8), it can be noticed that the injection solution concentration curve levels for H-3 and Cl-36 are different, but the observation solution concentration curves are somewhat similar. This could be interpreted as an indication of anion exclusion. In principle, the breakthrough is controlled by the apparent diffusion coefficient D_a (= D_e/ε in this case), but the outflow from the injection drillhole by the effective diffusion coefficient D_e. Therefore, H-3 and Cl-36 may have same D_a (that is, approximately similar breakthrough to observation drillhole) but different D_e (that is, different injection solution concentration decrease rate), if the porosity for the tracers is different. Since Cl-36 is a negatively charged anion for which some part of the rock porosity may be excluded (due to negative rock mineral surface charge), this is possible. The effect of anion exclusion is illustrated in Figure A-9. The blue lines correspond to approximately $D_a = 1 \times 10^{-11}$ m^2/s with porosities 0.5 % and 1.1 % and the red lines to $D_a = 2 \times 10^{-11}$ m^2/s with porosities 0.5 % and 1.1 %. For both observation drillholes PP324 and PP327, the red lines almost coincide and match to the first breakthroughs, but for injection drillhole, the 1.1 % porosity line somewhat follows the experimental H-3 profile until 500 days and the 0.5 % porosity line lies below the experimental profile for Cl-36. Accordingly, the porosity should be less than 0.5 % to match the injection drillhole Cl-36 profile. For observation drillhole PP324, the blue lines lie in the middle of the experimental point cloud and for observation drillhole PP327, the blue lines correspond to latest experimental points (within the time frame of TDE). For injection drillhole, the blue 1.1 % porosity line lies above the experimental H-3 profile until 500 days and the 0.5 % porosity line follows the experimental profile for Cl-36. Accordingly, the porosity should be more than 1.1 %

to match the injection drillhole H-3 profile. Based on these simulation results with the two apparent diffusion coefficients and two porosities (with the ratio of approximately 2), it could be deduced that the porosity for Cl-36 is less than half of the porosity for H-3.

The magnitude of the lowest detectable observation drillhole relative concentrations is approximately 10^{-6}, that is, one millionth of the injected concentration. The value demonstrates the accuracy of radiochemical detection techniques, but also poses a challenge for simulation accuracy in sense that the sensitivity to parameter values is high. For example, halving D_e from 2×10^{-13} m^2/s to 1×10^{-13} m^2/s means approximately 500 days difference in breakthrough time (PP327). Similarly, changing porosity from 0.5 % to 1.1 % means more than 500 days delay in breakthrough (for $D_e = 1 \times 10^{-13}$ in PP324). Given that the ranges for D_e and porosity in laboratory experiments for different samples are approximately 4×10^{-14} to 5×10^{-13} m^2/s (Ikonen et al. 2015) and 0.2–2 % (Voutilainen et al. 2018), respectively, the simulation results for observation drillholes should be considered rather indicating the feasibility of the model (if the model can predict breakthrough within TDE of not) and giving the order of magnitude of parameters than predicting accurate results.

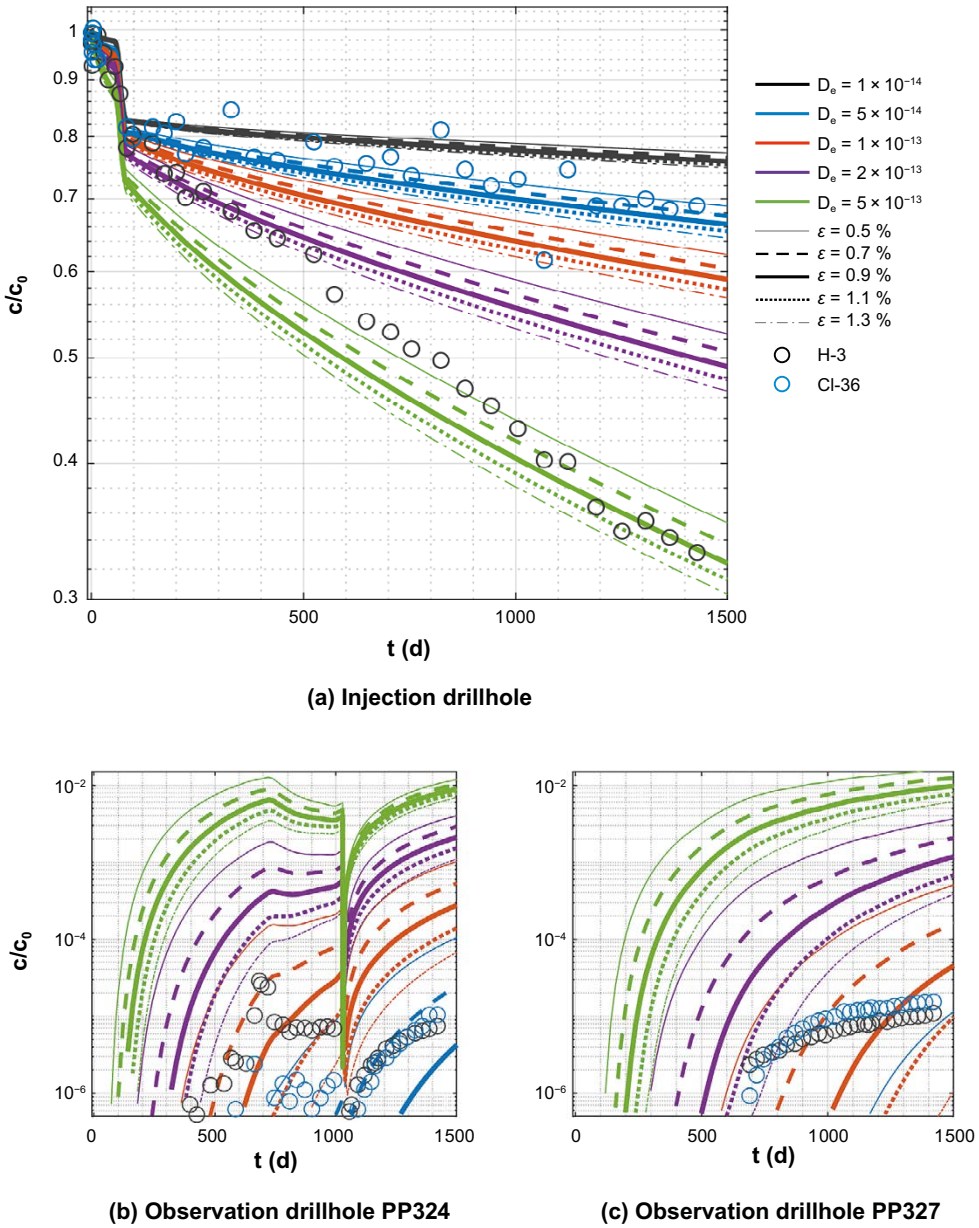

Figure A-8. *Linear model results. (a) Injection drillhole tracer concentration temporal evolution with different D_es (m^2/s) and porosities (ε) for non-sorbing tracers H-3 and Cl-36, (b) the tracer breakthrough to observation drillhole PP324 and (c) to PP327. c/c_0 is the relative activity, that is, the drillhole specific activity divided by the injection drillhole initial specific activity.*

For sorbing tracers, the injected activities provided in the task description have been used to calculate the initial specific activities, but the initial specific activities for non-sorbing tracers have been taken as average of the first measured values. These values are within 5 % of the values calculated using the injected activities (H-3: 198 MBq injected activity, 190 MBq if calculated from the specific activities of first samples; Cl-36: 5.5 MBq injected activity, 5.8 MBq if calculated from the specific activities of first samples).

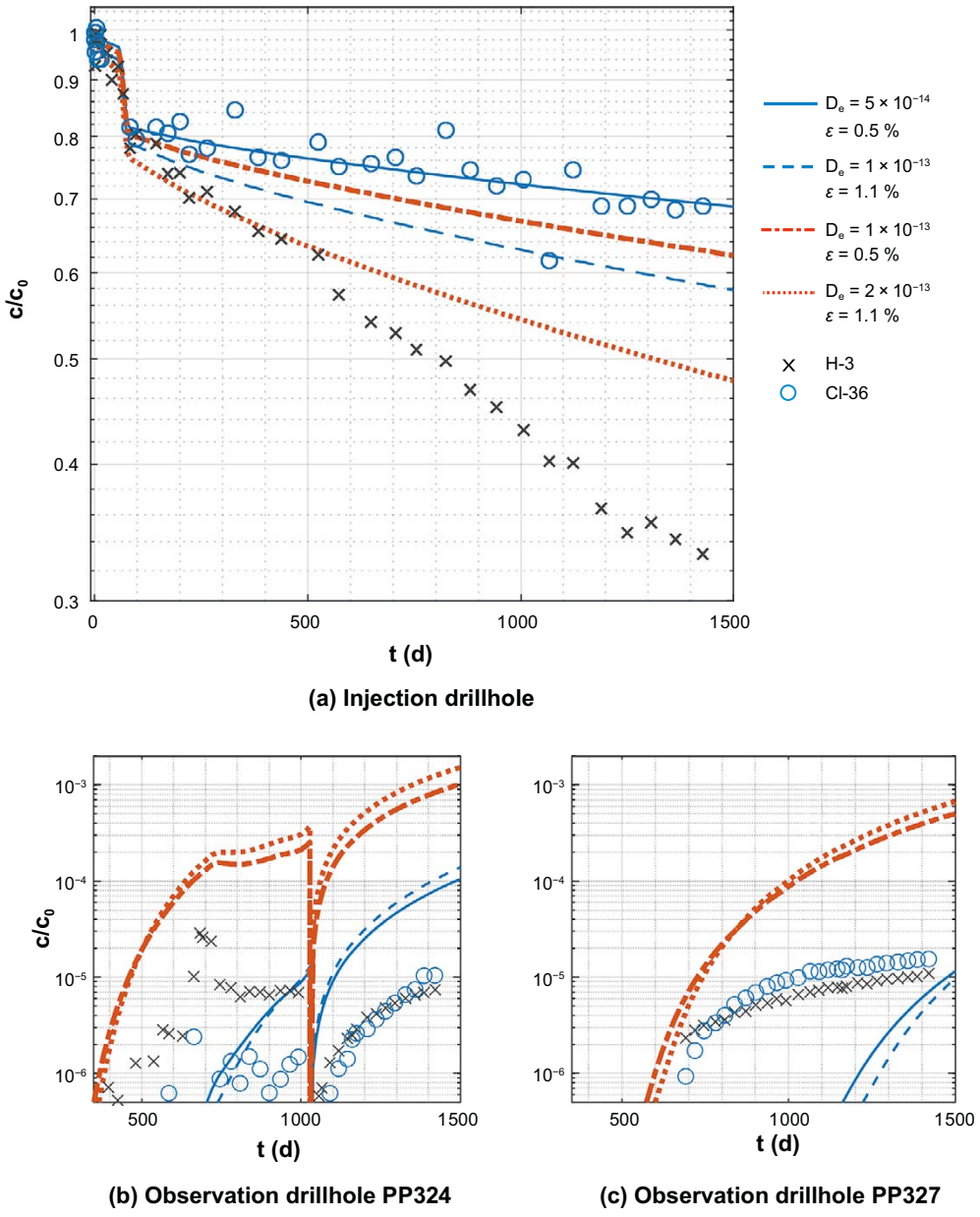

Figure A-9. *Illustration of effect of anion exclusion. (a) Injection drillhole tracer concentration temporal evolution with different D_es (m^2/s) and porosities (ε) for non-sorbing tracers H-3 and Cl-36, (b) the tracer breakthrough to observation drillhole PP324 and (c) to PP327. c/c_0 is the relative activity, that is, the drillhole specific activity divided by the injection drillhole initial specific activity. The blue lines correspond approximately to $D_a = 1 \times 10^{-11}$ m^2/s and red lines approximately to $D_a = 2 \times 10^{-11}$ m^2/s.*

A5.3 Advective model

In *Advective* model, slow water flow in the TDE rock has been added to *Linear* model (hydraulic conductivity matches intact rock that is assumed in simulations). Correspondingly, advection with the flow is added to diffusion as transport mechanism. Due to variations in the pressure levels in the experimental sections of the drillholes PP324, PP326 and PP327, the flow direction fluctuates towards or outward from the experimental sections within time. Similarly, the flow velocity varies within time (see Figure A-10a for an example of the flow field at one time point). This behaviour is likely overestimated by the model due to the quasistatic assumption, according to which the changes in drillhole pressures affect the flow field immediately. In reality, there is likely a time delay in the effect that depends on the local rock properties.

The time evolutions of the diffusive and advective flux magnitudes from the injection drillhole to bedrock are shown in Figure A-10b. In the beginning of TDE (until approximately 100 days), the diffusive flux is much higher than the advective flux due to the initially high tracer concentration in the injection drillhole, which means also high concentration gradient. Later, the flux magnitudes are of similar order of magnitude, but advective flux is mainly towards the injection drillhole, whereas the diffusive flux points outward from the drillhole. In accordance with these observations, the injection drillhole tracer concentration evolution graphs of simulation set C (Figure A-11a) show that the effect of advective flux is insignificant before approximately 100 days of TDE, but afterwards the advective flux seems to slow down injection drillhole tracer concentration decrease.

According to the simulations (with small hydraulic conductivities), the effect of advection on the breakthrough times to observation drillholes or on the observation drillhole concentration profiles is negligible (Figure A-11b,c).

Concluding, the advection may introduce local variations in the injection drillhole concentrations, but it seems have almost no effect on the observation drillhole concentrations.

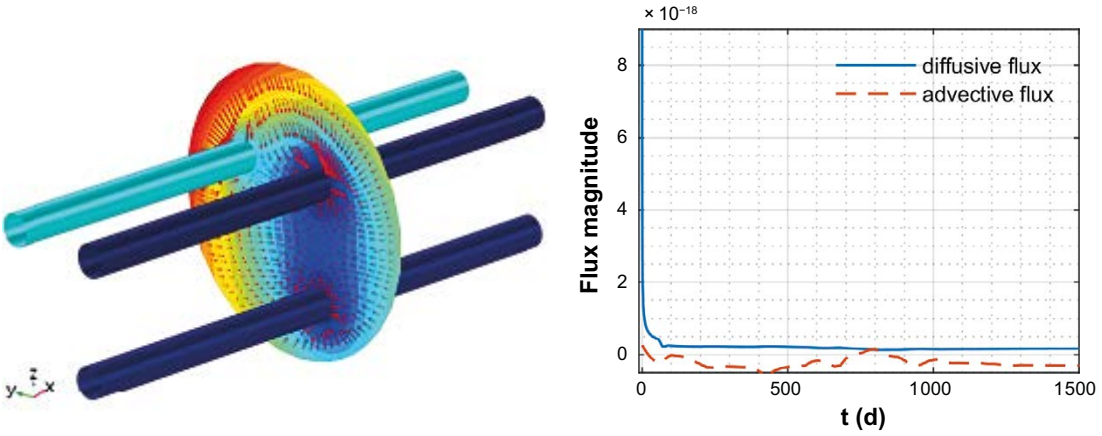

Figure A-10. *(a) An illustration of the water flow field and pressure levels on a plane across the experimental sections. (b) An example of the difference in diffusive and advective water fluxes from the injection borehole PP326 experimental section to bedrock. The maximum diffusive flux is double the scale in the figure.*

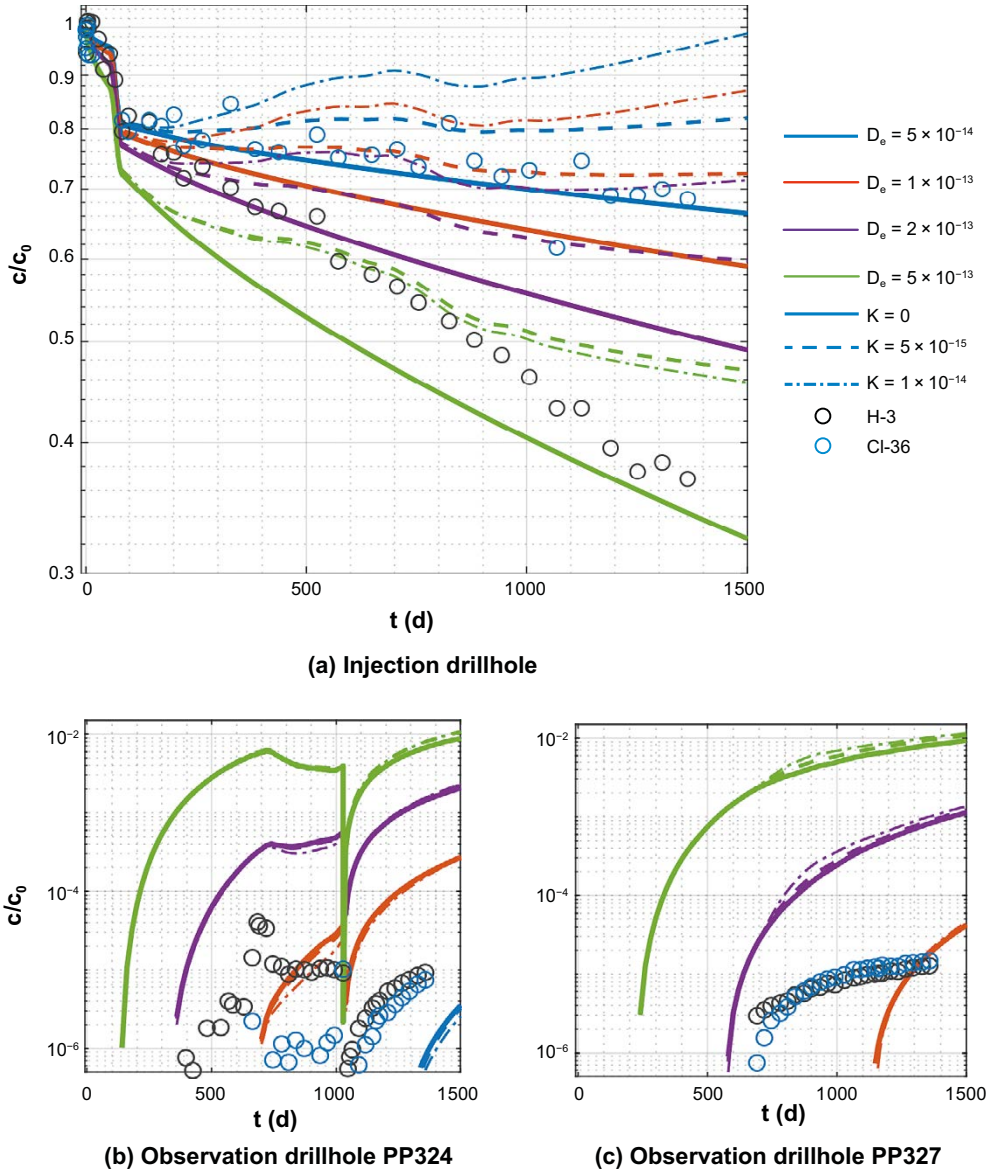

Figure A-11. *(a) Injection drillhole tracer concentration temporal evolution with different D_es (in units m^2/s) and Ks (in units m/s) for non-sorbing tracers H-3 and Cl-36, (b) the tracer breakthrough to observation drillhole PP324 and (c) to PP327. c/c_0 is the relative activity, that is, the drillhole specific activity divided by the injection drillhole initial specific activity.*

A5.4 Foliation model

In *Foliation* model, diffusion is anisotropic and it follows the TDE local foliation (foliation dip/dip direction around PP324, PP326 and PP327 is approximately 30°/150°). For injection drillhole concentrations, foliation increases the out-diffusion, that is, it lowers the levels of the concentration graphs. The size of effect with foliation strength 5 (diffusion along the foliation is 5 times higher than perpendicular) is of same order as the increase of porosity from 0.9 % to 1.3 % (compare Figure A-12a to Figure A-8a). For observation drillhole PP324 that is in somewhat neutral direction to foliation from the injection drillhole PP326, the effect of foliation is small (Figure A-12b), as expected. For observation drillhole PP327 that is somewhat perpendicular to foliation, the effect can be noticed (Figure A-12c). The foliation lowers the simulation graphs produced without foliation (with different D_es) towards the experimental values, but still the experimentally observed tracer level cannot be captured even with the highest foliation factor (that is 5).

Concluding, foliation may bring the simulated concentration profiles closer to experimental values, but the uncertainty in other parameters (D_e and porosity) is so high that the effect of foliation cannot be distinguished. More detailed experimental data on the spatial tracer concentration in TDE rock (e.g. by over-coring) would be needed to further investigate the effect of foliation.

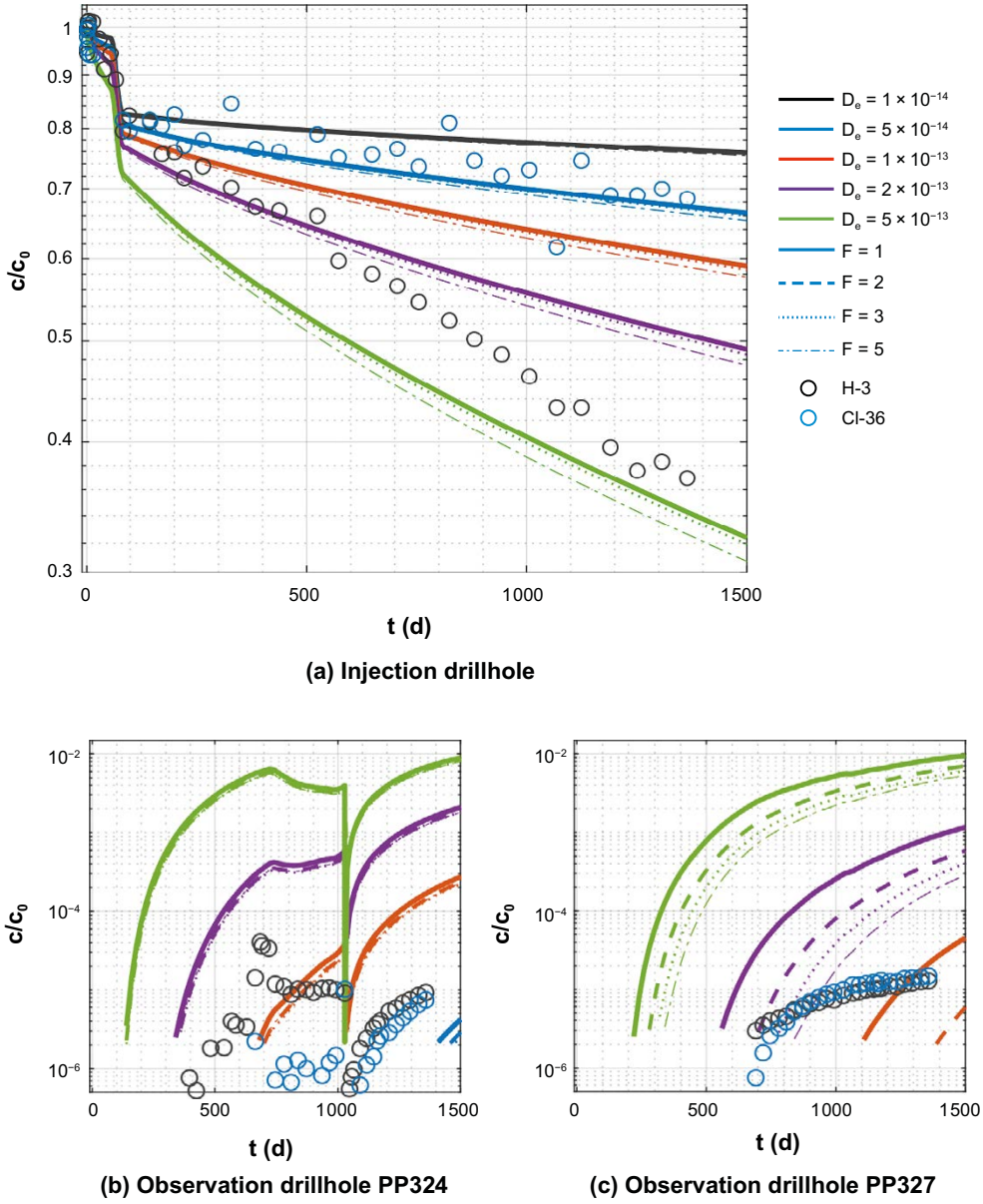

Figure A-12. *(a) Injection drillhole tracer concentration temporal evolution with different D_es (in units m^2/s) and foliation factors F for non-sorbing tracers H-3 and Cl-36, (b) the tracer breakthrough to observation drillhole PP324 and (c) to PP327 (c). c/c_0 is the relative activity, that is, the drillhole specific activity divided by the injection drillhole initial specific activity.*

A6 Concluding summary

Given the natural variations in TDE bedrock and the parameter uncertainties in laboratory experiments, the simulation results demonstrate that a linear, isotropic diffusion model with linear sorption can be used to explain the experimentally observed behaviour of TDE. Experimental injection tracer concentration profiles of Na-22 and Cl-36 approximately follow simulated diffusive profiles with the same effective diffusion coefficient (approximately 5×10^{-14} m^2/s) and porosity (0.7 %). H-3 experimental profile deviates from the simulated diffusive profiles although the range for effective diffusion coefficient suggested by the simulations is reasonable, $(2–5) \times 10^{-13}$ m^2/s). The simulations suggest higher K_ds for Ba-133 and Cs-134 than in laboratory experiments (probably due to not considering surface sorption to rock walls), but an order of magnitude lower K_d for Na-22, which is however in accordance with WPDE simulations.

The simulations indicate first breakthrough to observation drillholes for non-sorbing tracers (H-3, Cl-36) with reasonable effective diffusivities and porosities if compared to timing of first breakthrough in the experiment. For PP324, the concentration profiles match quite well diffusive profiles (after the experimental equipment renewal), but for PP327 the experimental profiles shape is flatter than the simulated one. In accordance with experimental findings, no breakthrough for sorbing tracers can be seen.

H-3 and Cl-36 injection drillhole (relative) concentration graphs are at different levels, but the observation drillholes graphs somewhat coincide. This indicates anion exclusion and, based on the simulations, the porosity for anionic Cl-36 (with elementary charge of −1) is less than half of the porosity for neutral H-3.

With hydraulic conductivities matching intact rock, the effect of advection on the observation drillhole profiles is small. For injection drillhole concentrations, diffusion dominates advection in the beginning of the simulations (< 100 days), but slows down the tracer flux out the injection drillhole later. The simulations also suggest that advection driven by pressure differences between the drillholes may introduce fluctuations to the injection drillhole tracer concentrations, if the drillhole pressure levels fluctuate.

The effect of foliation on the injection drillhole or on the observation drillhole PP324 (to neutral direction with respect to foliation) concentrations is small, whereas foliation affects the observation drillhole PP327 (somewhat perpendicular to foliation) concentrations by flattening the concentration profiles towards the experimental profile. The effect is not, however, enough to make the profiles match.

The time of first breakthrough to observation drillholes is very sensitive to model parameters. For example change in D_e from 1×10^{-14} m^2/s to 2×10^{-13} m^2/s or porosity from 1.3 % to 0.9 % means 500 days faster breakthrough. Therefore, natural local variations in TDE bedrock (e.g. minerology, porosity and foliation) may highly affect the breakthrough times and profiles. The effect, however, cannot be quantified without detailed experimental data on the spatial concentration variations inside TDE rock, which is only available by destructive methods. Consequently, the linear isotropic diffusion model with linear sorption could be said to match the level of uncertainty in data obtained with non-destructive experimental methods used in TDE.

A7 Appendix – Analytical solutions

A7.5 Injection hole

Consider a radial diffusion equation

$$\frac{\partial C}{\partial t} - D\left(\frac{\partial^2 C}{\partial r^2} + \frac{1}{r}\frac{\partial C}{\partial r}\right) = 0, \quad a < r < b,$$

with boundary conditions

$$V_1 \frac{\partial C}{\partial t}(a,t) = A_1 \varepsilon D_p \frac{\partial C}{\partial r}(a,t) - p_1 V_1 C(a,t)$$

and the initial condition

$$C(r,0)=\begin{cases}C_0, & r=a\\ 0 & a<r\le b.\end{cases}$$

With the scalings

$$\rho=\frac{r}{a},\quad \tau=\frac{Dt}{a^2},\quad C(r,t)=C_0u(\rho,\tau) \tag{A-48}$$

we can write our problem in a dimensionless form

$$\begin{aligned}&\frac{\partial u}{\partial\tau}-\left(\frac{\partial^2u}{\partial\rho^2}+\frac{1}{\rho}\frac{\partial u}{\partial\rho}\right)=0,\quad 1<\rho<\rho_0,\\ &n\frac{\partial u}{\partial\tau}(1,\tau)=\alpha\frac{\partial u}{\partial\rho}(1,\tau)-\beta u(1,\tau),\\ &u(\rho_0,\tau)=0,\\ &u(\rho,0)=\begin{cases}1, & \rho=1\\ 0 & 1<\rho\le\rho_0,\end{cases}\end{aligned} \tag{A-49}$$

where the dimensionless parameters are

$$\rho_0=\frac{b}{a},\quad \alpha=\frac{A_1\varepsilon aD_p}{V_1D},\quad \beta=\frac{p_1a^2}{D}.$$

The problem (1.49) can be solved by separating the variables. The radial part gives us the Bessel equation

$$\frac{d^2v}{d\rho^2}+\frac{1}{\rho}\frac{dd}{d\rho}+\mu^2v=0,$$

with (eigenvalue dependent) boundary conditions

$$\begin{aligned}&\alpha v'(1)+(\mu^2-\beta)v(1)=0,\\ &v(\rho_0)=0.\end{aligned}$$

The eigenvalues $0<\mu_1<\mu_2<\cdots$ are the solutions of the equation

$$\begin{aligned}&(\alpha\mu Y_1(\mu)+(\beta-\mu^2)Y_0(\mu))J_0(\mu\rho_0)\\ &\quad=(\alpha\mu J_1(\mu)+(\beta-\mu^2)J_0(\mu))Y_0(\mu\rho_0).\end{aligned}$$

Eigenvalues can be computed numerically.

Corresponding eigenfunctions are

$$v_n(\rho)=J_0(\mu_n\rho_0)Y_0(\mu_n\rho)-Y_0(\mu_n\rho_0)J_0(\mu_n\rho).$$

Eigenfunctions are orthogonal with respect to the inner product

$$\langle u,v\rangle=\alpha\int_1^{\rho_0}u(\rho)v(\rho)\rho d\rho+u(1)v(1).$$

The solution can be written as a series expression

$$u(\rho,\tau)=\sum_{n=1}^{\infty}a_n e^{-\mu_n^2\tau}v_n(\rho), \tag{A-50}$$

where the coefficients a_n are

$$a_n=\frac{v_n(1)}{\|v_n\|^2}$$

and

$$\|v_n\|^2=\frac{\alpha}{2\mu_n^2}\left(\rho_0^2 v_n'(\rho_0)^2-v_n'(1)^2\right)+\left(1-\frac{\alpha}{2}\right)v_n(1)^2.$$

A7.6 Observation hole

Consider the radial diffusion equation

$$\frac{\partial C}{\partial t}-D\left(\frac{\partial^2 C}{\partial r^2}+\frac{1}{r}\frac{\partial C}{\partial r}\right)=0,\quad a<r<b,$$

with the boundary conditions

$$V_1\frac{\partial C}{\partial t}(a,t)=A_1\varepsilon D_p\frac{\partial C}{\partial r}(a,t),$$
$$C(b,t)=0.$$

and the initial condition

$$C(r,0)=\begin{cases}C_0, & r=a\\ 0 & a<r\le b.\end{cases}$$

The solution of this system is obtained from the previous chapter by setting $\beta = 0$ there.

The concentration the observation hole (C_{obs}) was described with the equation

$$V_2\frac{dC_{obs}}{dt}(t)=-A_2\varepsilon D_p\frac{\partial C}{\partial r}(b,t)-p_2V_2C(b,t),$$

With the initial condition $C_{obs}(0) = 0$. Using the scalings (1.48) and

$$C_{obs}(t)=C_0\,w(\tau),$$

we get a dimensionless setup of our problem

$$\frac{\partial u}{\partial\tau}-\left(\frac{\partial^2 u}{\partial\rho^2}+\frac{1}{\rho}\frac{\partial u}{\partial\rho}\right)=0,\quad 1<\rho<\rho_0,$$
$$\frac{\partial u}{\partial\tau}(1,\tau)=\alpha\frac{\partial u}{\partial\rho}(1,\tau),$$
$$u(\rho_0,\tau)=0,$$
$$u(\rho,0)=\begin{cases}1, & \rho=1\\ 0 & 1<\rho\le\rho_0,\end{cases}$$

and

$$\frac{dw}{d\tau}(\tau) = -\gamma \frac{\partial u}{\partial \rho}(\rho_0, \tau) - \nu\, w(\tau), \quad w(0) = 0, \tag{A-51}$$

where

$$\gamma = \frac{A_2\, \varepsilon a D_p}{V_2 D}, \qquad \nu = \frac{p_2 a^2}{D}.$$

Using the solution (1.59) we can write the solution of the differential equation (1.60) in the form

$$w(\tau) = -\gamma \sum_{n=1}^{\infty} \frac{a_n v_n'(\rho_0)}{\mu_n^2 - \nu} \left(e^{-\nu\tau} - e^{-\mu_n^2 \tau} \right).$$

Appendix B

Royal Institute of Technology (KTH), Stockholm, Sweden

Luis Moreno

B1 Introduction

Task 9C is focused on predictive modelling of the Through Diffusion Experiment, TDE, which is part of the REPRO project carried out by Posiva at ONKALO in Olkiluoto, Finland. Three drillholes are used for the experiment: one (ONK-PP326) is used for injection of the tracers and the other two (ONK-PP324 and ONK-PP327) as observation holes. The tracers: HTO, ^{22}Na, ^{36}Cl, ^{133}Ba, and ^{134}Cs were injected in ONK-PP326 and then recirculated. More details of the experiment may be found in Task Description-9C (Andersson et al. 2020).

B1.1 Background

The drillholes are arranged as a right-angle triangle, which allows the tracer diffusion along and across the rock foliation. The experiment is carried out between 1 m long packed-off intervals located to distances between its centres of about 17 and 21 cm. The experimental set-up, geometries, physical and chemical data, and operation conditions are described in Andersson et al. (2020).

The calculations were done with using the multi-purpose simulation software COMSOL Multiphysics®. Analytical solutions were also used in comparison purpose.

B1.2 Objectives

The system due to its asymmetry requires a 3D modelling, which needed a large number of elements (nodes) and it is very time consuming. In the 2D modelling, it is assumed a system composed by very long drillholes, in which the end effects are neglected. The first objective of this report is to compare the results of 2D modelling with those obtained using a 3D modelling and the consequences of the use of 2D or 3D will be discussed.

Once these two models (3D and 2D) are compared for the non-sorbing tracer HTO and if the differences are not significant, calculations using the 2D model will be carried out for the other tracers in the experiments (HTO, ^{36}Cl, ^{22}Na, ^{133}Ba, and ^{134}Cs). Finally, some predictions will be done including uncertainty analyses, exploring the impact of artefacts, e.g.: loss of tracers due to leakages and sample collection.

B1.3 Scope and limitations

The scope of our work initially was to carry out blind simulation (predictive modelling) of the TDE experiment. However, the experiment has several artefacts that difficult the comparison of the predictions. When measuring the pressure in TDE, it was found that the pressure gradient between the drillholes was rather high or very high in some situations. Moreover, sudden leakages occurred in the control system, resulting in significant loss of tracer. In addition, samples are taken in the injection and observation drillholes at given time intervals for determining the variation of the activity in the injection and observation drillholes. These samplings volume may be properly quantified, but its effect is small if compared with the other artefacts, which are difficult or impossible to quantity. Therefore, the simulations were done neglecting all these artefacts.

B2 Methodology and model

B2.1 Conceptual description of features, events and processes of the experiments

In this simulation, it is assumed that the transport of the tracers from the injection drillhole to the observation drillholes take place only by diffusion. Transport by advection due to the pressure gradient existing between the drillholes is not considered. As explained in B1.3, the transport by advection between one drillhole to another is ignored since the data on pressure in the drillholes present large

variations and are very uncertain. The tracer removed when samples are taken for determining the activity in the drillholes is not into account, since this is small compared with other loss present in the experiment; e.g., sudden leakages.

In the 3D modelling, the transport by diffusion occurs mainly in the radial direction, but in the regions close at the bottom and top of the injection section the components perpendicular to these surfaces (bottom and top) are not negligible. These are the so-called end-effects. For the observation drillholes the end-effects are very small and, therefore, neglected.

Decay is not considered in the simulations since the results are expressed in activity corrected by time.

B2.2 Description of features, events and processes in the conceptual model

In the 3D modelling the only process considered is the diffusion through the rock matrix and the well mixing of the solution containing the tracers in the injection drillhole and in the observation drillholes. Transport by advection between the drillholes is not considered in the model. Tracers removed from the injection drillhole (and from the observation drillholes) when samples are taken are not considered in the simulations.

In the 2D modelling, moreover it is assumed that diffusion takes place only in the radial direction. The drillholes are assumed to be of infinite length (or very long), therefore, the end-effects are neglected.

In the preliminary simulations is assumed that the rock is isotropic, same diffusion in all directions. Some simulations are considering different diffusion coefficients along the foliation and perpendicular to the foliation. It is also assumed homogeneous rock matrix, equilibrium sorption and no chemical reactions.

B2.3 Model setup

Equation for diffusion in the rock matrix is given by

$$\left(\varepsilon_p + \rho k_p\right)\frac{\partial c_i}{\partial t} = \nabla\left(D_{eff}\nabla c_1\right)$$

Assuming constant diffusion coefficient in the matrix, the equation becomes

$$\left(\varepsilon_p + \rho k_p\right)\frac{\partial c_i}{\partial t} = D_{eff}\nabla(\nabla c_1)$$

The slots in the drillholes are simulated as a well-mixed volume; by applying a sufficiently high diffusion coefficient. In order to simplify the geometry, the slot is defined as the volume of the drillhole, before to introduce the dummy, with a porosity determined as the ratio between the volume of the slot and the volume of the drillhole. The volume of the slot includes the space between the drillhole wall and the dummy and the volume of the tubing used for circulating the solution containing the tracer.

The initial conditions are zero concentration in the rock matrix, and in the observation drillholes. The concentration in the injection drillhole is C = Co. The boundary conditions are no mass flow at the external borders located far away from the injection drillhole.

The 3D model, is comprised by the volume of rock matrix centred around the injection drillhole with a radius of 1 m, in which two sections may be distinguished: the upper section and the lower section. The upper volume of the rock matrix corresponds to the volume around the lower half of the 1-m section of the drillhole containing the tracers and the observation drillholes. The lower section of the rock matrix corresponds to the upper 0.5 m of the section with the inflated packer. The 3D system is shown in Figure B-1. The boundary conditions are close boundary conditions (no-flow, no-diffusion) along the cylinder walls.

The 2D model, is comprised by a three infinite or very long drillholes, perpendicular to the paper-plane. The 2D system is shown in Figure B-2. The boundary conditions are close boundary conditions (no-flow, no-diffusion) along the outer circumference.

Regarding the discretization used in the simulations, for the 3D model the number of nodes is about 500 000, with a computation time of about 40 min. The 3D model worked well for the non-sorbing tracer HTO. For the sorbing species the simulations are rather unstable, possibly the model requires a finer discretization.

For the 2D model, the number of nodes is around 100 000, with a computation time of about 2 minutes. In general, the simulation results are sufficiently stable.

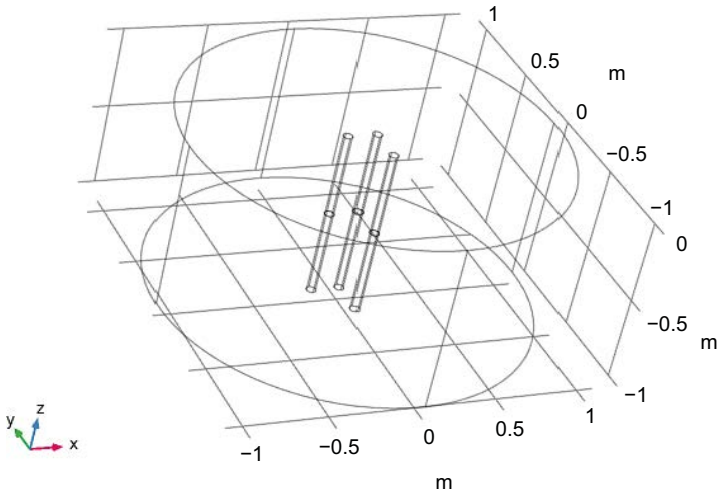

Figure B-1. *Set-up of the 3D system.*

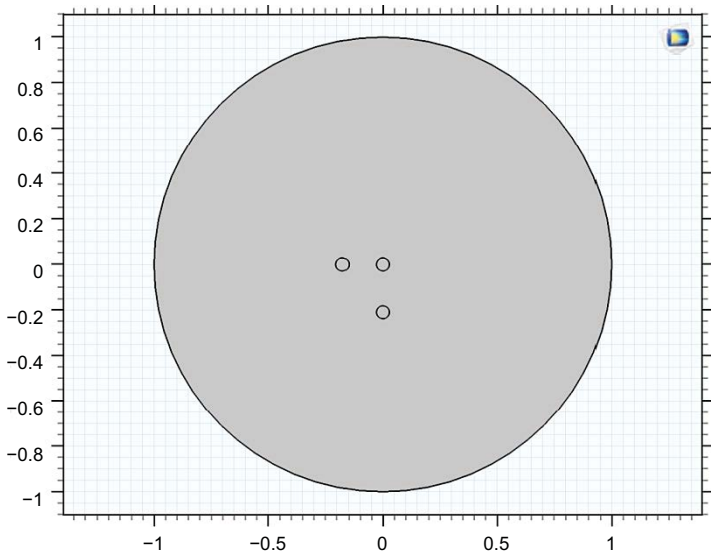

Figure B-2. *Set-up of the 2D system. Drillhole ONK-PP326 is located at the centre. Drillhole ONK-PP324 is located to the left-hand side of the central drillhole and the ONK-PP327 is located below from the central drillhole.*

B2.4 Input data

Data in Task Description (Andersson et al. 2020) will be used of preference in these simulations. Only a short summary of the used data is presented below.

Rock porosity

Rock Porosities have been obtained by water gravimetry, argon pycnometry and ^{14}C-PMMA autoradiography (Andersson et al. 2020). Rock porosity vary very strong between different locations around the drillholes. Taking a rough value of porosity for each drillhole, we can write

- ONK-PP324 0.006
- ONK-PP326 0.012
- ONK-PP327 0.0075

Therefore, a value of 0.01 will be used for these simulations.

As explained in 2.3, the slot is defined as the volume of the drillhole with a fictitious porosity is determined as the ratio between the volume of the slot (including tubing) and the volume of the drillhole. The values of these fictitious porosities are:

- Injection drillhole ONK-PP326 0.114
- Detection drillhole ONK-PP324 0.168
- Detection drillhole ONK-PP327 0.123

Rock matrix effective diffusivity and permeability

Here only samples from the TDE drill-holes are discussed. The following approaches were used to determine diffusion/permeability: a) Diffusion in water by using through-diffusion measurements, b) Gas phase through diffusion measurements, and c) Electromigration measurements (Andersson et al. 2020). The mean values for the different approaches are shown in Table B-1.

Table B-1. Effective diffusion coefficients.

Sample	D_e(HTO), m^2/s	D_e(Cl), m^2/s
Water diffusion, through experiment	3.9×10^{-13}	3.4×10^{-13}
Gas diffusion, through experiment	1.0×10^{-13}	1.0×10^{-13}
Electromigration	8.1×10^{-13}	8.1×10^{-13}

For HTO the value of 3.9×10^{-13} m^2/s is used, which is the effective diffusion coefficients (De) measured by the through experiment in water phase. For chloride the value 3.4×10^{-13} m^2/s is used. For the other species, the effective diffusion coefficient is determined by using the formation factor and the diffusion coefficient in water for the respective species.

$$D_e = F_f \cdot D_w$$

Where F_f is the formation factor and D_w is the diffusion coefficient in water (very large volume). For HTO the value of D_w is 2.1×10^{-09} m^2/s. Therefore, the value of the formation factor is 1.86×10^{-04}. The D_w for the other species and the respective D_e are shown in Table B-2.

Table B-2. Effective diffusion coefficients for the other species using the formation factor.

Species	D_w, m^2/s	D_e, m^2/s
Na [1]	1.33×10^{-09}	2.5×10^{-13}
Ba [1]	0.85×10^{-09}	1.6×10^{-13}
Cs [3]		3.0×10^{-13}

[1]) Buffle et al. 2007.

[3]) Andersson et al. 2020.

Sorption partitioning coefficients

Table B-3 shows the data used for the sorption partition coefficient.

Table B-3. Sorption partitioning coefficients.

Radionuclide	Rock type	Sorption partitioning coefficients (m^3/kg)
^{22}Na	Veined gneiss Pegmatitic granite	0.0013 ± 0.0003 0.0008 ± 0.0003
^{133}Ba	Veined gneiss Pegmatitic granite	0.06 ± 0.02 0.08 ± 0.02
^{134}Cs	Veined gneiss Pegmatitic rock	0.0310 0.0041

Injected activity

The injected (initial) activity in the injection drillhole is shown in Table B-4.

Table B-4. Injected activity.

Tracers	Injected Activity, MBq
^{3}H	198 ± 2.0
^{36}Cl	5.5 ± 0.2
^{22}Na	22.4 ± 0.2
^{133}Ba	1.92 ± 0.06
^{134}Cs	2.09 ± 0.04

Geometry and volumes used in TDE

Some values of geometry and volumes used for the TDE experiment are shown in Table B-5.

Table B-5. Geometries and volumes of the TDE experiment.

Description	Measure	Unit
Drillhole diameter of 1 m experiment section in ONK-PP324 (± 2 σ)	56.76 ± 0.07	mm
Drillhole diameter of 1 m experiment section in ONK-PP326 (± 2 σ)	56.92 ± 0.14	mm
Drillhole diameter of 1 m experiment section in ONK-PP327 (± 2 σ)	57.00 ± 0.16	mm
Outer diameter of dummy in ONK-PP324, 326, and 327	54.0	mm
Length of annular slot in ONK-PP324, 326, and 327 (also distance between inlet and outlet)	1.00	m
Distance of intact rock between test intervals ONK-PP326 to ONK-PP324 a	0.115	m
Distance of intact rock between test intervals ONK-PP326 to ONK-PP327 a	0.15	m
Total volume of water in ONK-PP324 test interval (including tubing)	291	mL
Total volume of water in ONK-PP324 test interval (including tubing from 2018-09-12)	424	mL
Total volume of water in ONK-PP326 test interval (including tubing)	290	mL
Total volume of water in ONK-PP327 test interval (including tubing)	313	mL

The simulations would be done for a time of 10 years, i.e. 3.16E8 s.

B2.5 Alternative models and sensitivity cases

In this section, we present sensitivity cases based in the value used for different parameters; e.g., effective diffusion coefficient, sorption partition coefficient and the geometry of the system.

The effective diffusion coefficient for Chloride including anion exclusion

For negative ions, such as Cl^-, the diffusion is influenced by the anion exclusion phenomenon. Due to the negative charges of the anions, they cannot move in the pores too much close to the pore walls, since the walls are negatively charged. The effective diffusion coefficient depends on the rock properties; e.g., pore size and rock composition. The value of the effective diffusion coefficient varies in a wide interval; therefore, simulations were done using different values for the effective diffusion coefficient. The values used were 3.9, 1, 0.39, 0.1×10^{-13} m^2/s.

The effective diffusion coefficient for Caesium including surface diffusion

The effective diffusion coefficient of Cs may be increased by the so-called surface diffusion (Skagius and Neretnieks 1988, Tsukamoto and Ohe 1993). The effective diffusion coefficient for Caesium varies in a wide interval. This value depends on the rock composition, porosity, and other rock properties. Therefore, simulations for Cs using a higher effective diffusion coefficient were carried out, the values chosen were 3.0×10^{-13} m^2/s without surface diffusion and 10.0 and 30.0×10^{-13} m^2/s with surface diffusion.

B3 Results and discussion

As described in Chapter 2.2, the calculations would be done using a 3D Model since the real system is 3D. But a 3D model requires a large number of nodes, therefore, the computation time is long. For the non-sorbing tracer HTO, the computation time for the 3D model is 40 minutes, while that if the 2D model is used the computation time is reduced to about 2 minutes. Moreover, the stability of the 2D model is better. For sorbing species, the computation times using 3D modelling are very long and the results unnstable.

The results for the tracer HTO will be first present using the 3D model and then the 2D model. The results for the 2D and 3D models are then compared. A good agreement is found for the tracer HTO. Later, the results for the 2D modelling for ^{36}Cl are presented, since the values for effective diffusion coefficient are very unsure, the calculations are done for different values of the effective diffusion coefficient. Following the results for the 2D modelling for ^{22}Na, ^{133}Ba, and ^{134}Cs are presented.

In order to verify the numerical solution obtained by using COMSOL©, constant concentration is assumed at the injection hole. Concentration profiles in the rock matrix for the new Comsol run were compared with the solutions obtained using MATLAB© (PDEPE-routine) and a good agreement was obtained. There is also an analytical solution for this problem, but the procedure is too complicated, since a large number of terms is required.

B3.1 The central prediction

Prediction for HTO

The results are first shown for the 3D modelling, following for the simulations using the 2D model. The results for 2D modelling will be compared directly with the 3D modelling

Prediction for HTO using 3D modelling

The 3D results are shown with help of surfaces through the injection hole and one of the observation holes. Figure B-3 shows the relative activity in a surface through the injection drillhole ONK-PP326 and the observation drillhole ONK-PP327. Figure B-4 shows the relative activity the surface through the injection drillhole ONK-PP326 and the observation drillhole ONK-PP324.

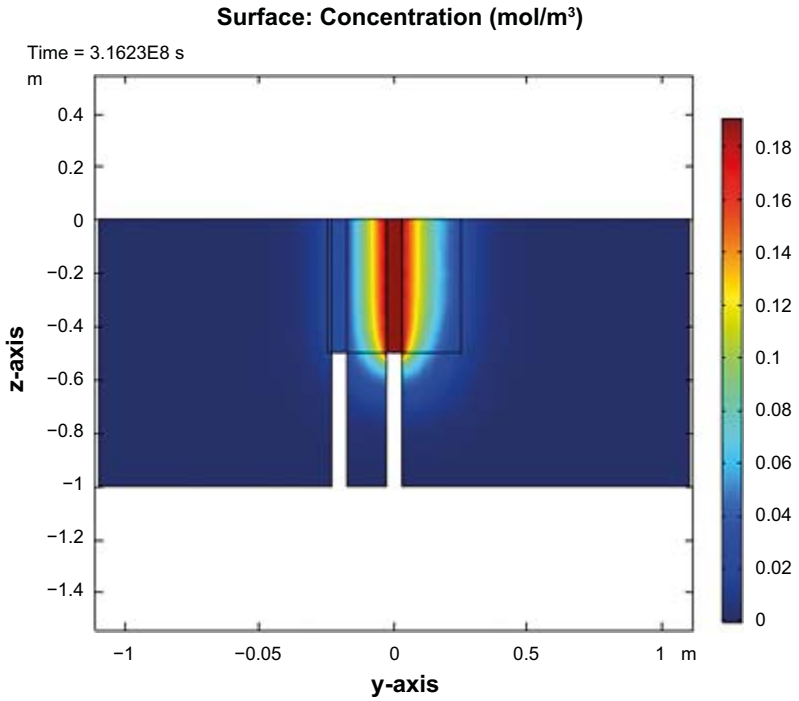

Figure B-3. *HTO relative activity along surface through the injection drillhole ONK-PP326 and the observation drillhole ONK-PP327.*

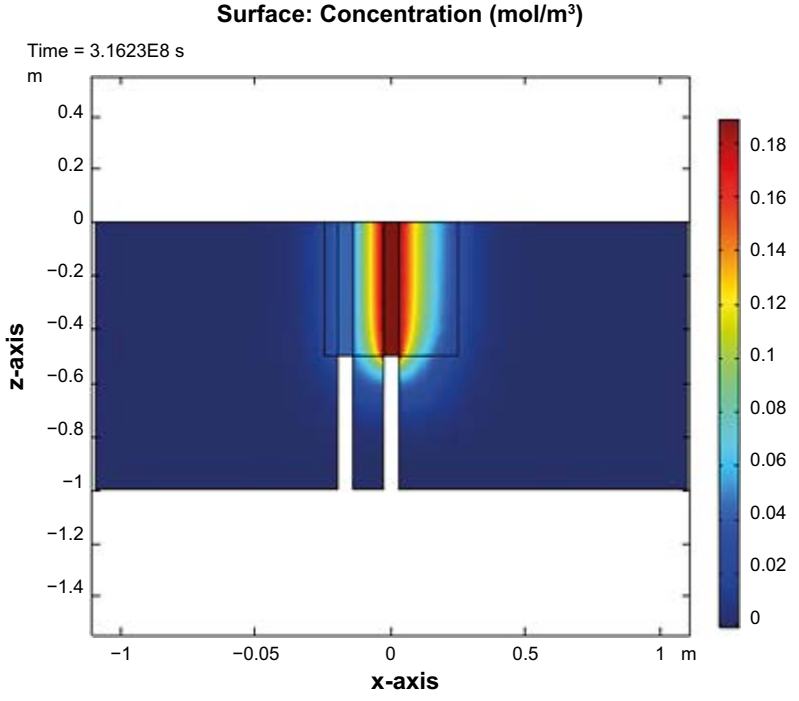

Figure B-4. *HTO relative activity along surface through the injection drillhole ONK-PP326 and the observation drillhole ONK-PP324.*

The variation of the relative activity as a function of time at the injection drillhole ONK-PP326 is shown in Figure B-5. The relative activity at the injection hole (ONK-PP326) shows a value of 0.19 at a time of 10 years.

Figure B-6 shows the relative activity at the observation drillholes ONK-PP324 and ONK-PP327. At a time of 10 years, the relative activities are 0.028 at the observation drillhole ONK-PP327 and 0.043 at the observation drillhole ONK-PP324.

The 3D-simulations are very time consuming (30–40 minutes) and require a very fine discretization of the system to be modelled resulting in a very large numbers of nodes (about 1 million nodes are required). The use of 2D modelling reduces the number of nodes that are required and therefore the calculation time. However, a 2D simulation assumes infinitely long tubes with mass flow occurring in a direction radial perpendicular to the drillholes axes. The end effects may be observed in Figure B-7, which shows the relative activity distribution at lower part of the lower 1-m section where the tracers are injected in detail. The same colour scale is used for easing the comparison. This shows that the end effects are not negligible, but not very important either. It is expected that the difference between the 3D and 2D modelling will be a few percent in the injection drillhole, but it would be very small at the observation drillholes, since the observation drillholes work as sink.

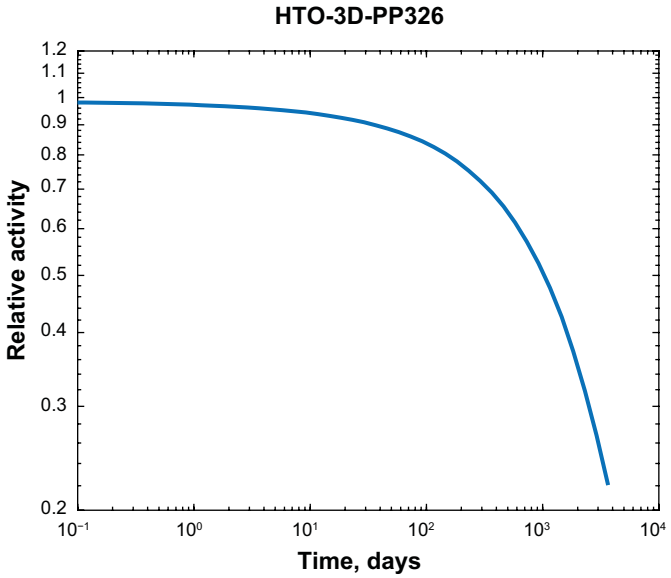

Figure B-5. *HTO relative activity as a function of time at the injection drillhole ONK-PP326.*

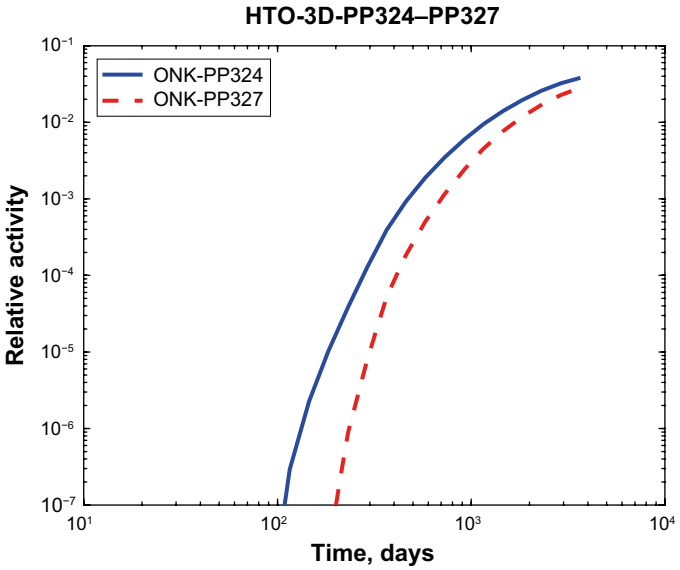

Figure B-6. *HTO relative activities as a function of time at the observation drillholes ONK-PP324 and ONK-PP327.*

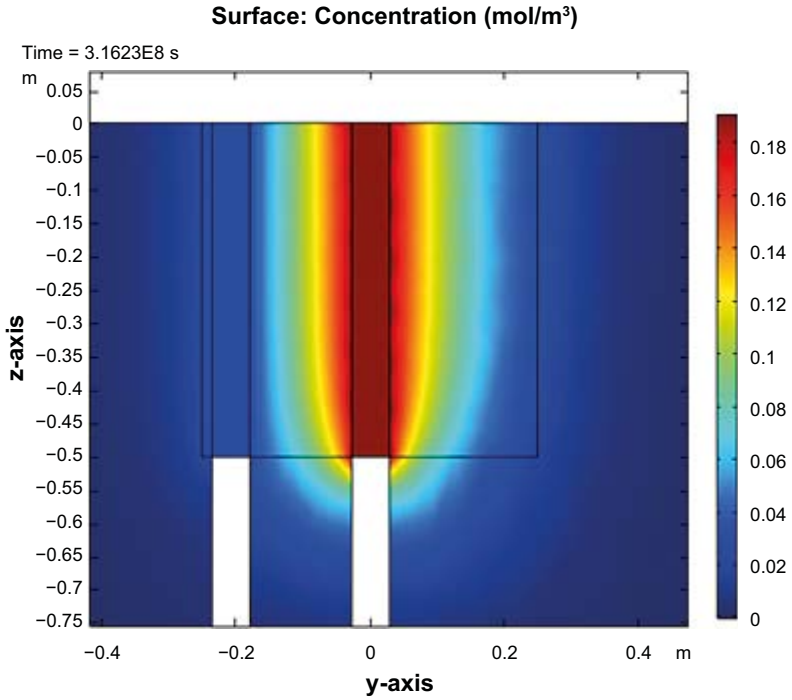

Figure B-7. *HTO relative activity at locations below the 1-m section showing the end-effects in detail.*

Prediction for HTO using 2D modelling and comparison with 3D modelling

The following figures show the relative activity as a function of time for the 2D modelling, which are compared with the results for 3D modelling. Figure B-8 shows the variation of the relative activity with time for the observation drillhole ONK-PP326 for both models; 2D and 3D. The activity decreases some more rapid for the 3D modelling compared with the 2D modelling. This difference, or part of this difference, could be explained by the end-effects, since a fraction of the tracer initially injected is located below of the 1-m section at time of 10 years. This does not occur in the case of 2D modelling where all the diffusion is in the direction radial.

Regarding the activity in the observation drillholes, it is found a well agreement between the 2D and 3D modelling. This is due to that the end-effects are negligible for the observation drillholes, since they act as sink. Figures B-9 and B-10 show the relative activities in the observation drillholes ONK-PP327 and PP324 respectively. The agreement is not good for very low activity, due to some instability of the results at relative activity below 1.0E−07 is observed when 3D modelling is used. Even, negative values are found.

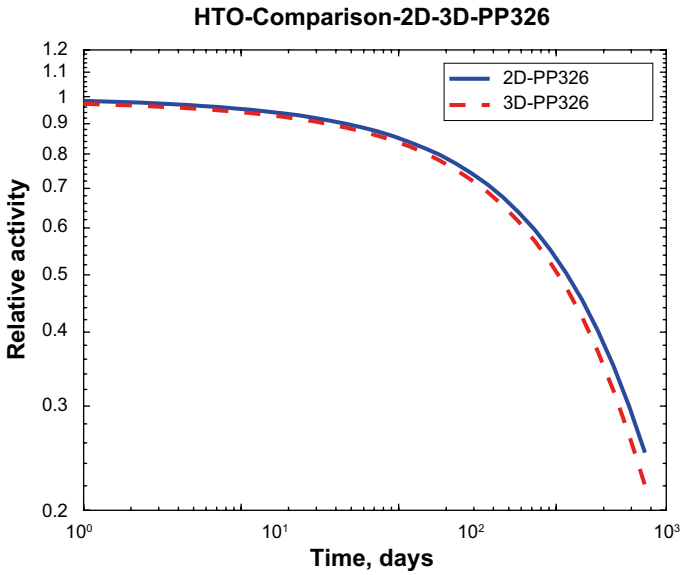

Figure B-8. *HTO relative activity in the injection drillhole, ONK PP326 for 2D and 3D modelling.*

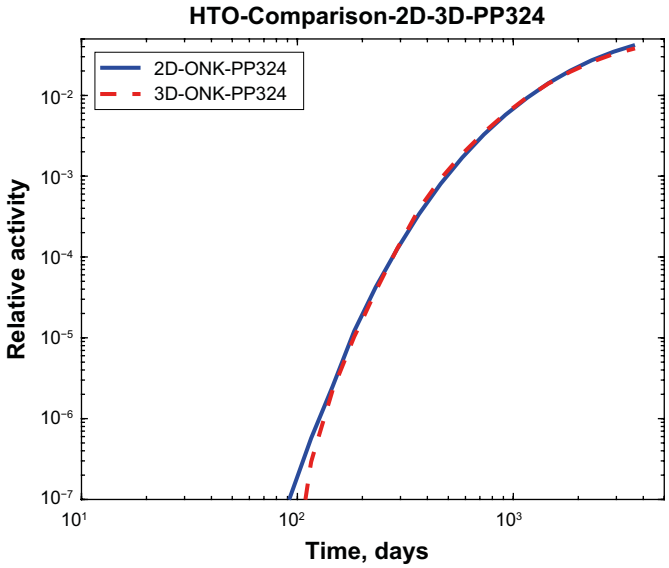

Figure B-9. *HTO relative activity in the observation drillhole, ONK PP324 for 2D and 3D modelling.*

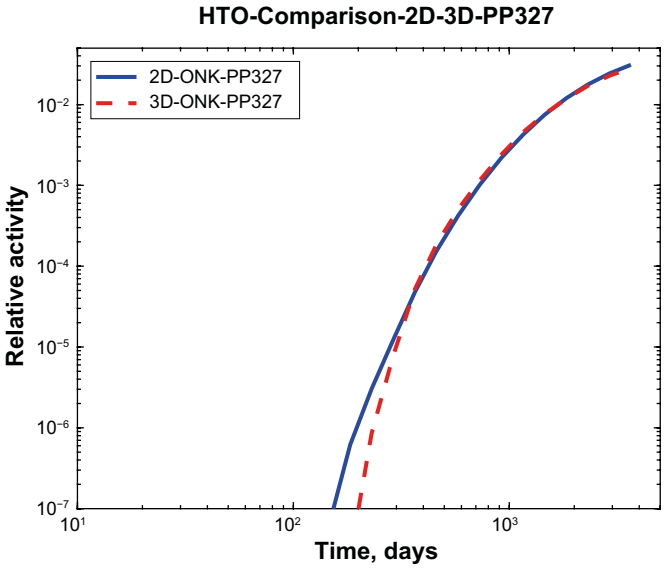

Figure B-10. *HTO relative activity in the observation drillhole, ONK PP327 for 2D and 3D modelling.*

Prediction for ^{36}Cl using 2D modelling and comparison with 3D modelling

For Cl, the effective diffusion coefficient is uncertain. The Task Description presents a value of 3.4×10^{-13} m^2/s for the effective diffusion coefficient (base value), which is used in this section. However, this value is too large, since it is expected that anion exclusion decreases the effective diffusion coefficient for a factor between 5 and 10. This is discussed in more detail in Section B3.2.

The results for chloride would be similar to those for HTO, since the difference in the effective diffusion coefficient is quite small. Therefore, only the predictions using the 2D model are presented here. Figure B-11 shows the relative activity in the injection drillhole ONK-PP326. For an effective diffusion coefficient of $3 \times 4 \cdot 10^{-13}$ m^2/s, the relative activity at 10 years is rather similar to that for HTO.

Figure B-12 shows the relative activity in the observation drillholes ONK-PP324 and PP327 respectively. The values are similar to those obtained for HTO.

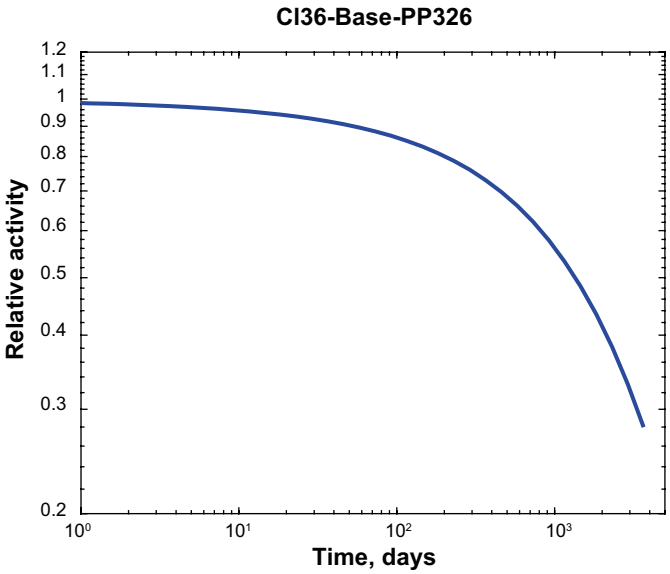

Figure B-11. *^{36}Cl relative activity as a function of time in the injection borehole ONK-PP326.*

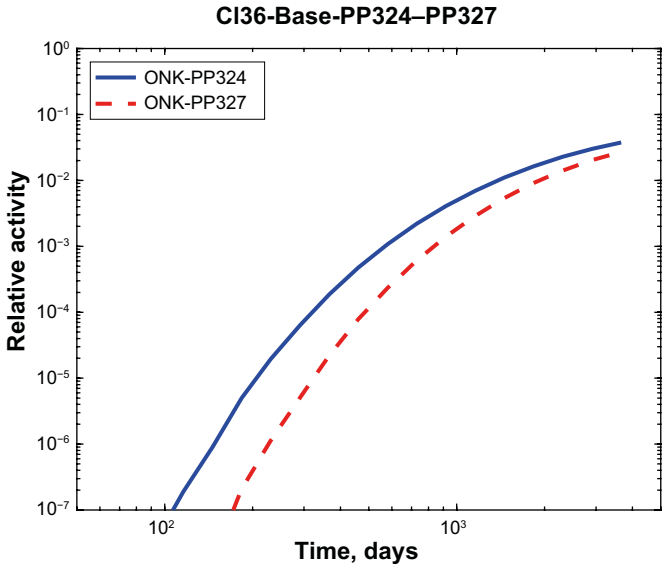

Figure B-12. *^{36}Cl relative activity as a function of time in the observation boreholes ONK-PP324 and PP327.*

Prediction for ^{22}Na using 2D modelling

For 3D modelling, in particular for sorbing species, the model requires a very fine discretization. The computation time is too long and the results are unstable. Therefore, only simulation using the 2D modelling were carried out for the sorbing species. A value of 0.0013 m^3/kg is used for the sorption partition coefficient and 2.5×10^{-13} m^2/s for the effective diffusion coefficient.

For the sorbing radionuclide ^{22}Na, no measurable activity is found in the observation drillholes at 10 years. At 10 years, the relative activity was less than 1.0×10^{-07} at a distance of 0.05 m from the centre of the injection drillhole, therefore, only the variation of the activity in the injection drillhole is shown. The activity in this drillhole initially decreases very fast, but for time longer than one few months, the activity decreases slowly. Figure B-13 shows the variation of the relative activity as a function of time in linear scale.

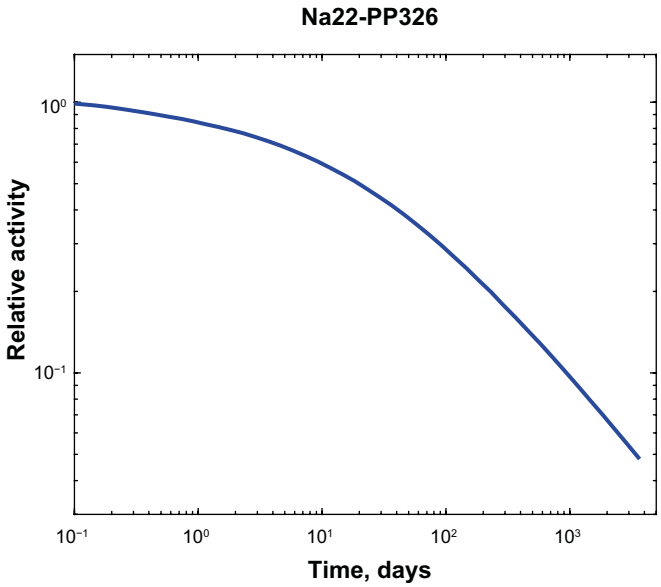

Figure B-13. *^{22}Na relative activity as a function of time in the injection drillhole PP326.*

Prediction for ^{133}Ba using 2D modelling

A value of 0.06 m^3/kg is used for the sorption partition coefficient and 1.6×10^{-13} m^2/s for the effective diffusion coefficient. For the sorbing radionuclide ^{133}Ba, no measurable activity is found in the observation drillholes. At 10 years, the relative activity was less than 1.0E−07 at a distance of 0.04 m from the centre of the injection drillhole, therefore, only the variation of the activity in the injection drillhole is shown. The activity in this drillhole initially decreases very fast, but for time longer than one-two months, the activity decreases slowly. Figure B-14 shows the variation of the relative activity as a function of time in linear scale.

Prediction for ^{134}Cs using 2D modelling

A value of 0.031 m^3/kg is used for the sorption partition coefficient and $3.0 \cdot 10^{-13}$ m^2/s for the effective diffusion coefficient. For the sorbing radionuclide ^{134}Cs, no measurable activity is found in the observation drillholes, therefore, only the variation of the activity in the injection drillhole is shown. The activity in this drillhole initially decreases very fast, but for time longer than one-two months, the activity decreases slowly. Figure B-15 shows the variation of the relative activity as a function of time in linear scale.

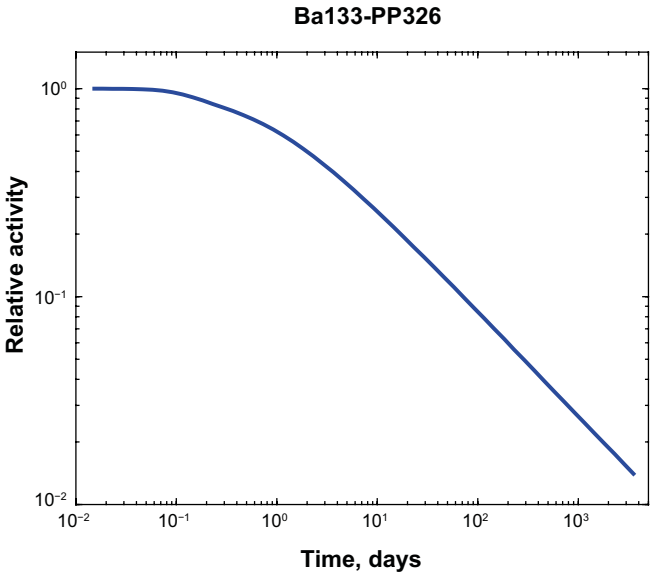

Figure B-14. *^{133}Ba relative activity as a function of time in the injection drillhole PP326.*

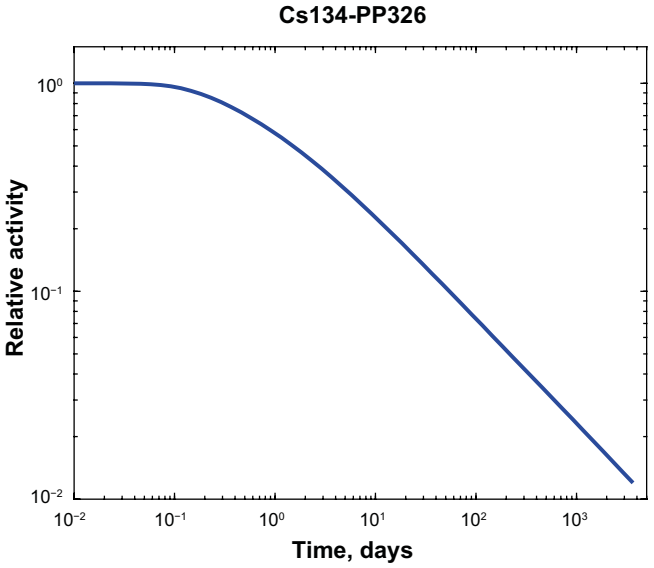

Figure B-15. *^{134}Cs relative activity as a function of time in the injection drillhole PP326, logarithmic scale.*

B3.2 Alternative models and sensitivity cases

In this section, we present some sensitivity cases based in the different values used for the:

- Effective diffusion coefficient due to surface diffusion.
- Effective diffusion coefficient due to anion exclusion.
- Geometry of the system.

The effective diffusion coefficient for Caesium including surface diffusion

For certain cations such as Cs and Sr, the effective diffusion coefficient is increased for diffusion along the pore walls. The effective diffusion coefficient for caesium varies in a wide interval. Therefore, simulations for Cs using a higher effective diffusion coefficient were carried out. The effective diffusivity without surface diffusion is 3.0×10^{-13} m^2/s, the effect of surface diffusion is simulated by increasing the effective diffusivity for a factor 3.33 and 10.0. Figure B-16 shows these results.

Effective diffusion coefficient for Chloride including anion exclusion

In the literature the values including anion exclusion are scarce and uncertain. In order to take into account anion exclusion, simulations are performed using different values for the effective diffusivity. The base value used in the predictions is 3.4×10^{-13} m^2/s. Anion exclusion is simulate decreasing the effective diffusivity by a factor 0.33 and 0.10.

Figure B-17 shows the relative activity in the injection drillhole ONK-PP326. For an effective diffusivity of 3.4×10^{-13} m^2/s, the relative activity at 10 years is rather similar to that for HTO. For the smallest effective diffusivity, 0.34×10^{-13} m^2/s, the relative activity at 10 years is very high in the injection drillhole, very close to the initial activity.

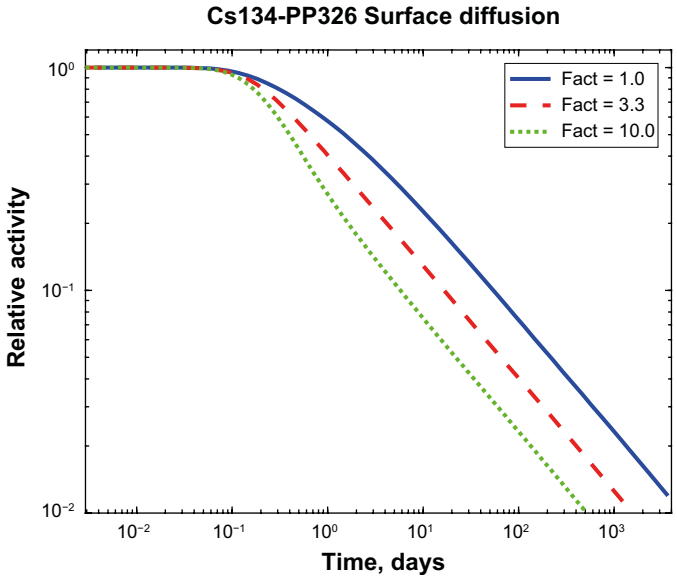

Figure B-16. *^{134}Cs relative activity as a function of time in the injection drillhole PP326 for different effective diffusivities by effect of surface sorption.*

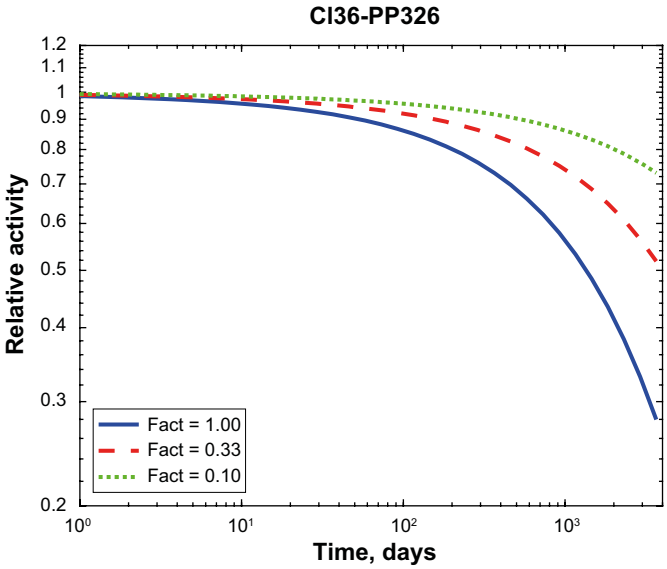

Figure B-17. *^{36}Cl relative activity as a function of time in the injection borehole ONK-PP326, for different values of effective diffusivity, decreasing from bottom to top.*

Figures B-18 and B-19 show the relative activity in the observation drillholes ONK-PP324 and PP327 respectively. For the observation drillhole ONK-PP324, for the smallest effective diffusion coefficient, 0.1×10^{-13} m^2/s, the relative activity is very small, below 1.0×10^{-07} at 10 years. For the other observation drillhole, ONL-PP327, the relative activity is very small, below 1.0×10^{-10} at 10 years.

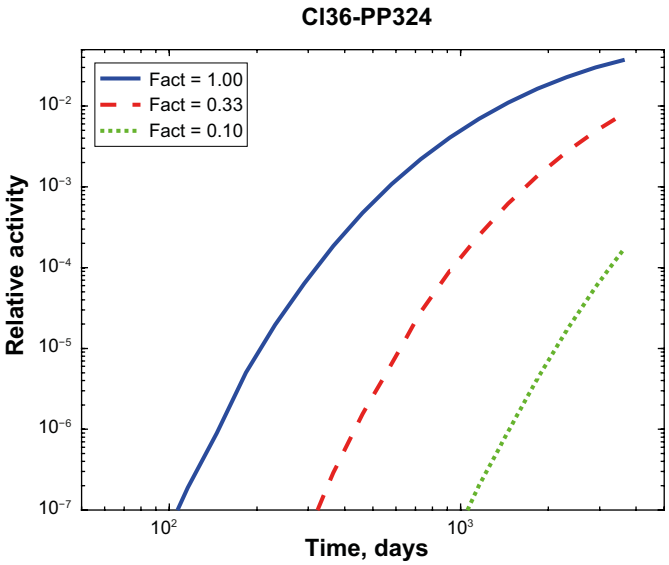

Figure B-18. *^{36}Cl relative activity as a function of time in the detection borehole PP324, for different values of effective diffusivity, decreasing from top to bottom.*

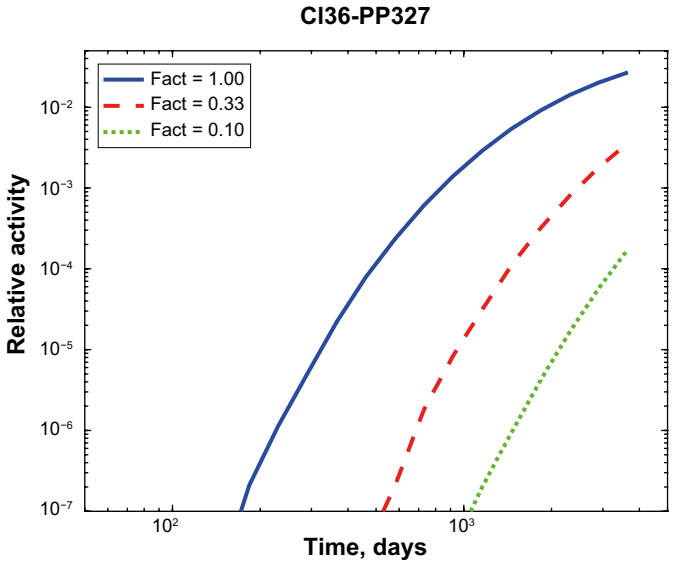

Figure B-19. *^{36}Cl relative activity as a function of time in the detection borehole PP327, for different values of effective diffusivity, decreasing from top to bottom.*

B3.3 Other results

Foliation

Foliation is parallel to the line that connects the injection drillhole and the observation drillhole PP324. Foliation is simulated increasing the effective diffusivity in the direction of the foliation. Amplification ratios of 3.3 and 10 were used, where the effective diffusivity perpendicular to the foliation was kept in 3.9×10^{-13} m^2/s.

Figure B-20 shows the relative activity as a function of time for the injection drillhole. The activity in the injection drillhole decreases faster when the effective diffusivity along the foliation is increased.

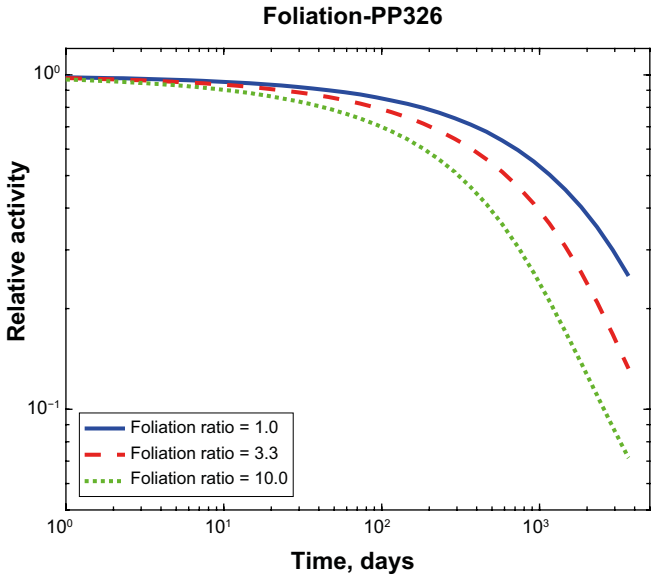

Figure B-20. *HTO relative activity in the injection drillhole as a function of time. Amplification factors increasing from top to bottom.*

The variation of the relative activity in the observation drillhole ONK-PP324 as a function of time is shown in Figure B-21. In this case, the diffusion from the injection drillhole to the drillhole PP324 is parallel with the foliation. In general, the activity in PP324 increases with increasing effective diffusion coefficient along the foliation, but a small diminution may be observed for the highest factor used in the simulations at times longer than three years, possibly due to the decrease of the activity in the injection drillhole (source term).

Figure B-22 shows the variation of the relative activity in the observation drillhole ONK-PP327. In this case, the diffusion from the injection drillhole to the observation drillhole ONK-PP327 takes place perpendicular to the foliation. The influence of the effective diffusion coefficient along the foliation is small on the activity in ONK-PP327.

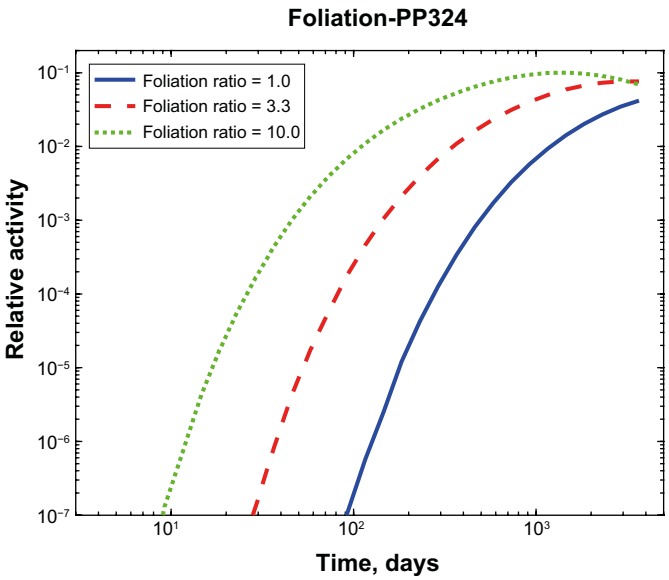

Figure B-21. *HTO relative activity in the observation drillhole ONK-PP324 as a function of time. Amplification factors decreasing from left to right.*

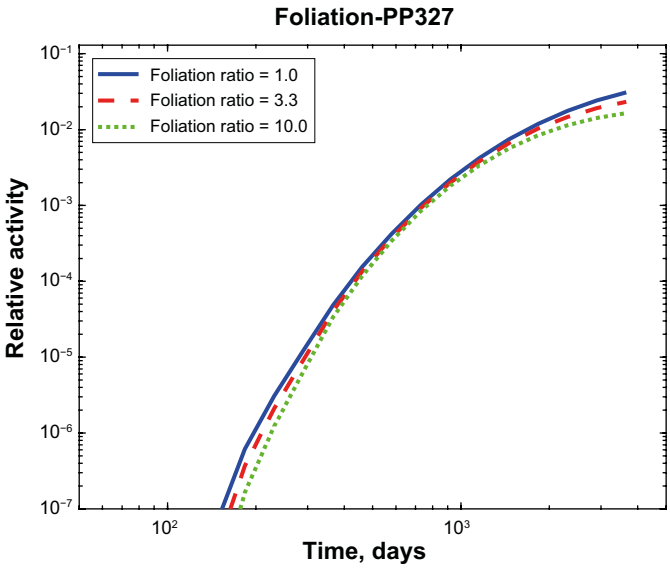

Figure B-22. *HTO relative activity in the observation drillhole ONK-PP327 as a function of time.*

Mass balance

Initially, the activity is only found in the injection drillhole ONK-PP326. During the experiment, a part of the activity is removed from the system by sampling for analyses. In addition, due to accidental situations a part of the activity is lost. Since the simulations were done for 10 years, the mass balance would be done for an intermediate time. The situation at 1 420 days (2019-10-09) after the start is used as the time for the mass balance. The calculations are only approximate, since the variation of the activity in the system is calculated without any alteration (sampling and leakages). Using this activity variation with time, the activity removed by sampling and the activity removed by leakage are determined. Other situations, as the partial clogging of the flow lines in the observation holes and high hydraulic gradients during certain periods of time were not considered. High hydraulic gradients (in the order of 100, or more) seem to prevail during long periods of time (Andersson et al. 2020), however, the new data for the rock permeability shows very low values and the impact of the possible water flow between drillholes is neglected. The mass balance is shown in Table B-6.

Table B-6. Mass balance at 1 420 days after start.

Location	HTO Relative activity	^{22}Na Relative activity	^{133}Ba Relative activity	^{134}Cs Relative Activity
ONK-PP326	0.460	0.081	0.022	0.019
ONK-PP324	0.014	0.0	0.0	0.0
ONK-PP327	0.007	0.0	0.0	0.0
Sampling	0.048	0.008	0.004	0.004
Leak, 16-01, 326	0.143	0.054	0.016	0.015
Within the rock	0.328	0.857	0.958	0.962

Impact of the volumes removed for sampling

In order to follow the activity in the injection drillhole and in the observation drillholes, samples are taken from the respective drillhole and the volume removed is replaced by the same volume of tracer free synthetic groundwater. This causes the dilution of the activity in the injection and observation drillholes.

The impact of the sampling in the injection drillhole is calculated adding two water flows; flow in and flow out. The flow out is for simulating the extraction of the sample and the flow in for simulating the tracer free water added to replace the extracted water volume. The value of the water flows is expressed for a function, which varies with time. The used parameters were fitted.

The effect of the sampling in the injection drillhole is small, since the volume of the extracted sample in each opportunity is very small, 0.2 mL. Therefore, it is expected a small difference between the activity without sampling and with sampling. The figure shows very small differences between results for simulations considering with and without sampling for the three drill holes; injection and observation drillholes. Therefore, Figure B-23 showing the relative activity in the injection drillhole is magnified, showing only a small section of the figure.

For sampling in the observation drillholes, the impact of sampling is more important, since the volume extracted from the observation drillholes were larger; 10 mL for the PP327. For the drillhole PP324, the most of the extracted volumes were 10 mL, except in seven samples, in which the extracted volume was 90 mL. The consequences for sampling in drillhole PP327 were determined and are shown in Figure B-24.

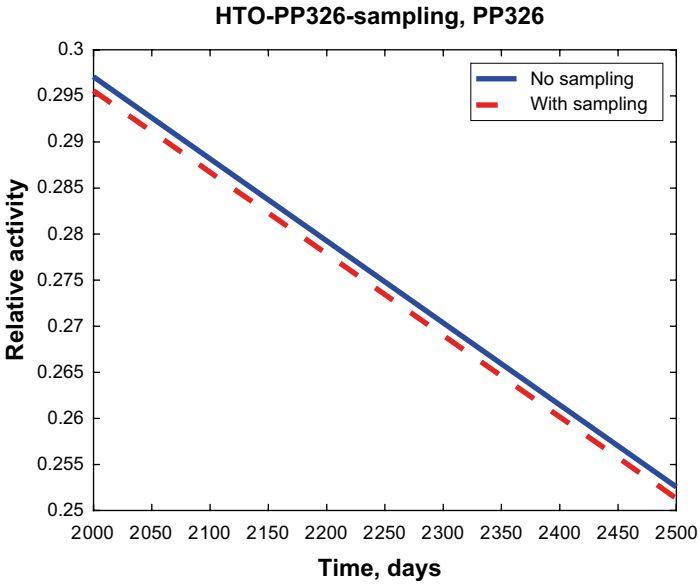

Figure B-23. *Comparison between the HTO relative activity in the injection drillhole, considering the cases with and without sampling.*

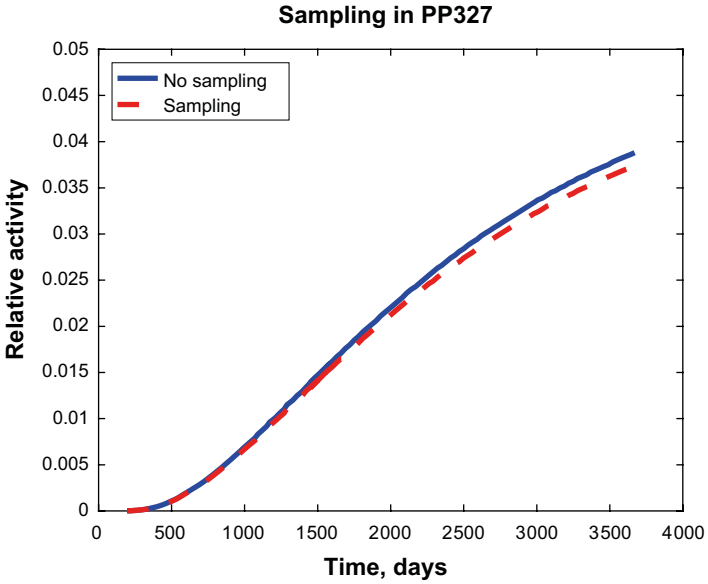

Figure B-24. *Comparison between the HTO relative activity in the observation PP327 drillhole, considering the cases with and without sampling in this drillhole.*

B3.4 Experimental results

The results experimental are presented for the first 1 265 days. Due to different experimental problems, the activities show rather chaotic results. This may be due to sorption on other surface of the circulation system, leakages, or other difficulties. Therefore, the inverse simulation is quite complicated. Figure B-25 shows the experimental results for ^{133}Ba and ^{134}Cs in the injection drillhole; ONK-PP326. The results for ^{22}Na, HTO, and ^{36}Cl in the same drillhole are shown in Figure B-26. For the observation drillhole ONK-PP324, the experimental results after 3 years are very small, relative activity is less than 1.0×10^{-05}, see Figure B-27. The experimental curves for the observation drillhole ONK-PP327 are shown in Figure B-28.

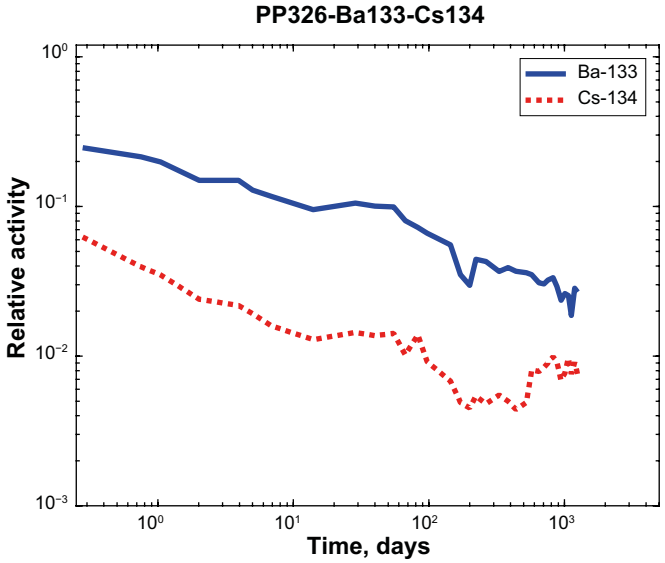

Figure B-25. Experimental results for ^{133}Ba and ^{134}Cs in the injection drillhole, ONK-PP326.

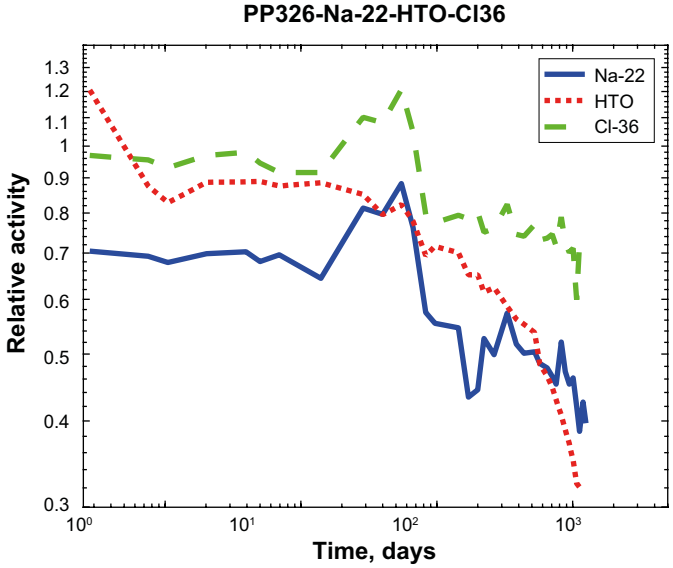

Figure B-26. Experimental results for ^{22}Na, HTO, and ^{36}Cl in the injection drillhole, ONK-PP326.

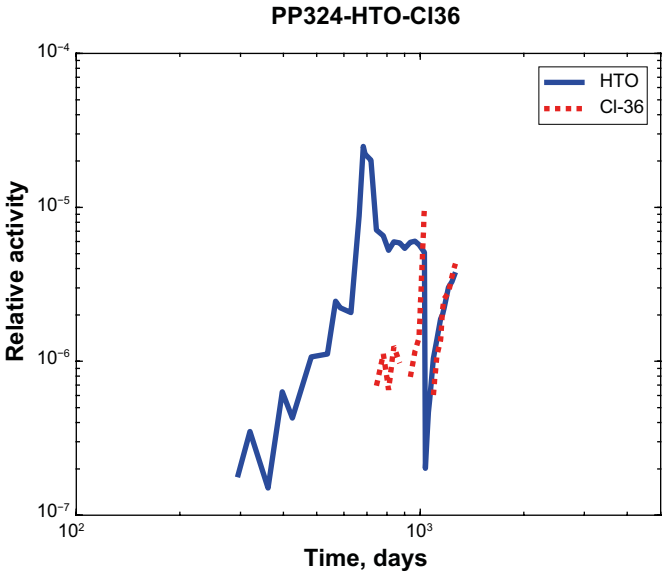

Figure B-27. *Experimental results for HTO, and ^{36}Cl in the observation drillhole, ONK-PP324.*

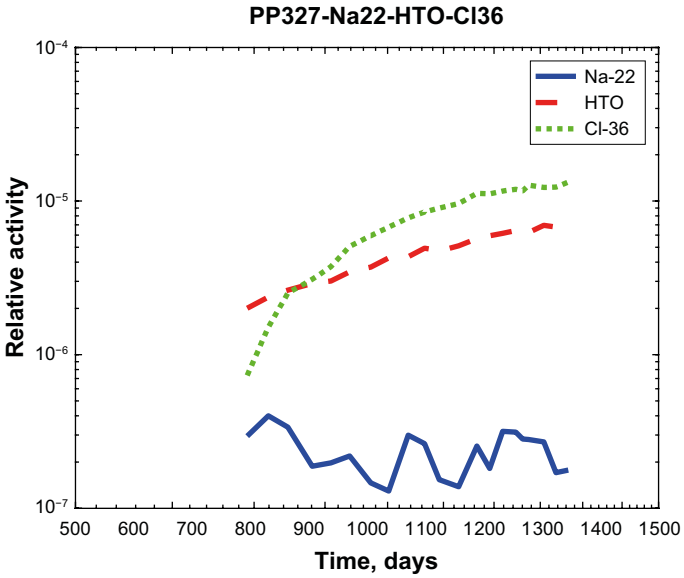

Figure B-28. *Experimental results for ^{22}Na, HTO, and ^{36}Cl in the observation drillhole, ONK-PP327.*

B4 Conclusions

The model used in the predictions includes diffusion from the injection drillhole into the rock matrix and the observation drillholes. For sorbing species, linear sorption is used, assuming a homogeneous rock matrix.

The results using the 2D and 3D models are similar, only small differences are found for the tracer HTO. This means that the end effects are not important. Therefore, the 2D model is used for the other tracers (^{36}Cl, ^{22}Na, ^{133}Ba, and ^{134}Cs).

Inverse modelling was omitted, due to that the results of the experiments are not good enough. Large variations were obtained, which may be only explained by several artefacts (leakages, error in the sampling technique, error in the analysis technique, etc).

Foliation was also modelled, the activity in the observation drillhole located in a direction parallel with the foliation, the variation in activity is very large. On the other hand, for the direction perpendicular to the foliation, the influence is small. Very similar values are obtained for the different foliation rates.

Appendix C

Amphos 21, Barcelona, Catalonia, Spain

Aitor Iraola, Paolo Trinchero

C1 Introduction

C1.1 Background

The SKB Task Force 9 focuses on the realistic modelling of coupled matrix diffusion and sorption in heterogeneous crystalline rock matrix at depth. This is done in the context of inverse and predictive modelling of tracer concentrations of the in situ experiments performed within LTDE-SD at the Äspö Hard Rock Laboratory in Sweden, as well as within the REPRO project at the ONKALO underground rock characterisation facility in Finland, focusing on sorption and diffusion. The ultimate aim is to develop models that in a more realistic way represent retardation in the natural rock matrix at depth (Andersson et al. 2020).

Task 9C focuses on the predictive modelling of the ongoing in situ Through Diffusion Experiment (TDE), which is a part of the REPRO project carried out by Posiva at ONKALO in Olkiluoto, Finland. The experiment is carried out between three parallel drillholes arranged as a right-angled triangle. One of these drillholes (ONK-PP326) is used as the injection hole for a cocktail of tracers while the other two drillholes (ONK-PP324 and ONK-PP327) act as observation holes (see Figure C-1). This facilitates tracer migration along, and across, the rock matrix's foliation. The experiment is carried out in 1 m long packed-off sections, at a distance of about 11 to 12 m from the tunnel wall and each drillhole is separated from the others a little more than one decimetre. Since the experiment takes place in a rock volume that lacks water-bearing fractures, any advective flow between drillholes is foreseen to be insignificant.

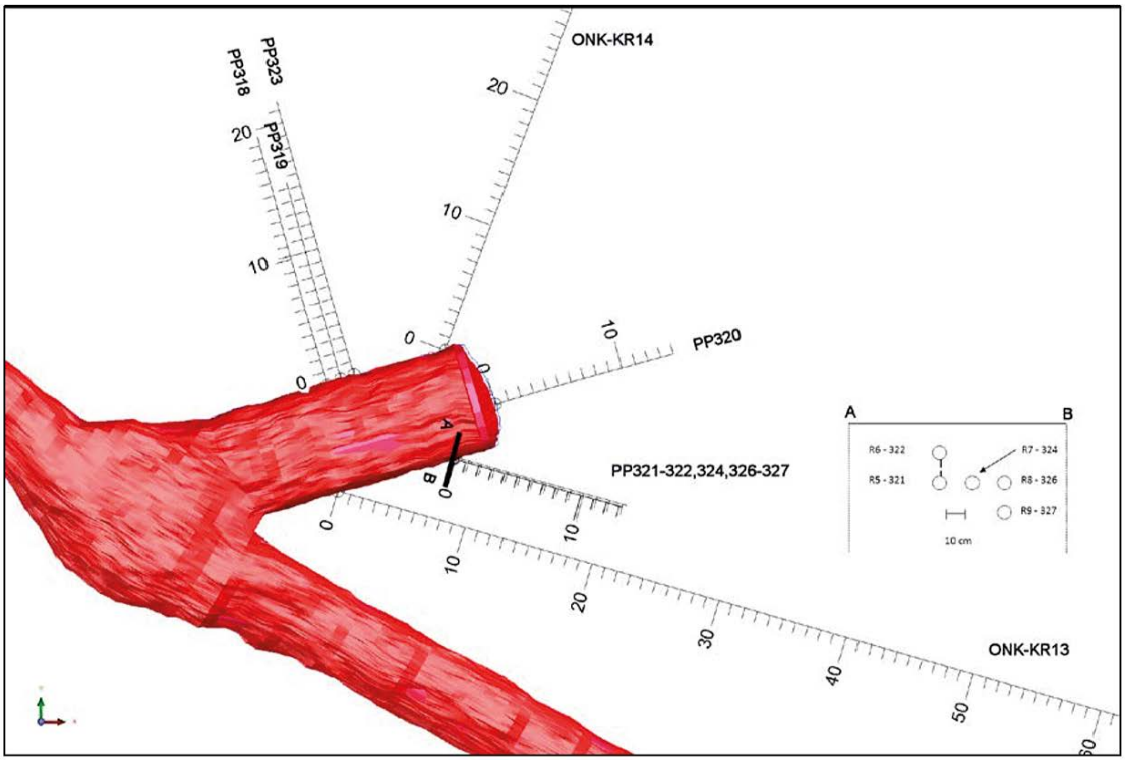

Figure C-1. *REPRO niche ONK-TKU-4219 and TDE drillholes ONK-PP321 to PP327.*

C1.2 Objectives and scope

The main objective of this work is to show the work that has been done to model the afore-mentioned Through-Diffusion-Experiment (TDE) and study the effects of rock foliation in the rock matrix.

This final report includes all the work done by Amphos 21 on the scope of the task 9C. Due to this broad scope, the work is divided in two main parts. The first part corresponds to the blind prediction stage, in which a model was built based on the experimental set-up. There, two different approaches were used to model rock foliation: a first one based on a full implementation of anisotropic diffusion in PFLOTRAN and a second approach based on stochastically generated heterogeneous and statistically anisotropic diffusion fields.

The second part focuses on the back-analysis stage in which, based on the published experimental results, the blind prediction stage model was upgraded (i.e. by adding a Borehole Deformation Zone (BDZ) and tuning the transport parameters) to fit the experimental data.

C1.3 Scope and limitations

The work presented here is a 2D model based on a slice perpendicular to the three boreholes and the surrounding matrix rock. It is assumed that advective flow through the rock matrix is negligible (i.e. due to the lack of conductive fractures at the considered local domain) and that reactive transport is mostly driven by diffusion. Diffusion is also expected to be affected by the moderate banded foliation of the veined gneiss.

In Section C2, the model set-up of the blind prediction stage is shown. Sections C2 and C3 focus on the results obtained using the blind prediction stage model. Section C4 shows the upgraded model of the back-analysis stage. In Section C5, the comparison between the experimental and numerical results obtained by the back-analysis stage model is shown. Finally, in Section C6, the main conclusions of the work are discussed.

C2 Blind prediction stage model

The model presented here is based on the set-up of the TDE experiment. A 2D slice perpendicular to the drilling direction has been considered as geometrical domain. In the next section, details of the model set-up are provided.

C2.1 Model set-up

TDE experiment

The TDE campaign is carried out between the three parallel drillholes ONK-PP326 (injection), ONK-PP324 (observation), and ONK-PP327 (observation) drilled from the right-hand wall of the REPRO niche. The drillholes have a dip of about −8°, meaning that they are drilled almost horizontally but with a slight dip downwards. In addition, there are two nearby observation drillholes, ONK-PP321 and ONK-PP322.

The experimental set-up consists of installations in the drillhole (installations performed on January 15th, 2015); equipment in two containers in the REPRO niche, one for injection and one for observation; and connecting tubing. Figure C-2 shows a side view illustration of one of the experiment intervals utilised in the campaign. The equipment is identical to the one used in the WPDE tests (i.e. Task 9A) with the exception of the length of the isolated interval. A 1 m long drillhole interval has been packed off by using inflatable packers. The ends of the packers, facing the experiment interval, have been teflonized to avoid interactions with the tracers. An inert and non-porous dummy of PEEK (PolyEtherEtherKetone) has been placed within the packed-off drillhole section, with the aim to reduce the water volume of the test intervals.

As it can be seen in Figure C-2, the diameter of the dummy is 54 mm while the diameter of the drillhole is about 56.5 mm. This leaves a 1.25 ± 0.1 mm annular slot between the dummy and the drillhole wall. Locally the drillhole diameter may change, due to surface roughness and minor irregularities of the drillhole wall.

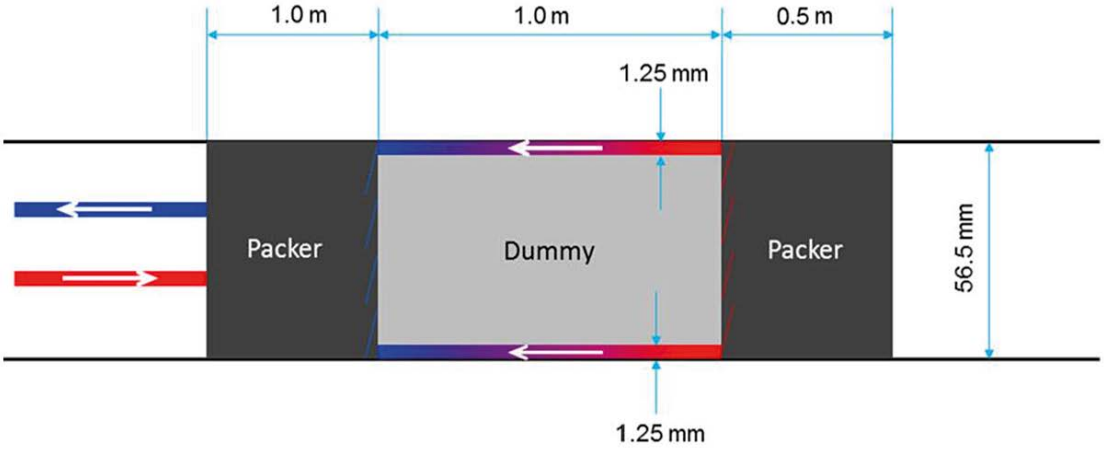

Figure C-2. *The experimental setup of the TDE in situ campaign. Side view of the experimental section. Red colour signifies ingoing circulating water and blue colour outgoing water.*

The bedrock surrounding the drillhole test intervals is veined gneiss (VGN). The veined gneiss shows a weak to moderate banded foliation but locally also irregular foliation. The general orientation of the foliation is almost parallel to the drilling direction. The drillholes also intersect a skarn lens (or layer). Only few fractures intersect the drillholes (Toropainen 2012) but there is only one part of the local rock volume, with a length of 1 m or more, that is completely free from fractures in all three drillholes. This local rock volume is chosen for the experiment. The orientation of the drillholes was chosen to study diffusion along and perpendicular to the foliation. Using drillhole ONK-PP326 as injection drillhole and ONK-PP324 as observation hole allows for diffusion along the foliation. Diffusion from the injection hole towards observation hole ONK-PP327 is perpendicular to the foliation. Drillholes ONK-PP321 and ONK-PP322 are located very close to the three experimental drillholes (about 0.1 m from PP324). These holes were therefore plugged with packers in order to avoid creating a hydraulic sink.

Geometry and mesh

The full 3D layout of the TDE experiment has been simplified as a 2D slice perpendicular to the drilling direction. Figure C-3 shows a schematic layout of the considered geometry.

In Figure C-3, one can see the two main regions considered in our model: the rock matrix (in orange) and the annular fractures of the drillholes (in blue). The ONK-PP326 borehole will be used as the injection borehole, while the ONK-PP324 and ONK-PP327 boreholes will be the observation boreholes, the first located parallel to the direction of the foliation, and the second perpendicular to that direction. As it is mentioned in the task description (Andersson et al. 2020), there is an uncertainty in the measured distance between the drillholes (i.e. due to difficulties to drill absolutely straight drillholes and accurately measure the deviations of the drillholes). Thus, the inter-drillhole distances (i.e. the minimum distance of rock matrix between drillholes) used in this work are the ones measured at drillhole length 12.0 m (i.e. 0.115 m from ONK-PP326 to ONK-PP324 and 0.15 m from ONK-PP326 and ONK-PP327). The inner radius of the annular fracture of the drillholes is 54 mm and the outer radius is 56.5 mm. The rock matrix domain that surrounds the drillholes is represented by a 0.7 m x 0.7 m square.

To discretize the considered domain, a semi-structured prismatic mesh has been used (meaning that the domain is actually pseudo-2D). This mesh has been generated using GiD (CIMNE 2009), which is a powerful pre- and post-processor developed by CIMNE, the International Centre of Numerical Methods in Engineering of Barcelona. The calculations have been carried out using PFLOTRAN (Hammond et al. 2014). Figure C-4 shows a close-up look of the mesh.

As it can be seen in the figure, the mesh that has been used is unstructured. In this way, the annular shapes of the boreholes can be accurately modelled. Far from the borehole, regular cubic elements have been used in order to improve numerical accuracy for the anisotropic diffusion method that has been implemented in PFLOTRAN. The numerical mesh consists of 481 916 elements and 967 030 nodes.

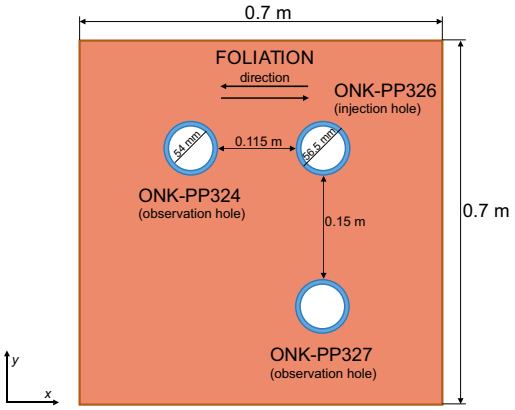

Figure C-3. *Schematic layout of the geometry of the model. The orange region represents the rock matrix while the blue rings represent the borehole. Foliation direction is set on the x-axis.*

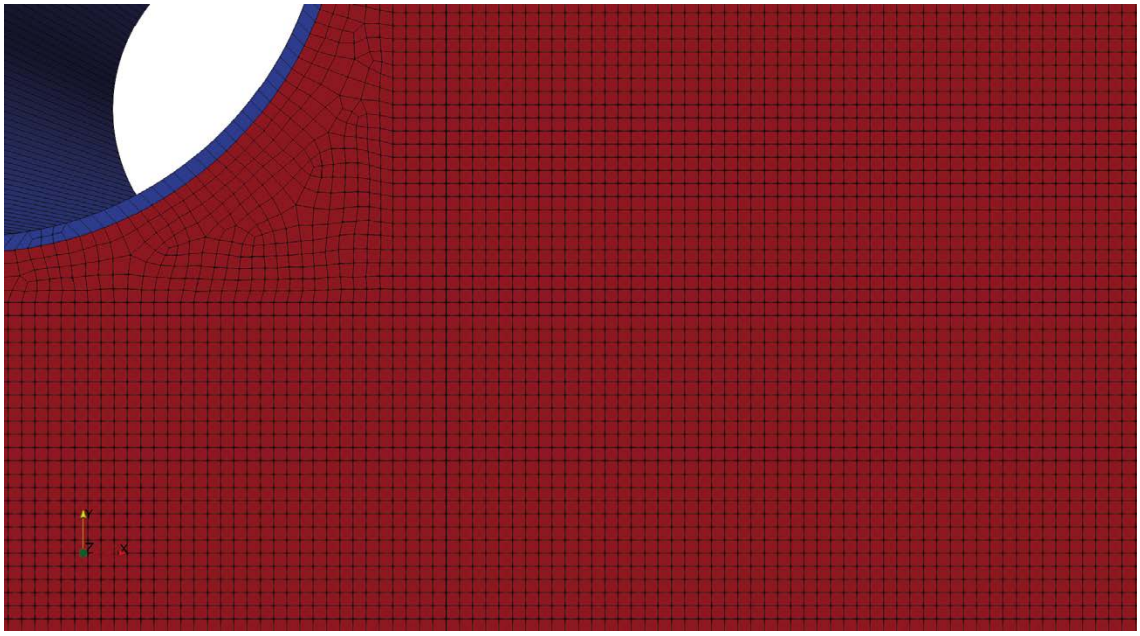

Figure C-4. *Close-up view of the mesh of the model. Notice that the mesh is fully structured far from the boreholes and unstructured close to them.*

To import the mesh generated in GiD to PFLOTRAN, a software called iGP (Iraola 2015) has been used. iGP stands for *interface between GiD and PFLOTRAN* and it was developed on Amphos 21. It is essentially a plugin that runs inside GiD and allows to apply different conditions and materials in the model.

Initial and boundary conditions

Regarding the initial and boundary conditions of the model, an initial mass of the considered radionuclides is placed in the injection borehole (i.e. the ring-shaped region of ONK-PP326). In the rest of the domain (i.e. the rock matrix and the two observation boreholes) zero initial concentration is applied. Zero flux boundary conditions are applied to the four external sides of the model. With these initial conditions, radionuclides are let to diffuse through the matrix for a total time of 10 years.

Figure C-5 shows a sketch summarizing the initial and boundary conditions of the model.

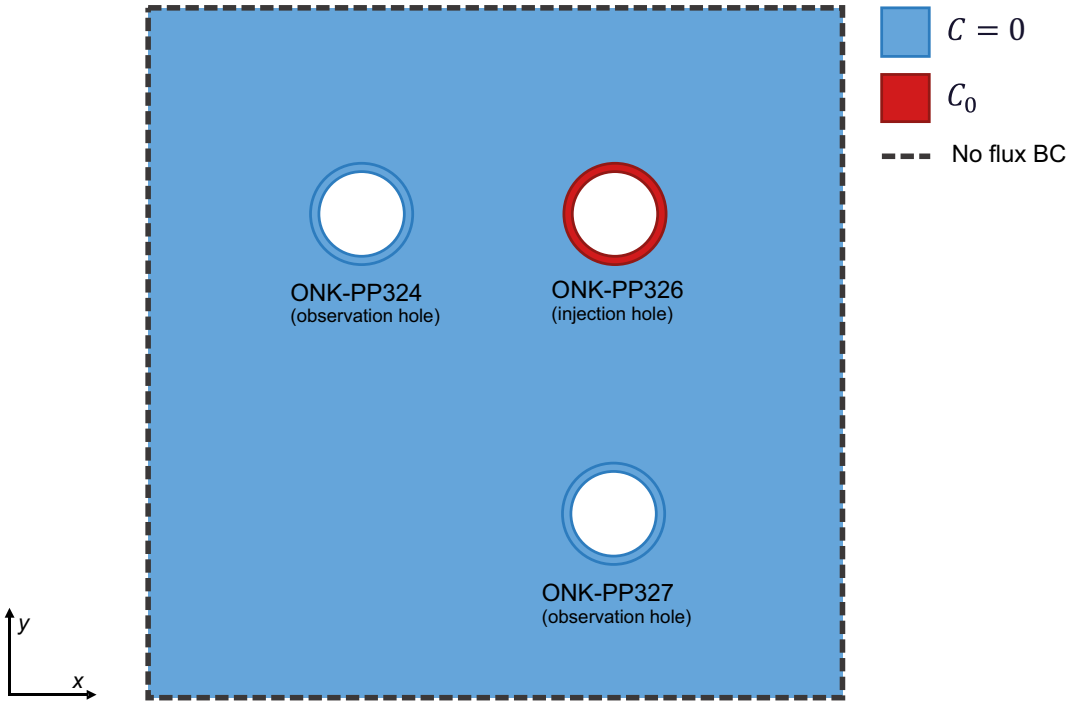

Figure C-5. *Initial and boundary conditions of the model. Blue color means initial zero concentration and red color represents the initial concentration in the injection borehole. Dashed lines show the no flux boundary condition applied to the boundaries of the domain.*

Simulation cases

As mentioned before, the blind prediction stage model focuses on simulating the TDE experiment with special focus on how foliation affects radionuclide diffusion. Two approaches have been used to mimic anisotropic diffusion due to foliation. The first one, which is based on the implementation of an anisotropic diffusion tensor in PFLOTRAN, is here denoted as *Anisotropic Diffusion approach.* The second approach, which is based on the generation of statistically anisotropic heterogeneous fields, is here denoted as *Heterogeneous Diffusion Field approach.* Among all the simulations runs, 4 main simulation cases have been selected to illustrate the differences between the two modelling approaches that have been considered.

The first case scenario is called *Central Case*. In order to point out the effect of anisotropic diffusion, a *Zero Case* has been defined, where a homogeneous isotropic diffusion field is considered.

In the *Heterogeneous Diffusion Field approach*, diffusion fields have been generated using three different gaussian distributions. For each distribution, 10 different realizations have been simulated, which adds up to a total of 30 simulations.

Among these 30 simulations, two case scenarios have been carefully assessed: the *Upper Case*, which is based on the numerical realization that shows the highest foliation, and the *Lower Case*, which is the simulation that shows less foliation. The *Upper Case* belongs to the set of diffusivity fields computed using the highest variance whereas the *Lower Case* is one of the realizations of the set of fields generated with the lowest variance.

Diffusion parameters

Effective diffusion coefficient ($D_e - \phi\tau D_0$, where ϕ is the porosity, τ is the tortuosity and D_0 is the molecular diffusion in water) is the key parameter that controls diffusion. In this work, two conceptual models for foliation have been studied, in which diffusion is defined either as an anisotropic tensor or as a statistically heterogeneous anisotropic field.

It is known that the effective diffusion coefficient for the different tracers is around 3×10^{-13} m^2/s (Table 5-5 and Table 5-6 of the task description). Thus, this will be the mean value used in the simulations.

The porosity in the matrix is set to $\phi_{matrix} \simeq 0{,}.006$ (Ikonen et al. 2015), which gives a value of tortuosity of $\tau = 0.05$, resulting in a pore diffusitivity value of $D_p = 5 \times 10^{-11}\ m^2/s$. In the slot, pore diffusivity is set equal to the value in unconstrained solution ($D_p = 1 \times 10^{-9}\ m^2/s$) and porosity is set equal to one.

For the *Central Case*, an effective diffusion coefficient of $2 \times 10^{-13}\ m^2/s$ is set along the direction perpendicular to foliation, and it is twice as much in the foliated direction ($4 \times 10^{-13}\ m^2/s$).

The *Zero Case* uses the mean value to define the isotropic effective diffusion coefficient ($3 \times 10^{-13}\ m^2/s$).

The *Upper Case* and the *Lower Case* (as well as the other realizations of the *Heterogeneous Diffusion Field approach*) are based on different diffusion fields whose statistical distribution is specified below.

Sorption model

A linear isotherm reaction based on K_d is used to simulate sorption. The partitioning coefficients for the different tracers used in the simulations have been taken from the task description. For Na-22 and Ba-133, the partitioning coefficients were measured from batch experiments using a few crushed samples from the veined gneiss rock, collected from different drill core locations. The sorption data for Cs-134 is based on the batch experiments and in-diffusion experiments into monolithic rock cubes from Olkiluoto (Muuri et al. 2017). Table C-1 shows the data of sorption used in the models.

Table C-1. Sorption partitioning coefficients obtained in batch experiments on crushed rock of different size fractions or intact rock cubes at Helsinki University. Uncertainty estimates, if available, represent one standard deviation.

Radionuclide	Rock type	Sorption partitioning coefficients (m^3/kg)	Source
Na-22	Veined gnesis	0.0013 ± 0.0003	Unpublished data
Ba-133	Veined gnesis	0.06 ± 0.02	Unpublished data
Cs-134	Veined gnesis	0.031	-

Radionuclides and injected activities

The injected TDE tracer cocktail used in the experiment contained the following radionuclides: ^{3}H, $^{22}Na^{+}$, $^{36}Cl^{-}$, ^{133}Ba and ^{134}Cs. However, in this work $^{36}Cl^{-}$ is not considered. Table C-2 lists the radioactive elements used in this modelling work and the injected decay corrected activities.

Table C-2. List of tracers for TDE experiment.

Isotope	Activity (MBq)	Decay mode	Half-life (y)
^{3}H	198 ± 2	β^{-}	12.3
$^{22}Na^{+}$	22.4 ± 0.2	$\epsilon + \beta^{+}$	2.6
^{133}Ba	1.92 ± 0.06	ϵ	10.5
^{134}Cs	2.09 ± 0.04	β^{-}, ϵ	2.1

C2.2 Modelling of the effect of rock foliation

In this stage, two different modelling approaches have been used to simulate the effect of rock foliation. Numerically, a foliated system can be conceptualised as a system with a preferential diffusive direction. The first approach to model this preferential diffusion is to explicitly increase the effective diffusion coefficient in that direction. This is what is done in the *Anisotropic Diffusion approach*. However, the current version of PFLOTRAN does not support the capability to simulate anisotropic diffusion.

In the second approach, statistically anisotropic heterogeneous diffusivity fields are used to mimic the effect of foliation. This has been done by stochastically generating non-homogeneous diffusion fields that are thought to behave as a foliated system. In this case, the default capabilities of PFLOTRAN can be used and no internal coding is needed.

Implementation of anisotropic diffusion in PFLOTRAN

Since PFLOTRAN is an open-source code, anyone can access and build his own customised version. In this section, a summary of the steps done to implement the *Anisotropic Diffusion approach* in PFLOTRAN are explained.

The strategy followed to implement Anisotropic diffusion has been to find the part of the code where the effective diffusion coefficient is calculated, and scale it with a factor that depends on the angle between the mesh connections and the foliation direction. The analogous variable used in PFLOTRAN to calculate diffusion is called *hydrodynamic_dispersion*.

Figure C-6 shows the piece of code calculates the afore-mentioned coefficient.

A scaling factor is multiplied to the calculation of hydrodynamic dispersion, which depends on the angle between the foliation orientation and the direction vector between the centroids of two mesh elements (i.e. angle θ in Figure C-7). If the direction vector (i.e. vector $\hat{\delta}$ in Figure C-7) is parallel to the foliation direction, the scaling factor has a value of $w_{\parallel}$, and if the vectors are perpendicular, the scaling factor is set to $w_{\perp}$ (being $w_{\parallel}$ and $w_{\perp}$ the principal components of the considered tensor, in this case diffusivity). A linear relationship is assumed between the scaling factor and angle θ.

```
! hydrodynamic dispersion = mechanical disperson + &
!   saturation * porosity * tortuosity * molecular diffusion
hydrodynamic_dispersion_up(:) = &
  max(mechanical_dispersion_up + &
      sat_up * material_auxvar_up%porosity * &
      material_auxvar_up%tortuosity * molecular_diffusion_up(:), &
      1.d-40)
```

Figure C-6. *Fortran fragment of the PFLOTRAN code showing the default place where hydrodynamic dispersion is calculated.*

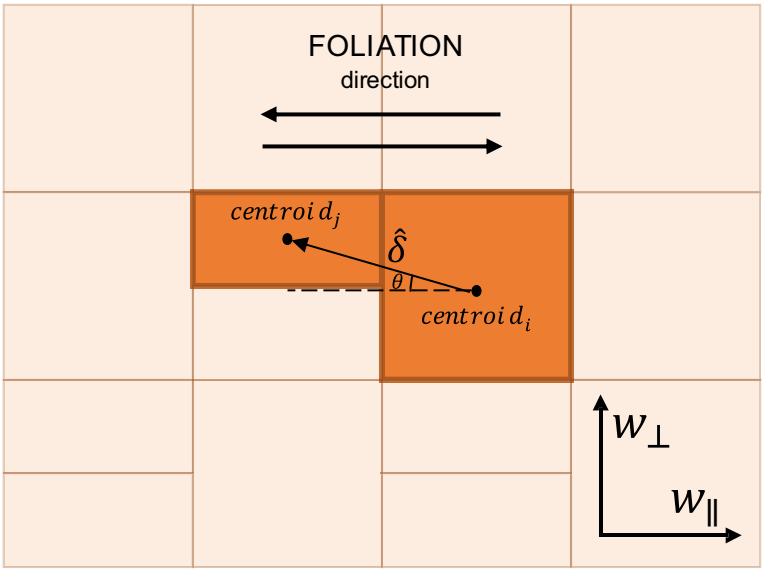

Figure C-7. *Sketch summarizing the method used to implement anisotropic diffusion on PFLOTRAN.*

Defining angle θ as

$$\theta = \text{atan}\frac{|\delta_y|}{|\delta_x|}$$

the scaling factor can be calculated in the following way:

$$SF(\theta) = \frac{2}{\pi}(w_{\perp} - w_{\parallel})\theta + w_{\parallel}$$

Notice that θ has always a positive value since anisotropic diffusion does not depend on the direction.

This scaling factor is then included in PFLOTRAN in the way shown in Figure C-8.

The final version of the modified piece of code includes the possibility to define the scaling factors for the foliation (i.e. factors $w_{\parallel}$ and $w_{\perp}$). Two keywords have been implemented: *ANISOTROPIC_DIFF_X* and *ANISOTROPIC_DIFF_Y*, allowing to control anisotropic diffusion on the *x* and *y* axis directly from the PFLOTRAN input deck. In the model presented here, a scaling factor of 2 has been used for the *Central Case*, doubling the effective diffusion coefficient in the *x*-axis.

The implementation of the *Anisotropic Diffusion approach* has been validated with a well-known benchmark exercise of 2D diffusion from a point source.

```
! hydrodynamic dispersion = mechanical disperson + &
!   saturation * porosity * tortuosity * molecular diffusion

theta = atan(abs(dist(2))/abs(dist(1)))
diff_factor = 2/PI_2*(rt_parameter%anisotropic_diff_y-rt_parameter%anisotropic_diff_x)* &
theta+rt_parameter%anisotropic_diff_x

hydrodynamic_dispersion_up(:) = &
  max(mechanical_dispersion_up + &
      sat_up * material_auxvar_up%porosity * &
      material_auxvar_up%tortuosity * molecular_diffusion_up(:)*diff_factor, &
      1.d-40)
```

Figure C-8. *Fragment of the PFLOTRAN code modified to simulate anisotropic diffusion.*

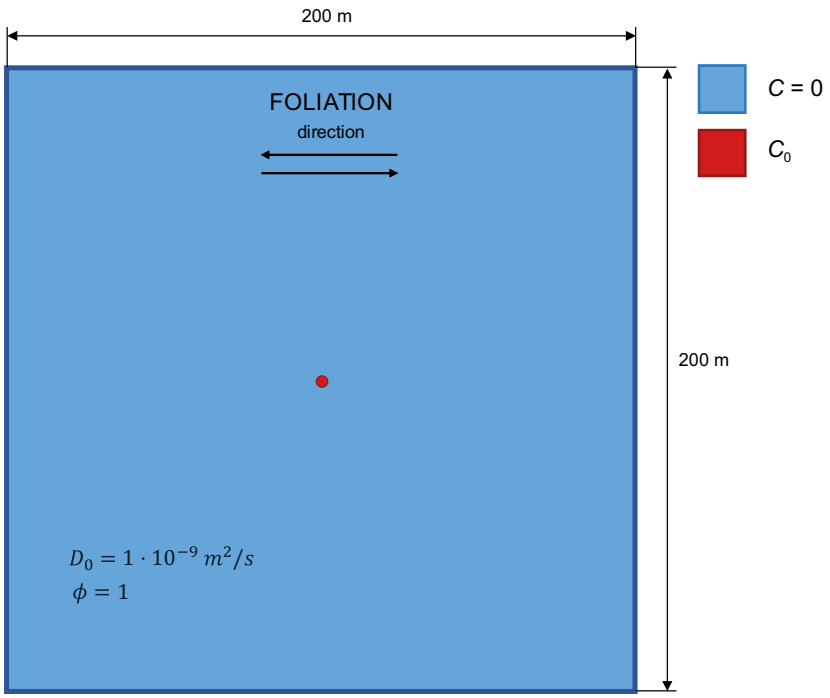

Figure C-9. *Sketch showing the benchmark example used to verify the implementation of anisotropic diffusion in PFLOTRAN.*

The benchmark assumes as initial concentration a Dirac's delta distribution (i.e. $C_0(x, y) = \delta(x)\delta(y)$). The following equation shows the governing Partial Differencial Equation for the transient anisotropic diffusion in 2D:

$$\frac{\partial C(x,y,t)}{\partial t} = D_x \frac{\partial^2 C(x,y,t)}{\partial x^2} + D_y \frac{\partial^2 C(x,y,t)}{\partial y^2}$$

This PDE has an analytical solution for the chosen initial condition,

$$C(x, y; t_0) = \frac{C_0}{4\pi t_0 \sqrt{D_x D_y}} \exp\left(-\frac{x^2}{4D_x t_0} - \frac{y^2}{4D_y t_0}\right)$$

Here, t_0 is the time, D_x is the pore diffusion coefficient in the x-axis and D_y is the pore diffusion coefficient in the y-axis. In this benchmark example, x-axis diffusion is twice the diffusion in the y-axis (i.e. $D_x = 2D_y$).

The benchmark was solved in PFLOTRAN, and the results have been compared with the analytical solution computed along two perpendicular directions at a given time (t_0 = 7 000 y). Figure C-10 shows a snapshot of concentration distribution computed at t = 7 000 y while Figure C-11 shows the comparison between the analytical and numerical models.

In Figure C-10 one can see that the isocontours have an elliptical shape as a result of anisotropic diffusion. It can be calculated that de ratio of the semi-axis of that ellipse is ($\sqrt{Dx/Dy}$), giving a ratio of $\sqrt{2}$ in this particular case. In contrast, the isotropic diffusion case has circular shaped isocontours.

The agreement between the analytical and numerical models is good. Thus, it can be concluded that the implementation of *Anisotropic Diffusion approach* is valid.

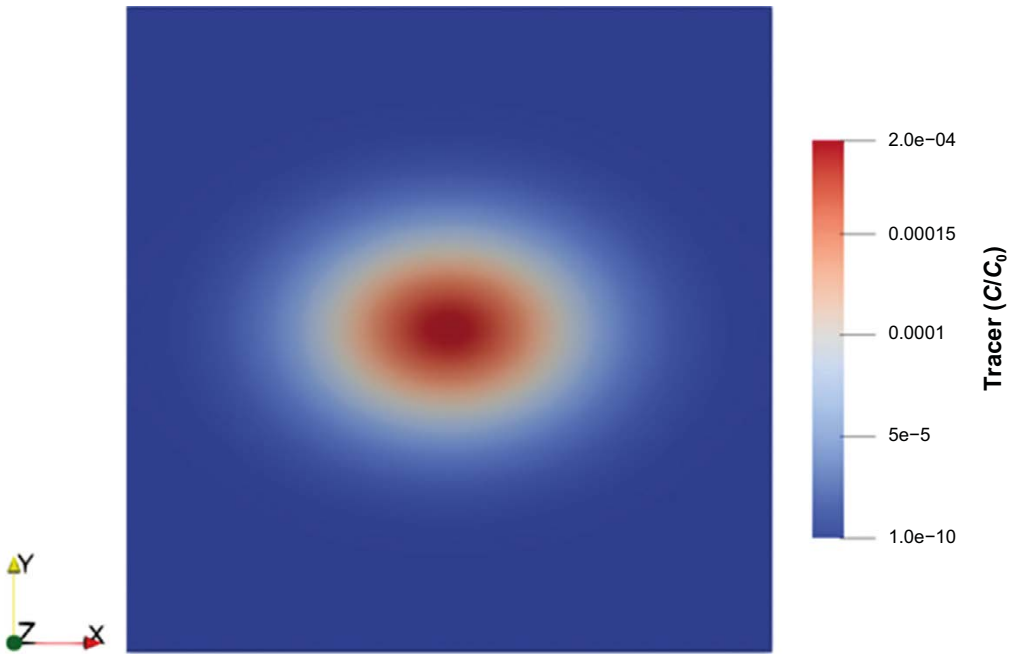

Figure C-10. *2D plot the benchmark example as solved by PFLOTRAN. The results correspond to* $\mathbf{t_0 = 7000\ y}$.

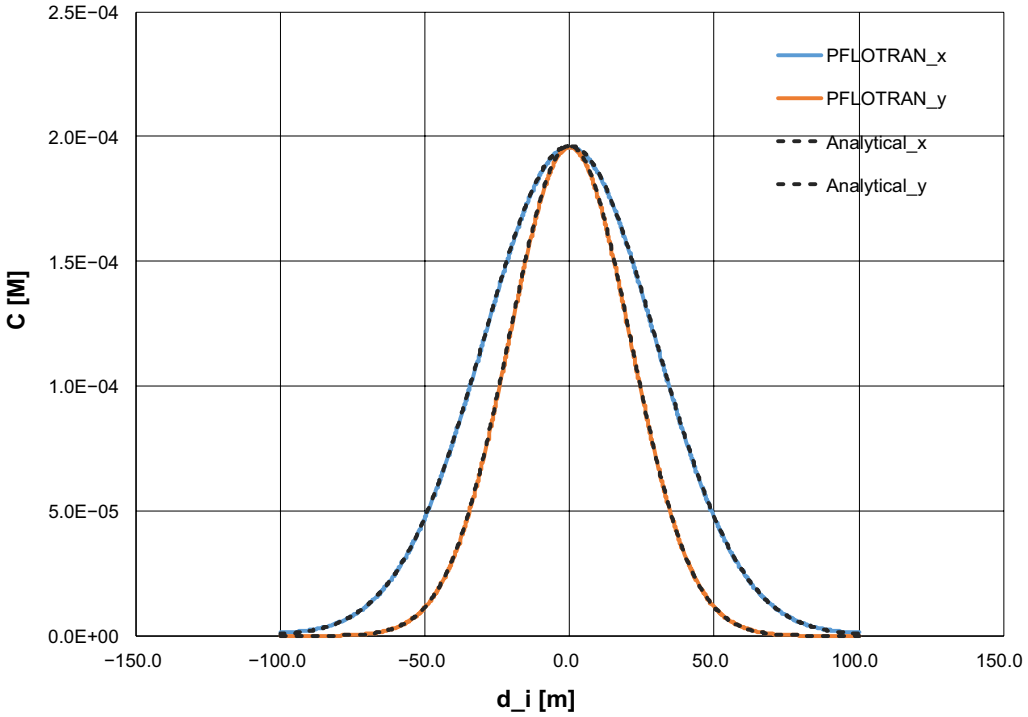

Figure C-11. *Comparison between the analytical solution for anisotropic diffusion and the replica set-up on PFLOTRAN. Underscore x/y represent a line that intersects with the origin (0,0) in the x/y direction. The results are computed at time* $\boldsymbol{t_0 = 7000\ y}$.

Generation of statistically anisotropic diffusion fields

Sequential Gaussian Simulations have been used to produce three sets of heterogeneous diffusivity fields. For each set, ten equiprobable realisations have been generated. Each set is modelled using a spherical semivariogram, with range in the direction parallel and perpendicular to foliation respectively equal to $\lambda_x = 3.5 \times 10^{-1}$ m and $\lambda_y = 1.75 \times 10^{-2}$ m ($\lambda_x / \lambda_x = 19$). The first set (*Low set*) has a variance of $\sigma^2 = 1 \times 10^{-26}$, in the second set (*Mid set*) the variance is increased by a factor of 2 ($\sigma^2 = 2 \times 10^{-26}$) and in the last set (*Max set*) the variance is increased by a factor of 4 ($\sigma^2 = 4 \times 10^{-26}$).

Using a longer range (i.e. a longer correlation length) in the direction parallel to foliation implies that the resulting fields will have significantly elongated low and high diffusivity structures (Figure C-12, right), which are qualitatively similar to the foliated bands observed from PMMA autoradiographs (Figure C-12, left). On the other hand, the increase in variance (from *Low set* to *Max set*) increases the contrast of diffusivity between high and low diffusivity regions. The diffusivity fields, which were generated using the geostatistical code GCOSIM3D (Gómez-Hernández and Journel 1993), were interpolated onto the numerical grid of PFLOTRAN. The distribution was truncated to a minimum value of effective diffusivity of 1×10^{-17} m^2/s.

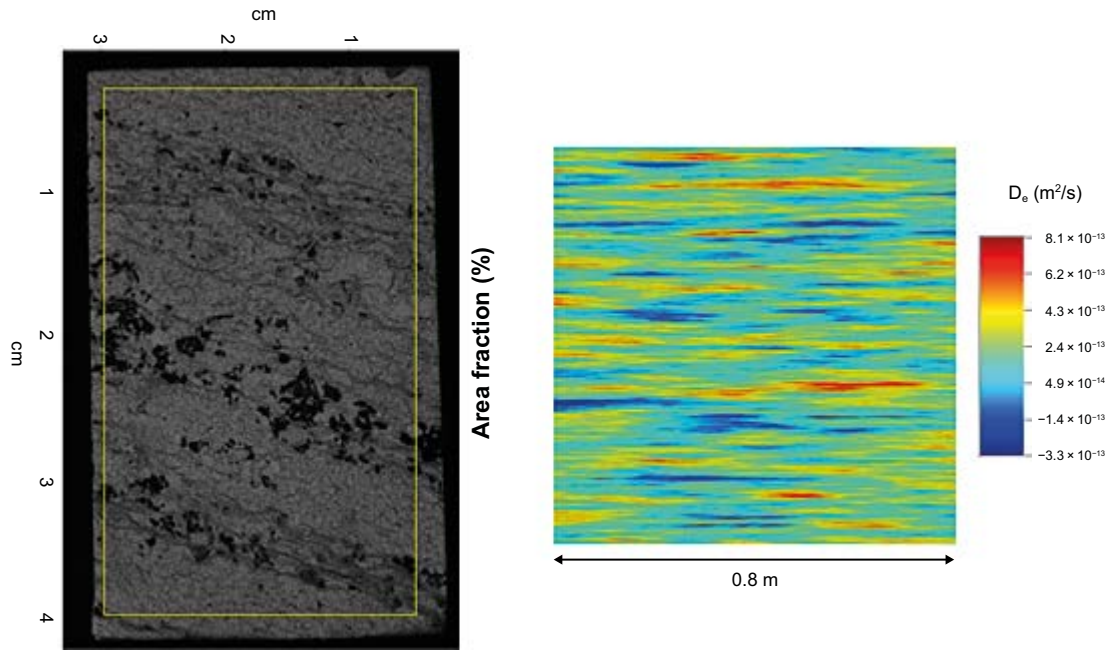

Figure C-12. *(left) Autoradiograph of the 11.92 surface of sample ONK-PP327 (11.92–11.95 m) (modified from Ikonen et al. 2015) and (right) one realization of the Max set.*

C2.3 Simplifying assumptions

The models are based on a number of simplifying assumptions that should be considered when analysing the results:

- The geometry of the model is 2D and this implies that possible three-dimensional effects happening at the beginning/end of the sampling sections are neglected.
- PEEK tubing of ONK-PP326 is considered only for the calculation of the initial injected concentration but not included in the model.
- The effects that sampling as well as other possible artefacts (e.g. leakage along the system) have on the mass balance are not considered.
- Possible local advective patterns are neglected.
- Sorption sites are assumed to be available in the whole rock matrix, while there is evidence of their sparse distribution and the influence of this limited availability on diffusive patterns (e.g. Iraola et al. 2017).

C3 Results of the blind prediction stage

In this section, simulation results of both modelling approaches will be shown. These results will consist of breakthrough curves (BTCs) obtained at each drillhole. 2D plots will also be provided. Both sorbing and non-sorbing tracers have been included in the simulations, however, none of the sorbing tracers reached the observation borehole within the time frame of 10 years used for the simulations. A sensitivity analysis, in which the distribution coefficient of Na-22 was reduced by one order of magnitude, was also included in the set of calculations.

All the simulations were run on a powerful Linux workstation with 44 cores.

C3.1 Anisotropic diffusion (*Central case)*

The first set of simulations was focused on assessing rock foliation using anisotropic diffusion. Thus, the *Central Case* results (i.e. anisotropic diffusion) were compared to the *Zero Case* (i.e. isotropic diffusion).

HTO

Figure C-13 shows a qualitative 2D comparison of both the *Central Case* and the *Zero Case* for HTO at t = 10 *y*. All the other figures of this section (i.e. Figure C-14 to Figure C-21) are computed using the *Central Case*.

By visually inspecting the plots, it can be seen that the *Central Case* shows preferential diffusion along the x-axis with an elliptical shape of the plume, in contrast to the circular plume observed in the *Zero Case.*

In Figure C-14, BTCs of the observation boreholes computed with the *Central Case* and the *Zero Case* are shown and compared to each other.

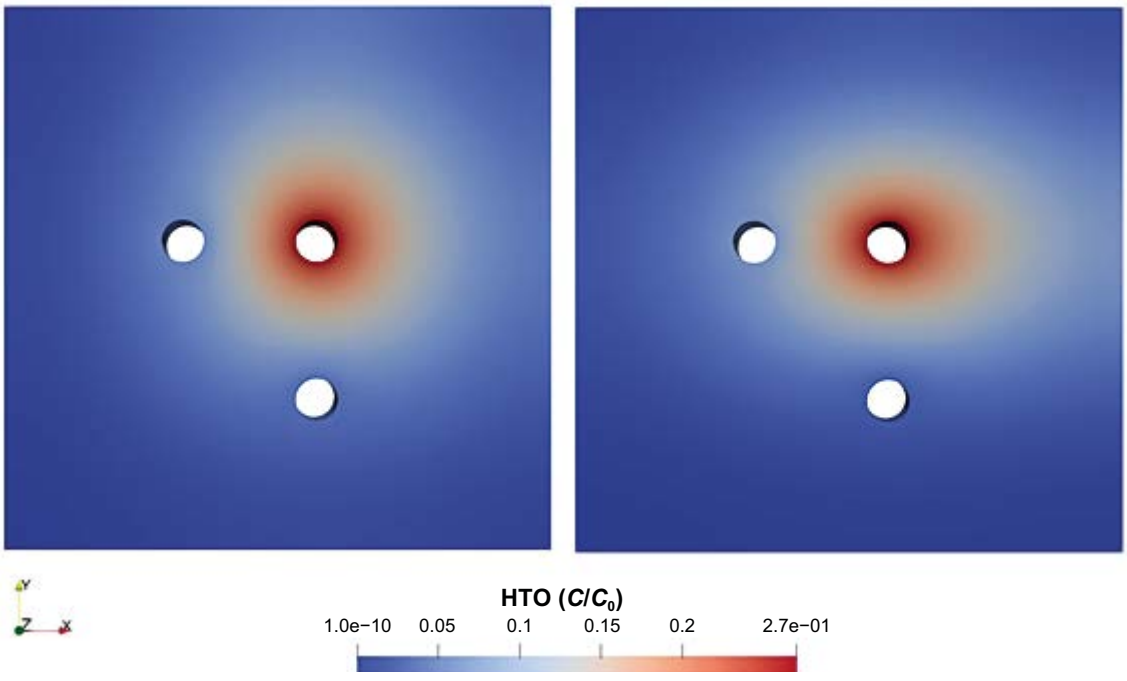

Figure C-13. *HTO concentration at time* t_0 **= 10** ***y****. Comparison of the Zero Case (left) and the Central Case (right). Notice the elliptical shape that can be seen for the anisotropic case in contrast to the circular isocontours of the isotropic case.*

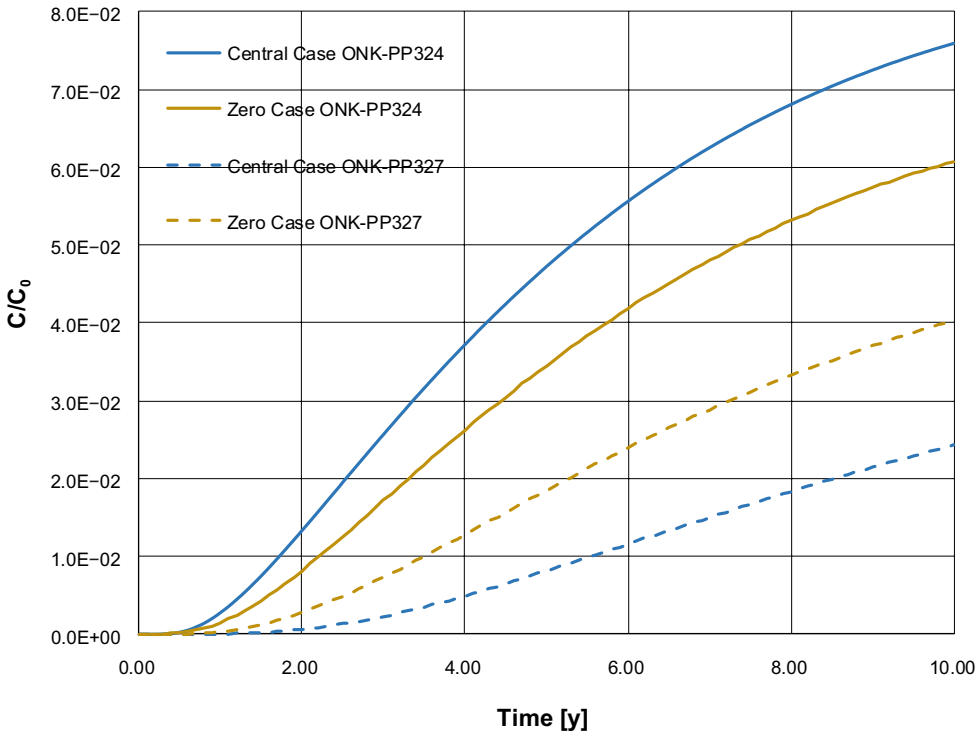

Figure C-14. *BTCs of HTO computed at the observation boreholes (ONK-PP324 and ONK-PP327) for the* Central Case *and the* Zero Case*. Notice that due to the different distance between the injection borehole and the observation boreholes, an earlier arrival in ONK-PP324 is observed also for the* Zero Case*.*

The distance between the injection hole (ONK-PP326) and the observation hole in the direction parallel to foliation (ONK-PP324) is slightly shorter (0.115 m) than the distance between the injection hole and the observation hole in the direction perpendicular to foliation (0.15 m). This affects the arrival times of the tracers and the final concentration at the observation boreholes.

A mass balance has been performed for the *Central Case*. It has been assumed that the mass can be (1) in ONK-PP326 (i.e. the injection borehole), (2) in ONK-PP324 (observation borehole parallel to the rock's foliation), (3) in ONK-PP327 (i.e. the observation borehole perpendicular to the rock foliation), (4) in the aqueous phase within the rock matrix or (5) sorbed in the rock matrix. Thus, the following quantity,

$$m_{tot} = m_{326} + m_{324} + m_{327} + m_{matrix} + m_{sorbed}$$

should be conserved.

In the case of non-sorbing tracers (e.g. HTO), obviously there is no sorbed mass ($m_{sorbed} = 0$).

Figure C-15 shows the mass balance plot for the *Central Case*. At the end of the simulation time frame, most of the mass of HTO is found in the rock matrix (60 %) while the mass in the injection slot has decreased to 25 %.

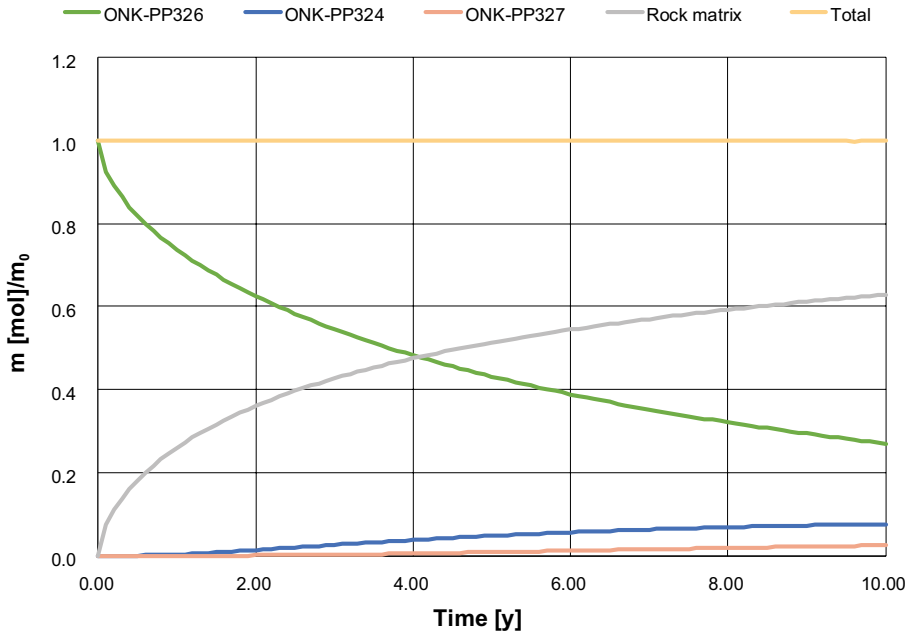

Figure C-15. *Mass distribution for HTO.*

Sorbing tracers

None of the sorbing tracers (Table C-1) is observed in the observation boreholes within the considered time frame. Ba-133 and Cs-134 have the highest partitioning coefficients and they do not penetrate much in the rock matrix (i.e. almost all the mass is sorbed nearby the injection borehole). Na-22 has a smaller partitioning coefficient and thus, it penetrates more. The spatial distribution of aqueous and sorbed concentration is shown in Figure C-16 and Figure C-17.

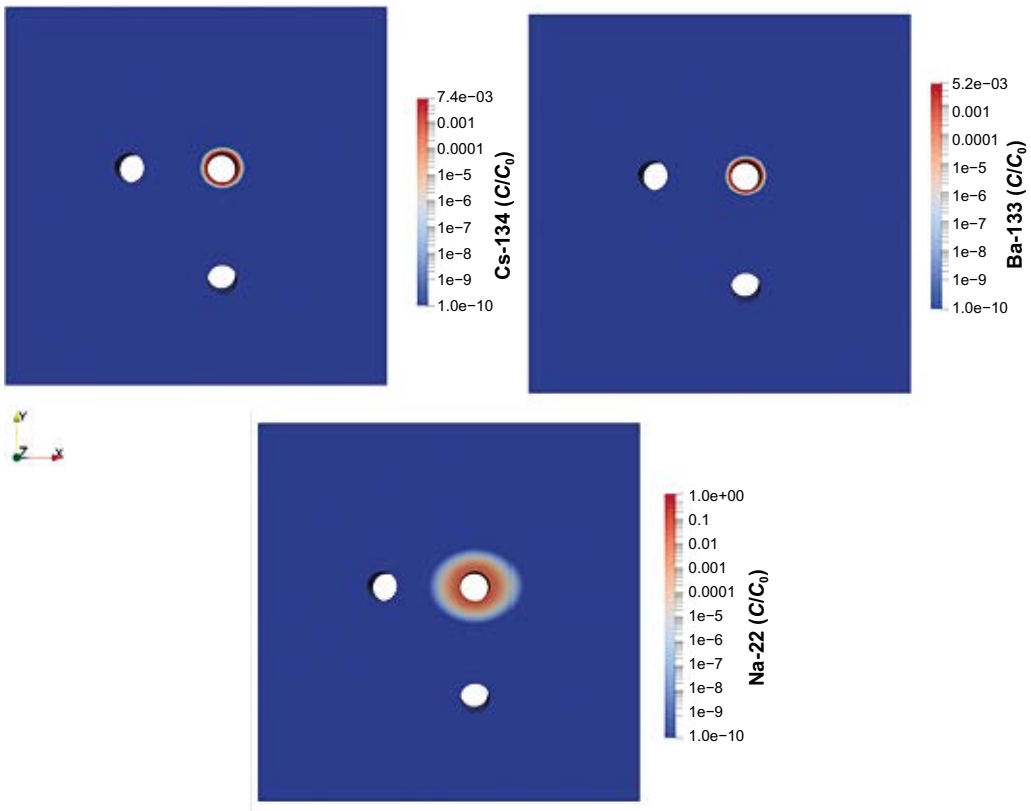

Figure C-16. *2D plots of radionuclide aqueous concentration (log color scale) computed with (top left) Cs-134, (top right) Ba-133 and (bottom) Na-22 at* t_0 **= 10** ***y***.

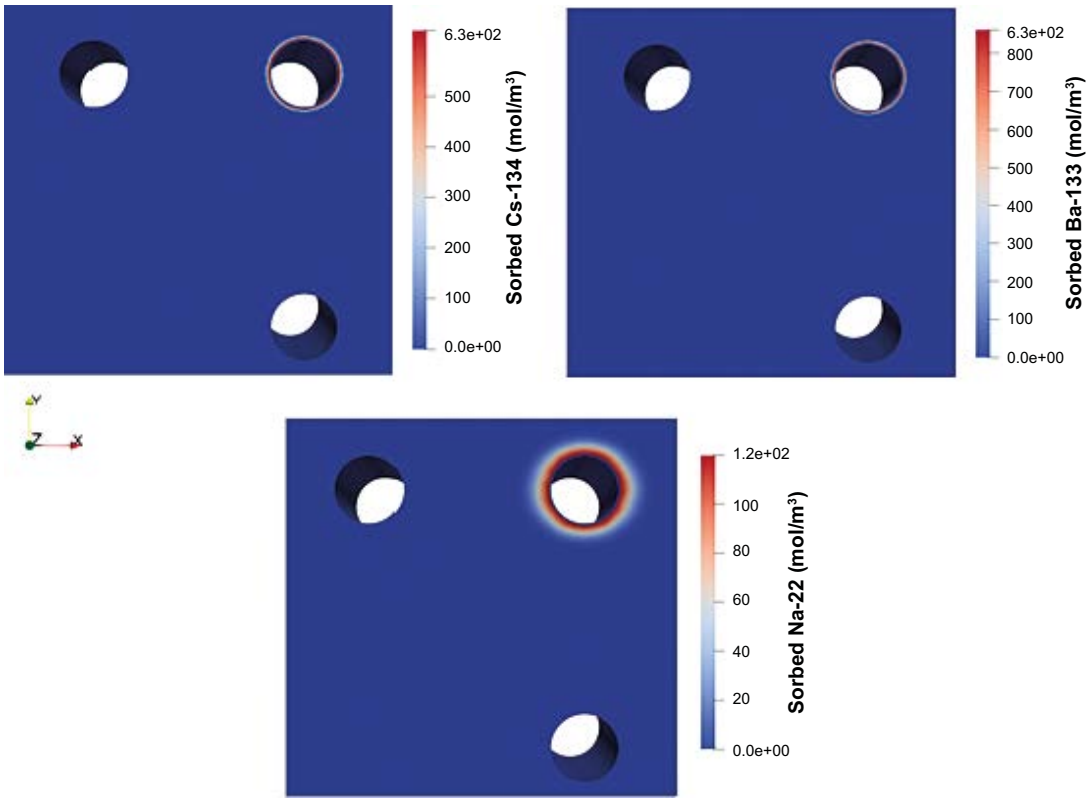

Figure C-17. *2D plots of sorbed radionuclide aqueous concentration (log color scale) computed with (top left) Cs-134, (top right) Ba-133 and (bottom) Na-22 at* t_0 **= 10** ***y****. For visualization purposes, a zoom over the borehole region is shown.*

Figure C-18 shows the evolution of radionuclide concentration in the injection borehole. All the curves, but particularly those of strongly sorbing radionuclides (i.e. Cs-134 and Ba-133) show a similar trend, with a steep decrease in concentration at early times and a smoother slope at later times. The steep slope observed at early times corresponds to the almost instantaneous equilibration of the dissolved radionuclide mass with the available minerals at the interface borehole-rock mass. The smooth slope corresponds to the typically observed diffusion-limited regime.

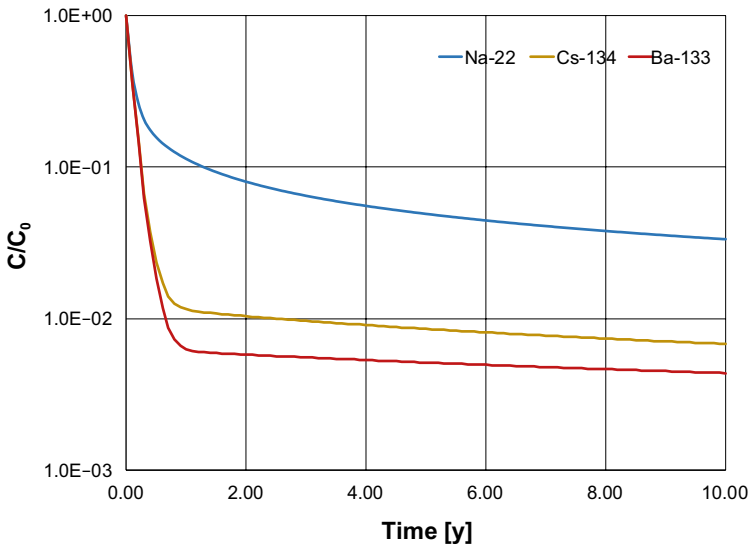

Figure C-18. *Log-normal plot of normalized BTCs at the injection borehole for strongly sorbing tracers. Note that the higher the sorption partitioning coefficient the steeper is the first part of the BTC.*

As mentioned before, a sensitivity analysis to the value of Na-22 partitioning coefficient has been carried out. This sensitivity analysis aims at somehow consider that active mineral grains are indeed sparsely distributed, meaning that the effective distribution coefficient observed in the field is different from what measured in the lab from crushed material. Figure C-19 shows the Na-22 concentration computed with this lower value of distribution coefficient.

Figure C-20 shows the BTC of Na-22 computed for this sensitivity run. With this low value of distribution coefficient, Na-22 is observed in ONK-PP324 (borehole parallel to foliation direction) but not in ONK-PP327 (borehole perpendicular to foliation direction). Note that, to avoid numerical problems, a low initial concentration value is used to set the initial conditions of the model.

Figure C-21 shows the mass balance for Na-22. It is worthwhile noting the striking difference between the mass balance of Na-22 and the mass balance of HTO (Figure C-15). Even considering a low value of distribution coefficients, most of the mass of Na-22 gets sorbed while most of the mass of HTO is found in the aqueous phase within the rock matrix.

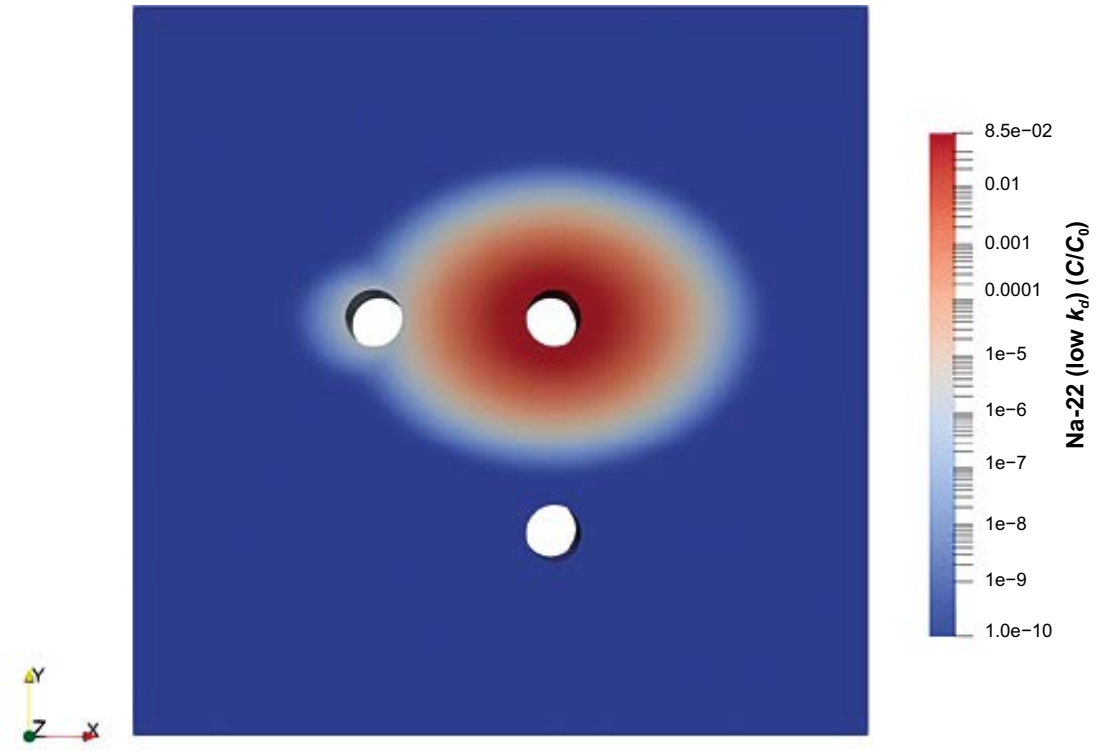

Figure C-19. *2D plot (log color scale) of Na-22 computed with a lower distribution coefficient at* t_0 **= 10** ***y***.

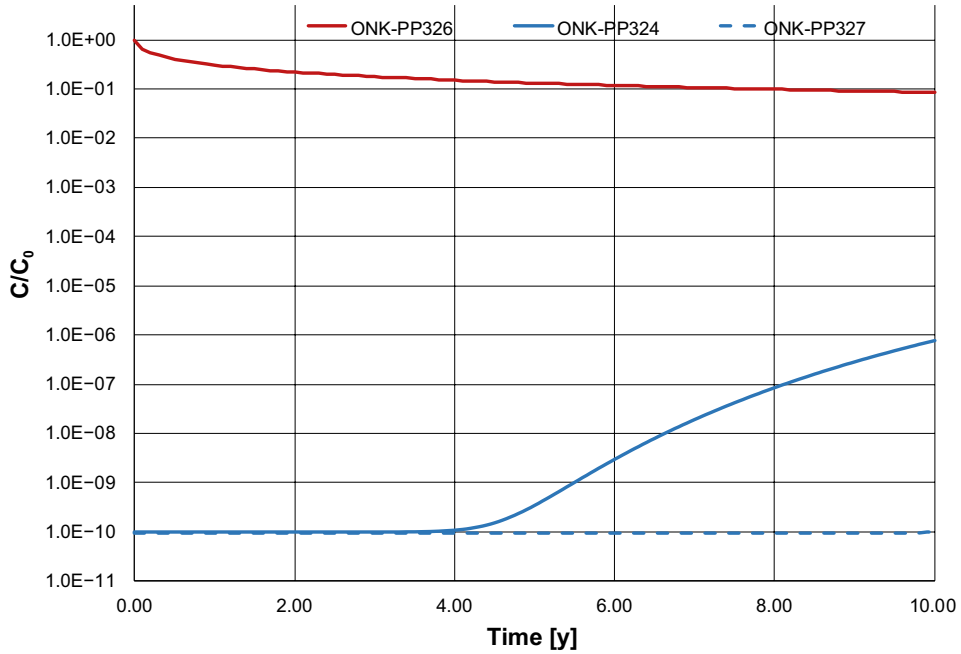

Figure C-20. *BTCs computed at the ONK-PP326 injection borehole (red line), ONK-PP324 observation borehole (blue thick line) and ONK-PP327 observation borehole (blue dashed line) for Na-22 using the lower value of distribution coefficient. Notice that the tracer is only observed in ONK-PP324 (i.e. the borehole parallel to the foliation direction).*

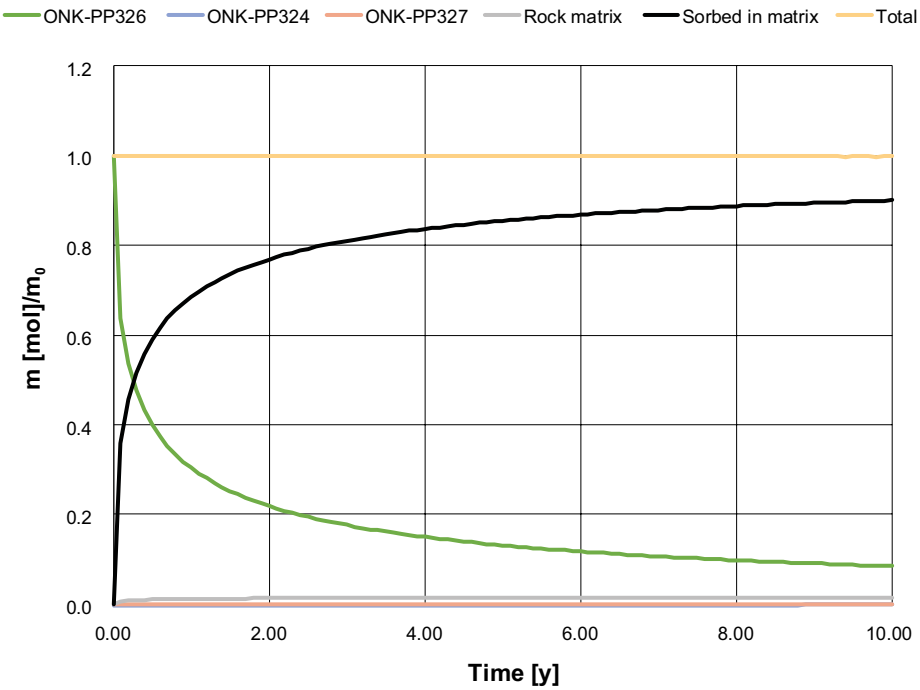

Figure C-21. *Mass distribution for Na-22, computed with the reduced value of distribution coefficient.*

C3.2 Heterogeneous diffusion

The different heterogeneous diffusivity fields described in Section 3.2.2 are here used to simulate the TD experiment. As explained in Section 3.2.2, the statistical distributions of the three considered sets of fields only differ in the variance, σ^2: *Max set* ($\sigma^2 = 4 \times 10^{-26}$), *Mid set* ($\sigma^2 = 2 \times 10^{-26}$) and the *Low set* ($\sigma^2 = 1 \times 10^{-26}$).

For each set, 10 diffusion fields have been generated, giving a total of 30 simulations. Figure C-22 shows a randomly selected realisation with the three corresponding diffusion sets.

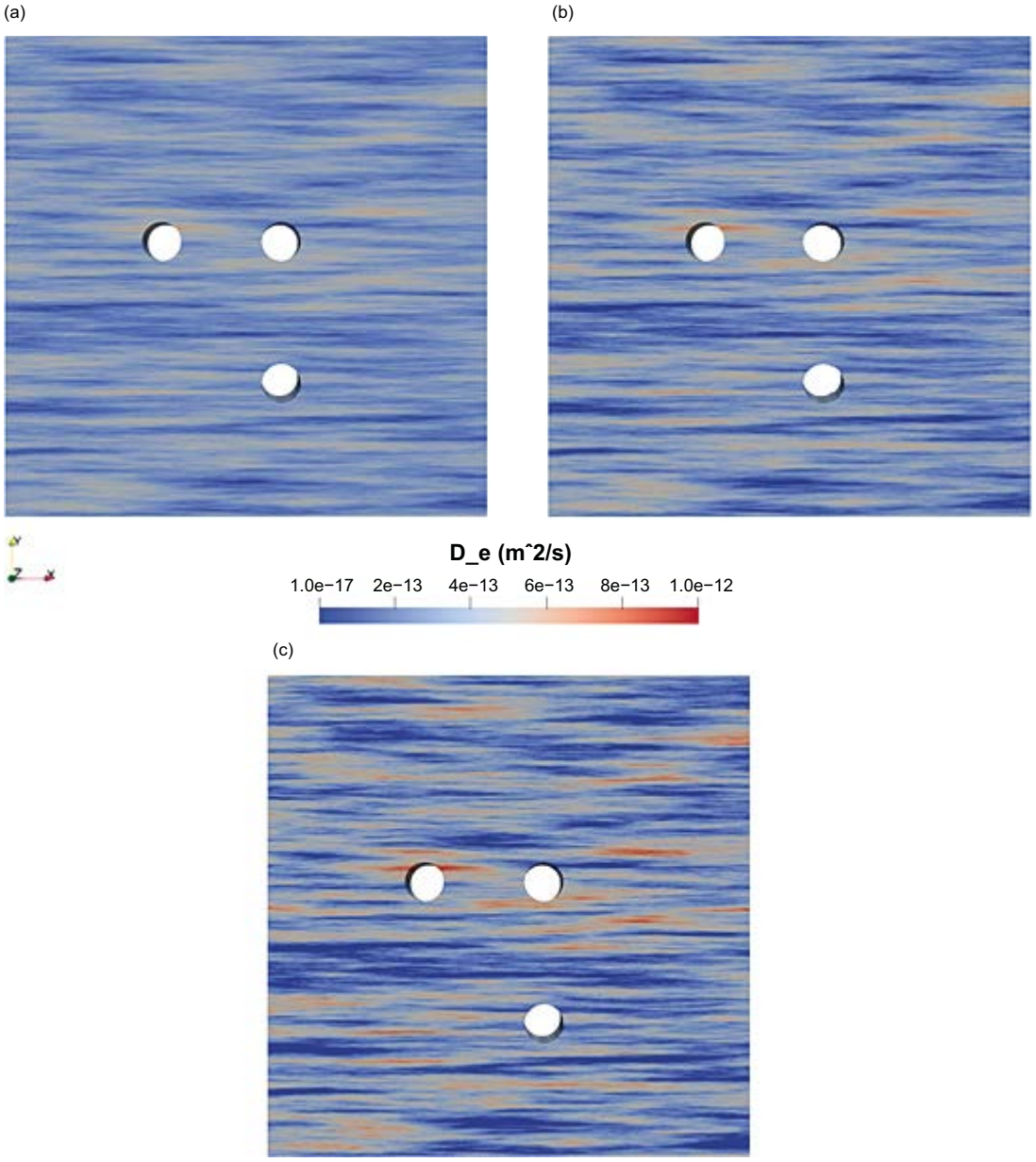

Figure C-22. *Heterogeneous effective diffusion field for a given realization and different diffusivity sets. (a) corresponds to the Low Set that has a variance of* $\boldsymbol{\sigma^2 = 1 \times 10^{-26}}$. *(b) corresponds to the Mid Set which is defined with a variance of* $\boldsymbol{\sigma^2 = 2 \times 10^{-26}}$ *and (c) corresponds to the Max Set with a variance of* $\boldsymbol{\sigma^2 = 4 \times 10^{-26}}$.

Non-sorbing tracer

All the 30 realisations have been used to simulate HTO diffusion. Based on the results of HTO (BTCs), two realisations have been selected (*Lower Case* and *Upper Case*) and used to simulate the evolution of the sorbing tracers.

Figure C-23, Figure C-24 and Figure C-25 show the BTCs of HTO for each diffusivity set. The BTCs of the *Central Case* have also been plotted for comparison, as well as the mean value for each set of realizations.

It can be seen that the system is quite sensitive to the variance used to define the distributions. The higher the variance, the higher the heterogeneity of the realisation.

As a general trend, increasing the variance leads to an increase of the mean value in the direction parallel to foliation and a decrease in the direction perpendicular to foliation.

All the realisations of the *Lower Set* show less anisotropic effects compared to the *Central Case*. A few realisations of the *Mid Set* show higher anisotropic effects while the variability of the *High Set* is significant.

A cumulative distribution function (CDF) has been built for each set based on the time when 1 % of the initial tracer concentration is observed ($\frac{C}{C_0} = 0.01$).

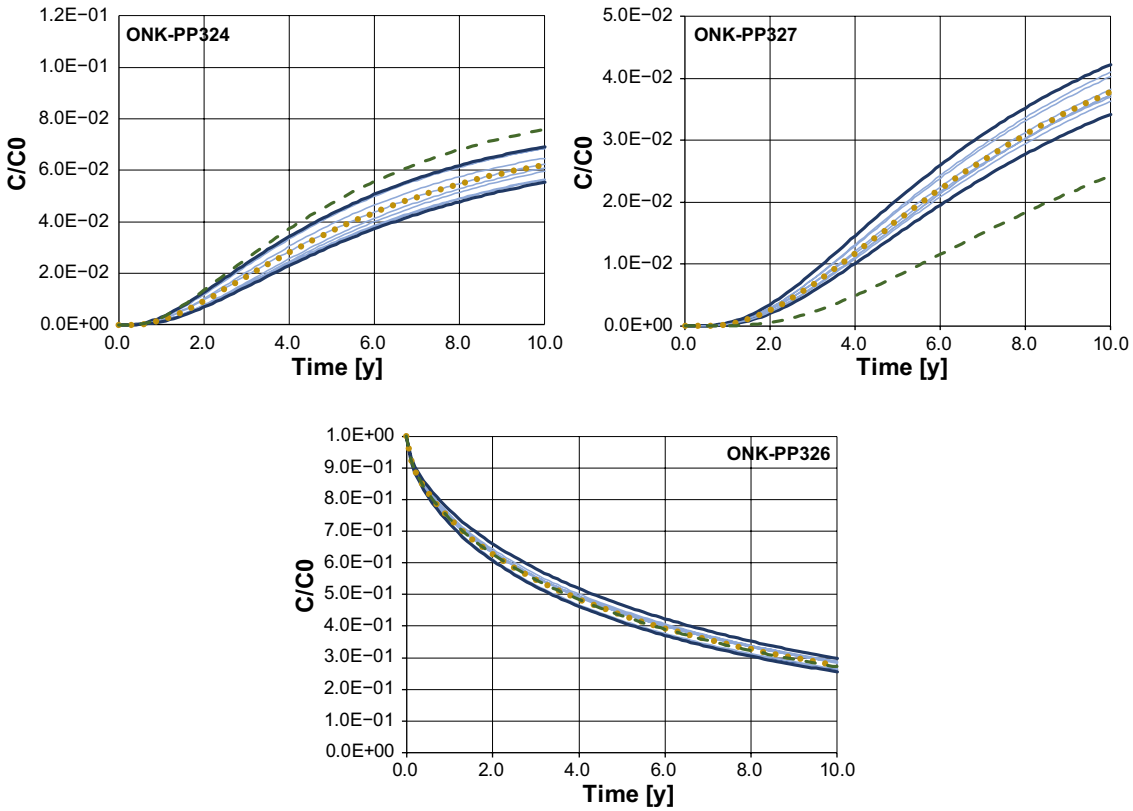

Figure C-23. *BTCs for the HTO for each of the ten realizations of the* Low Set. *Thin blue lines represent different realizations of the set, the most extreme realizations have been painted in darker blue. Yellow dots represent the mean value of the 10 realizations. The thick green line is the* Central Case *BTC.*

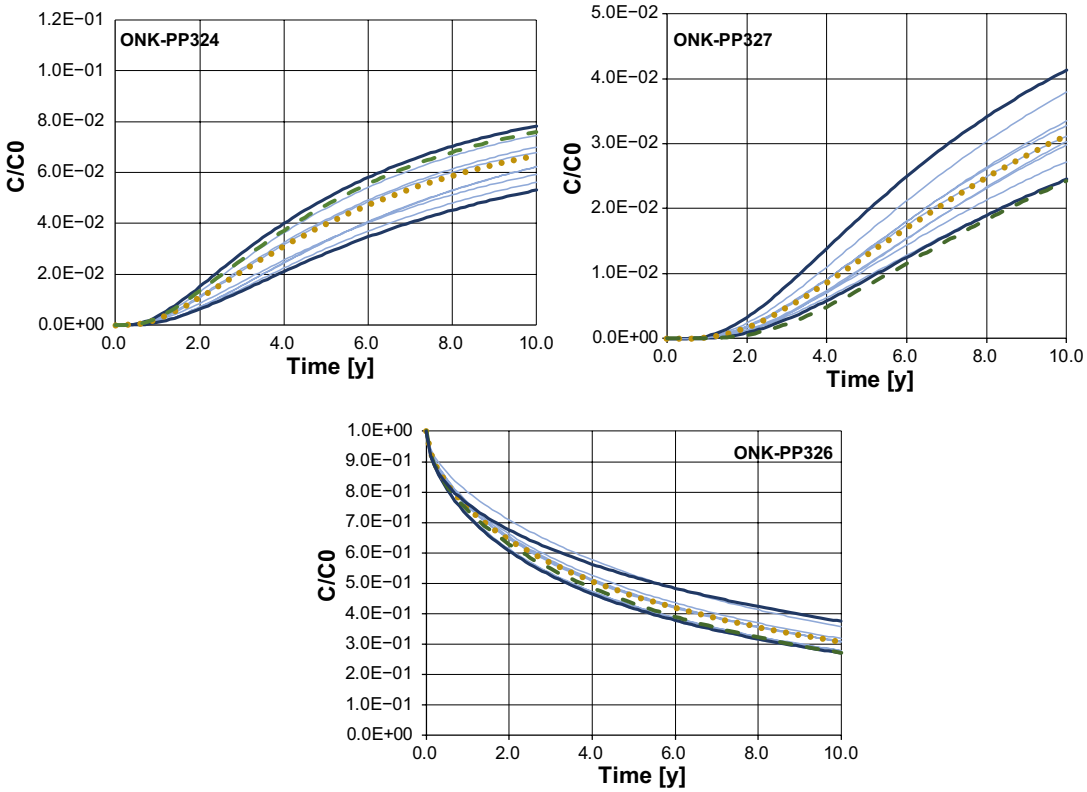

Figure C-24. *BTCs for the HTO for each of the ten realizations of the* Mid Set*. Thin blue lines represent different realizations of the set, the most extreme realizations have been painted in darker blue. Yellow dots represent the mean value of the 10 realizations. The thick green line is the* Central Case *BTC.*

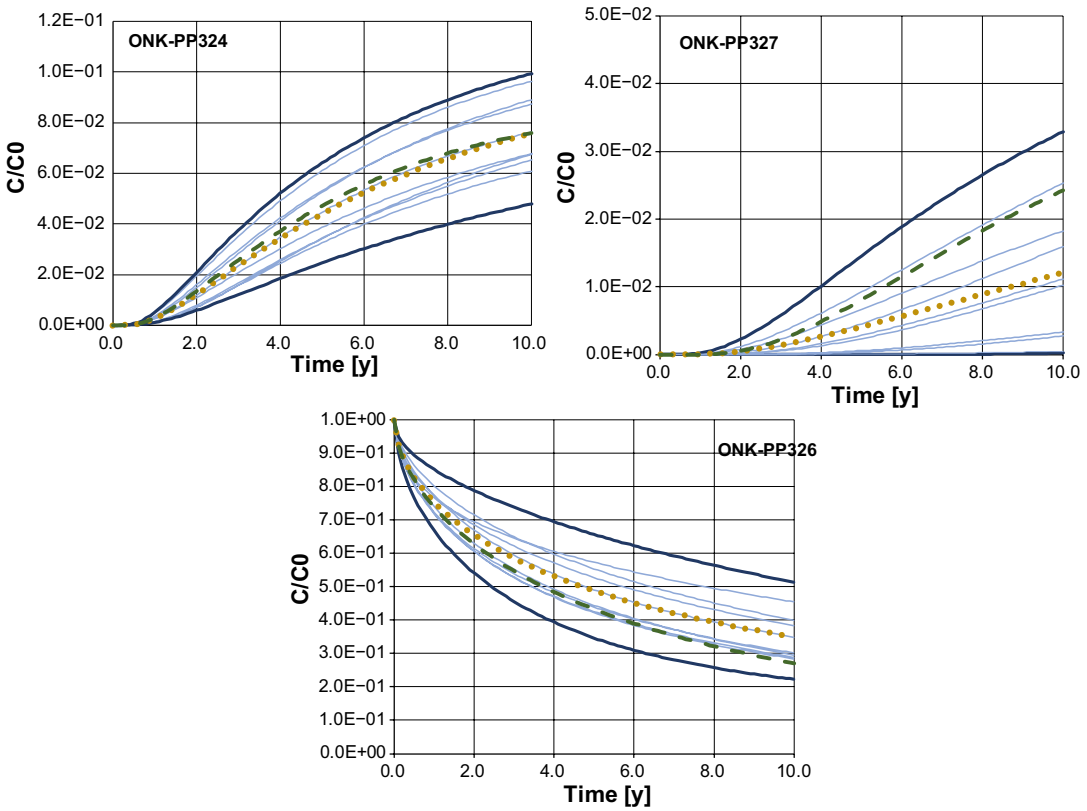

Figure C-25. *BTCs for HTO for each of the ten realizations of the* Max Set*. Thin blue lines represent different realizations of the set, the most extreme realizations have been painted in darker blue. Yellow dots represent the mean value of the 10 realizations. The thick green line is the* Central Case *BTC.*

Figure C-26 and Figure C-27 show the cumulative distribution functions along the two considered directions. Figure C-26 corresponds to the CDF in ONK-PP324 (i.e. the borehole parallel to the foliation direction). As variance increases, a wider range of arrival times is spanned with the median value approaching the arrival time of the *Central Case*. Qualitatively similar results are observed for ONK-PP327. As already discussed above, all the realizations of the *Low Set* have shorter arrival times compared to the *Central Case*.

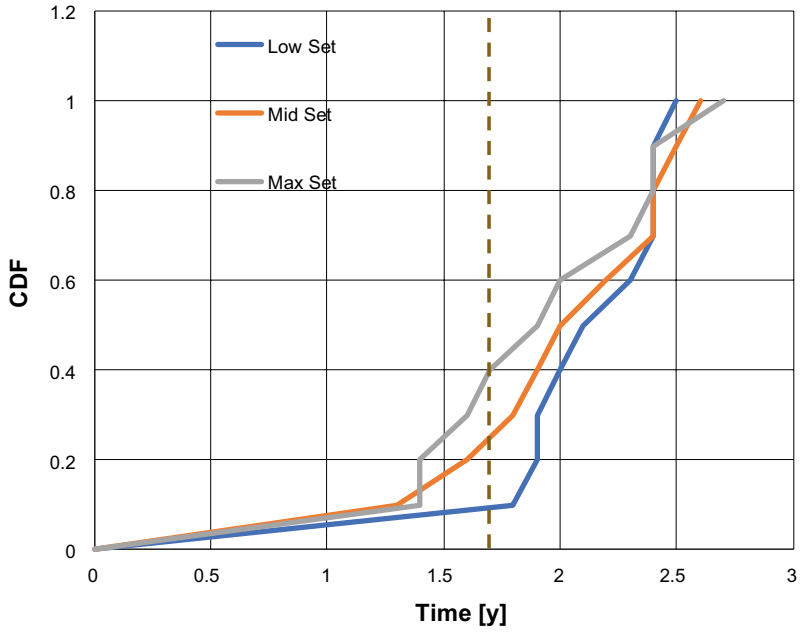

Figure C-26. *Cumulative Distribution Function (CDF) for all the realizations for ONK-PP324. The CDFs are computed using the arrival times for the 1 % of the initial concentration (i.e. the times where $C/C_0 = 0.01$ is measured in the observation borehole). The dashed line indicates the arrival time for the Central Case.*

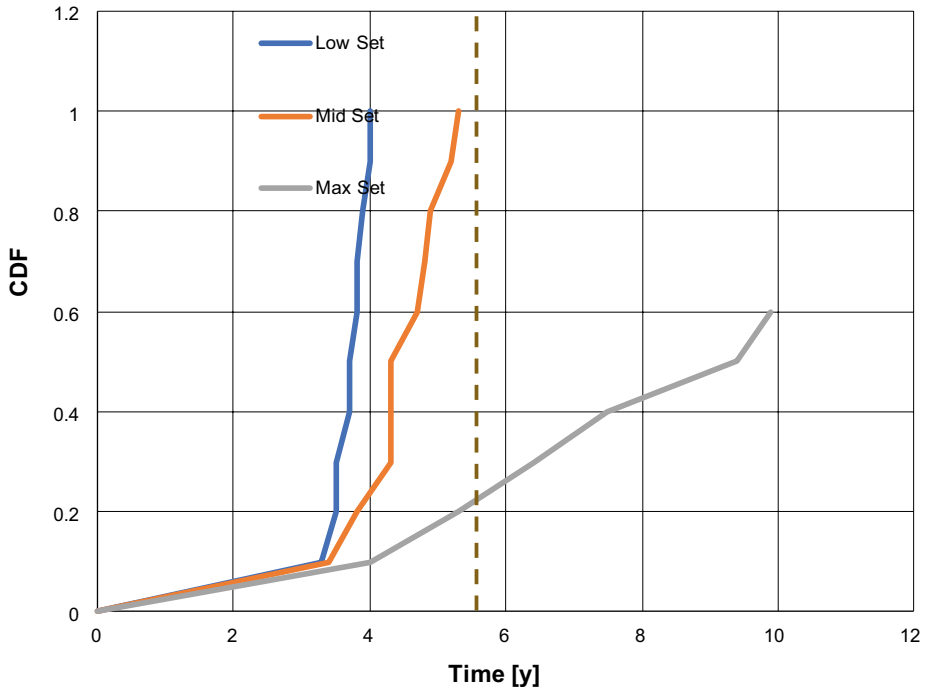

Figure C-27. *Cumulative Distribution Function (CDF) for all the realizations for ONK-PP327. The CDFs are computed using the arrival times for the 1 % of the initial concentration (i.e. the times where $C/C_0 = 0.01$ is measured in the observation borehole). The dashed line indicates the arrival time for the Central Case.*

Figure C-28 shows a comparative plot of HTO for the *Zero Case, Central Case, Lower Case* and *Upper Case.* As it can be seen, the homogeneous isotropic run (*Zero Case*) compares quite well with the *Lower Case*, where effects due to heterogeneous diffusion are observed. On the other hand, it is visually clear that in the *Upper Case* there are bands of low diffusivity that prevent the arrival of HTO at ONK-PP327. Figure C-29 shows the BTCs for each of the models above.

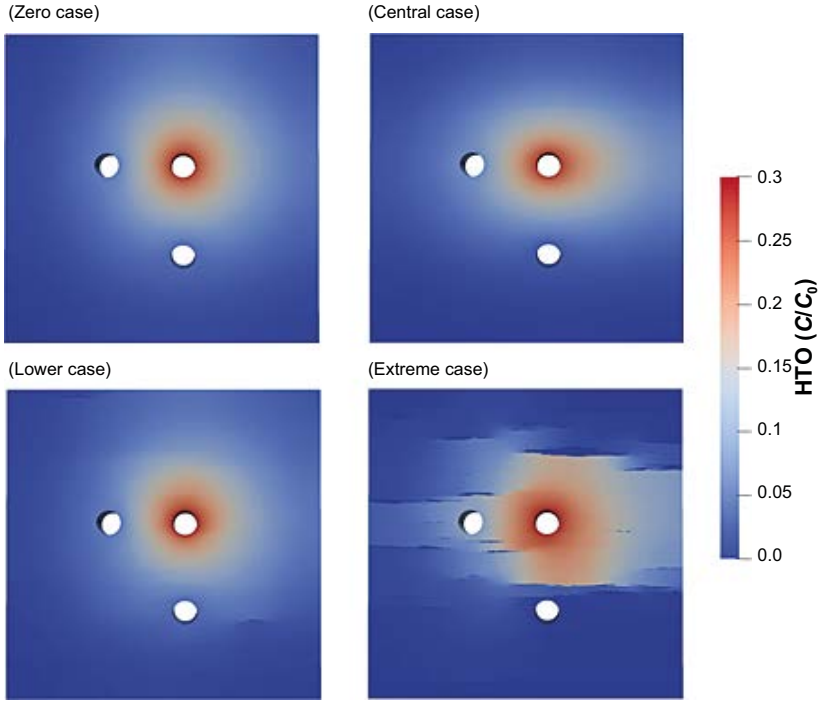

Figure C-28. *2D plots for HTO, computed at 10 y.*

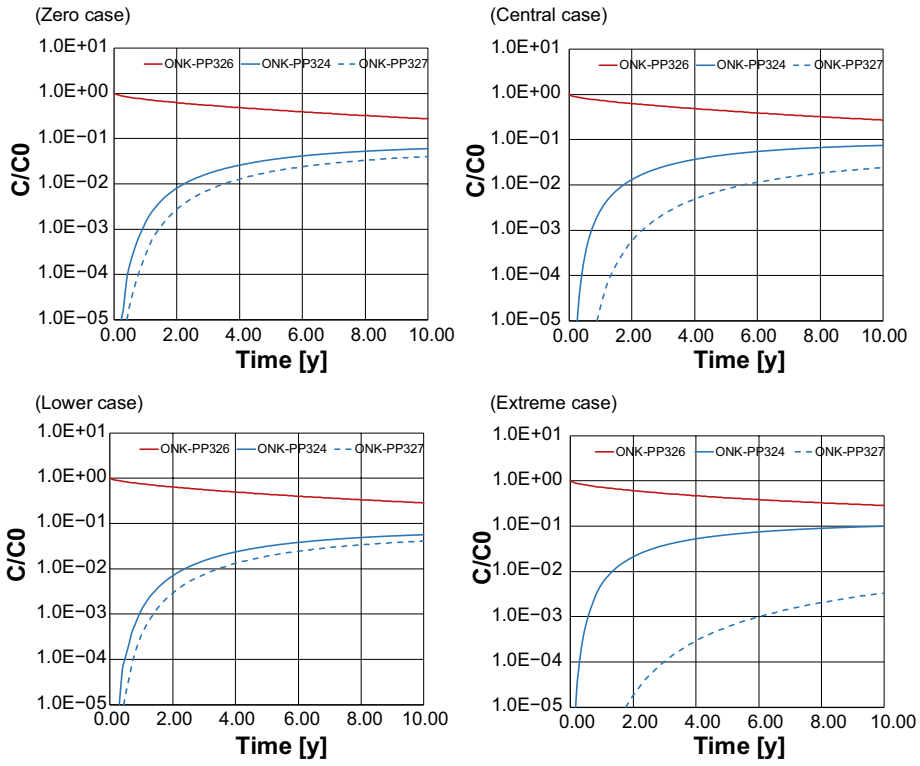

Figure C-29. *BTCs computed on both the injection and observation boreholes for each main case for the non-sorbing tracer.*

Sorbing tracers

Here, the same comparison procedure of the previous section has been followed, but now for the sorbing tracers. The main conclusion for the strongly sorbing tracers is that none of them arrives in measurable concentrations at the observation boreholes. Thus, the comparison plots have been made using Na-22 and with the reduced value of partitioning coefficient.

Figure C-30 shows the 2D plots for each case. Note that the 2D plots of Figure C-30 are presented with a log-color scale, which amplifies small increases in concentration.

Figure C-31 shows the BTCs observed at both the observation and injection boreholes.

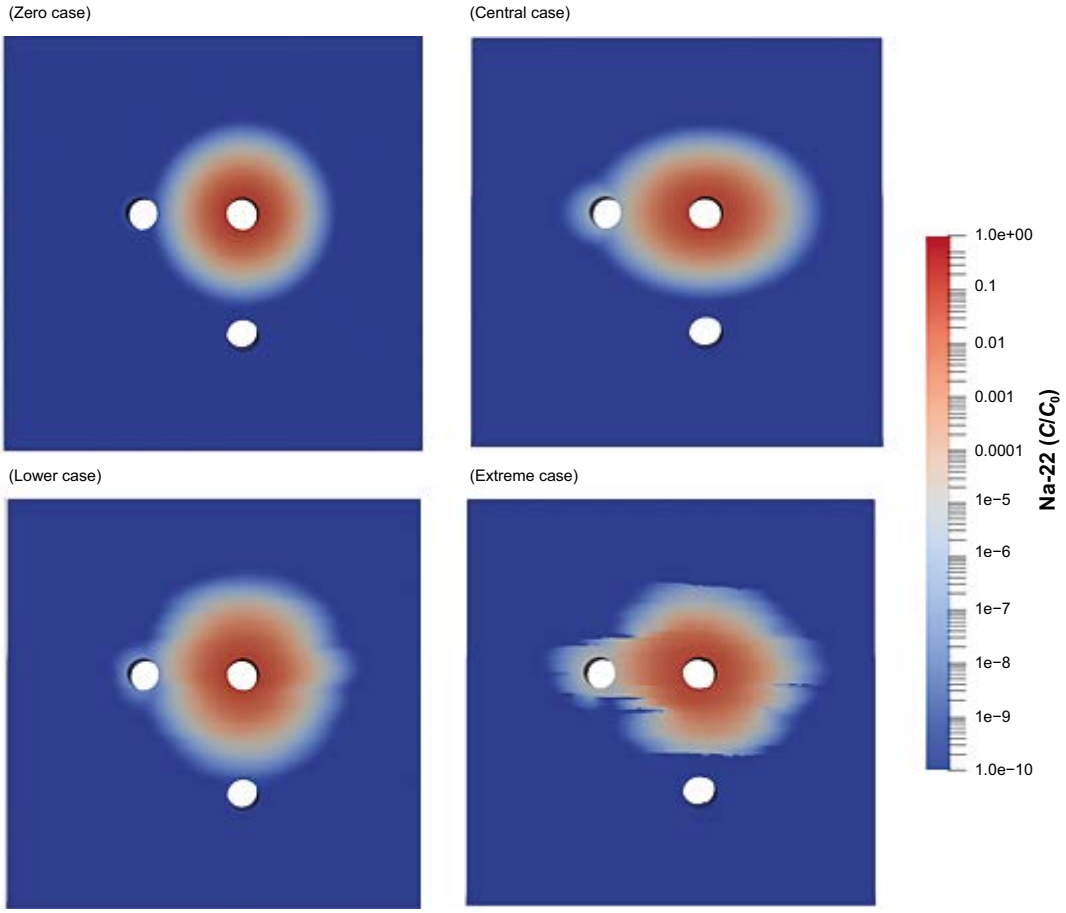

Figure C-30. *2D plots for Na-22 (log-color scale) at 10 y.*

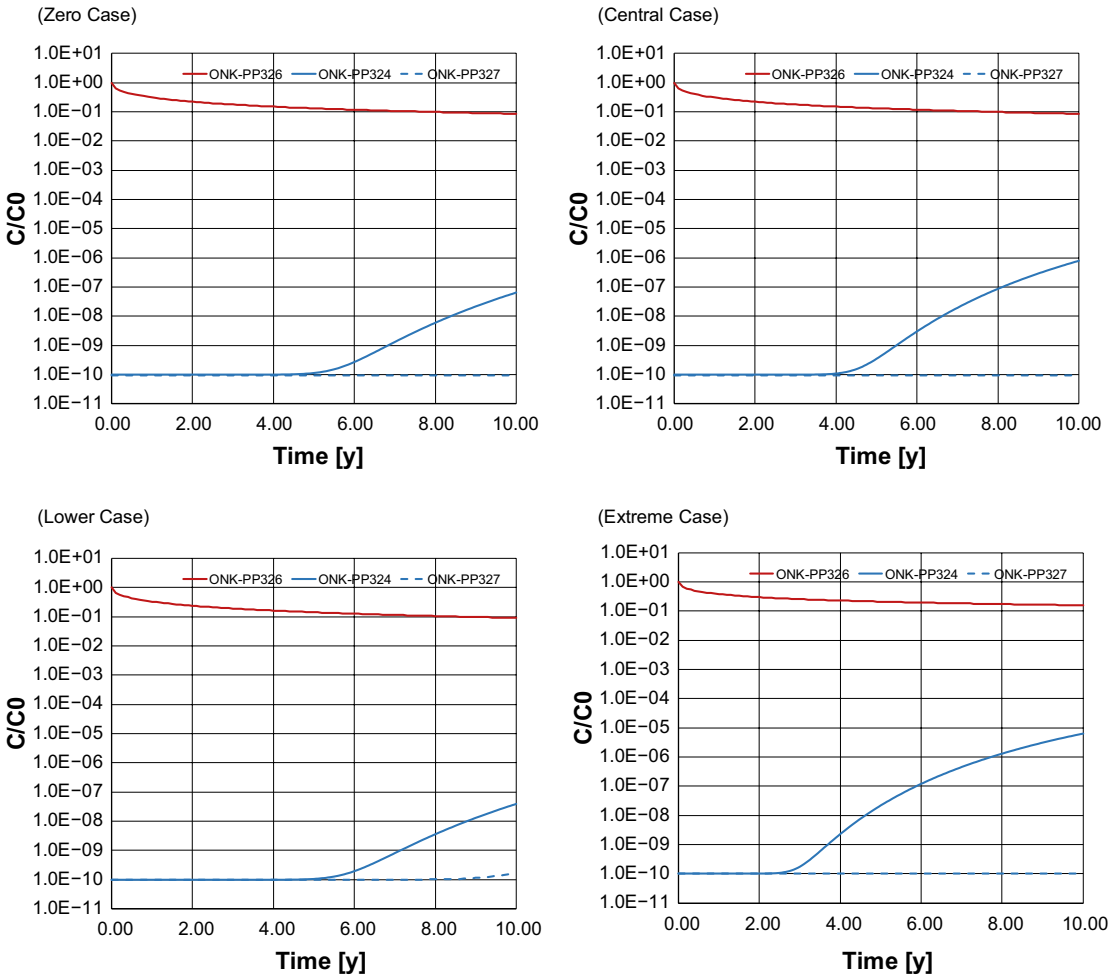

Figure C-31. *BTCs of Na-22 (reduced partitioning coefficient) computed on both the injection and observation boreholes for each main case for the weakly-sorbing tracer.*

C4 Back-analysis stage model

C4.1 Introduction

The second stage of the work started when the experimental results of the REPRO-TDE were published. The work of the modelling teams focused on, first, comparing the results obtained by the blind prediction model with the experimental data, and, then, updating the blind prediction model to improve the fitting with the recently published experimental data.

As a general trend, all the modelling teams showed a relatively good agreement on the predictions done for the evolution of the non-sorbing tracers at the ONK-PP326 borehole (i.e. the injection borehole). However, both the evolution of the sorbing tracers at the ONK-PP326 borehole and the arrival times of all tracers at the observation borehole did not fit well with the experimental data. In particular, the computed observation breakthrough curves of the radionuclides showed a much quicker first arrival and much higher diffusive fluxes.

As mentioned before, the objective of the back-analysis stage is to upgrade the blind prediction model to a new model that fits the experimental data. However, in our case, there is not a single blind prediction model that can be used as a reference due to the large number of simulations we carried out to understand the effects the rock foliation may had on radionuclide diffusion. This added an extra layer of complexity that may had interfered with the new objective in hand. Due to this, the decision of focusing on a purely homogeneous and isotropic diffusion model was taken. Moreover, the final set-up of the model contains a Borehole Deformation Zone (for now on, BDZ) surrounding each of the boreholes.

C4.2 Model set-up

Geometry and mesh

The geometry of the back-analysis stage model is similar to the blind prediction stage model's one. The key difference is the presence of the aforementioned BDZ surrounding each of the boreholes. This perturbated zones are often caused when the boreholes of the experimental set-up are drilled and can significantly alter the material properties at the first few millimetres surrounding the borehole. Details of the geometry of the back-analysis stage model are sketched in Figure C-32. As shown there, the geometry of the model can now be divided in three main regions: the boreholes (in blue) represent the void space of the drillholes in which water is in circulation and they are used to compute the breakthrough curves of the considered radionuclides after the simulation is done. The rock matrix (in orange), represents the intact core of the rock, and it is conceptualized by two parameters (i.e. porosity and tortuosity) that can be tuned to fit the experimental data. Finally, the BDZ is represented by the yellow ring that surrounds each of the boreholes. This is the zone that have been altered due to the drilling of the cores and it is parameterized by a certain width and a given porosity and tortuosity values. The width of the BDZ has been chosen to be 21.75 mm while the rest of the dimensions have been kept equal to the blind prediction stage model.

The mesh of the model is a semi-structured prismatic mesh and it contains 527 000 elements (Figure C-33). Notice that here, in contrast of the hexahedral elements used in the blind prediction stage model, triangular prisms are used as mesh elements. The reason behind is that it is no longer needed to simulate anisotropic diffusion, and thus, we are not forced to have face normals aligned with the cartesian directions.

Different mesh sizes have been assigned to the geometrical regions defined in Figure C-33. The annular region that represents the borehole (the blue region in Figure C-33) is the most refined region and has an average mesh size of $5 \times 10^{-4}\ m$. The BDZ region (the yellow region in Figure C-33) has a mean mesh size of $7.5 \times 10^{-4}\ m$, and in the rock matrix (the orange region in Figure C-33), the mesh size has been regularly increased to a mean value of $1.5 \times 10^{-3}\ m$. This fine refinement close to the interfaces between the boreholes and the BDZ allows to effectively capture the diffusion patterns of the different tracers, specially the out-diffusion from the injection borehole of the sorbing radionuclides.

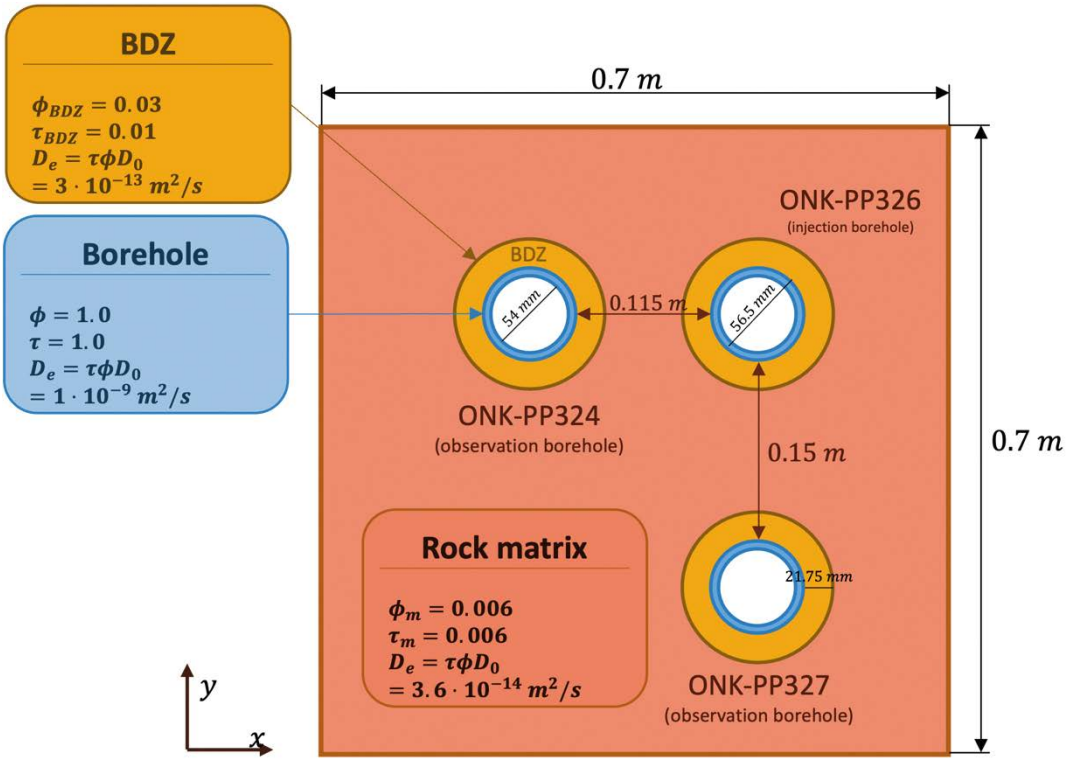

Figure C-32. *Model set-up of the back-analysis stage model. The key material properties of the considered three zones (i.e. the rock matrix, the boreholes and the Borehole Deformation Zone (DBZ)) are shown.*

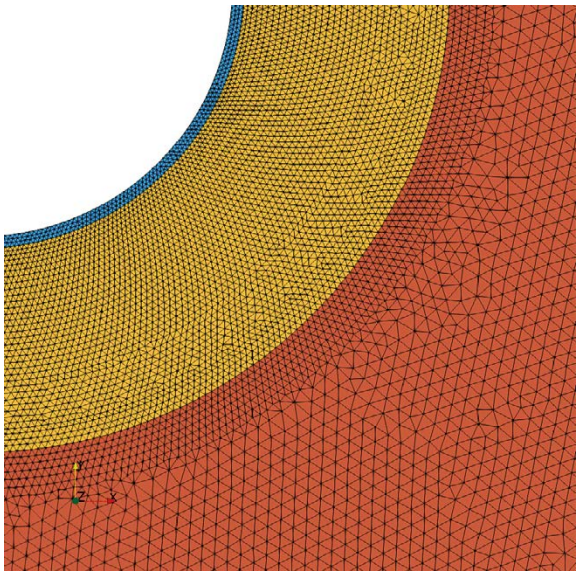

Figure C-33. *Top view of the back-analysis stage model mesh. Notice the dynamic refinement among the different regions: the mesh is highly refined at the borehole region (in blue), it gradually gets coarser as the region changes to the BDZ (in yellow) and it reaches it maximum size at the rock matrix (in orange).*

Initial and boundary conditions

The set-up of the initial and boundary conditions is equal to the one presented in Section C2.1 for the blind prediction stage model. As shown in Figure C-34, the radionuclide cocktail is initially set at the injection borehole while the rest of the domain is assigned with zero concentration of the considered radionuclides. In all the external boundaries of the model (i.e. the sides of the square and the circular interface of each borehole) a Neumann (zero gradient) boundary condition is applied.

The reactive transport parameterization of the back-analysis stage model is covered in Section C5.2. These parameters (i.e. the diffusion coefficients at the different domains and the distribution coefficients of the sorbing radionuclides) have been fitted to match the evolution of the experimental data.

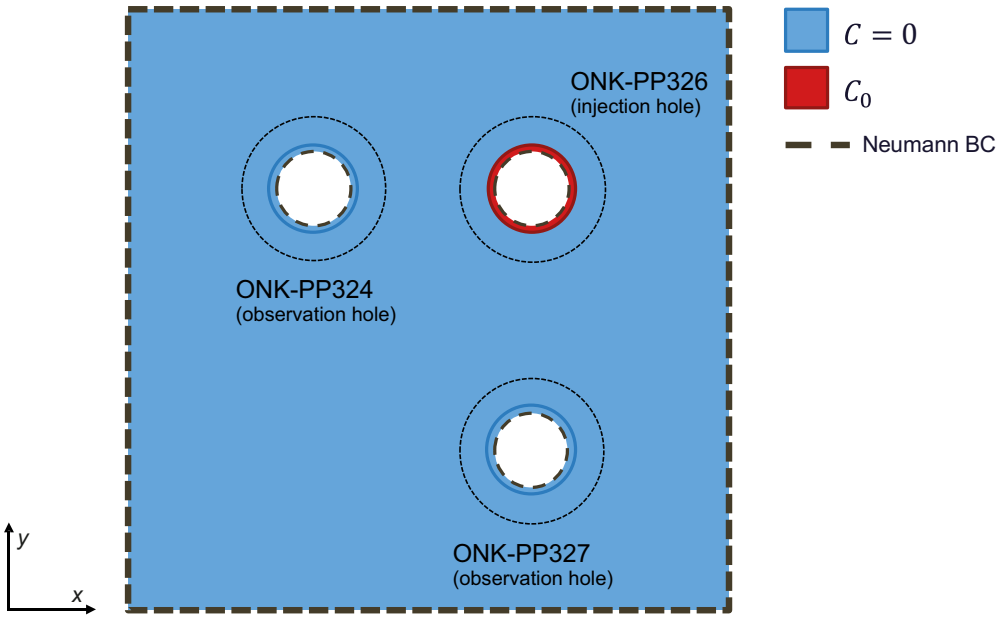

Figure C-34. *Sketch summarizing the reactive transport initial and boundary conditions. The cocktail of radionuclides is initially set-up at the injection borehole (ONK-PP326) while the rest of the domain is set with zero concentration of the radionuclide cocktail. At the boundaries of the domain and each of the boreholes, a Neumann boundary condition (zero gradient) is applied.*

C5 Results of the back-analysis stage

This chapter goes through the steps that have been taken to fit the results of the back-analysis model to the experimental data. It starts by doing an introductory analysis to the provided datasets. After that, the fitted parameterization of the numerical model is shown and finally, the results of the experiment are compared with the back-analysis stage model.

C5.1 REPRO-TDE experimental results

Figure C-35, Figure C-36 and Figure C-37 show a summary of the latest (updated the 26-03-2020) measured activities in both the injection and observation boreholes. The experimental data has been provided to the modelling teams regularly and we have been adjusting the models to the new available data. The figures also have labels that signal some of the most relevant events that happened during the experiment. Since some of these events could have a significant effect on how the back-analysis stage model performs, this chapter will go through the different hypothesis and considerations that have been taken to compare the numerical model with the experimental results.

During the REPRO experiment, there were some events that interfered with the expected behavior of the experiment. We have detected some of these events that may have an effect in how our back-analysis stage model performs when reproducing the experimental data. The first event corresponds to the circulation stop that happened around 550 days after the launch of the experiment. We have considered that the change in the measured evolution of HTO that is observed after 500 days in the injection borehole is due to this event. Thus, when fitting the results of HTO, only the data prior to 500 days has been considered.

Moreover, two main leakage events have been reported during the course of the experiment. These leakages caused significant variations of pressure that lead to high pressure gradients between the boreholes. Immediately after the exposure to the gradients, both observation boreholes reported a regular increase of the activity measurements of HTO and Cl-36. Thus, it is possible that this immediate concentration increase is caused by advective transport due to the high pressure gradients. Besides that, after 1 000 days running the experiment, the experimental section water was replaced by a new synthetic groundwater. Since the back-analysis stage model does not consider any advection or sampling related effects, its predictive capacity of the observation borehole evolution may have been affected. Section C2 shows a work we did after the blind prediction stage to study how to implement measured pressure gradients on the model.

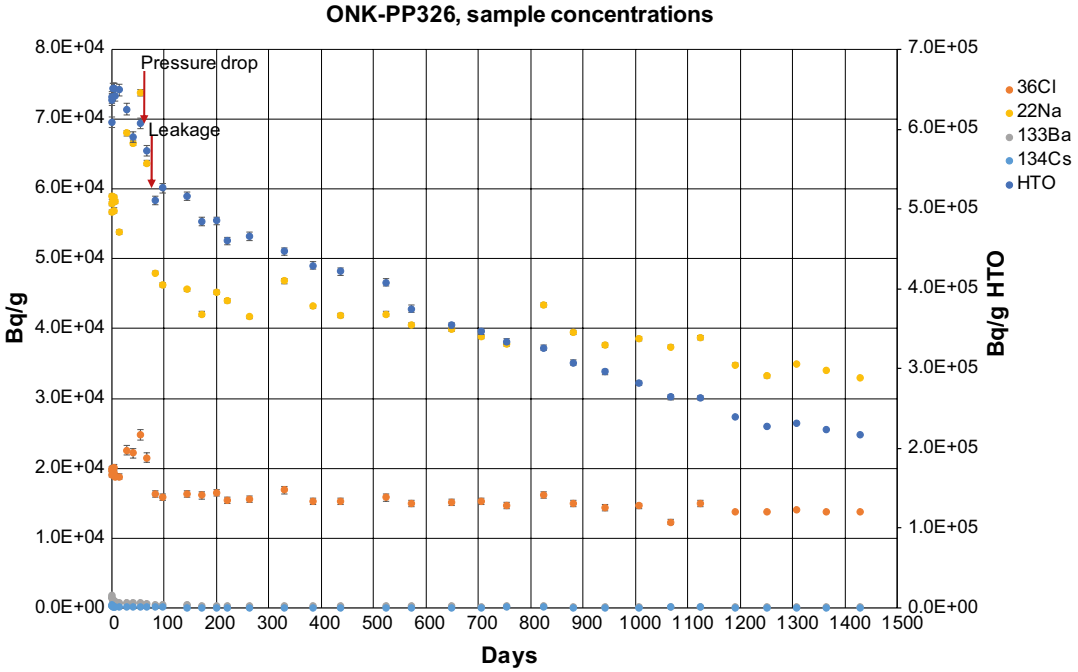

Figure C-35. *Plot showing the experimental data obtained for the injection borehole (ONK-PP326) of the REPRO-TDE experiment. Some of the key events that happened during the experiment are shown with arrows.*

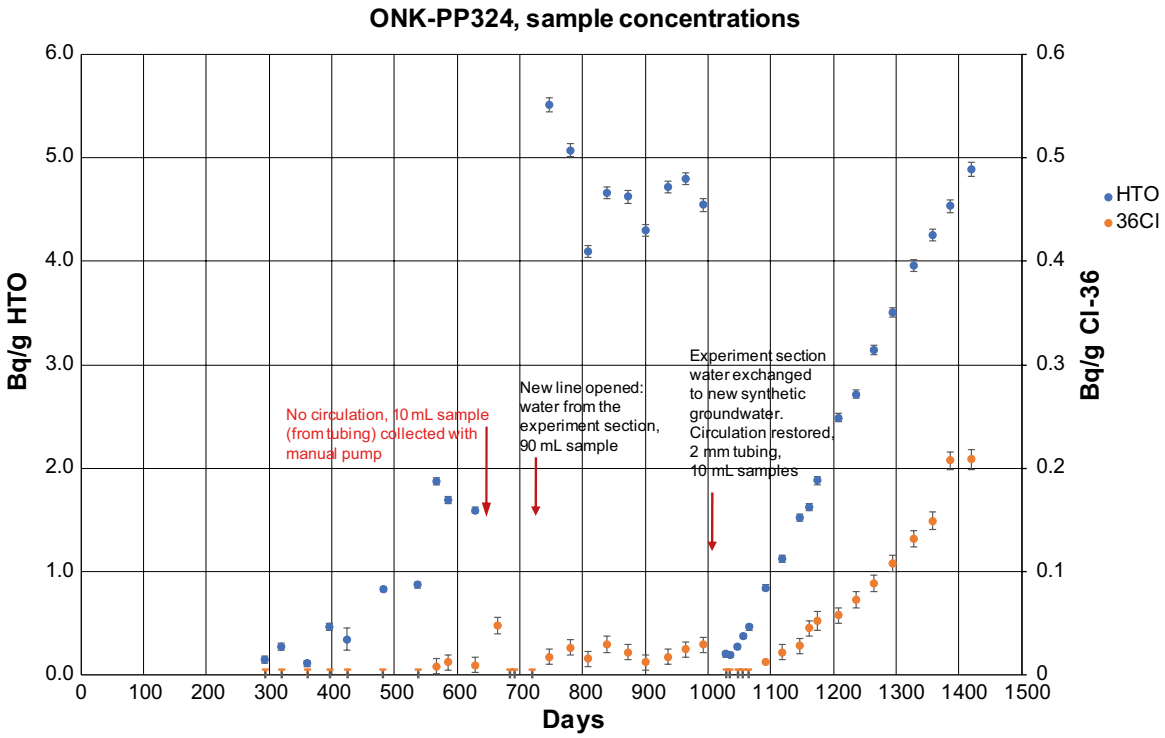

Figure C-36. *Plot showing the experimental data obtained for the observation borehole parallel to foliation (ONK-PP324) of the REPRO-TDE experiment. Some of the key events that happened during the experiment are shown with arrows.*

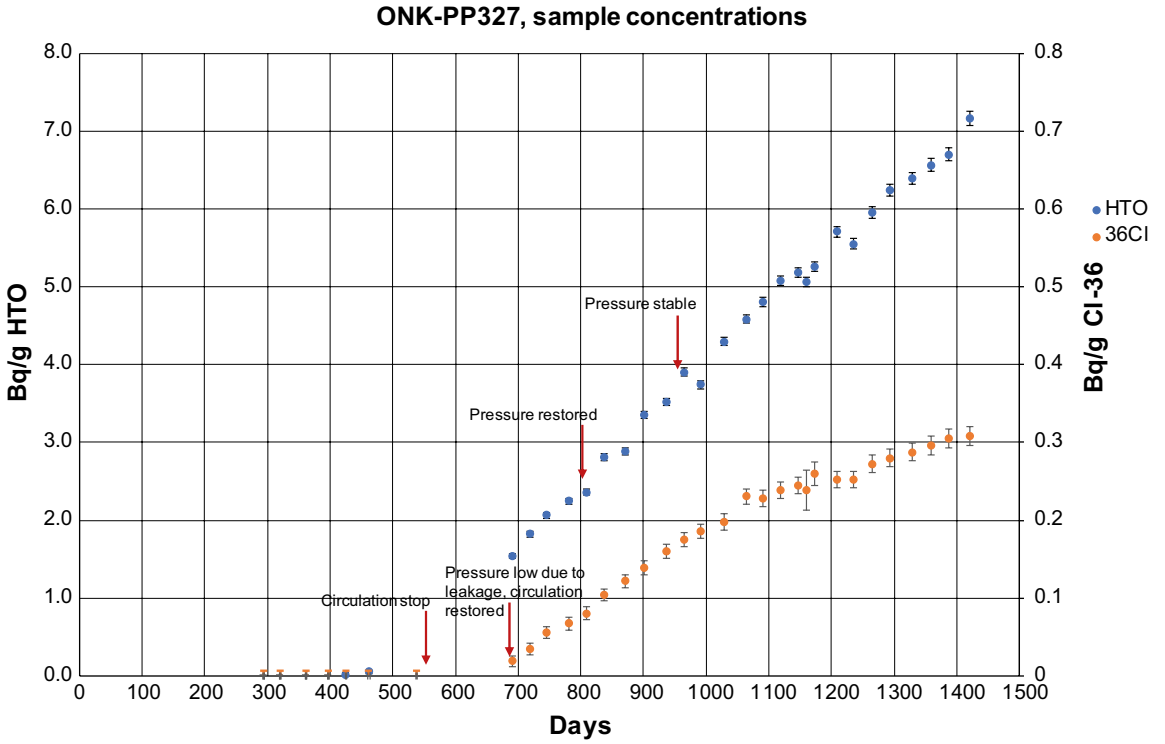

Figure C-37. *Plot showing the experimental data obtained for the observation borehole perpendicular to foliation (ONK-PP327) of the REPRO-TDE experiment. Some of the key events that happened during the experiment are shown with arrows.*

C5.2 Simulation cases and fitting criteria

After comparing the results obtained by the blind prediction model with the available experimental data, several issues were detected. On the one hand, it was clear that the models were overestimating the effective diffusion of the tracers through the rock matrix, since the amount of measured concentration at the observation boreholes of the conservative tracers (i.e. HTO and Cl-36) was far lower than the predicted value. However, the evolution of the injection borehole due to the out-diffusion of the tracers matched quite well with the experimental data. Due to this, the decision of adding a BDZ close to the boreholes was taken. This BDZ would retain the transport parameters used in the blind prediction stage model to capture the evolution of the injection borehole. On the rest of the domain, the diffusion coefficient would be reduced to fit the measured observation breakthrough curves. On the other hand, the out-diffusion evolution of the sorbing radionuclides at the injection borehole did not match perfectly with the experimental data. This mismatch was especially notorious for the case of Na-22, for which the experimental data suggested a much lower sorption capacity. Thus, the decision to fit the distribution coefficients (k_d values) of the sorbing radionuclides was taken.

The cocktail of radionuclides used for the blind prediction stage was extended here with the addition of a new conservative tracer, the Cl-36. This radionuclide is known to undergo anion exclusion processes, and thus, a lower diffusion coefficient was applied to it.

In summary, the fitting process can be divided in three main steps. First, the evolution of the HTO is fitted by finding the best matching values for the diffusion coefficients of the rock matrix and the BDZ. These values are expected to work for the other conservative tracers too, however, to fit the Cl-36, its base molecular diffusion is lowered to assess for anion exclusion. Finally, the k_d values of the sorbing radionuclides have been individually tuned to capture the evolution of them at the injection borehole.

Parameterization of the reactive transport model

As mentioned before, the reactive transport model has been parameterized by the effective diffusion coefficient of the different material domains and the k_d values of the different sorbing radionuclides. The values that best fitted the experimental data are summarized in Table C-3.

It is worthwhile noting that, as mentioned before, the effective diffusion coefficient of the BDZ is equal to the blind prediction stage model's one. The reason behind is that the blind prediction stage model already captured quite well the evolution of the conservative tracers at the injection borehole. Thus, the same value has been used for the BDZ. For the rest of the domain, an order of magnitude lower diffusion coefficient has been used.

The sorption coefficients of Ba-133 and Cs-134 of the back-analysis stage model do not significantly differ to the ones that were considered at the blind prediction stage model (i.e. they are in the same order of magnitude). However, a dramatic change is observed for the Na-22 distribution coefficient. In fact, as shown in Table C-3, a much lower distribution coefficient for Na-22 needs to be considered in order to fit the injection borehole experimental data. This suggests that in our experimental set-up, Na-22 behaves as a very weakly sorbing radionuclide.

Finally, as mentioned before, the molecular diffusion coefficient of the Cl-36 has been reduced to $7.0 \times 10^{-10}\ m^2/s$, which is 30 % less than the value used for the other tracers (i.e. $D_0 = 1.0 \times 10^{-9}\ m^2/s$).

Table C-3. Comparison of the reactive transport parameters between the blind prediction stage and back-analysis stage models.

	Parameter	Blind prediction stage model	Back-analysis stage model	Units
Diffusion related parameters	Matrix porosity ϕ_m	0.006	0.006	$\frac{m^2}{s}$
	Matrix tortuosity τ_m	0.05	0.006	-
	Matrix effective diffusivity $D_{eff} = \phi_m \tau_m$	3.0×10^{-13}	3.6×10^{-14}	$\frac{m^2}{s}$
	BDZ porosity ϕ_m	-	0.03	$\frac{m^2}{s}$
	BDZ tortuosity τ_m	-	0.01	-
	BDZ effective diffusivity $D_{eff} = \phi_m \tau_m$	-	3.0×10^{-13}	$\frac{m^2}{s}$
Sorption related parameters	$k_d^{Na\text{-}22}$	1.3×10^{-3}	6.5×10^{-6}	$\frac{m^3}{kg}$
	$k_d^{Ba\text{-}133}$	6.0×10^{-2}	1.5×10^{-2}	$\frac{m^3}{kg}$
	$k_d^{Cs\text{-}134}$	3.1×10^{-1}	9.0×10^{-1}	$\frac{m^3}{kg}$
Cl-36 parameters	Cl-36 molecular diffusion in water	-	7.0×10^{-10}	$\frac{m^2}{s}$

The initial activities of the radionuclides that have been set-up in the injection borehole are summarized in Table C-4. These activities have been divided by the water volume on the injection borehole, which is 252 ml.

Table C-4. List of tracer activities used at the back-analysis stage model.

Isotope	Activity per volume (Bq/g)
HTO	6.8×10^5
Na-22	7.7×10^4
Cl-36	1.9×10^4
Ba-133	6.6×10^3
Cs-134	7.2×10^3

C5.3 Final model results

The numerical simulation of the back-analysis stage model has been run using PFLOTRAN on a regular workstation using 48 computational cores. The simulation took approximately 3 h to complete, which means that the computational model presented here converges smoothly and does not have a high computational burden.

The results shown in this chapter compare the breakthrough curves at the injection and observation boreholes of the REPRO-TDE experimental data and the back-analysis stage model. The chapter is divided in three main blocks: in the first one, the results of the conservative tracer (HTO) are compared and discussed. The second block focuses on the comparison of Cl-36 and, in the third block, the breakthrough curves of the sorbing radionuclides (i.e. Na-22, Ba-133 and Cs-134) are compared and discussed.

HTO

In Figure C-38, the experimental activity of the HTO at the injection borehole (i.e. ONK-PP326) is compared with the activity predicted by the back-analysis stage model. As mentioned in Section C5.1, the back-analysis stage model does not consider advective effects caused by pressure drops that happened during the experiment. Thus, the model is fitted using the data before the event in which the circulation was stopped for some days (this happened around 550 days after the launch of the experiment). This way, the back-analysis stage model shows a good agreement with the data for the first 500 days. After that, the predicted tail of the curve does not fit the experimental data, which is assumed to be due to this previous event.

Regarding to the evolution of the observation boreholes, as mentioned in Section C5.1, the effects caused by the events that happened during the experiment have not been included in the numerical model. Because of that, it is hard to accurately predict the breakthrough curves at the observation boreholes. As shown in Figure C-39 and Figure C-40, the experimental breakthrough curves at the observation boreholes do not fit in shape with the predicted breakthrough curves. However, both the predicted arrival times and activities are in the same order of magnitude than the experimental data.

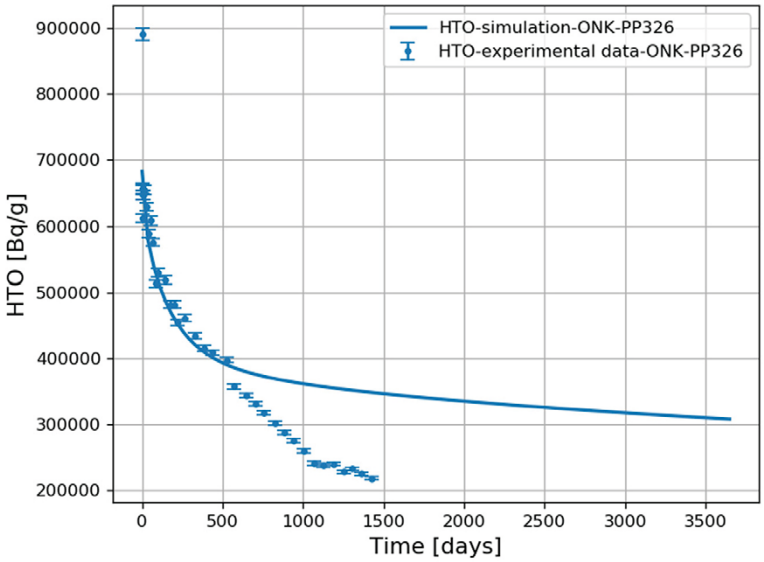

Figure C-38. *Plot comparing the experimental data of HTO activity at the injection borehole (ONK-PP326) over time with the breakthrough curve obtained for the back-analysis stage model. The experimental data is represented by points including error bars and the numerical model by the solid line.*

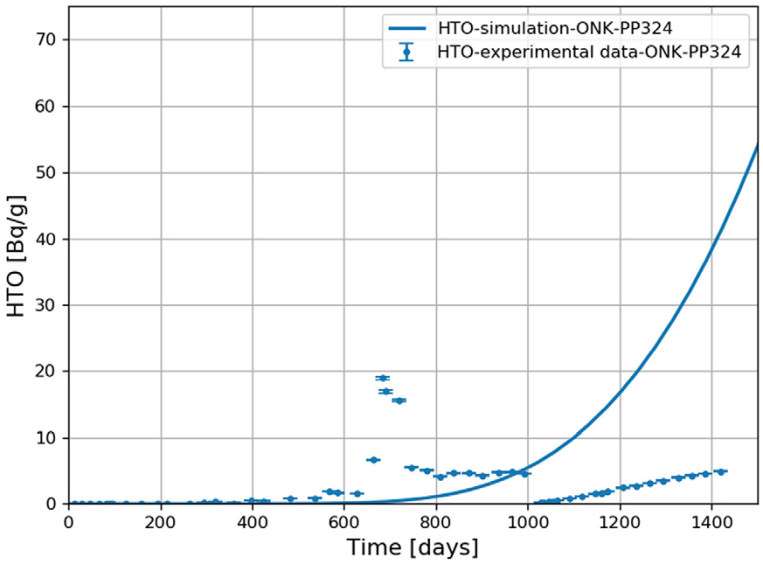

Figure C-39. *Plot comparing the experimental data of HTO activity at the observation borehole parallel to foliation (ONK-PP324) over time with the breakthrough curve obtained for the back-analysis stage model. The experimental data is represented by points including error bars and the numerical model by the solid line.*

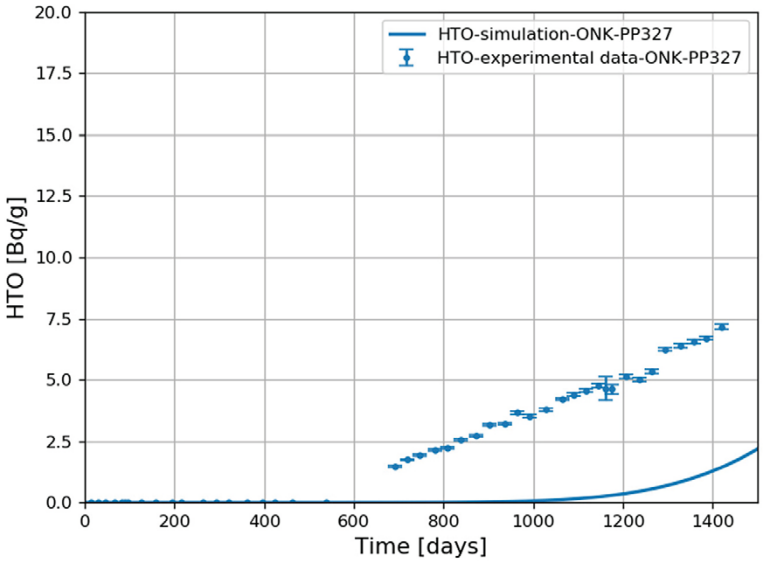

Figure C-40. *Plot comparing the experimental data of HTO activity at the observation borehole perpendicular to foliation (ONK-PP327) over time with the breakthrough curve obtained for the back-analysis stage model. The experimental data is represented by points including error bars and the numerical model by the solid line.*

Cl-36

In the case of Cl-36, the predicted activity breakthrough curve at the injection borehole (ONK-PP326) (Figure C-41) shows a very good agreement with the experimental data. In this case, the circulation stop event does not seem to have an effect. Regarding to the observation boreholes (Figure C-42 and Figure C-43), the breakthrough curves show a pattern similar to the HTO case: the predicted arrival times are longer than the experimental ones, but the activity evolution lies at the same order of magnitude.

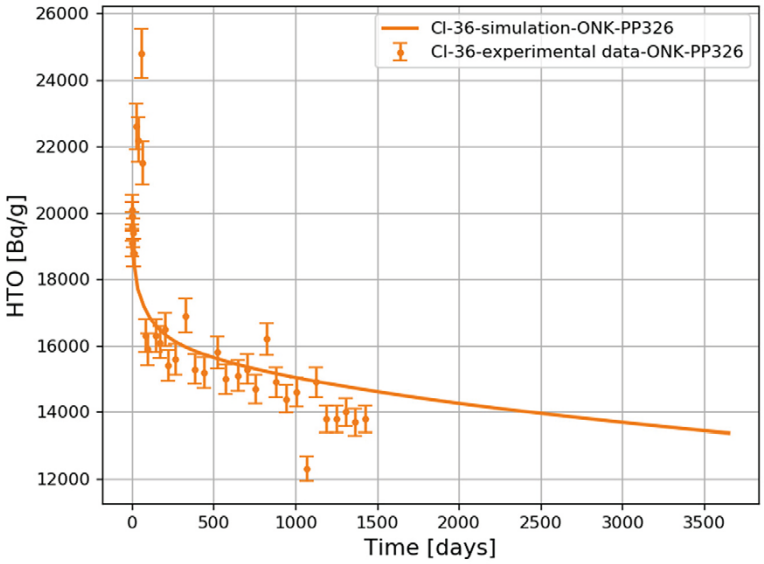

Figure C-41. *Plot comparing the experimental data of Cl-36 activity at the injection borehole (ONK-PP326) over time with the breakthrough curve obtained for the back-analysis stage model. The experimental data is represented by points including error bars and the numerical model by the solid line.*

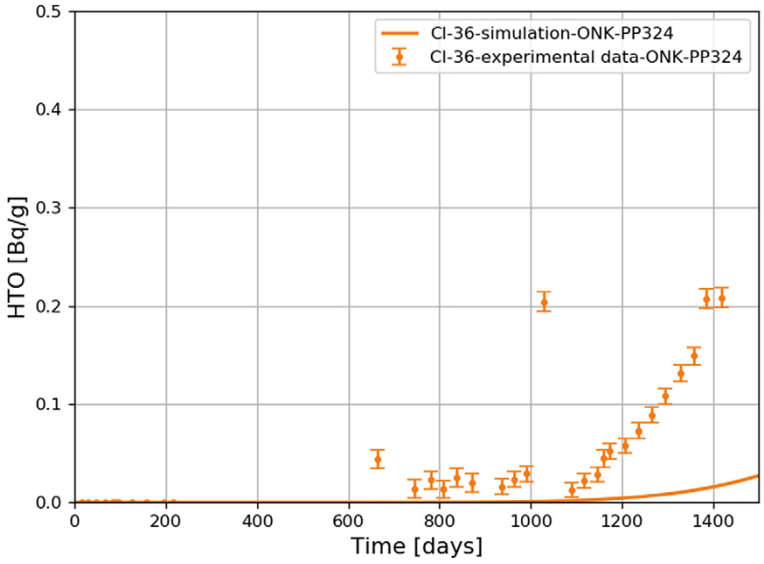

Figure C-42. *Plot comparing the experimental data of Cl-36 activity at the observation borehole parallel to foliation (ONK-PP324) over time with the breakthrough curve obtained for the back-analysis stage model. The experimental data is represented by points including error bars and the numerical model by the solid line.*

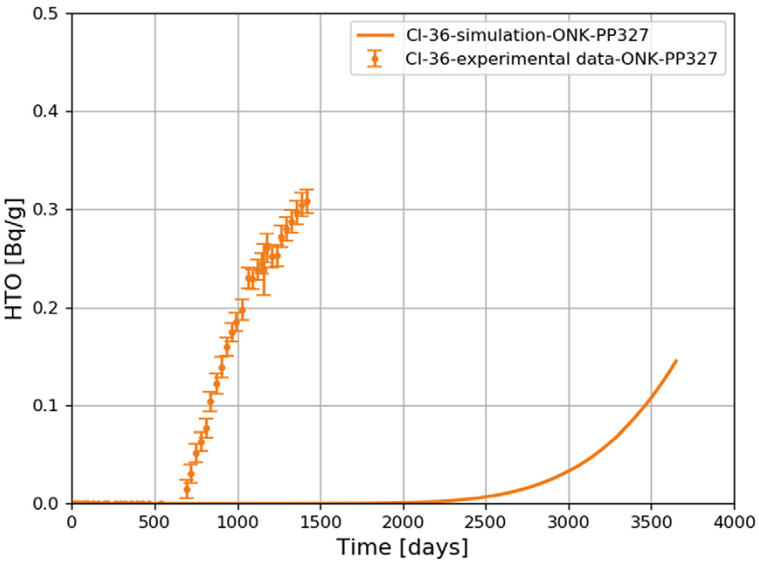

Figure C-43. *Plot comparing the experimental data of Cl-36 activity at the observation borehole perpendicular to foliation (ONK-PP327) over time with the breakthrough curve obtained for the back-analysis stage model. The experimental data is represented by points including error bars and the numerical model by the solid line.*

Sorbing tracers

Both the experimental data and back-analysis stage model predictions agree that none of the considered sorbing tracers has still arrived to neither of the observation boreholes. Thus, the comparison of the sorbing tracers has been limited to predict the evolution of the injection borehole (ONK-PP326).

Na-22

The comparison between the experimental activities measured at the injection borehole and the predicted activities by the numerical model for Na-22 is shown in Figure C-44. It can be seen that the fitting between the two is quite good. However, to obtain such fit, the sorption capacity of Na-22 has been significantly reduced by almost three orders of magnitude compared to the blind prediction stage model. Due to this, Na-22 behaves as a very weakly sorbing radionuclide.

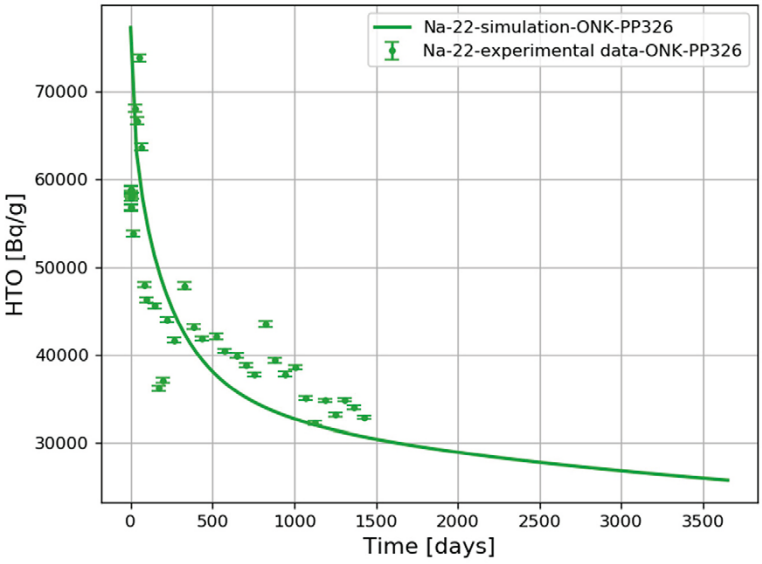

Figure C-44. *Plot comparing the experimental data of Na-22 activity at the injection borehole (ONK-PP326) over time with the breakthrough curve obtained for the back-analysis stage model. The experimental data is represented by points including error bars and the numerical model by the solid line.*

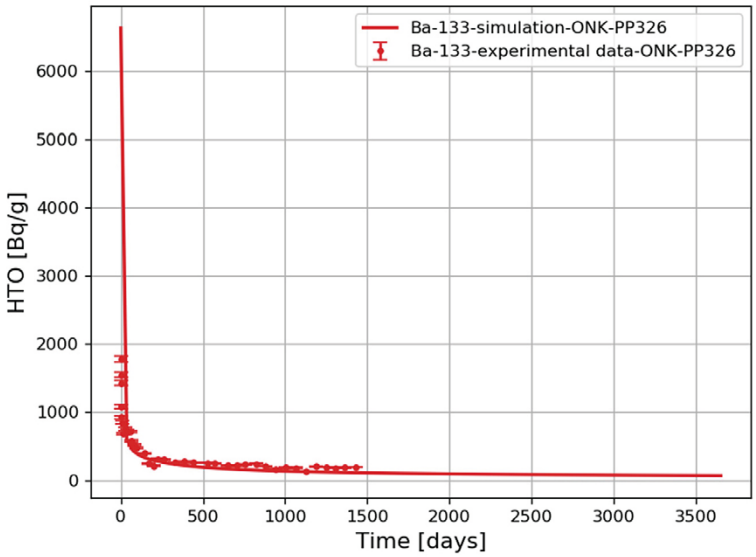

Figure C-45. *Plot comparing the experimental data of Ba-133 activity at the injection borehole (ONK-PP326) over time with the breakthrough curve obtained for the back-analysis stage model. The experimental data is represented by points including error bars and the numerical model by the solid line.*

Ba-133

Ba-133 is assumed to be a strongly sorbing radionuclide (i.e. as Cs-134) and both the experimental data and the predicted breakthrough curve agree on that. The fit between the two (Figure C-45) is quite good and it shows the quick drop in concentration that is typically observed for the strongly sorbing radionuclides. This quick drop happens because the radionuclide gets quickly sorbed once it diffuses out from the injection borehole, which drops the aqueous concentration in the vicinity of the borehole and generates high diffusive gradients that keep pushing out the radionuclide.

Cs-134

The behavior of the Cs-134 is similar to the one observed for the Ba-133. They both are strongly sorbing radionuclides and it can be seen in the breakthrough comparison (Figure C-46) that the considered homogeneous k_d based model is enough to capture the evolution of the sorbing tracers at the injection borehole.

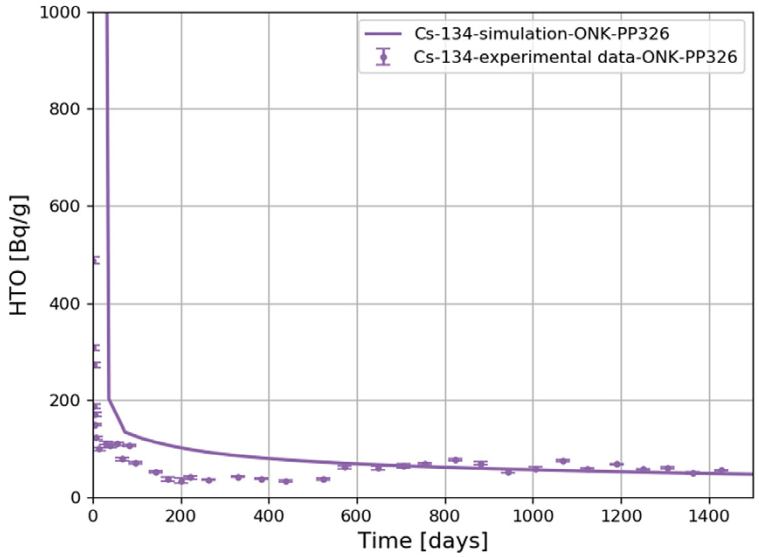

Figure C-46. *Plot comparing the experimental data of Cs-134 activity at the injection borehole (ONK-PP326) over time with the breakthrough curve obtained for the back-analysis stage model. The experimental data is represented by points including error bars and the numerical model by the solid line.*

C6 Conclusions and final remarks

Following this work's structure, the conclusions can be divided in two main blocks. Regarding the blind prediction stage, we have presented a number of calculations focused on assessing the possible influence that rock foliation has on radionuclide diffusion in the rock matrix. Besides process understanding, the results are intended to provide blind predictions of the evolution of concentration in the TDE experiment carried out at Onkalo (Finland).

We have shown that when anisotropic diffusion is modelled with an anisotropic diffusion tensor, the observed shape of the radionuclide plume is ellipsoidal and is more elongated along the principal direction of foliation. These results are not particularly novel, as analytical solutions for 2D anisotropic diffusion are well known. However, the current "standard" version of PFLOTRAN does not include the capability of defining an anisotropic diffusion coefficient. Thus, a customised implementation of the code has been developed and validated. This version is now available and could potentially be used in future more complex calculations.

Of more interest is the analysis of possible representations of the underlying heterogeneous structure of diffusivity. This part of the work has been done using geostatistical methods, namely Sequential Gaussian Simulations. By using an anisotropic semivariogram, with a longer correlation length along the direction of foliation, we have been able to represent heterogeneous diffusivity fields that visually reproduce the foliated structures observed from e.g. PMMA-autoradiography measurements and at the same time honour the average diffusivity measured in the laboratory. The main advantage of this stochastic approach is that the (strong) underlying uncertainty related to the heterogeneous structure of the considered rock domain is quantitatively accounted for in e.g. Monte Carlo simulations. This has been illustrated in our results that are also presented in terms of cumulative distribution functions (CDFs) of arrival times.

It is worthwhile noting that the proposed heterogeneous fields are not intended to be strictly representative of the foliation observed in the TDE experiment. This is in fact intended to be a first qualitative step toward the realistic representation of the heterogeneity in the rock sample tested in the TDE experiment. The next step forward is to carry out a seriography analysis (i.e. to infer the structure of the semivariogram) using the available PMMA-autoradiography data. As this analysis will be carried out at a much smaller scale compared to the scale of the experiment, appropriate upscaling techniques will be also tested.

The back-analysis stage has been focused on building a model able to reproduce the experimental data of REPRO-TDE. However, as discussed in Section C5.1, it has been proven that a simplified model set-up (as the one used for the back-analysis stage) is not enough to accurately reproduce the evolution of the observation boreholes. Even though the original experimental set-up was relatively easy to implement, the leakages and other events that happened over the course of the experiment added extra layers of uncertainties that were difficult to reproduce using the numerical model. Despite the trouble matching the observation breakthrough curves, the back-analysis stage model is able to predict quite accurately the breakthrough curves of the injection borehole for the considered radionuclides. Even the evolution of the sorbing radionuclides can be reproduced using a simple linear isotherm reaction based on fitted distribution coefficients.

C7 Appendix: update including time dependent pressure BC

C7.1 Background and motivation

The SKB Task Force 9 focuses on the realistic modelling of coupled matrix diffusion and sorption in heterogeneous crystalline rock matrix at depth. This is done in the context of inverse and predictive modelling of tracer concentrations of the in situ experiments performed within LTDE-SD at the Äspö Hard Rock Laboratory in Sweden, as well as within the REPRO project at the ONKALO underground rock characterisation facility in Finland, focusing on sorption and diffusion. The ultimate aim is to develop models that in a more realistic way represent retardation in the natural rock matrix at depth (Andersson et al. 2020).

Task 9C focuses on the predictive modelling of the ongoing in situ Through Diffusion Experiment (TDE), which is a part of the REPRO project carried out by Posiva at ONKALO in Olkiluoto, Finland. The experiment is carried out between three parallel drillholes arranges as a right-angled triangle. One of these drillholes (ONK-PP326) is used as the injection hole for a cocktail of tracers while the other two drillholes (ONK-PP324 and ONK-PP327) act as observation holes (see Figure C-47). This facilitates tracer migration along, and across, the rock matrix's foliation. The experiment is carried out in 1 m long packed-off sections, at a distance of about 11 to 12 m from the tunnel wall and each drillhole is separated from the others a little more than one decimetre. Since the experiment takes place in a rock volume that lacks water-bearing fractures, any advective flow between drillholes is foreseen to be insignificant.

In this stage of the modelling activity, Amphos 21 has focused on incorporating the pressure gradients that were measured during the TDE experiment in the models. Thus, the current models include advection besides molecular diffusion. These pressure gradients were facilitated to the modelling teams on an appendix of the task description (Andersson et al. 2020). As mentioned there, groundwaters pressures have been measured in all test sections and guard sections of the TDE boreholes. Even though at the early phase of the experiment the pressures were controlled and set to a given pressure (about 1 MPa), in February 2016, a sudden leakage occurred in the pressure control system of PP326, resulting in a loss of tracer. It was therefore decided to instead allow the pressures in the individual intervals to reach their ambient pressures. This caused a non-neglectable change in the pressure gradients of the system.

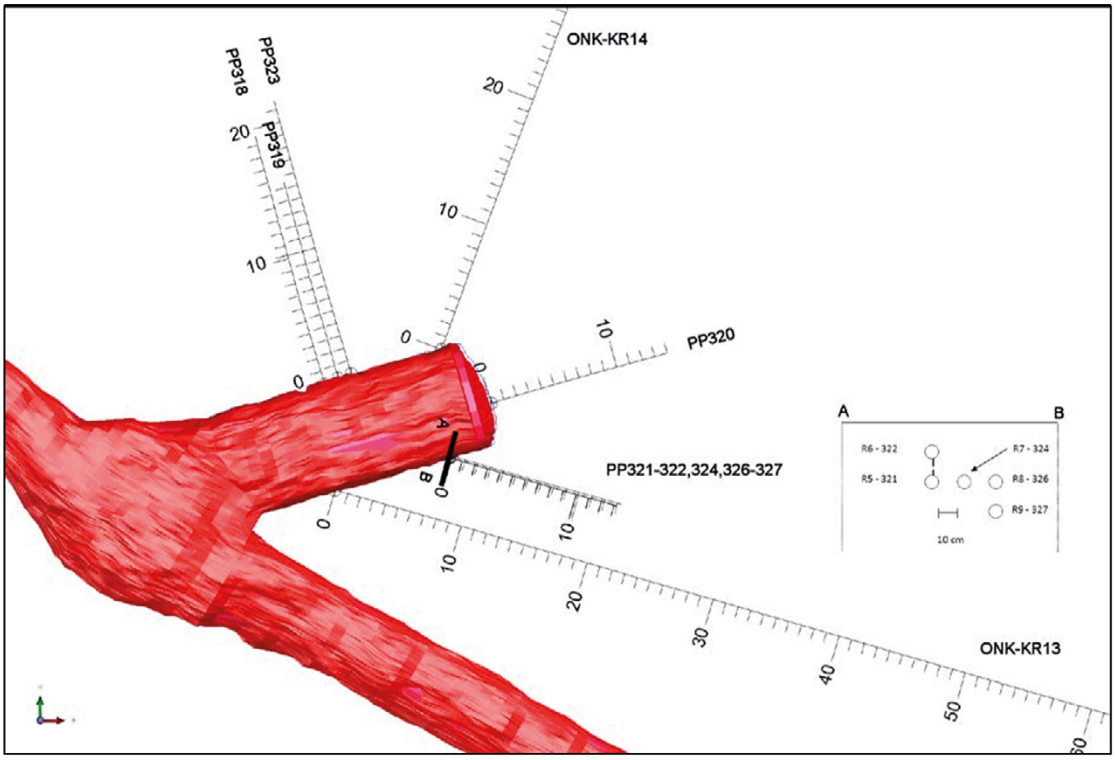

Figure C-47. *REPRO niche ONK-TKU-4219 and TDE drillholes ONK-PP321 to PP327.*

C7.2 Conceptual model

In order to implement the gradients measured in the boreholes, a conceptual change needs to be done to the previous model set-up. In the previous model set-up in fact diffusion was the driving force for reactive transport. In this updated model, groundwater flow need to be included.

This implementation has been done in two steps. First, the measured pressure values on the boreholes have been smoothed and interpolated on a finer time domain (i.e. to improve numerical convergence of the model). Then, for each modelling case, (i.e. the homogeneous cases and the heterogeneous cases), a suitable permeability field has been created based on the updated information of the task description.

Pressure interpolation

The absolute pressure values measured on both the injection and observation boreholes have been used to create a time dependent pressure function for each borehole. However, since the measuring time intervals were not constant, these pressure functions have been interpolated. This interpolation also applies a slight smoothing to the data to avoid abrupt pressure changes that may lead to numerical problems.

A python script has been developed to interpolate the data. The interpolation algorithm is based on monotonic cubic splines to find the value between data points.

Figure C-48, Figure C-49 and Figure C-50 show the comparison between the measured pressure data and the interpolated pressure function.

These interpolated pressure functions have been applied as time-dependent Dirichlet boundary conditions on each of the annular fractured of the boreholes. Figure C-51 shows a sketch of the pressure boundary conditions that have been applied on the model.

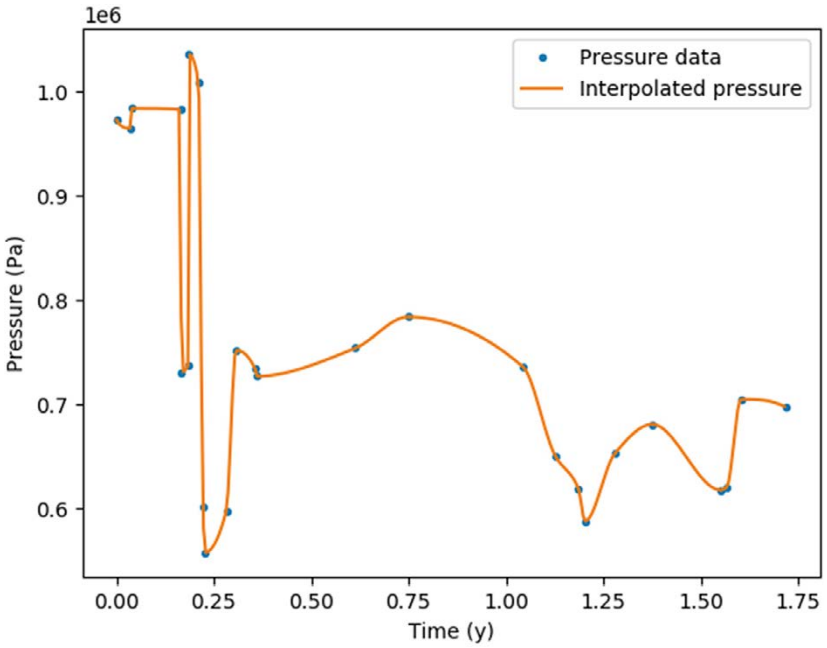

Figure C-48. *Experimental pressure data versus the interpolated pressure function for the PP-326 injection borehole.*

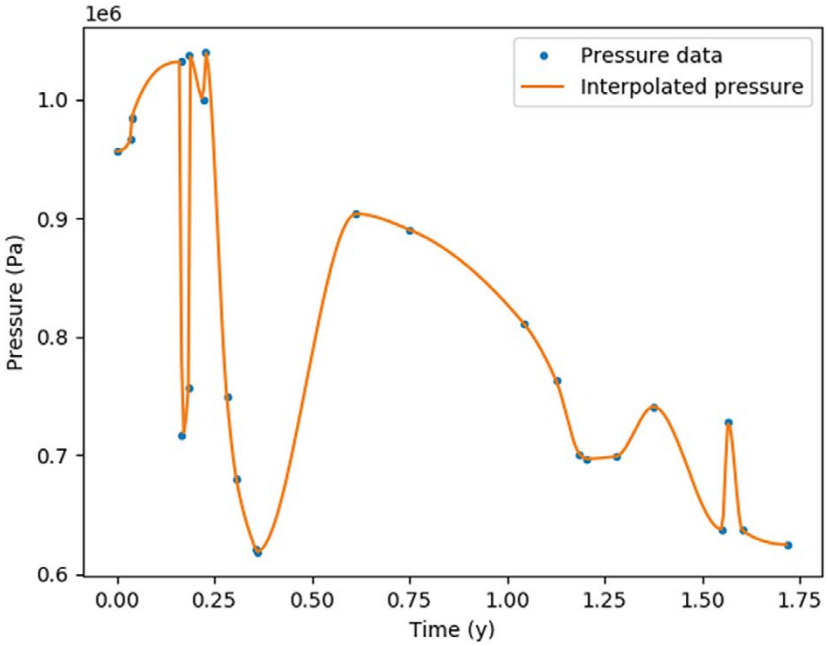

Figure C-49. *Experimental pressure data versus the interpolated pressure function for the PP-324 injection borehole.*

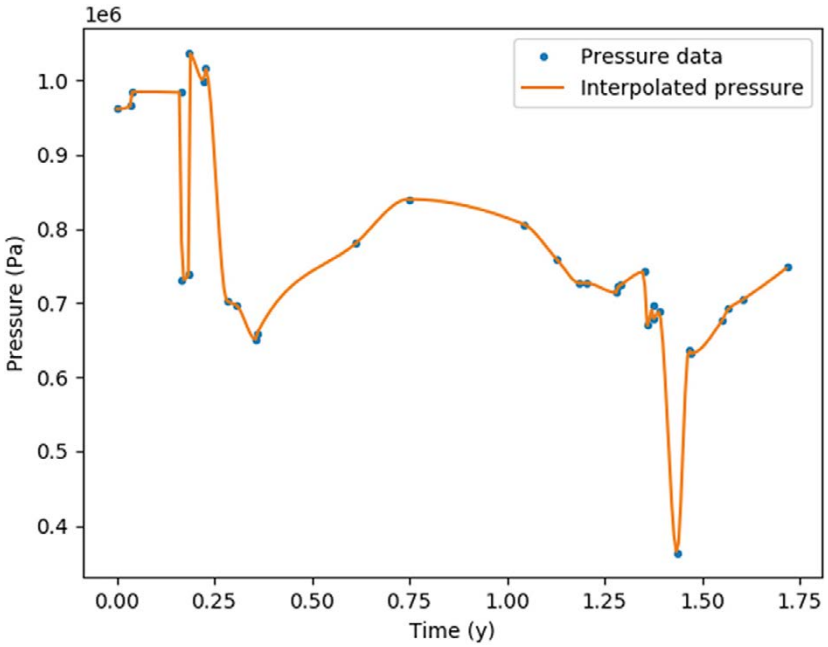

Figure C-50. *Experimental pressure data versus the interpolated pressure function for the PP-327 injection borehole.*

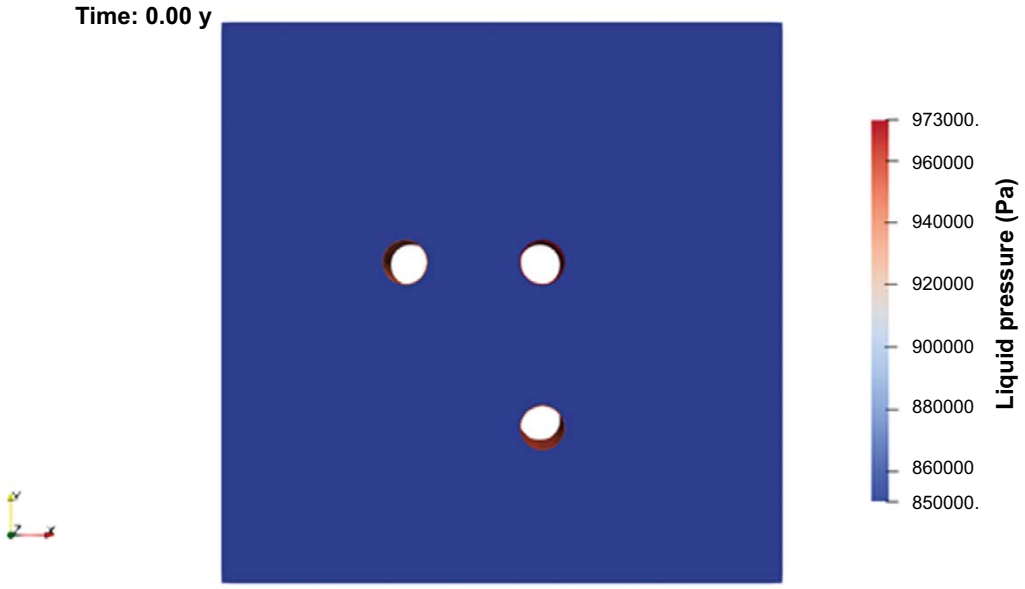

Figure C-51. *Pressure field at the first timestep. Time-dependent Dirichlet BC are applied on both the injection and observation boreholes.*

Permeability field

To model groundwater flow, a permeability field needs to be defined and included. In our previous delivery we presented two different models; one where diffusivity was homogeneous but anisotropic and the second based on heterogeneous and statistically anisotropic diffusion fields. Thus, to be consistent with that approach, a homogeneous case and a heterogeneous case have been considered here.

Homogeneous case

In the homogeneous case, a constant permeability value has been applied to both the rock matrix and the drillhole section. These values come from the field measurements that were made by measuring the inflow to the experimental sections during several weeks prior to the TDE experiment. Details of the measuring process can be found in Andersson et al. (2020).

A range of values for hydraulic conductivity is given for the core tests:

$$K = [2.0,100.0] \cdot 10^{-13} m/s$$

In order to reduce high hydraulic conductivity contrasts that may difficult numerical convergence, the smallest value has been chosen and permeability is computed:

$$k_{drillhole} = \frac{\mu}{\rho g} K_{drillhole} = 1.8 \cdot 10^{-20}\ m^2$$

The same document provides a hydraulic conductivity range for the rock matrix, which is significantly smaller compared to the hydraulic conductivity in the core tests. In this case, the arithmetic mean value has been used all over the rock matrix.

$$k_{matrix} = 4.0 \cdot 10^{-22}\ m^2$$

Heterogeneous case

The chosen strategy to build the permeability fields has been to map the tortuosity field used in the previous model set-up with a linear transformation. Thus, the resulting permeability field mimics the heterogeneous structures present on the diffusion fields. The linear mapping function scales the tortuosity values to the range of hydraulic conductivity values defined in the updated task description:

$$k(\tau) = \frac{k_{max} - k_{min}}{\tau_{max} - \tau_{min}}\tau + \frac{k_{min}\tau_{max} - k_{max}\tau_{min}}{\tau_{max} - \tau_{min}}$$

Here, $k_{min} = 9.01 \times 10^{-23}\ m^2$ and $k_{max} = 1.81 \times 10^{-21}\ m^2$. The extremal values of the tortuosity field vary depending the case scenario and are computed automatically.

Since the results obtained with the heterogeneous case have not shown a measurable change compared to the diffusion only case, a less realistic case scenario has also been considered in the work. In this non-realistic case, the range of the permeability field has been increased keeping its mean value fixed. To do so, the mapping function has been changed in the following way:

$$k(\tau) = \frac{\sqrt{k_{min}K_{max}}}{\sqrt{\tau_{min}\tau_{max}}}\tau$$

Now, the permeability field is directly scaled by the tortuosity field.

For both the homogeneous and the heterogeneous cases, the permeability fields have been exported to hdf5 files on a cell-by-cell structure to later be imported on PFLOTRAN.

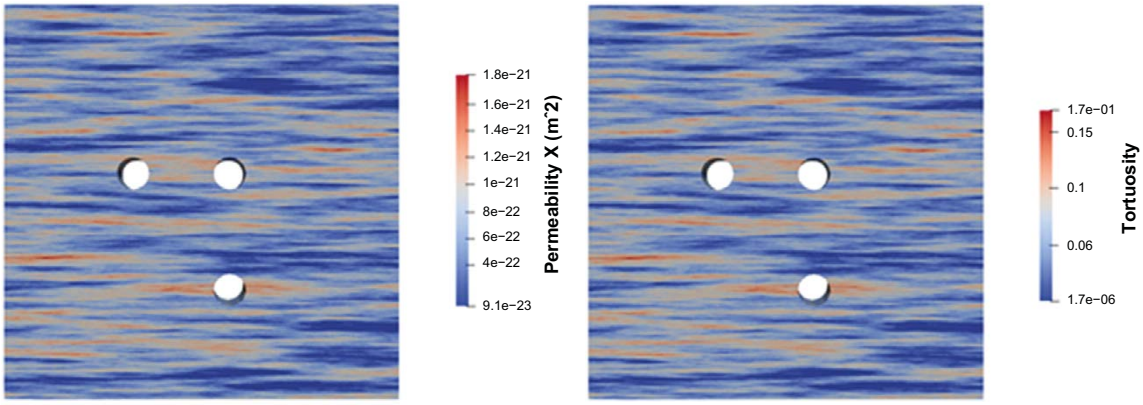

Figure C-52. *Comparison between the mapped permeability field and the tortuosity field of the Upper Case. For visualization purposes, the borehole area is not shown here.*

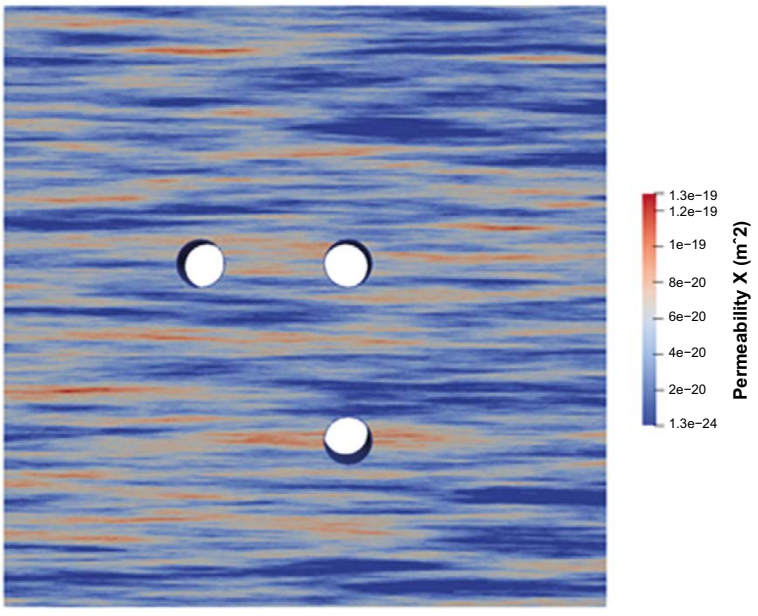

Figure C-53. *Permeability field for the non-realistic case scenario.*

Appendix D

Technical University of Liberec (TUL), ÚJV Řež (UJV), Czech Technical University in Prague (CTU), PROGEO

Milan Hokr, Jakub Říha (TUL)
Václava Havlová, Dagmar Trpkošová (UJV)
Aleš Vetešník, Dan Reimitz, Jakub Višňák, Dušan Vopálka (CTU)
Libor Gvoždík, Martin Milický, Michal Polák (PROGEO)

This chapter is adopted from the report by Hokr et al. (2020), which is a result of the contract between SURAO and Czech modelling teams for participation in Task 9 of TF GWFTS. It is also published in revised form as SKB report P-20-22 (Hokr et al. 2021).

The participation of Czech individual organisations was not uniform across all the tasks and ended before the final evaluation of Task 9C with contributions from other international teams. In particular, the inverse models presented here were made before they were included as an option in the Task definition. This subtask focuses on the modelling of an in situ through-diffusion experiment (TDE) performed by POSIVA in Finland.

D1 Summary of the task description and the data

The TDE experiment was launched in November 2015, as part of the REPRO project performed by POSIVA at ONKALO, Olkiluoto, Finland. Information for the needs of the model solution in the framework of GWFTS is given in the task description (Andersson et al. 2020). The experiment takes place between three parallel sub-horizontal boreholes arranged in a right-angle triangle (Figure D-1 – No. 324, 326 and 327, the entire designation is ONK-PP324, etc). Borehole 326 serves as an injection borehole and the other two as monitoring boreholes. The geometry of the experiment is motivated by the effort to capture the migration of tracers in the direction perpendicular and parallel to the rock foliation. Each of the boreholes has a radius of 28.25 mm.

Sections measuring 1 m are open within the boreholes, the transverse distance between the borehole walls is 10–15 cm, and the mutual difference of position between the boreholes in the direction of the axes is in units up to the first tens of centimetres (Table D-1). The open sections are at a distance of 11–12 m from the tunnel wall and next to them are so-called guard sections (separated by other packers), interconnected internally and externally, which reduce the hydraulic gradient around the experiment. The packer sections are connected to the apparatus in the underground laboratory by a circulation system with documented volumes of its individual parts (Table D-2). The device presented in the WPDE experiment is used, i.e. the borehole is fitted with a cylinder and a solution flows through the slot between the cylinder and the borehole wall.

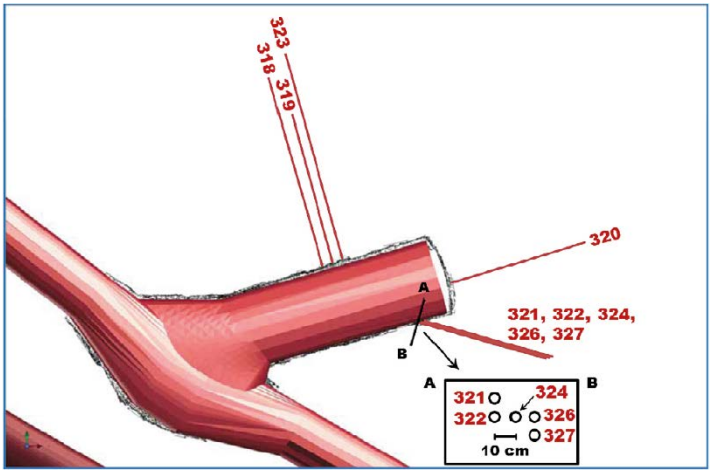

Figure D-1. *Borehole assembly at and around the TDE experiment – the injection borehole is number 326 and the monitoring boreholes are 324 and 327 (taken from Andersson et al. 2020).*

A “cocktail” containing the following tracers was injected: HTO, Na-22, Cl-36, Ba-133 and Cs-134. Both the decreasing concentrations in injection borehole 326 and increasing concentrations in boreholes 324 and 327 are monitored. Concentrations are measured both by online detection of total gamma activity inside the boreholes and on the basis of samples of documented volumes, which are replaced by synthetic groundwater of the same volume without the tracer. Table 3-1 of the task description (Andersson et al. 2020) includes the total injected activities and detection methods.

The aim of modelling is to predict the course of activity or the concentrations in the boreholes over a period of 10 years, although the breakthrough of strongly sorbing tracers is not expected. The model includes the full balance of the tracers in the individual rock forms and individual parts of the experimental apparatus. Decay-corrected activities, i.e. concentrations corresponding to a conservative tracer, are evaluated, and the results presented below are also processed in this way.

The parameters for the model (Table D-3) are set the same by all investigators in the case of data from the task description (Andersson et al. 2020): porosity based on Table 5-4 as an average of 13 samples from experimental borehole sections, effective diffusion coefficient of tritium from Table 5-5 as the average of three samples and the sorption coefficient for Na-22 and Ba-133 from Table 5-8 (value for VGN rock). The task description did not state the effective diffusivities for sodium and barium, which were taken from the task description of Task 9A (the experiment performed in the same rock). Furthermore, the parameters used for Cs-134 are taken from experimental results by UJV concerning the LTD experiment at the Grimsel Test Site. Data for Cl-36 were interpreted differently, either considering the anion exclusion (TUL, ÚJV) according to the data from Task 9A, or as the reference porosity (CTU).

The technical data of the experiment in the task description was revised during the task solution and the models were subsequently modified. The data presented in this report correspond to the final version and, therefore, may differ from those presented at the executive meetings and stated in the interim reports. The main changes of input parameters are included in Table D-1 and Table D-2.

Several problematic aspects were encountered during the measurement i.e. problems with the circulation in PP324 meant the borehole had to be flushed and the piping re-installed, leading to an ambiguous interpretation of the arrival of HTO. A continuous increase starts after 1 000 days; however, qualitatively the first arrival of HTO should be considered about 300 days, of course without realistic concentration values.

Table D-1. Task 9C – coordinates of the centres of the open boreholes and the distance between the boreholes.

Borehole	X [m]	Y [m]	Z [m]	Distance from ONK-PP326 [m]		
				centre–centre Original task description	wall–wall Original task description	wall–wall Revised task description 11/2018
ONK-PP324	0.43	0.48	−0.31	0.2665	0.153	0.15
ONK-PP326	0.34	0.23	−0.29			
ONK-PP327	0.33	0.27	−0.45	0.1652	0.119	0.115

Table D-2. Task 9C – volumes of solutions in boreholes, including the supply piping (a detailed differentiation of individual contributions to the total volume is included in the task description, see Andersson et al. 2020).

Borehole	Volume of solution in the borehole [mL]	
	Original task description	Revised task description 11/2018
ONK-PP324	268	291
ONK-PP326	252	290
ONK-PP327	268	313

Table D-3. Model transport parameters of the used tracers.

	ε(-)	K_d ($m^3 \cdot kg^{-1}$)	D_e ($m^2 \cdot s^{-1}$)	D_w ($m^2 \cdot s^{-1}$)
H-3	0.0094	0	3.90E−13	2.30E−09
Na-22	0.0094	0.0013	4.65E−13	1.33E−09
Cl-36 (TUL, ÚJV)	0.000175	0	5.00E−15	2.03E−09
Cl-36 (CTU)	0.0094	0	3.40E−13	2.03E−09
Ba-133	0.0094	0.060	3.00E−13	1.69E−09
Cs-134	0.0094	0.031	3.00E−13	2.07E−09

D2 Implementation of the models

D2.1 Solution of Task 9C using Flow123d (TUL)

This is an ad-hoc balance model with Flow123d at its core. The model evaluates the concentrations in the boreholes, which are then used as boundary conditions for a transport simulation in Flow123d. The input of the model are the injected activities (or masses) of the individual tracers together with the volumes of solutions (effective part of the experimental section together with the inlets) in each of the boreholes. Flow123d runs the model with a given time step, evaluates the mass balance (Flow123d output) and recalculates the concentrations in the boreholes. It also sets the last known concentration distribution in the rock matrix as the initial condition for the next step of the calculation. The model may also simulate the sampling.

Diffusion (migration process) and linear sorption (retardation process) are simulated in Flow123d. Advection was considered only in the context of test calculations.

Several simplifications were made to prepare the model:

- The rock matrix is simulated as being homogeneous in the prediction. Possible heterogeneity of the model is considered in the inverse model.
- Experimental artefacts (e.g. concentration leaks during the experiment) are not considered. The presence of these artefacts is known, but not sufficiently documented. Their omission from the existing simulations was carried out based on a recommendation from the task leaders.
- Geometry of the model (and thus the discretisation mesh) is only 2D. This simplification was adopted in order to reduce computational requirements.
- Zero mass flux as a boundary condition of the transport is prescribed at the outer boundary of the simulated domain. This boundary condition is necessarily incorrect because the model domain is finite, and its boundaries are not at a significant distance from the experimental section. An alternative would be to prescribe a zero concentration at the boundary, which is no more accurate. The solution would be to extend the model domain, whereby reducing the impact of the boundary condition (at the expense of increased computational requirements).
- An ideal mixing of the tracers in the water volumes is assumed.
- The pressure gradient and advective transport are not considered. The pressure difference was measured between the individual boreholes during the experiment. The effect of the pressure gradient on the model results was tested separately (see below).

The geometry of the model is given by the position of three boreholes according to Table D-1. For 2D geometry, the depth of the individual boreholes in the experimental sections is irrelevant. However, in a 3D model, it would have to be taken into account.

The computational area was discretised by triangular elements with local refinement around the boreholes (0.25 mm) and at their joints (2.5 mm), within the remainder of the area with the step 10 mm. The resulting mesh consists of 39 325 elements (Figure D-2).

Our aim was to simulate the transport, where the only driver of concentration spreading is molecular diffusion. Therefore, the flow model parameters were set to minimise the pressure gradients and thereby also the flow velocities. The hydraulic conductivity of the rock matrix is constant throughout

the region $K = 2.8731 \times 10^{-12}$ m/s (calculated from the average permeability $k = 3.825 \times 10^{-19}$ m^2). A zero piezometric head is prescribed as a boundary condition at the edge of the injection borehole, with a homogeneous Neuman boundary condition (zero flow) used on the remaining model boundaries. The transport model parameters are summarised in Table D-3.

The boundary conditions of transport on the circumference of the boreholes are given by the concentrations of tracers in the borehole solution (they change over time). A homogeneous Neuman boundary condition is prescribed at the outer boundary of the model. The initial volumes of the solutions in each borehole are shown in Table D-2. The volumes of the solutions change during the experiment due to sampling. However, this was not included in the predictive simulation due to the absence of input data in that time. Nevertheless, the model is ready for this.

The total simulation period was set to 10 years according to the requirements of the task leaders. The internal step of the balance model was different for the individual tracers (0.1 year for HTO, 0.01 year for Na-22 and Cl-36 and 0.005 year for Ba-133 and Cs-134). Strongly sorbing tracers needed a shorter time step to avoid oscillations (given by the stability limit of the explicit method). In Flow123d, the discontinuous Galerkin method (implicit in time) was used to calculate the transport in the individual steps.

The results of the simulations are presented in Section 4.3 in the comparison of the results of the individual investigators.

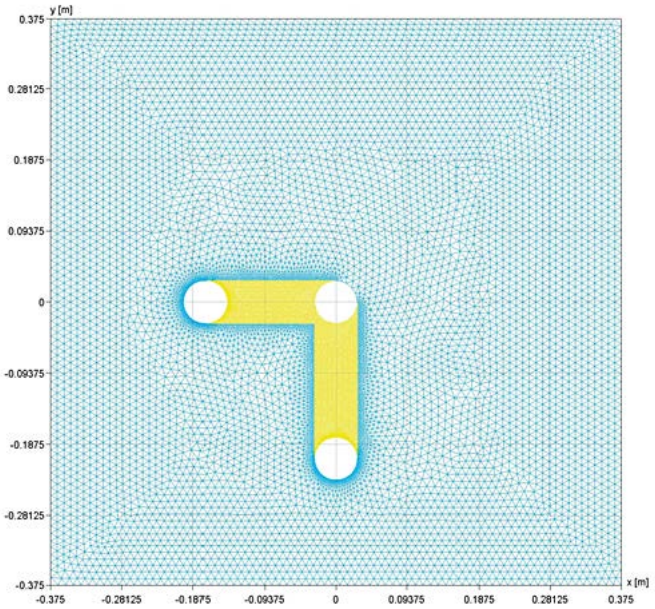

Figure D-2. *Task 9C – Flow123d – computational mesh of the model.*

D2.2 Solution of Task 9C using GoldSim (ÚJV)

The subject of the experiment in the initial phase of the solution was to simulate the transport of radionuclides H-3, Na-22, Cl-36, Ba-133, Cs-134 from the specified section in the injection borehole to the specified section on each of the two monitoring boreholes. The following features were omitted from the experiment:

1. Unsteady pressure conditions in defined sections of the borehole.
2. Changes in the radionuclide activity in the boreholes due to the sampling (taking a certain amount of water of a given activity, subsequently replacing this volume with water without a tracer).
3. Radioactive decay.

Due to these assumptions, diffusion transport is simulated, where the breakthrough of radionuclides through the rock environment is retarded by their sorption on the rock matrix.

The GoldSim program (commercial license, version 12.0) was used to solve Task 9C and the "Cell pathway" component was selected. The use of this component is a volumetric approach, where the model area is represented by a network of interconnected cells (Cell Net). The density of the radionuclide in one cell can be varied both by diffusion and/or advection transport between adjacent cells, and by radioactive decay of the radionuclide itself, or of the parent radionuclide contained within the cell. The control equations for the "Cell pathway" component are described in Chapter 2 of Hokr et al. (2020, 2021).

The results of the comparison between two variants of a preliminary 1D radial model showed that the presence (position) of the monitoring borehole influenced the development of the activity in the injection borehole in all cases. In variant 1, the activity in the monitoring boreholes was also influenced by the position of the boundary condition c = 0, which was at an insufficient distance. A new model was used for the subsequent solution.

The task is solved in 2D, discretisation of the model area was solved separately for non-sorbing radionuclides (H-3, Cl-36) and for strongly sorbing radionuclides (Ba-133, Cs-134). In the case of the transport simulation of Na-22, such detailed discretisation was not as necessary as in the case of strongly sorbing radionuclides. On the other hand, the degree of discretisation used for non-sorbing radionuclides was insufficient. The discretisation for strongly sorbing radionuclides has a fundamental influence on model results, while maintaining the transport parameters. In the case of insufficiently detailed discretisation, different results are obtained for different types of discretisation of the model area. For this reason, the choice of discretisation was given great attention.

For non-sorbing radionuclides, two types of discretisation with different division between injection (IB) and monitoring (MB) boreholes (10 and 20 parts between IB and MB, respectively) were tested, with the results being very similar in both cases. The model area consists of 37 cells in the x-axis direction and 37 cells in the y-axis direction, and a total of 1 369 cells in the model. For highly sorbing radionuclides, suitable discretisation was searched until the spreading of the resulting radionuclide in the model region was dependent only on the change of model parameters. In the case of highly sorbing radionuclides, the model area does not contain the monitoring borehole due to the transport of the monitored nuclides over a significantly shorter distance than that between the boreholes. The geometry of the model region for non-sorbing radionuclides is shown in Figure D-3 and Figure D-4 and for the sorbing radionuclides in Figure D-5 and Figure D-6, and in table form in Table D-4 to Table D-6. Two variants, uniform and non-uniform, were tested for highly sorbing radionuclides. The uniform region consists of 41 cells in the x-axis direction and 41 cells in the y-axis direction, and a total of 1 681 cells in the model; the non-uniform region consists of 51 cells in the x-axis direction and 51 cells in the y-axis direction.

As the boundary condition on the outer sides of the model area, there is zero flow of radionuclides across the boundary; therefore, for non-sorbing radionuclides, an area extending far beyond the monitoring borehole is selected. Monitoring boreholes are located on the outer boundary of the model area in all of the models, in which an increase in radionuclide activity is monitored in order to confirm the validity of the selected boundary condition.

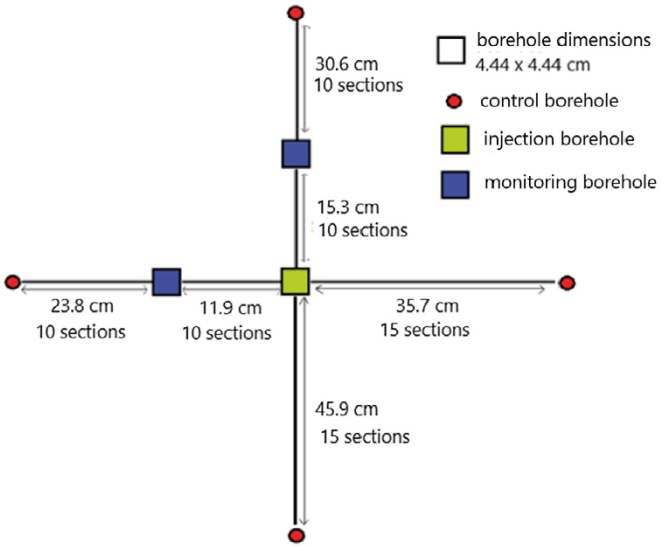

Figure D-3. *Representation of discretisation for non-sorbing radionuclides, coarser division of the model area between the monitoring and injection boreholes.*

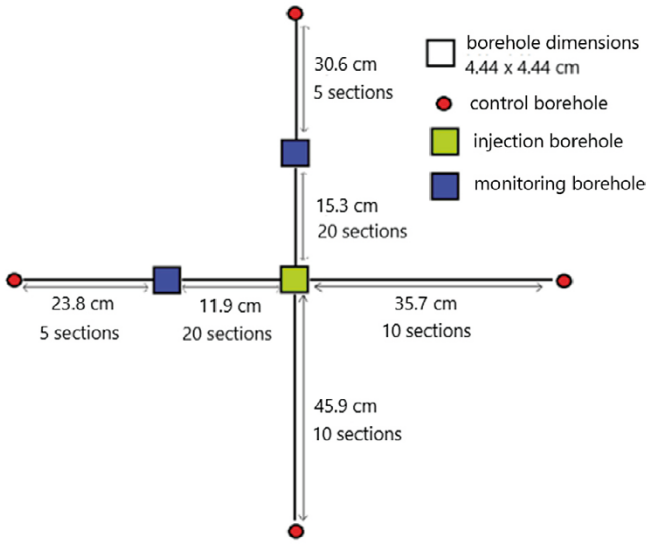

Figure D-4. *Representation of discretisation for non-sorbing radionuclides, finer division of the model area between the monitoring and injection boreholes.*

The injection and monitoring boreholes are simulated as square areas of 4.44 × 4.44 cm and 100 cm in length, the dimensions of a circular borehole with a diameter of 5.65 cm were converted to the foregoing dimensions of the square borehole, in order to maintain the same surface area, through with diffusion takes place, as in the case of the circular borehole.

Table D-4. Discretisation of the model area for non-sorbing radionuclides, values are in cm.

Non-sorbing radionuclides				
Model name	**Step in the x direction between IB – MB**	**Step in the y direction between IB – MB**	**Length of the area in the x direction**	**Length of the area in the y direction**
Coarser discretisation	1.19	1.53	80.28	100.68
Finer discretisation	0.595	0.765	80.28	100.68

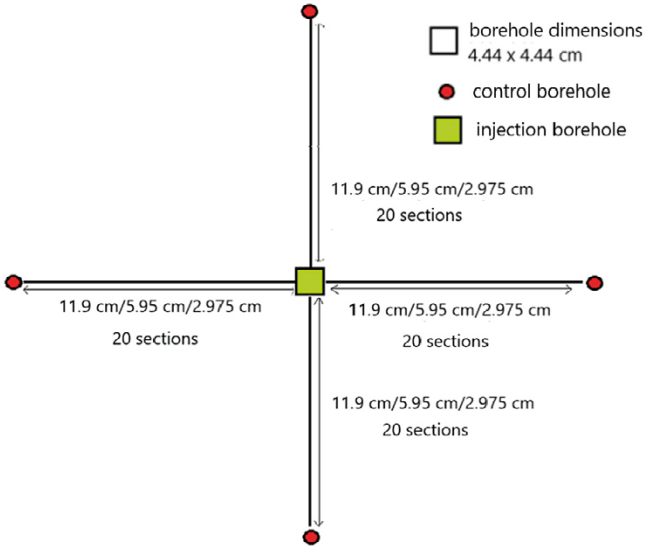

Figure D-5. *Representation of uniform discretisation for sorbing radionuclides, size and discretisation of the model area was made in three variants.*

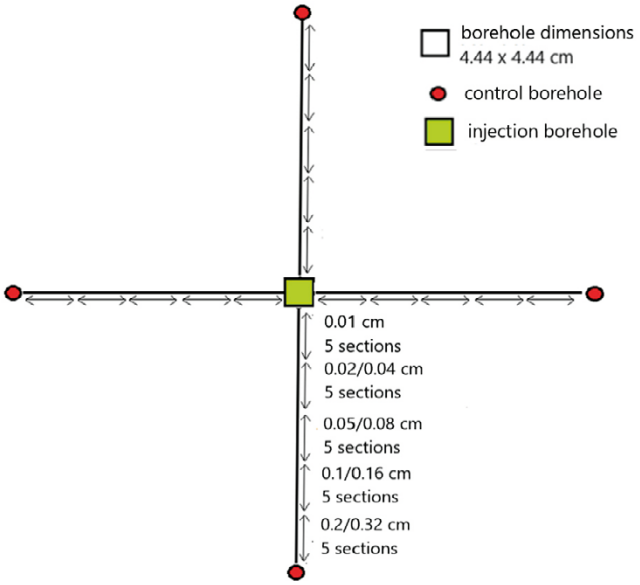

Figure D-6. *Representation of non-uniform discretisation for sorbing radionuclides, discretisation of the model area was made in two variants, the discretisation in the x-axis direction is the same as the discretisation in the y-axis direction.*

Table D-5. Uniform discretisation of the model region for sorbing radionuclides, values are in cm.

Sorbing radionuclides				
Model name	**Step in the x direction**	**Step in the y direction**	**Length of the area in the x direction**	**Length of the area in the y direction**
Coarser discretisation	0.595	0.595	28.24	28.24
Finer discretisation	0.2975	0.2975	16.34	16.34
The finest discretisation	0.149	0.149	10.39	10.39

Table D-6. Non-uniform discretisation of the model region for sorbing radionuclides, values are in cm.

Sorbing radionuclides				
Model name	**Step in the x direction**	**Step in the y direction**	**Length of the area in the x direction**	**Length of the area in the y direction**
Discretisation non-uniform_1	0.01/0.02/0.05/0.1/0.2	0.01/0.02/0.05/0.1/0.2	8.24	8.24
Discretisation non-uniform _2	0.01/0.04/0.08/0.16/0.32	0.01/0.04/0.08/0.16/0.32	10.54	10.54

After experience with Task 9A (Soler et al. 2019, Hokr et al. 2020, 2021), the porosity fraction, which assumes that not all pores are available for contaminant transport, was not used due to the fact that the results from ÚJV were not comparable with those of other research groups. In Task 9C, another porosity was only selected for Cl-36, similar to Task 9A. The model parameters used are shown in Table D-3 and commented on in the introduction (Section D1).

The results of the discretisation evaluation are presented as part of the comparison with other models (Section D3).

D2.3 Solution of CTU (GoldSim and analytical variant)

A model was created at the Faculty of Nuclear Sciences and Physical Engineering of CTU to represent the boreholes and the surrounding rock using a planar network of Cell elements. The network diagram is shown in Figure D-7. The network was designed to allow the simulation of five radionuclides with K_d values from the interval $K_d = [0, 0.001]\,[m^3 \cdot kg^{-1}]$. Therefore, we chose a non-equidistant grid refined around the boreholes where the highest concentrations of sorbing radionuclides can be expected. The grid was generated automatically, the volumes and diffusion areas of the elements corresponding to the boreholes were manually adjusted to agree with the cylindrical shape of the boreholes.

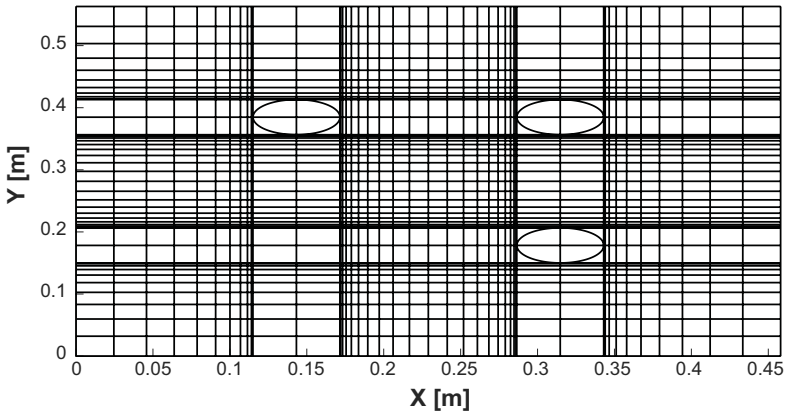

Figure D-7. *Planar 2D grid in GoldSim for Task 9C.*

The model does not allow the modelling of advective flow, which may have occurred due to possible pressure gradients between the boreholes during the experiment. A finer grid model was created as a control. The results and the comparison between the two types of discretisation showed that radionuclides H-3 and Cl-36 are able to break through the observation boreholes due to diffusion. On the contrary, sorbing radionuclides, especially Ba-133, Cs-134, do not break through and at the same time the transport results for the monitoring boreholes are sensitive to discretisation. Therefore, we proposed to use the 1D radial model around the injection borehole as an alternative for the sorbing radionuclides. To estimate the radius of the domain in which the 1D model around the injection borehole may be considered, we used an analytical solution to the diffusion transport problem of a hollow cylinder with boundary conditions defined inside and at the edge of the cylinder shell. The diffusion equation in the radial coordinate r may be written in a 1D form

$$\frac{\partial C}{\partial t} = \frac{1}{r}\frac{\partial}{\partial r}\left(rD\frac{\partial C}{\partial r}\right).$$

If on the inner surface ($x = a$) is maintained a constant concentration $C_a > 0$, and on the outer surface, ($r = b$), a constant zero concentration, $C_b = 0$, and if the concentration within the layer is initially ($t = 0$) zero, $C_0 = 0$, then the concentration in the layer can be expressed by the series (Huang and Yen 2002)

$$C(r,t) = C_a\left\{-\frac{ln\left(\frac{r}{b}\right)}{ln\left(\frac{b}{a}\right)} + \pi\sum_{n=1}^{\infty}\frac{J_0^2(b\alpha_n)[J_0(r\alpha_n)Y_0(a\alpha_n) - Y_0(r\alpha_n)J_0(a\alpha_n)]}{J_0^2(a\alpha_n) - J_0^2(b\alpha_n)}e^{-D\alpha_n^2 t}\right\},$$

where J_0 is the Bessel function of the first kind, Y_0 is the Bessel function of the second kind and α_n are the roots of the equation

$$J_0(a\alpha)Y_0(b\alpha) - J_0(b\alpha)Y_0(a\alpha) = 0.$$

For a stationary case, the 1D diffusion equation is simplified to

$$\frac{d}{dr}\left(r\frac{dC}{dr}\right) = 0.$$

The solution equation for the considered boundary conditions has the form

$$C(r) = -\frac{C_a \ln(r/b)}{\ln(b/a)}.$$

Flow through the layer in the stationary case has the shape

$$J_\infty = -D\frac{dC}{dr} = \frac{DC_a}{\ln\left(\frac{b}{a}\right)}\frac{1}{r}.$$

Flow through the outer surface ($r = b$) is

$$J_\infty^b = -D\left(\frac{dC}{dr}\right)_{r=b} = \frac{DC_a}{b\ln(b/a)}.$$

Based on a comparison of the analytical and numerical solutions, we designed and implemented a single non-equidistant 1D radial grid, which we used for all three of the considered radionuclides. The spacing of the elements over a length of 115 mm, starting at a radius of 28.25 mm, forms a geometric sequence. The step for the borehole with 100 elements is approximately 0.4 mm and the step at the opposite end is about 2.2 mm. Using this model we obtained results for Na-22, Ba-133 and Cs-134.

D3 Comparison of the solution with the reference variants

Processing of the models by the three research institutions on the basis of an agreed uniform choice of input data enabled a direct comparison of the results and mutual verification, and in certain cases, determination of hypotheses regarding the effects on the accuracy of the calculation. The presented results correspond to the final variants after they were corrected based on partial comparisons at the executive meetings, in particular by modifying the discretisation.

Figure D-8 shows the course of the concentrations for HTO in both the injection borehole and the detection boreholes. All of the results have a corresponding trend, slight deviations of the values are appropriate to the different processing of the geometry approximation (both GoldSim calculations) and to the differences in the numerical scheme. The lower increase in concentration in borehole 327 relative to borehole 324 corresponds to their different distances from the injection borehole.

Comparison of Cl-36 (Figure D-9) is only performed between GoldSim (ÚJV) and Flow123d (CTU), where anion exclusion was applied in the same way (uniform parameters). Similar to HTO, the differences are appropriate to the differences in geometry and the effects of the numerical scheme.

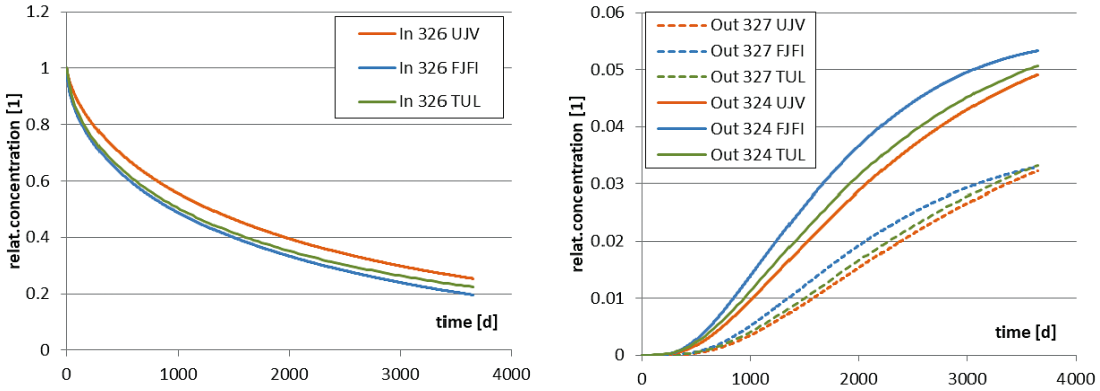

Figure D-8. *Comparison of results of individual investigators/software for the reference parameters – tracer HTO, course in the injection borehole on the left and in both detection boreholes on the right.*

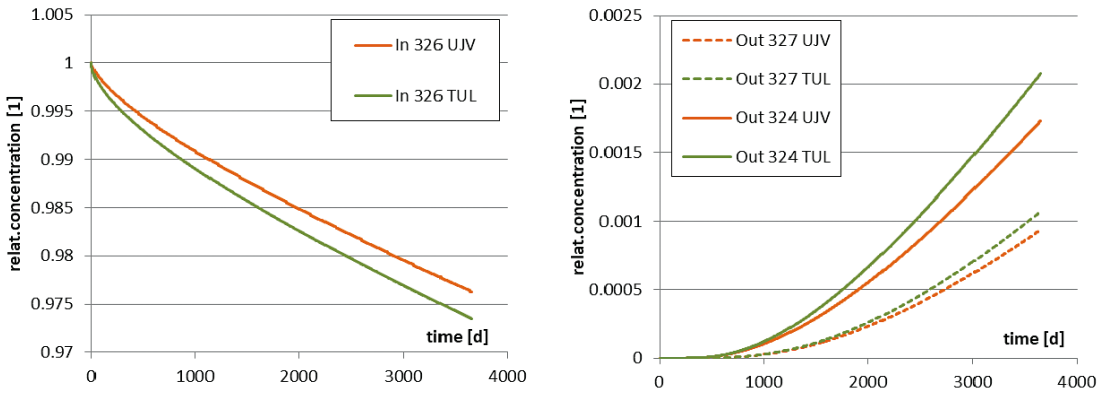

Figure D-9. *Comparison of results of individual investigators/software for the reference parameters – tracer Cl-36, course in the injection borehole on the left and in both detection boreholes on the right.*

The results for Na-22 are given only in the form of a concentration drop in the injection borehole (calculated concentrations in the detection or control borehole of the ÚJV model, were many orders of magnitude below the detection level of the laboratory measurements) in Figure D-10. In this case, an effect of discretisation around the injection borehole was already observed, similar to the previous tasks. The results with the finest discretisation are presented, in the case of the ÚJV model, in a uniform and non-uniform variant. The differences are mainly in the slope of the initial drop and may be explained precisely by the discretisation, given the delimitation by both variants of the ÚJV model. Despite certain differences, the models may be used with sufficient accuracy to interpret the measured data, which themselves are burdened with a comparatively large error. The results do not include the 1D model from CTU, which were likely affected by the external boundary condition.

For strongly sorbing tracers Ba-133 and Cs-134 (Figures D-11 and D-12), the differences between the models are significantly larger. In the long-term, the results fit into up to one order of magnitude range. On the other hand, the curves form an almost systematic series and it can therefore be assumed that this is a quantitatively escalating phenomenon, not a "gross" error in the input data. This again indicates the influence of discretisation. Considering that Flow123d uses the same discretisation in all cases, the agreement with the fully refined 1D model is sufficient.

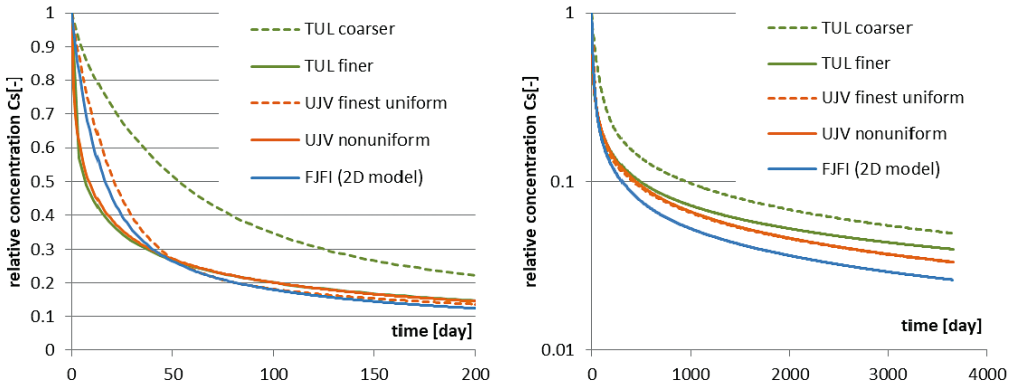

Figure D-10. *Comparison of results of individual investigators/software for the reference parameters – tracer Na-22, course in the injection borehole in two different axis scales.*

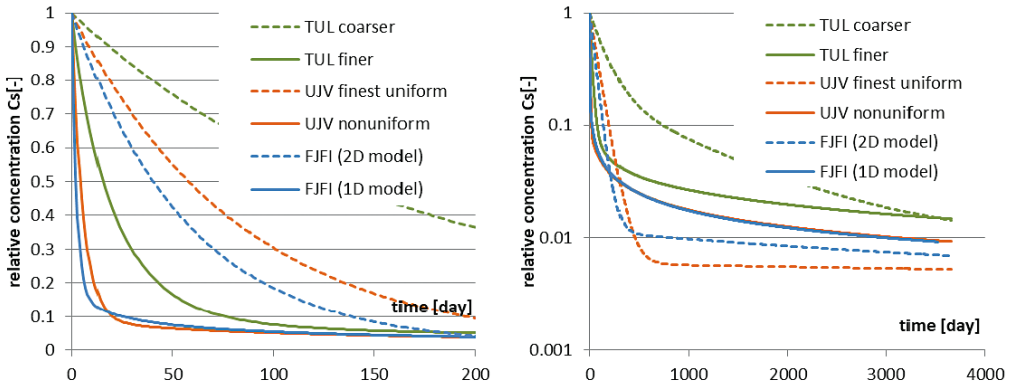

Figure D-11. *Comparison of results of individual investigators/software for the reference parameters – tracer Ba-133, course in the injection borehole.*

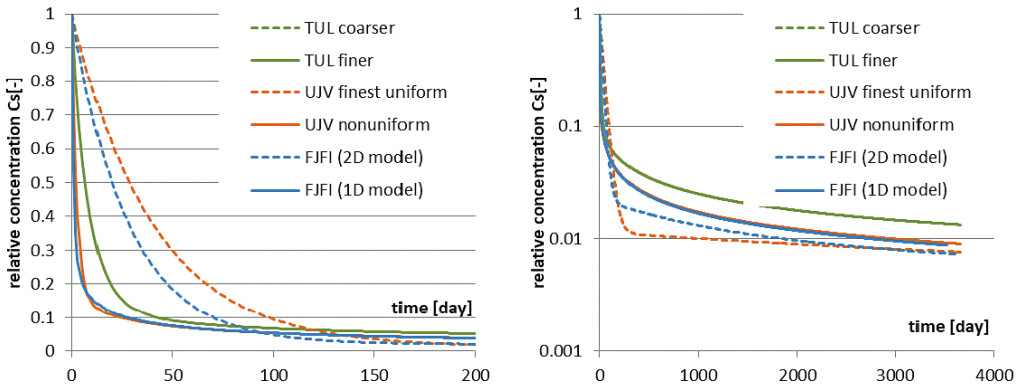

Figure D-12. *Comparison of results of individual investigators/software for the reference parameters – tracer Cs-134, course in the injection borehole.*

A partial comparison of the influence of discretisation was performed in the framework of the models of the individual investigators. In the ÚJV model, the H-3 and Cl-36 variants were finer and coarser, and the differences were only very small in the source and detection boreholes. Figures D-13, D-14 and D-15 show the fundamental influence of the discretisation of the model region for sorbing radionuclides. Although the size of the model area in the finest discretisation and discretisation non-uniform_2 versions is similar, a more detailed division around the monitoring borehole in the discretisation non-uniform_2 version yields different results than the uniform division in the finest discretisation version. When comparing the model versions discretisation non_uniform_1 and discretisation non_uniform_2 (Table D-6), it is clear that by further decreasing the step size of the division of the model area no other results are obtained, so the discretisation level in the variant discretisation non-uniform_2 is sufficient. This was confirmed for other tracers, Ba-133 and Cs-134.

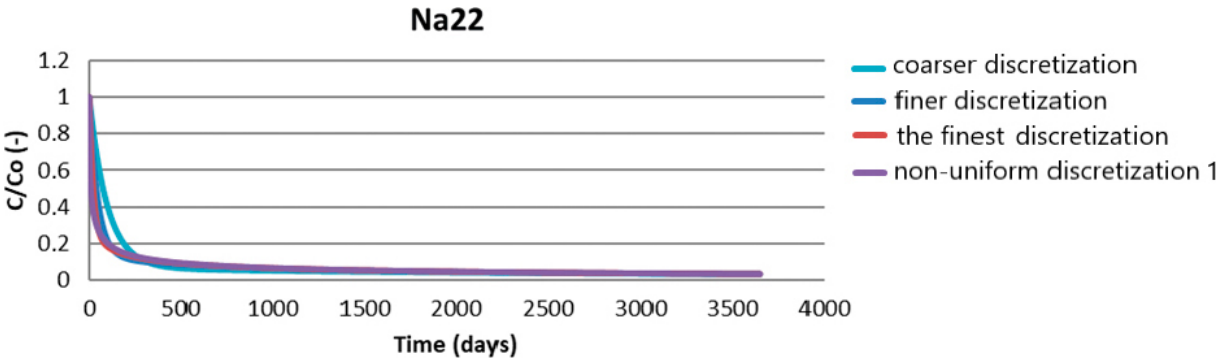

Figure D-13. *Development of Na-22 activity in the injection borehole for the four considered types of discretisation of the ÚJV-GoldSim model.*

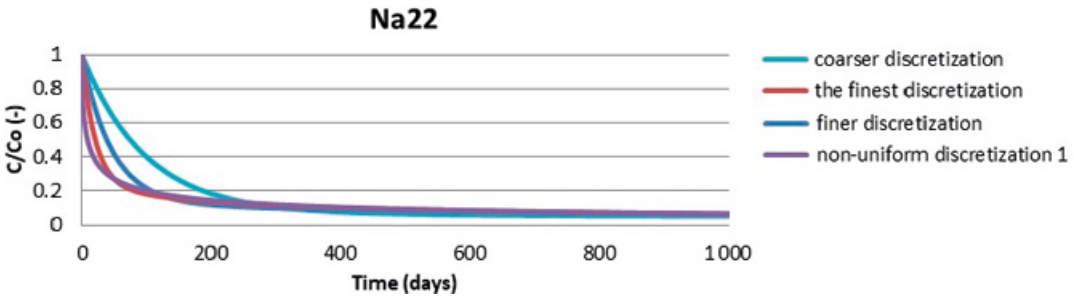

Figure D-14. *Detail of the development of Na-22 activity in the injection borehole for the four considered types of discretisation of the ÚJV-GoldSim model.*

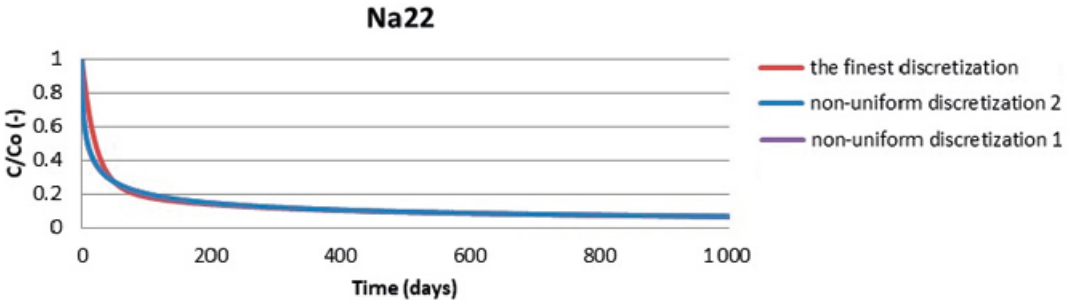

Figure D-15. *Detail of the development of Na-22 activity in the injection borehole according to the ÚJV-GoldSim model – comparison of uniform and non-uniform division of the model area, curves for the non-uniform division of the area overlap.*

D4 Analysis of the influence of advection

Due to the pressure gradient documented between the experimental sections of the individual boreholes, it can be assumed that in addition to diffusion and sorption, advection will also be an important transport process.

Three simulations were performed, two based on an artificial constant pressure gradient in the given direction, and the third based on pressure differences taken from the task description. All three simulations were performed for the conservative tracer HTO.

In the first simulation, the pressure gradient was set so that the advection was from the injection borehole to the monitoring boreholes. During the first year of the simulation period, the pressures were balanced, for the remainder of the simulation (up to 10 years) a boundary flow condition in the form of a piezometric head equal to 10 m was prescribed at the boundary of the injection borehole. This corresponds to a pressure difference of 0.1 MPa. The development of the relative activity in the individual borehole is shown in Figures D-16 and D-17.

It is apparent from the results that after the "switching on" the advection, the transport of the tracer towards the monitoring borehole will be significantly accelerated.

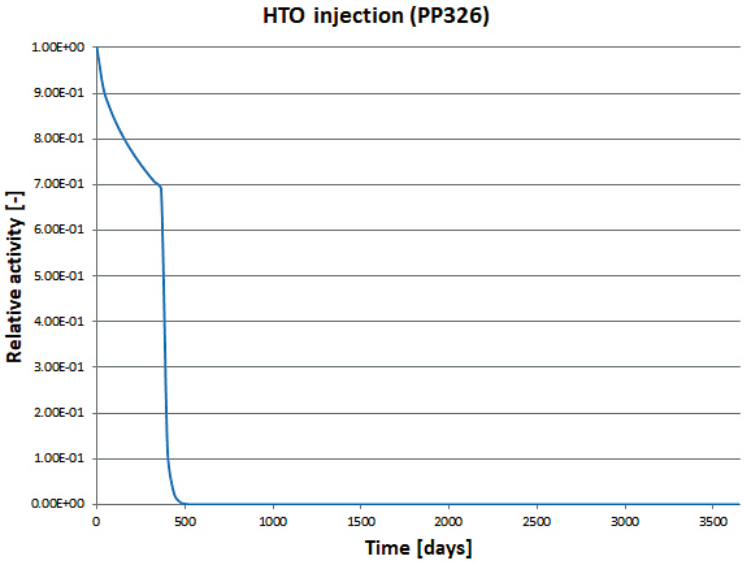

Figure D-16. *Task 9C – Flow123d – influence of pressure gradient – artificial pressure gradient – advection towards the injection borehole – dependence of relative activity on time in the injection borehole.*

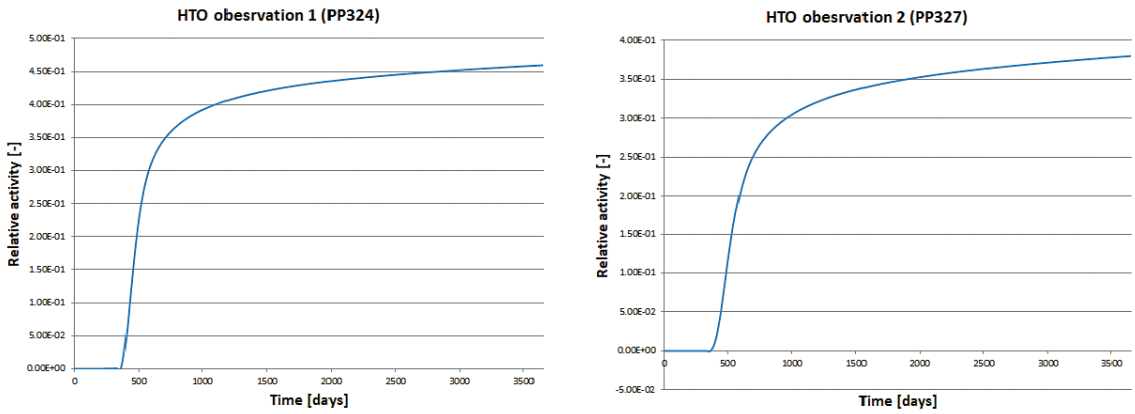

Figure D-17. *Task 9C – Flow123d – influence of pressure gradient – artificial pressure gradient – advection towards the injection borehole – dependence of relative activity on time in the monitoring boreholes.*

In the second simulation, the pressure gradient was set so that the advection was from the monitoring boreholes towards the injection borehole. During the first year of the simulation period, the pressures were balanced, for the remainder of the simulation (up to 10 years) a boundary flow condition in the form of a piezometric head of 10 m was prescribed for the monitoring borehole. This corresponds to a pressure difference of 0.1 MPa. The development of the relative activity in the individual boreholes is shown in Figures D-18 and D-19.

It is apparent from the results that after the advection has been "switched on", the direction of migration of the tracer back to the injection borehole will quickly reverse. This is also documented by the visualisation of the concentration field in Figure D-20.

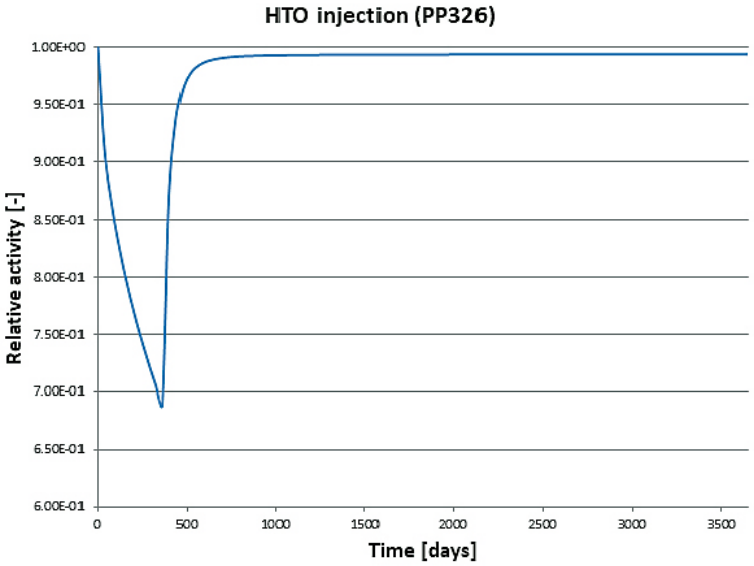

Figure D-18. *Task 9C – Flow123d – influence of pressure gradient – artificial pressure gradient – advection towards the injection borehole – dependence of relative activity on time in the injection borehole.*

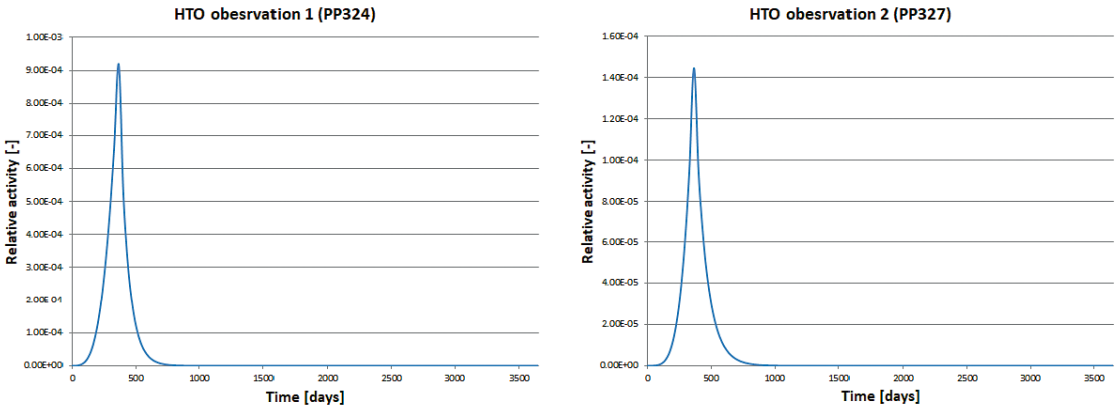

Figure D-19. *Task 9C – Flow123d – influence of pressure gradient – artificial pressure gradient – advection towards the injection borehole – dependence of relative activity on time in the monitoring boreholes.*

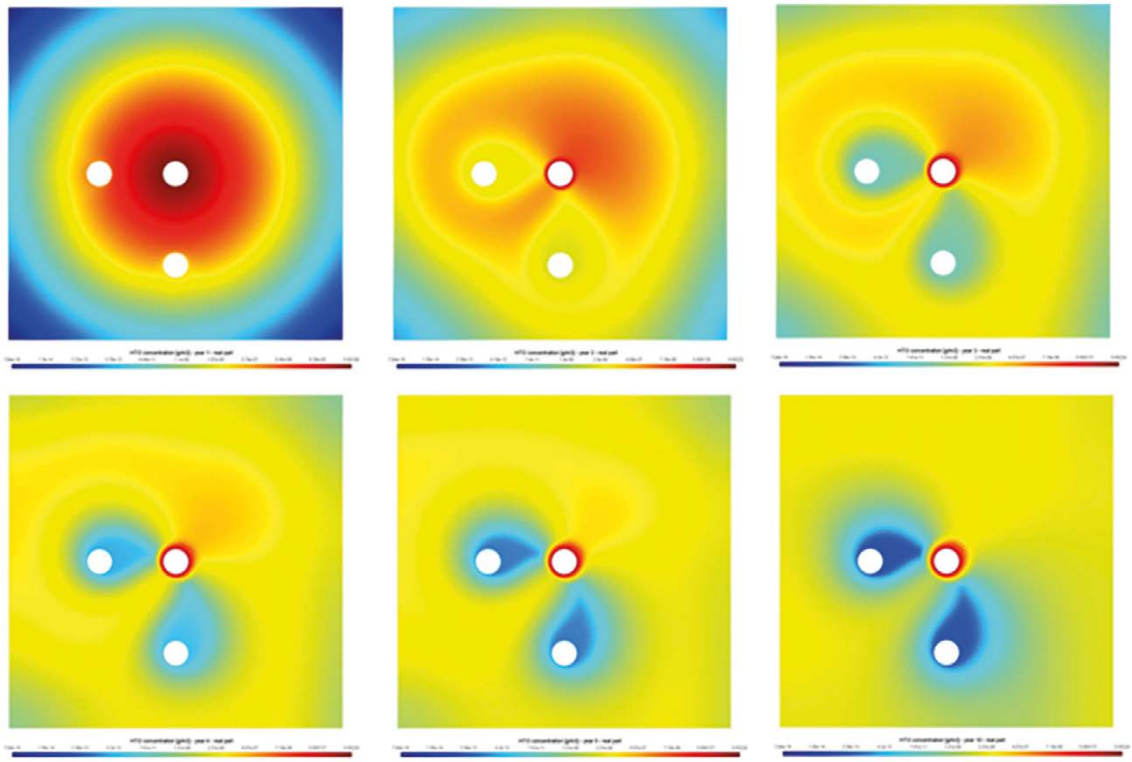

Figure D-20. *Task 9C – Flow123d – influence of pressure gradient – artificial pressure gradient – advection towards the injection borehole – development of the concentration field (in time 1, 2, 3, 4, 5 and 10 years).*

In the third simulation, the pressure gradient was given by the measured data (pressures in the boreholes), which was part of the task description. The model in each step adjusts the boundary flow conditions based on the measured data (Figure D-21). In the times between the two measurements, the pressures are calculated by the linear interpolation method. The simulation period was shortened to the range of measured data (629 days).

The development of the relative activity in the individual boreholes is shown in Figures D-22 and D-23. As a result, as the direction of the pressure gradient changes, the direction of migration of the tracer also changes.

To conclude, the pressure gradient and the advection it induces may have a significant effect on the simulation results. However, it is debatable whether the measured borehole pressures reflect the actual hydraulic conditions at the site of the experiment or whether this is an experimental artefact.

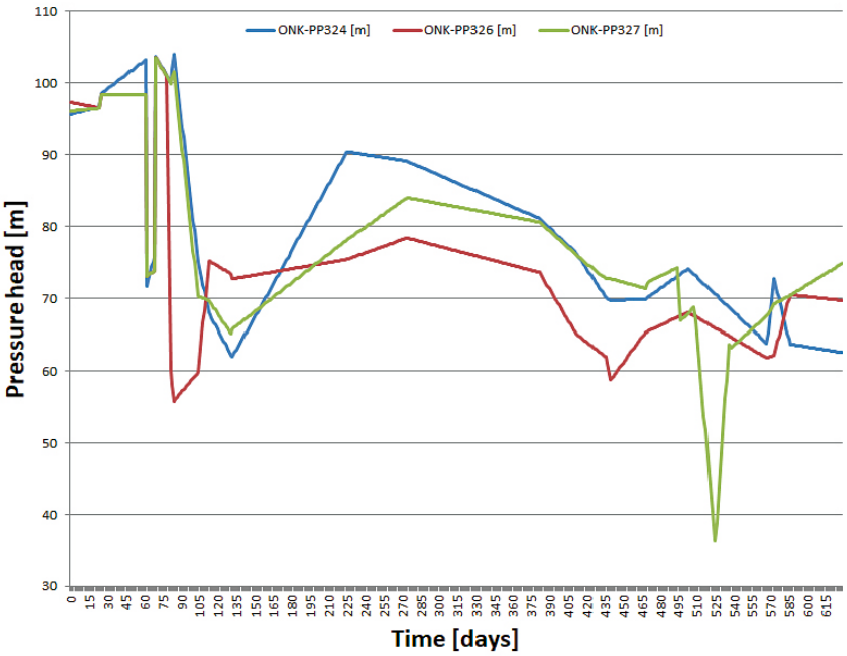

Figure D-21. *Task 9C – Flow123d – influence of pressure gradient – measured pressure gradient – development of boundary conditions of flow dependence of the relative activity on time in the monitoring boreholes.*

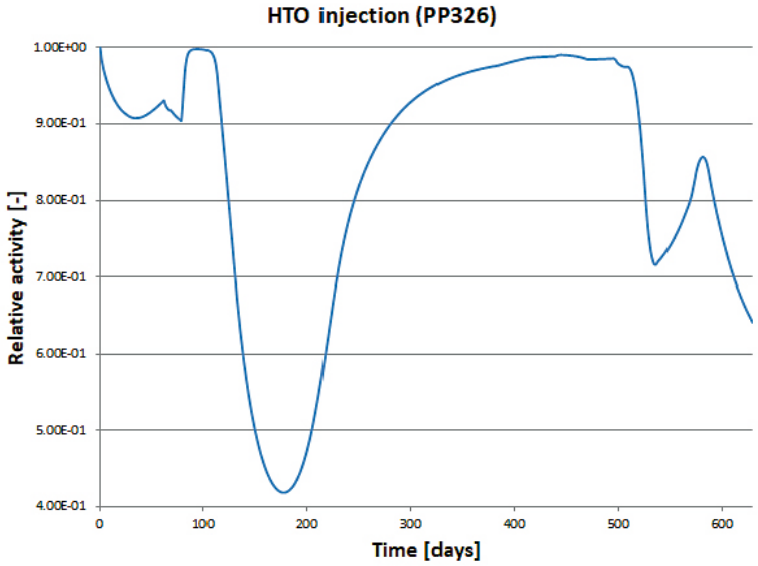

Figure D-22. *Task 9C – Flow123d – influence of pressure gradient – measured pressure gradient – dependence of the relative activity on time in the injection boreholes.*

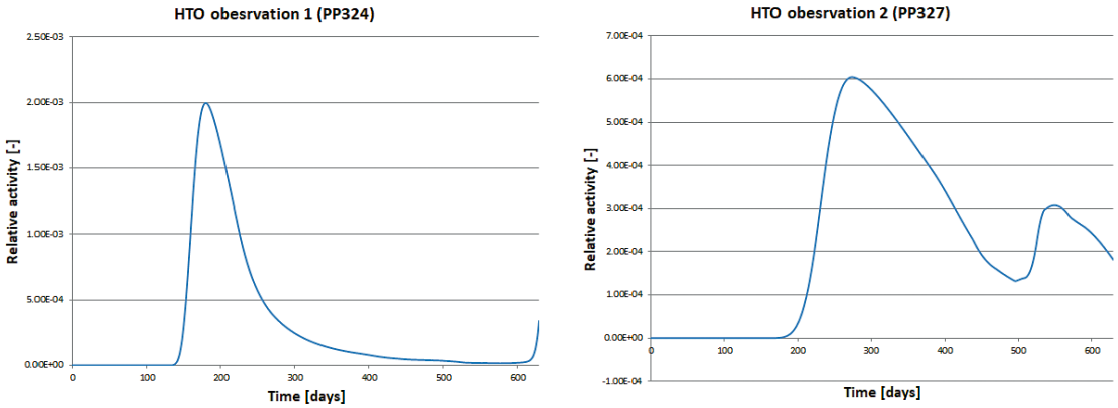

Figure D-23. *Task 9C – Flow123d – influence of pressure gradient – measured pressure gradient – dependence of the relative activity on time in the monitoring boreholes.*

D5 Inverse model in Flow123d (TUL)

The aim of the inverse model was to achieve an agreement between the results of the simulation and the measured data by changing the parameters. Specifically, the time courses of concentrations of individual tracers were evaluated, especially in the injection borehole. In the monitoring boreholes the concentrations of some of the tracers did not reach measurable values during the duration of the experiment; therefore, agreement between the simulation and the measurements is evaluated only to a limited extent.

Compared to the blind prediction described above, several changes were made to the model. These were partly motivated by an update to the task description and partly by the need to modify the model to make it more feasible and flexible to calibrate its parameters. These changes included:

- Update of the water (solution) volumes in the experimental sections (according to new version of the task description):
  - ONK-PP324 (monitoring No. 1): 240 ml,
  - ONK-PP326 (injection): 254 ml,
  - ONK-PP327 (monitoring No. 2): 262 ml.
- A new computer mesh considering the disturbance zone around each borehole.
- Implementation of sampling – during the course of the experiment, significant amounts of the solution were taken from the experimental sections, which are replaced by pure water, which has an obvious impact on the simulation results.
- Implementation of water/solution exchange in borehole ONK-PP324 at 1 028 days (for HTO and Cl-36, not used elsewhere).

Figure D-24 shows the updated computational mesh. It consists of 38 868 triangular elements with the finest discretisation being near the boreholes. The figure shows the extent of the disturbance zone under consideration, which is 5 cm from the wall of each borehole. The mesh step sizes are 1 mm at the wall of the borehole, 2.5 mm at the BDZ interface and 10 mm in the rest of the model.

To calibrate the model to the measured data, the concept of a linear decrease in porosity from the borehole wall towards the interface of the BDZ/intact rock was adopted. Figure D-25 shows the distribution of porosity in the model area as from the manual calibration of the model.

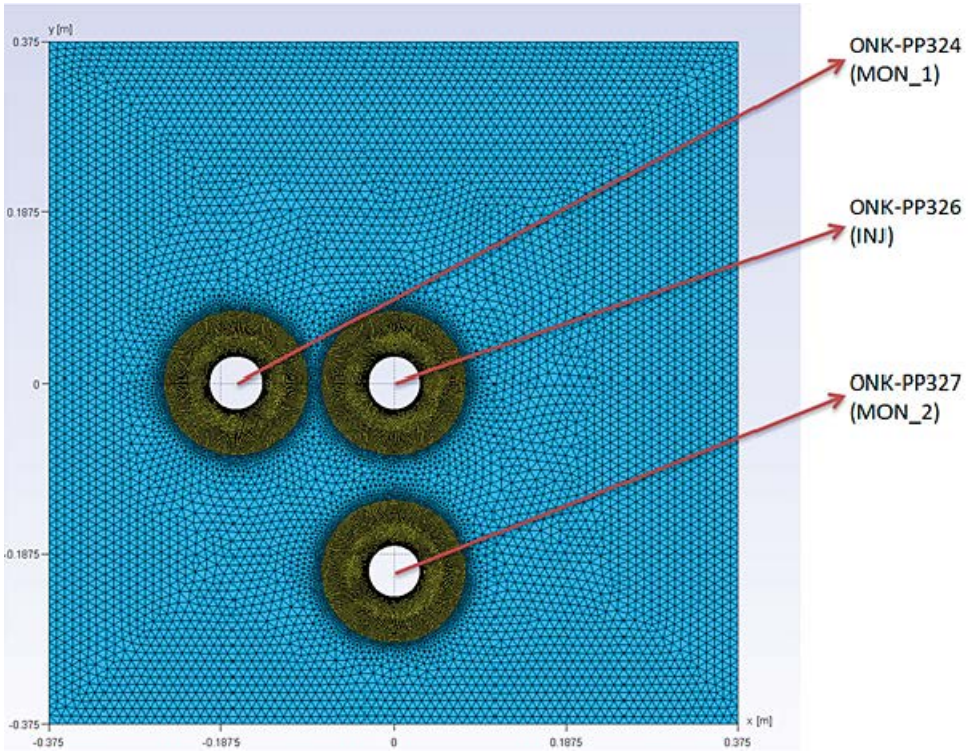

Figure D-24. *Task 9C – Flow123d – updated computational mesh for the inverse model.*

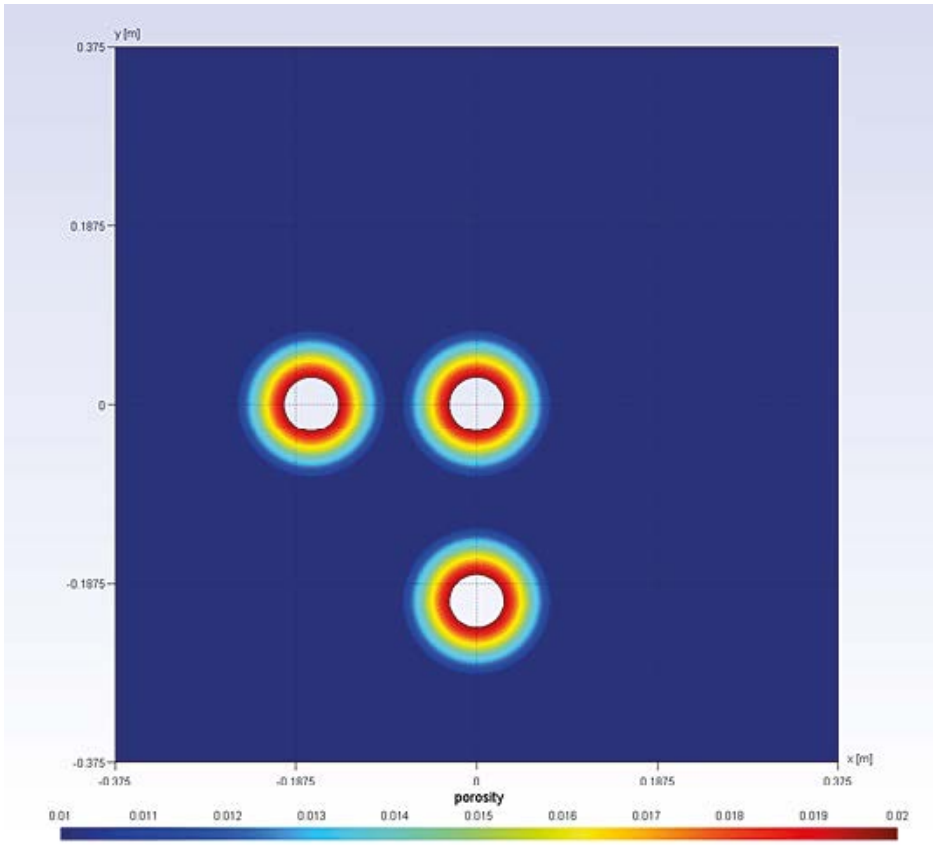

Figure D-25. *Task 9C – Flow123d – distribution of porosity in the model area.*

Other model parameters that can be used to calibrate the measured data are effective diffusivity, which also depends on porosity, and linear sorption distribution coefficient (except for the conservative HTO and Cl-36 tracers). For clarity, the parameters resulting from the manual model calibration together with the parameters used in the blind prediction are shown in Table D-7. For effective diffusivity in the disturbance zone, the maximum value (for the borehole walls) is always given in the table, the minimum value is the effective diffusivity in the intact rock. The character of the decrease follows the decrease in porosity, but not linearly, since the coefficient of effective diffusivity in Flow123d is proportional to the porosity powered by $\frac{4}{3}$. The table shows that in addition to the accepted concept of the linear decrease in porosity with depth, which also implies minor changes in the effective diffusivity, the calibration coefficient was primarily the distribution coefficient of linear sorption, which changed by several orders in both directions (compared to the values used in the blind prediction).

Figure D-26 shows the results of the inverse model for HTO. The figure shows that by using the parameters given in Table D-7, a very good agreement was achieved in the injection borehole. On the contrary, the simulated concentrations in the monitoring boreholes are significantly higher than the measured concentrations. Figure D-27 shows the results of the model with the same parameters except for effective diffusivity in the intact rock, which is forty times lower. A better agreement is seen especially in monitoring borehole PP327, but the agreement in the injection borehole is worse. It is evident from the figure (also as in Figure D-28) that the current model concept does not sufficiently capture the measured profiles in the monitoring boreholes since the measured values show an earlier onset in borehole PP327, which is further away from the injection borehole than borehole PP324. Moreover, it is situated perpendicular to the direction of foliation; a non-isotropic tensor of the coefficient of molecular diffusion, which would accentuate the PP326–PP327 direction, would be difficult to justify.

Figure D-28 shows the results of the inverse model for Cl-36. Again, we see a good agreement in the injection borehole and a poor agreement in the monitoring boreholes. The same conclusions discussed in the previous paragraph apply here.

Figure D-29 shows the results of the inverse model for Na-22. The agreement in the injection borehole is relatively good, with the curve representing the simulation results decreasing more sharply than the measurement curve. In order to achieve such an agreement, it was necessary to reduce the linear sorption distribution coefficient by three orders of magnitude. Again, agreement in monitoring boreholes is not good; the curves representing the results of the simulations clearly fluctuate, which documents the effect of sampling very well.

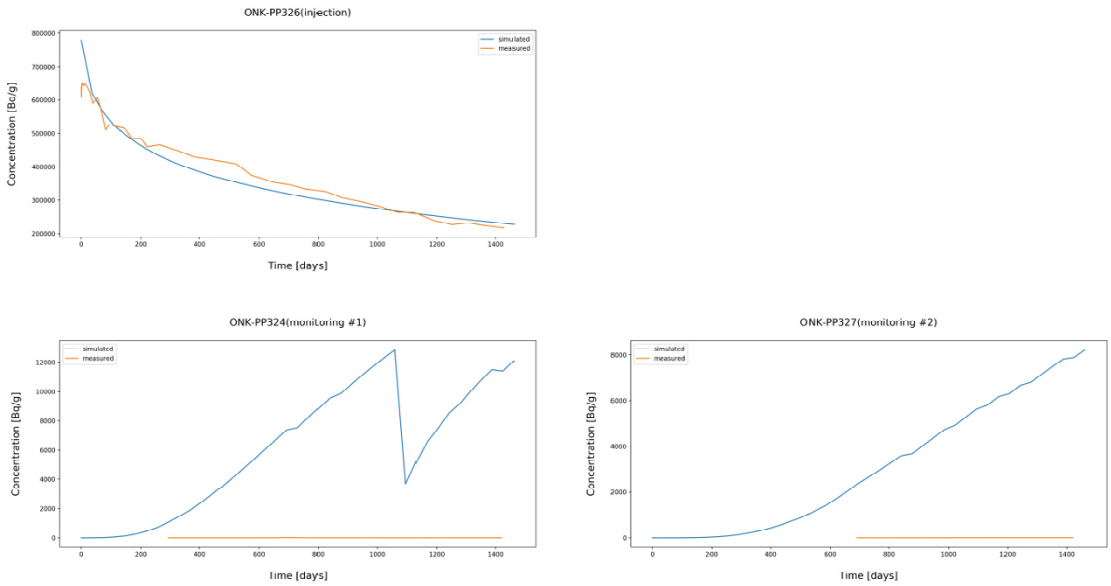

Figure D-26. *Task 9C – Flow123d – results of the inverse model, HTO.*

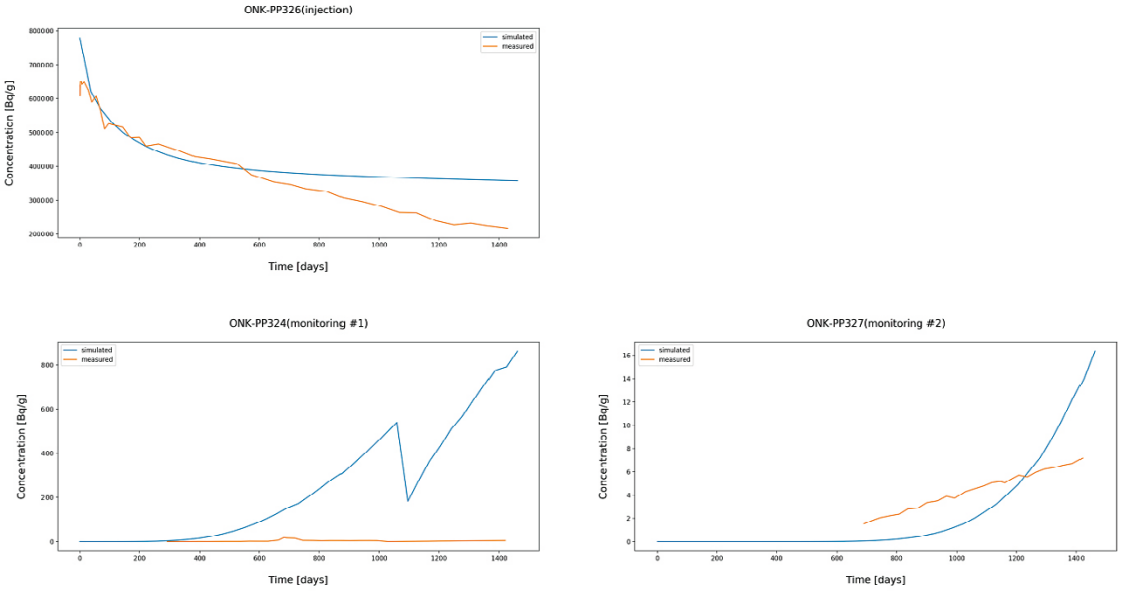

Figure D-27. *Task 9C – Flow123d – results of the inverse model, HTO variant 2.*

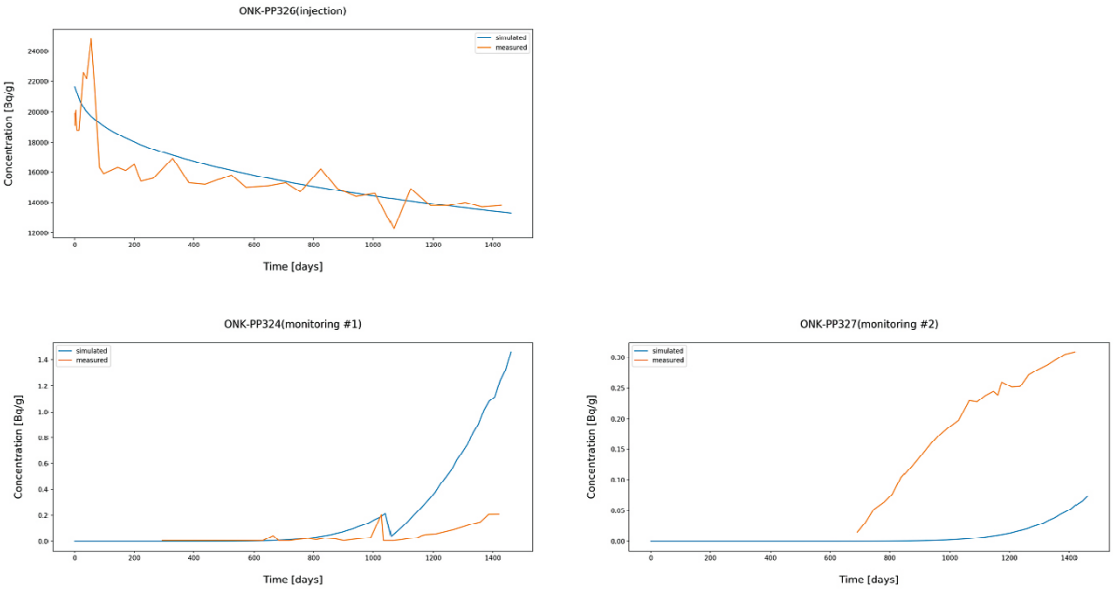

Figure D-28. *Task 9C – Flow123d – results of the inverse model, Cl-36.*

For Ba-133 and Cs-134, no activity was detected in the monitoring boreholes during the experiment. Similarly, there was no activity in the model outputs. Therefore, only the profiles in the injection borehole are depicted for these tracers, in Figure D-30 for Ba-133 and in Figure D-31 for Cs-134, and in both cases for clarity with the logarithmic scale of the y-axis. In both cases, it is apparent that the simulated profile has an onset significantly higher than the measured profile (this is indeed true for all five tracers). The initial value of the simulated concentration in the injection borehole is calculated from the known volume of the experimental section and the known value of the injected amount (activity) of the tracer. If we take these measurements as a paradigm, then the simulated curve cannot look otherwise. The measured curves would then be burdened with an experimental error, the origin of which we can only guess. In the case of Ba-133, the difference between the initial values of the profiles is not an order of magnitude; For Cs-134, however, the difference is large, so the aim of the calibration was to capture the trend, not to achieve full agreement.

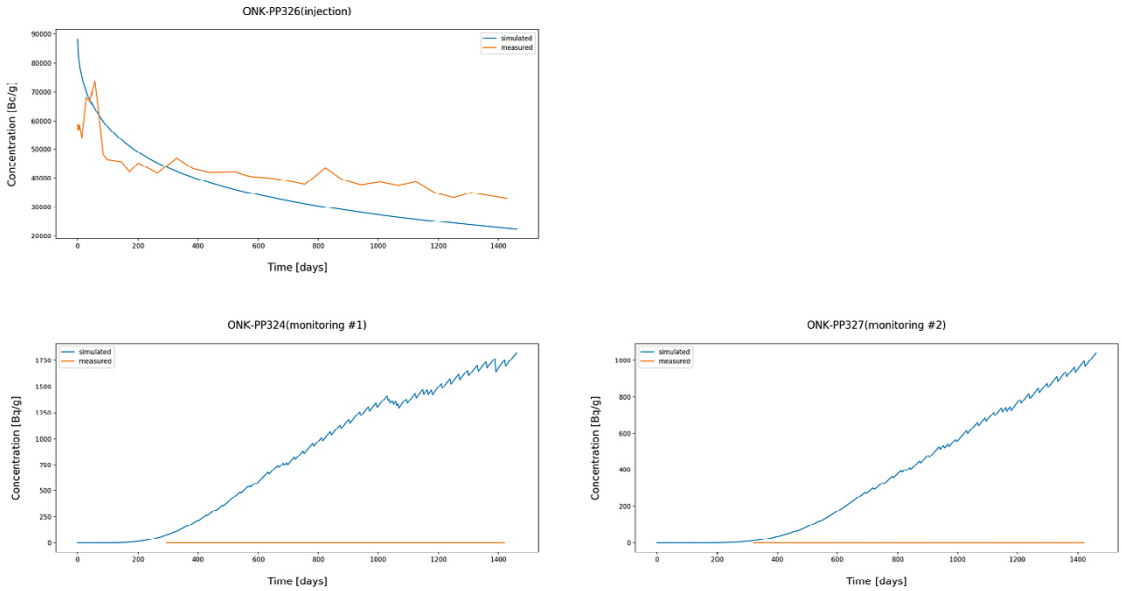

Figure D-29. *Task 9C – Flow123d – results of the inverse model, Na-22.*

In conclusion we can summarise that the chosen model concept is not able to reflect the measured profiles in the monitoring boreholes (for the reasons described above). In the injection borehole, the model can capture the trend, but the question of the initial concentration value remains open, whereby the measured value does not correspond to the amount injected. Alternatively, the model concept could consider the first measured value as the initial concentration value. The resulting parameters of the calibrated model would surely be different. Finally, it is worth mentioning that a similar combination of parameters could achieve similar model results. The selected parameters (see Table D-7) are physically backed – realistic.

Table D-7. Task 9C – Flow123d – parameters resulting from calibration together with the blind prediction parameters.

Tracer	Porosity [-]	D_e BDZ max [m^2/s]	D_e rock [m^2/s]	K_D BDZ [m^3/kg]	K_D rock [m^3/kg]
Original (blind prediction)					
HTO	0.0094	-	3.90E−13	-	0
Cl-36	1.75E−4	-	5.00E−15	-	0
Na-22	0.0094	-	4.65E−13	-	0.0013
Ba-133	0.0094	-	3.00E−13	-	0.06
Cs-134	0.0094	-	3.00E−13	-	0.031
Modified (result of the manual calibration process)					
HTO	0.01–0.02	1.07E−12	4.24E−13	0	0
Cl-36	0.01–0.02	1.26E−13	5.02E−14	0	0
Na-22	0.01–0.02	1.27E−12	5.05E−13	1.3E−6	1.3E−6
Ba-133	0.01–0.02	8.20E−13	3.25E−13	0.6145	0.0307
Cs-134	0.01–0.02	8.20E−13	3.25E−13	0.6191	0.03095

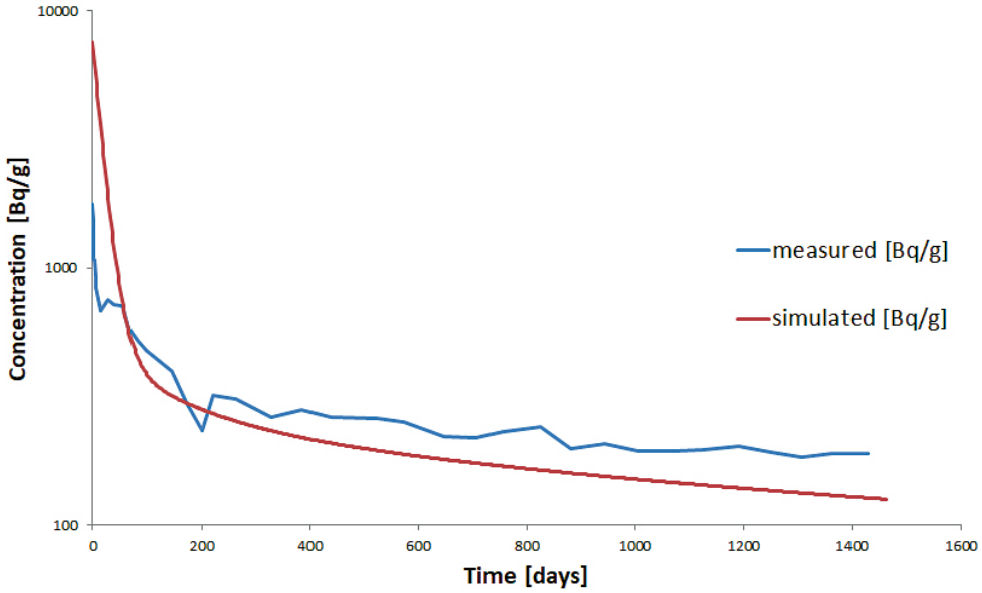

Figure D-30. *Task 9C – Flow123d – results of the inverse model, Ba-133.*

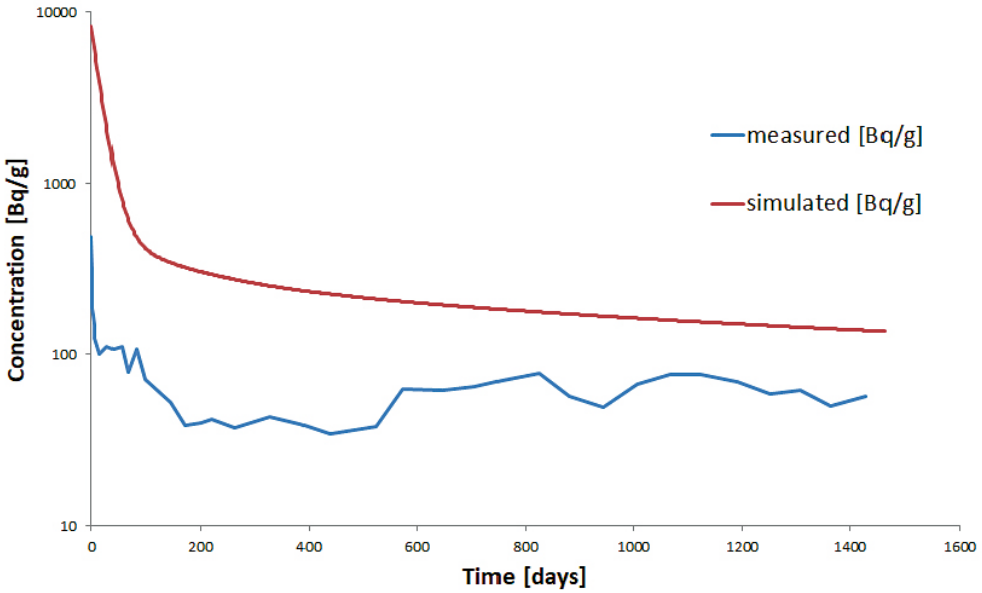

Figure D-31. *Task 9C – Flow123d – results of the inverse model, Cs-134.*

D6 Inverse model in GoldSim (ÚJV)

After the experimental data were released by the organiser, inverse modelling was performed, where the model parameters were changed in order to achieve the best agreement between the model and the measured results. Discretisation marked “finer discretisation” was used for the non-sorbing nuclides, (Table D-4, Figure D-4, and the discretisation of the sorbing radionuclides was marked “non-unifrom_1” (Table D-6, Figure D-6). The parameters of the model area remained homogeneous; the model area is not divided into closer and more distant zones around the boreholes.

In addition to the calibration of material parameters, attention was also paid during the inverse modelling to a critical evaluation of the measured data. In many cases (especially in the absence of data from the monitoring boreholes), similar model curves were achieved for different combinations of model parameters. The resulting model parameters are shown in Table D-8, with other possible combinations in Table D-9.

Table D4-8. Final calibrated parameters.

	Porosity	Kd (m^3/kg)	De (m^2/s)	Dw (m^2/s)
H-3	9.40E−03	0.00E+00	7.00E−13	2.30E−09
Na-22	9.40E−03	5.00E−05	9.00E−14	1.33E−09
Na-22 cropped	9.40E−03	9.00E−05	3.00E−14	1.33E−09
Cl-36	9.40E−03	0.00E+00	2.00E−13	2.03E−09
Cl-36 cropped	9.40E−03	0.00E+00	3.50E−14	2.03E−09
Ba-133	9.40E−03	2.00E−03	1.47E−13	1.69E−09
Cs-134	9.40E−03	5.00E−03	3.00E−13	2.07E−09

Table D4-9. Variant model parameters.

	Porosity	Kd (m^3/kg)	De (m^2/s)	Dw (m^2/s)
Na-22 var 1	9.40E−03	5.00E−05	9.00E−14	1.33E−09
Na-22 var 2	9.40E−03	9.00E−05	9.00E−14	1.33E−09
Na-22 var 3	9.40E−03	1.00E−05	2.00E−13	1.33E−09
Na-22 cropped var 1	9.40E−03	9.00E−05	3.00E−14	1.33E−09
Na-22 cropped var 2	9.40E−03	1.00E−05	6.00E−14	1.33E−09
Ba-133 var 1	9.40E−03	2.00E−03	1.47E−13	1.69E−09
Ba-133 var 2	9.40E−03	3.00E−03	1.47E−13	1.69E−09
Cs-134 var 1	9.40E−03	5.00E−03	3.00E−13	2.07E−09
Cs-134 var 2	9.40E−03	3.10E−02	5.00E−14	2.07E−09

D6.1 H-3

A comparison between the measured and model results including the actual measured results is given in Figures D-32 to D-35. Figure D-32 shows that there is a sharp decrease in activity in the injection borehole during the first few hours. This decrease is attributed to the geometry of the experiment, it is not a property of the rock, which is characterised by the calibrated material parameters. Therefore, the data were cropped, and the initial activity was lowered by this cropping, so the initial amount injected is not 891 000 Bq/g, but 647 000 Bq/g.

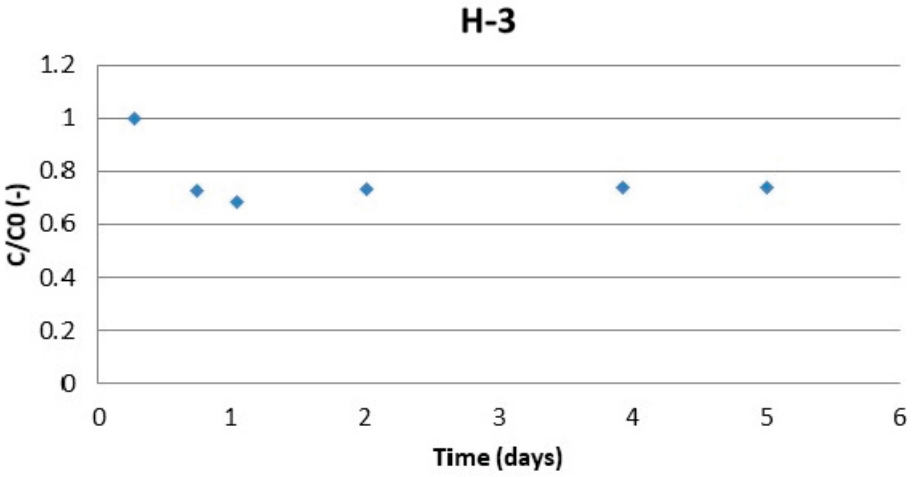

Figure D-32. *Original measurement data, steep decrease during the first day attributed to the setup of the experiment.*

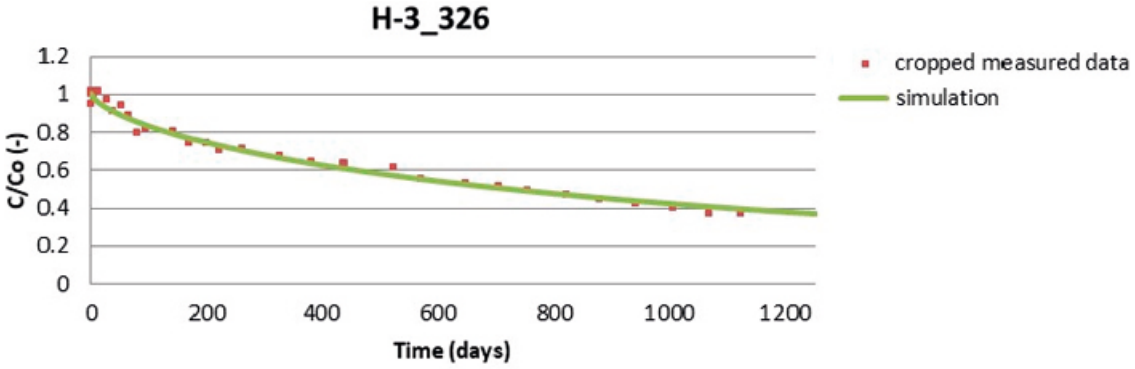

Figure D-33. *Development of activity in the injection borehole.*

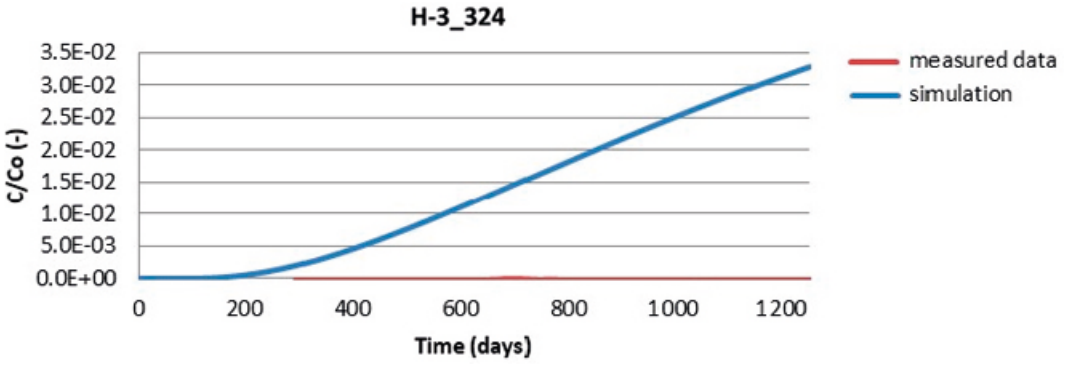

Figure D-34. *Development of activity in the monitoring borehole.*

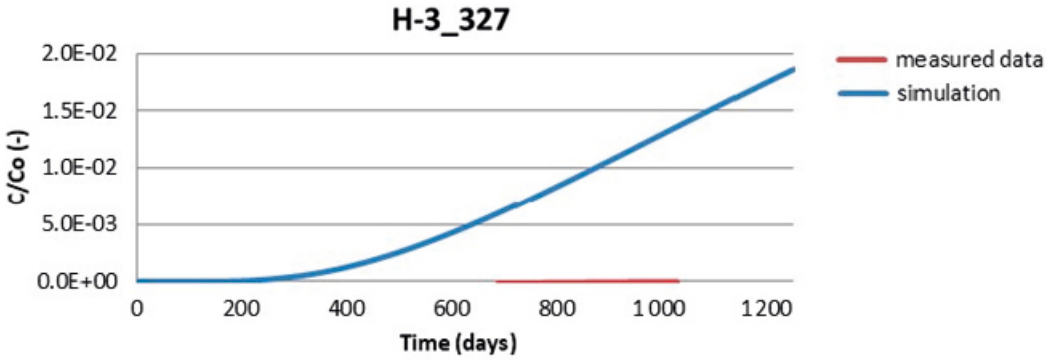

Figure D-35. *Development of activity in the monitoring borehole.*

D6.2 Na-22

Two variants of measured data were simulated for Na-22. Firstly, the original published data (Figure D-36) and secondly, the cropped data (Figure D-37). The graphs showing the uncropped data show an experimental artefact where the activity in the injection borehole during the measurement increases above the initial injected activity. Therefore, in the second (cropped) variant, the first 80 days during which this artefact occurred were neglected and the initial activity was set to an activity value of 80 days, i.e. an injected amount of 48 000 Bq/g (compared to the initial published value of 58 900 Bq/g). In both variants, we also faced a greater degree of freedom in the task due to the absence of data from the monitoring boreholes, whereby we obtained very similar model curves when combining the various parameters.

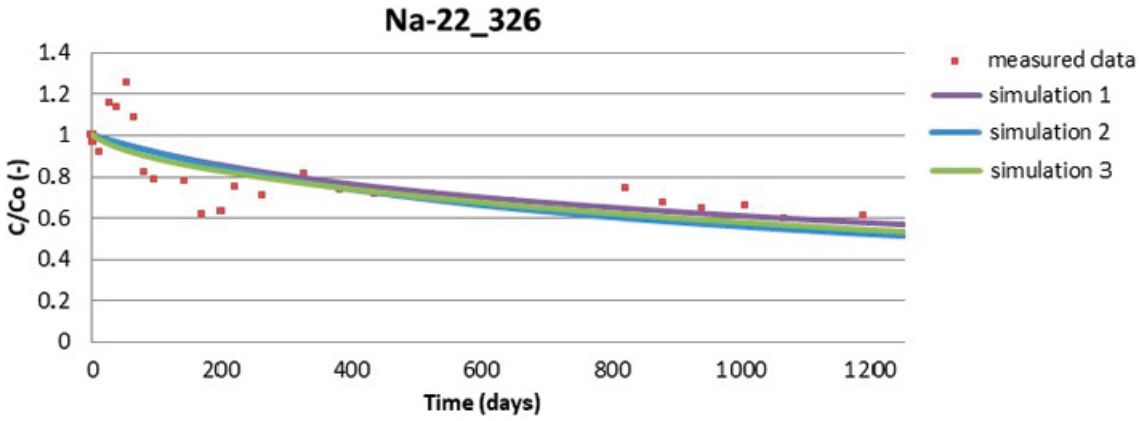

Figure D-36. *Agreement between the measured and model results for the originally published data for the different combinations of model parameters.*

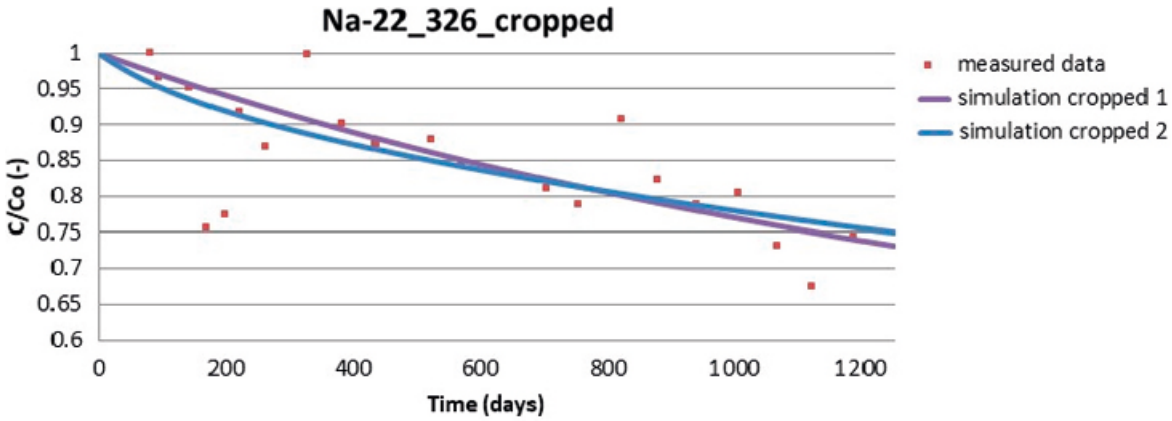

Figure D-37. *Agreement between the measured and model results for the cropped data for the different combinations of model parameters.*

D6.3 Cl-36

For Cl-36, there was the same problem with greater activity in the injection borehole during measurement than the originally injected activity as for Na-22. Therefore two sets of data were also used, the originally published and cropped data, with an initial injection amount of 16 300 Bq/g (compared to the originally published value of 19 900 Bq/g). The agreement between the measured and model results for the originally published data is shown in Figures D-38, D-40 and D-41, and the agreement for the cropped data is shown in Figures D-39, D-40 and D-41. Due to the presence of the monitoring boreholes, the same agreement in model curves was not achieved for the different combinations of model parameters. Therefore, the monitoring data reduces the degree of freedom of the mathematical model. The comparison of the development in the monitoring borehole shows that the rock environment is better described by the parameters obtained after cropping the original model parameters.

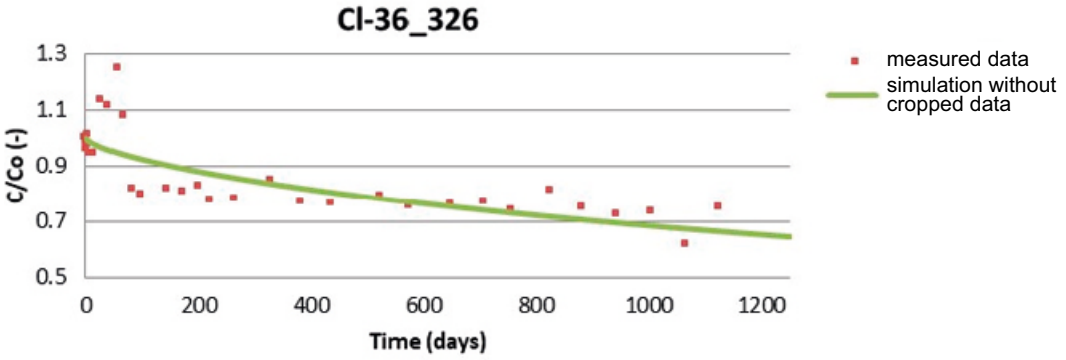

Figure D-38. *Agreement between the measured and model results for the originally published data, development of activity in the injection borehole.*

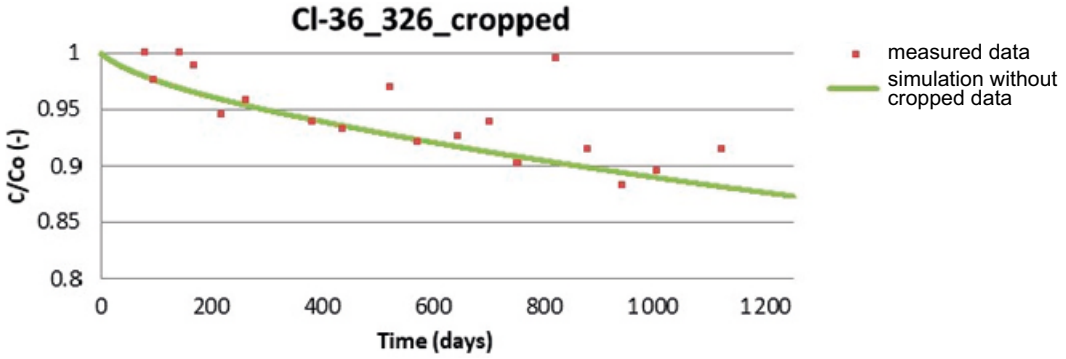

Figure D-39. *Agreement between the measured and model results for the cropped data, development of activity in the injection borehole.*

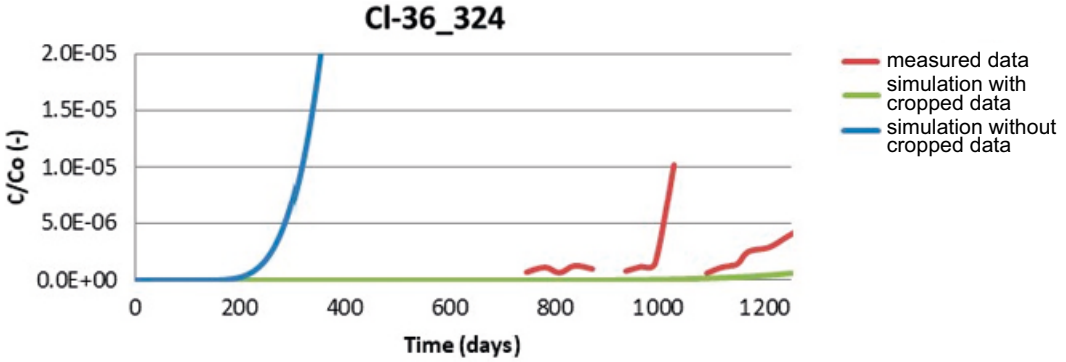

Figure D-40. *Agreement between the measured and model results in the monitoring borehole.*

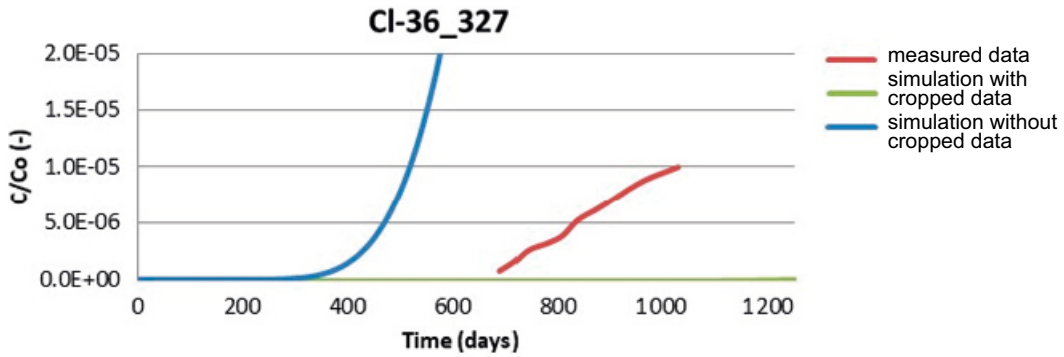

Figure D-41. *Agreement between the measured and model results in the monitoring borehole.*

D6.4 Ba-133

A comparison of the development of the measured and modelled activity in the injection borehole for Ba-133 is shown in Figure D-42. Due to the absence of data from the monitoring boreholes, similar modelling curves for different combinations of parameter are again achieved.

D6.5 Cs-134

A comparison of the development of the measured and modelled activity in the injection borehole for Cs-134 is shown in Figure D-43. Due to the absence of data from the monitoring boreholes, similar modelling curves for different combinations of parameters are again achieved. When calibrating the mathematical model, attention was given to data up to approximately day 500; the increase in activity after this time is attributed not to the behaviour of the rock environment, but to the setup of the experiment.

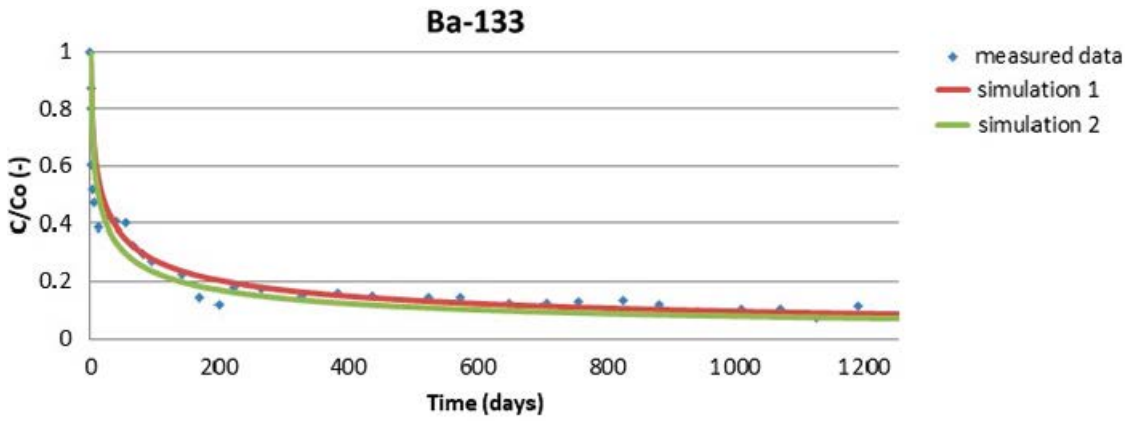

Figure D-42. *Agreement between the measured and model results for different combinations of model parameters, development of activity in the injection borehole.*

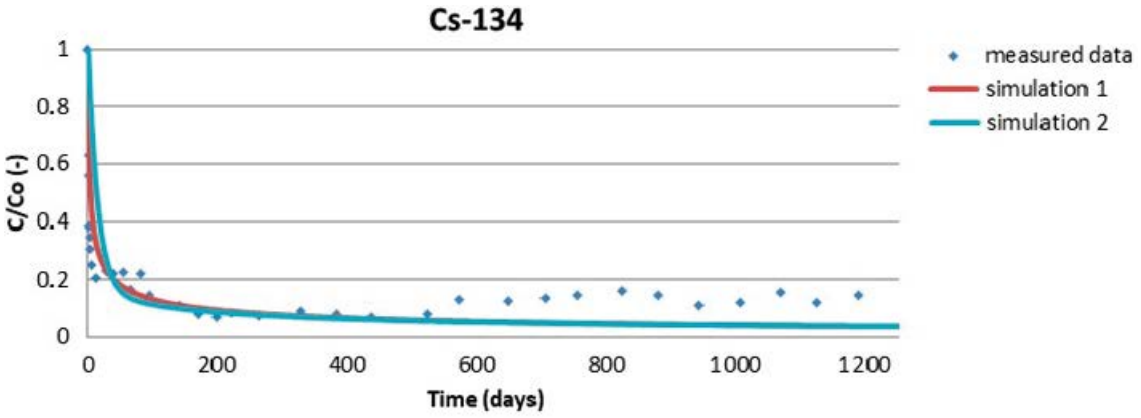

Figure D-43. *Agreement between the measured and model results for different combinations of model parameters, development of activity in the injection borehole.*

To specify the model parameters, it is recommended to drill out the rock around the experimental boreholes, thereby reducing the degree of freedom of the mathematical models. Furthermore, for sorbing nuclides, it should be verified that the resulting model curves are not dependent on the discretisation of the area, whereby a change in the discretisation of the areas of the other model curves would be obtained for the same material parameters (Figure D-14).

D7 Inverse model in MT3D and the evaluation made by PROGEO

The solution of Task 9C at PROGEO was not originally planned. The motivation for solving Task 9C, in addition to the work performed out in the framework of the Transport 4 project, was as follows:

1) More detailed knowledge of the implementation and results of the TDE experiment, analysis of instrumentation and errors in the experiment, analysis of measured data – the experiment is related to similar projects implemented by the co-investigator PROGEO (PAMIRE (Havlová et al. 2017), Transport 1 (Havlová et al. 2019), Fracture connectivity (Zuna et al. 2020)).
2) Application of the MT3DMS program for simulation of a pure diffusion problem, possibilities of utilisation, analysis of software and computational solver behaviour.
3) Application of heterogeneous properties of the rock matrix on a larger scale – assignment of micro-connectivity according to the methodology used in the simulation of laboratory diffusion experiments in the Transport 1 project (utilisation of C14-PMMA micrographs) and influence on the results of simulations.
4) Calibration of the measured data and model evaluation of one selected tracer – HTO (however, very similar measured activities in the observation boreholes were measured for both non-sorbing tracers HTO and Cl-36).

Comments and suggestions on the implementation and results of the experiment obtained from the analysis of the task description for Task 9C and the provided results of measurements – several relatively significant and problematic events occurred during the implementation of the experiment, which very likely influenced the course and results of the experiment.

- The first problem was a leakage of approximately 40 ml of the solution from injection borehole PP326 within 60 to 90 days of the start of the experiment and a 15 % drop in source activity of all tracers (the leaked solution was supplemented with “pure” water).
- The leakage of the solution was accompanied by a drop and complete “spreading” of pressure conditions between the boreholes for the remainder of the experiment – the pressure difference between the “failed” connection of boreholes PP321/PP322 and the nearest borehole PP324 (approximately 10 cm away), and the other experimental boreholes PP326 and PP327 was relatively significant. The pressure in PP321/PP322 is 100 kPa higher than in the other boreholes(!); however, this difference is not mentioned in the presentations or the provided data (attention is devoted only to significantly smaller pressure differences between the three tested boreholes). The influence of

these pressure gradients on the experiment is of course unknown, but purely theoretically it relates to a hydraulic conductivity of the rock matrix of 10^{-12} m·s^{-1} and porosity of 0.005 with an advective flow rate of the tracer of tens of centimetres per year(!).

- Recommendations for possible similar experiments performed at Bukov Underground Research Facility – in terms of instrumentation and the above-mentioned uncertainties regarding pressure differences, it seems much more beneficial to locate the boreholes in a cross-shape with a central source borehole.
- Observation boreholes PP324 and PP327 also had experimental problems – pressure, circulation, piping problems, etc – representative breakthrough curves were only obtained from approximately 1 000 days for PP324 (after a complete re-installation of the test section) and 700 days for PP327.
- Despite the experimental problems, the measured data clearly show the relatively fast arrival of tracers HTO and Cl-36 in the observation boreholes – approximately 300 days for PP324 (the closer borehole; 12 cm) and 400 days for PP327 (15 cm).
- Interesting and unexpected comparisons of the breakthrough curves of the relative activity of HTO and Cl-36 in the observation boreholes (see Figure D-44) – a linear shape probably indicates a steady flow between the source and observation boreholes, the effective diffusion coefficient is represented by the slope of the breakthrough curve and indicates a lower value for HTO than Cl-36(!).
- Very low relative activity of HTO and Cl-36 in the observation boreholes (five orders of magnitude lower than in the source borehole) correlates very well with the almost zero decrease in Cl-36 in the source borehole. However, the high decrease in HTO activity in the source borehole of 70 %, which is further commented on in the model results section, is ambiguous (and problematic from the point of view of overall balance).

MT3DMS was used for solving the transport Task 9C, similar to the solution of other Task 9 tasks. The task is solved in a simplified one-layer model in 2D with a model domain consisting of a rectangular grid of computational cells 1 × 1 mm, see Figure D-45. The axial symmetry of the task is used and only a quarter-circle slice with a 500 mm radius is simulated. The thickness of the model layer is 1 m and corresponds to the length of the tested borehole section. The source and observation boreholes are given as an open fracture (annulus) with the corresponding porosity (single-unit) so that the volume of water in the boreholes (total volume in the fracture and piping) corresponds to the task description. Therefore, no boundary conditions are prescribed for the source and observation boreholes, but only the initial values of activity in the source volume (according to the activity in the solution) and zero initial activity in the rock matrix and observation boreholes are defined.

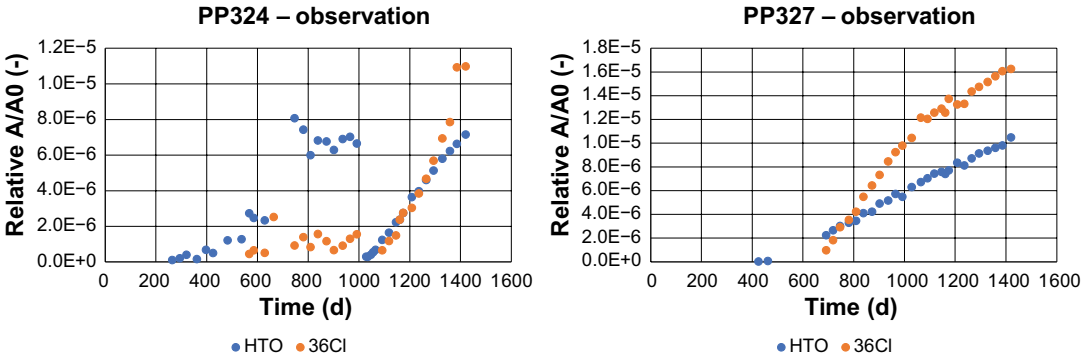

Figure D-44. *Task 9C – measured relative activity of HTO and Cl-36 in observation boreholes PP324 and PP327.*

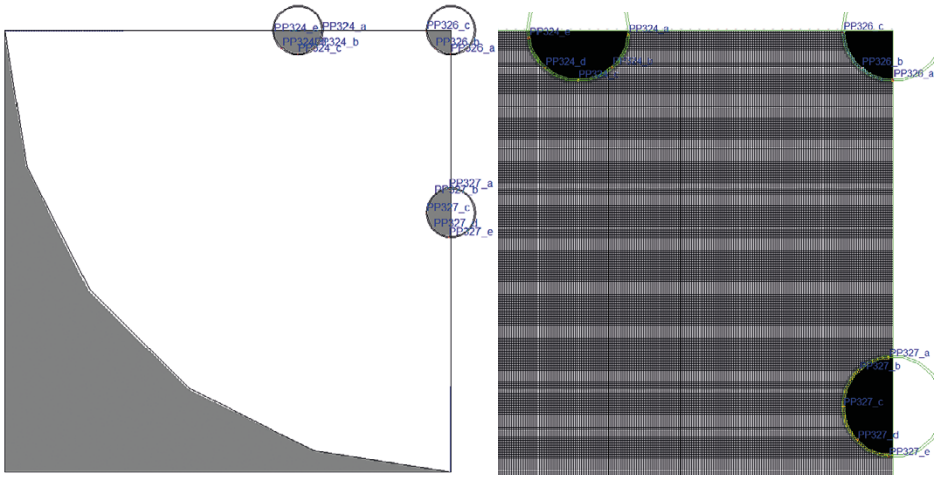

Figure D-45. *Tack 9C – MT3DMS – discretisation of the model domain – size of the whole model 500 x 500 mm on the left, the cutting with the grid of model cells 1 x 1 mm on the right.*

Task 9C was solved as a purely diffusion model (zero hydraulic gradient, zero sorption) with radioactive decay and a half-life of HTO of 12.3 years. The porosity and pore diffusion coefficient values were calibrated during the simulations to achieve a reasonable agreement between the measured and model breakthrough curves. In the models, homogeneous (same) values of transport parameters were entered in the whole space of the rock matrix. A disturbance zone (BDZ) with slightly higher parameter values was considered in the limited range of 1 mm from the borehole wall (a range of 1 mm was entered based on experience from previous modelling works). It should be emphasised that from the point of view of the geometry of the task and the mutual distance of 10–15 cm between the boreholes, we do not expect any significant influence of the BDZ on the transport of non-sorbing tracers HTO and Cl-36 (but it is important for sorbing tracers Na-22, Cs-134 and Ba-133).

The task was solved with a total of three variants, because for HTO it was not possible to calibrate the curve in the injection borehole and the observation borehole(s) at the same time:

1) Calibration of activity in injection borehole PP326 – comparison of the modelled and measured evolutions in the injection borehole and the observation boreholes is shown in Figure D-46. The calibrated values of the rock matrix parameters are:
   – Porosity (n) – 0.009 – this value compares relatively well to the measured porosity in the samples and values adopted by other co-investigators.
   – Pore diffusion coefficient (D_p) – 4.63×10^{-11} $m^2 \cdot s^{-1}$ – effective diffusion coefficient ($D_{eff} = D_p \cdot n$) 4.17×10^{-13} $m^2 \cdot s^{-1}$ again corresponding to the measured values and the resulting values adopted by other investigators.

The graph shows a very good agreement of the course of activity in the injection borehole. On the contrary, the measured and model activity in the observation boreholes is very problematic. The model values follow the trend of the measured values, but they are plotted on the secondary axis and are three orders of magnitude higher than the measured values(!). The problem is mainly in terms of the activity balance of HTO – a high drop in the injection borehole over the measured period of 1 500 days (by 70 % and 55 %, respectively, after deduction of 15 % through leakage) and practically zero activity in the rock matrices of the observation boreholes.

2) Calibration of activity in observation boreholes PP324 and PP327 – A comparison of the modelled and measured evolutions in the injection borehole and the observation boreholes is shown in Figure D-47. The calibrated values of the rock matrix parameters are:
   – Porosity (n) − 0.000003 – extremely low calibrated value by more than three orders of magnitude lower (!) than the measured value.
   – Pore diffusion coefficient (D_p) – 7.5×10^{-11} $m^2 \cdot s^{-1}$ – comparable to the previous variant; however, effective the diffusion coefficient ($D_{eff} = D_p \cdot n$) 2.3×10^{-16} $m^2 \cdot s^{-1}$ is three orders of magnitude lower than the given low porosity. However, a value in the order of 10^{-16} corresponds to the value determined by the analytical calculation in Section D8.

The graph shows a very good agreement of the course of activity in both boreholes PP324 and PP327 (with respect to the almost same measured relative activities of HTO and Cl-36, the given calibrated values are valid for both tracers). The very low value of activity in the observation boreholes is associated with the modelled very low decrease in activity in the source borehole, which, while not corresponding to the measured decrease in HTO activity, agrees very well with the minimal decrease in the measured activity of Cl-36.

Therefore, the course of Cl-36 may be relatively well simulated in both the injection and observation boreholes using a low porosity value. The question is how to explain the mismatch between the low HTO activity in the observation boreholes and the high decrease in activity in the source borehole (or whether it is a measurement error, the effect of pressure differences between the boreholes or advective flow, etc).

3) Application of micro-porosity – in an attempt to explain the uncertainties in the measured values of HTO, a variant with a heterogeneous distribution of the micro-porosity of the rock matrix was simulated according to the image obtained by the C14 PMMA method. This variant was only a test, the actual image from the given location was not available for such a large model domain (0.5 × 0.5 m), a modified micrograph processed within subproject "Transport 1" was used, see Figure D-48. The aim was to verify whether the course of HTO activity could be explained by heterogeneities in the rock matrix. The model in this variant was not calibrated, but the results of the simulations yielded very similar conclusions to the previous two variants with a homogeneous distribution of porosity. Although in this variant the properties of the rock matrix between the boreholes are specified with a high degree of heterogeneity, the overall "behaviour" of the domain entered over a distance between boreholes of 11–15 cm is more or less homogeneous.

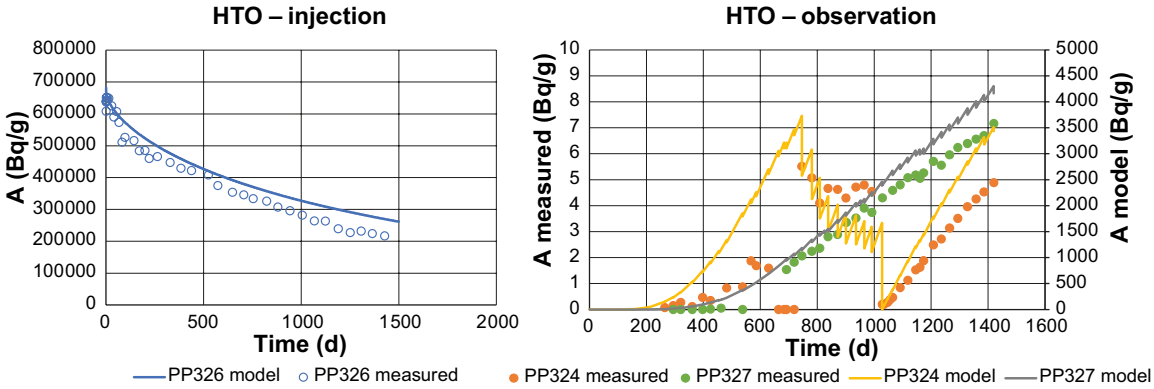

Figure D-46. *Task 9C – simulation of HTO in MT3DMS – Variant 1 – calibration of activity in injection borehole PP326. Comparison of the measured and model evolutions in the injection boreholes on the left and breakthrough curves in the observation boreholes on the right.*

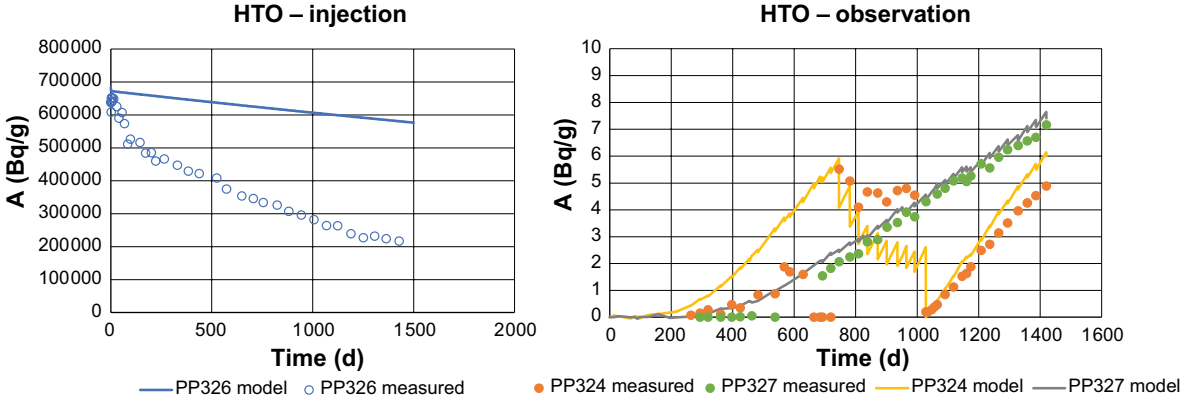

Figure D-47. *Task 9C – simulation of HTO in MT3DMS – Variant 2 – calibration of activity in observation boreholes PP324 and PP327. Comparison of the measured and model evolutions in the injection boreholes on the left, in the observation boreholes on the right.*

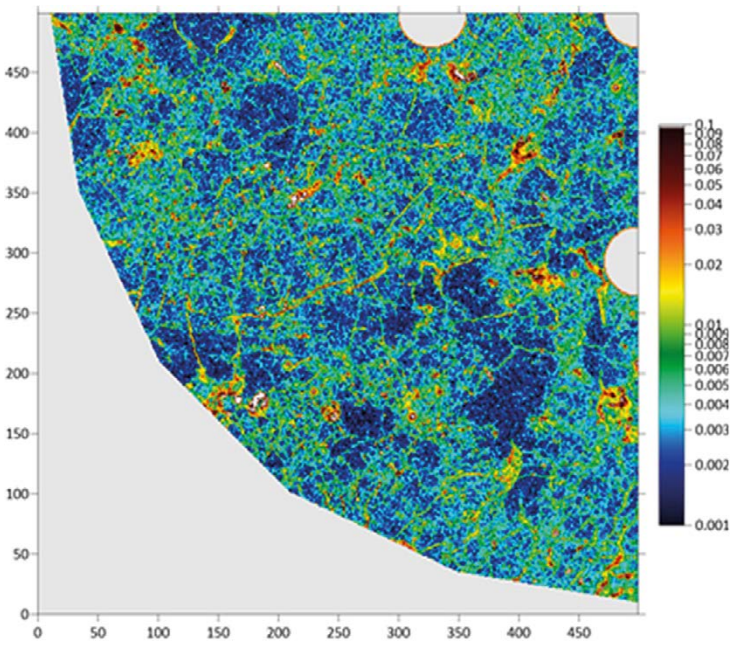

Figure D-48. *Task 9C – Variant 3 – heterogeneous porosity based on the rock matrix micrograph.*

D8 Simplified analytical solution(TUL)

Due to the fact that the course of the measured concentrations in the detection boreholes is linear over a relatively long period of time (Figure D-49), this can be interpreted as a constant flow of substances into the borehole. Therefore, it is possible to consider this state as a quasi-steady state of the concentration field between the source and detection borehole, while simplifying the geometry into radial symmetry (dilution in the detection borehole distributed throughout the perimeter) and assuming a constant concentration in the source and target boreholes (which is true for the given reservoir volumes and for a reasonably short period of time). The following applies for the flow in the segment corresponding to the dimensions of the detection borehole

$$Q_c = \varphi d D_e \frac{c_1 - c_2}{\ln r_2/r_1}$$

This must also be consistent with the balance in the monitoring borehole, i.e. the rate of concentration increase, as follows

$$\frac{dc}{dt} = \frac{Q_c}{V}$$

The slopes of the curves are shown in Figure D-49 and in Table D-10. On the basis of the first relation, the corresponding effective diffusion coefficient is determined (further columns in Table D-10). Obviously, the value is unrealistically low. Otherwise, the slow increase cannot be explained without the existence of at least part of the volume by with a low coefficient. At the same time, this value does not correspond to the rate of decrease in the source borehole (at a very low D_e, the decrease would practically not occur), so it can be expected that part of the affected rock matrix will have a value near the predicted value, but there will be a barrier in the monitored area with a several orders of magnitude lower coefficient.

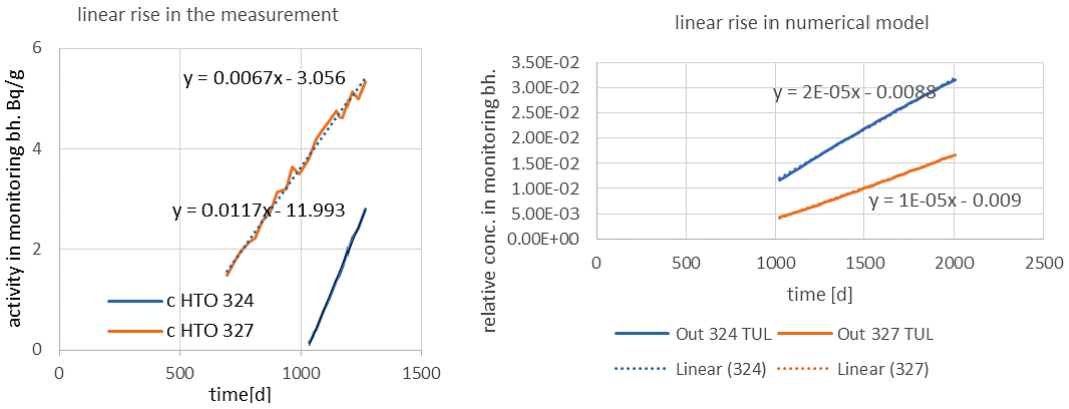

Figure D-49. *Verification of assumption of a linear increase in concentrations and the associated constant mass flow.*

Table D-10. Results of the analytical solution and interpretation of flow rate between the boreholes.

	dc/dt measured [1/s]	De fit analytical [m²/s]	De by correcting the drop of the injection borehole [m²/s]
Borehole 324	2.14E−13	4.7E−16	9.4E−16
Borehole 327	1.19E−13	2.55E−16	4.6E−16

D9 Alternative evaluation (CTU)

The time course of the relative concentrations in borehole PP324 is non-monotonous, after the water exchange at approximately 1 000 days, the increase in concentrations over time is linear. To analyse and interpret this course, several calculations were performed at CTU using a 2D model created in GoldSim.

Based on the pilot calculations, it was determined that it is not possible to use a 2D model to simultaneously describe data measured in the injection borehole (PP326) and observation boreholes (PP324 and PP327). Therefore, we used the measured concentrations in injection borehole PP326 as the boundary conditions to calculate the time courses in PP324. Specifically, we applied the GoldSim Lookup Table element to interpolate the concentration in the Cell Pathway elements, which represented PP326 in each step. Because the 2D model is homogeneous, we searched for optimal *De* values for each observation borehole.

Figure D-50 shows a comparison of concentration time courses in PP324, the black solid line corresponds to the detected data, the red line is the calculated values for the model without boundary conditions in PP324. The simulation was obtained for $D_e = 4.35E{-}14$ m²/s, which is an order of magnitude lower than expected (porosity of 0.0094). In the time interval up until the water exchange, i.e. up to approximately 1 000 days, the detected concentration was higher. On the contrary, the simulated increase is steeper. It can be expected that a higher concentration in the first interval resulted in diffusion from observation well PP324 into the matrix, which in turn may affect the diffuse flow into PP324 after the exchange, i.e. after 1 000 days. To verify this hypothesis, we constructed an alternative model that had a boundary condition on the time interval of 1–1 000 days in PP324 based on the detected data (red dashed line in Figure D-50). The results of the simulation show that the influence of the boundary condition has no observable effect on the course of the concentration increase in PP324 during the course of the exchange.

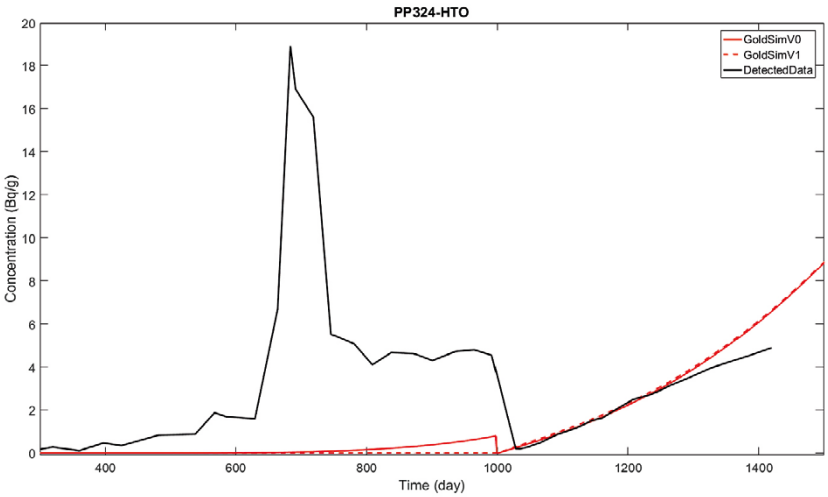

Figure D-50. *Comparison of the time course of concentrations in PP324 for a model with PP324 without boundary conditions.*

D10 Conclusions

The transport task solved in the framework of Task 9C is important from the point of view of modelling because of its relation to the ongoing in situ diffusion experiment TDE (REPRO project). Simulation of the task, where specific measured data are available, is always better for comprehensive verification of the methodology of the modelling procedures, analysis, processing and evaluation of input and output data than simulation of a hypothetical task (with only input transport parameters, e.g. Task 9D). The experiment itself is interesting, because it can be used as a source of experience for the possible design of transport experiments, e.g. in the Bukov underground laboratory.

Appendix E

Japan Atomic Energy Agency (JAEA)

Yuta Fukatsu, Tsuyoshi Ito, Yukio Tachi

E1 Introduction

E1.1 Background

In Japan, high-level radioactive waste (HLW) will be disposed of in a geological repository at depths deeper than 300 meters in accordance with the "Designated Radioactive Waste Final Disposal Act". The Final Disposal Act has been enacted based on the H12 report (JNC 1999) published by the Japan Atomic Energy Agency (JAEA) in 1999. Nuclear Waste Management Organization of Japan (NUMO) was established in 2000, as an implementing body authorized by the Final Disposal Act. Japanese government and JAEA have been conducting research and development (R&D) on geological disposal of HLW in order to improve the technical reliability of geological disposal, including the enhancement of scientific knowledge and safety assessment methods.

Crystalline rocks such as granitic rocks are one of the potential host rocks for geological disposal in Japan. The H12 report (JNC 1999) and recent safety reports (NUMO 2013, JAEA 2015) have focused on the crystalline rocks as reference host rocks. In order to obtaining reliable migration data and to develop and validate the radionuclide migration model at the in situ migration tests, JAEA has joined international projects such as Grimsel Test Site (GTS) project in Switzerland. The Long-Term Diffusion (LTD) project at the GTS is one of key projects to develop the migration model and related dataset for the performance assessments in Japan. Task 9 of SKB Task Force on Modelling of Groundwater Flow and Transport of Solutes can give us the opportunity to test the modelling approaches developed in the LTD project for different types of granitic rocks and in situ migration experiments.

E1.2 Objectives

The transport of radionuclides in fractured crystalline rocks can be conceptualised by a dual-porosity model where radionuclides are transported by advective water flow through the fractures and by diffusion and sorption in the surrounding rock matrix (Neretnieks 1980). Diffusion and sorption of radionuclides in the matrix adjacent to the fracture are one of the key phenomena that control the transport of radionuclides in the rock. Therefore, for the safety assessment of the geological disposal, it is required to obtain diffusion and sorption data of the radionuclides in rock matrix, and to predict the transport of radionuclides for long-term safety assessments.

Laboratory experiments provide diffusion and sorption data for the rock matrix and mechanistic understanding under well-defined boundary conditions. On the other hand, in situ experiments provide site-specific data under actual deep geological conditions. However, diffusion and sorption parameters are typically derived from laboratory experiment using drilled or crushed rock samples, which have different properties in porosity, pore-connectivity and reactive surface area in comparison with in situ conditions. Therefore, the laboratory measurements can lead to overestimation of matrix diffusion and sorption properties. In order to set reliable parameter values of matrix diffusion and sorption relevant to the performance assessment, it is necessary to understand in detail the processes of diffusion and sorption both in the laboratory and in situ experiments, and to develop a way to extrapolate from the laboratory to in situ conditions.

These issues have been investigated by coupling laboratory and in situ experiments as part of the LTD project at the GTS, Switzerland (Soler et al. 2015, Tachi et al. 2015, 2018). Based on the comparative experimental and modelling studies between laboratory and in situ conditions, we concluded that the following mechanisms are important for predicting radionuclide migration in the Grimsel granodiorite. The cation excess diffusion is a key mechanism in the Grimsel granodiorite, whereas the anion exclusion effect seems to be relatively minor. The high sorption at the disturbed surface in cored samples for laboratory experiments is critically important to evaluate radionuclide transport in both laboratory and in situ tests. The difference in porosity between laboratory and in situ conditions is also a key factor to scale laboratory data to in situ conditions.

In order to verify the applicability of the scaling approach from laboratory to in situ conditions in various sites, further studies are required as a target of different features of crystalline rocks. Task 9 of SKB Task Force focuses the realistic modelling of coupled matrix diffusion and sorption in heterogeneous crystalline rock matrix. Task 9C has focused on the in situ Through-Diffusion Experiment (TDE) of the REPRO project (rock matrix REtention PROperties) at the ONKALO underground rock research facility. The specific properties of the rock and the test concept can provide a good dataset for testing our approach. Predictive modelling of the in situ tracer experiments based on the scaling approach has been performed. The applicability of the concept has been assessed by comparing the predictive model results with in situ experimental data.

E1.3 Scope and limitations

JAEA's approach is based on the scaling approach from laboratory to in situ conditions, developed through the LTD project in granodiorite. In this approach, the parameters regarding diffusion and sorption derived from the laboratory experiments are scaled by considering the differences in the porosity and surface area of the rock between laboratory and in situ conditions. In addition, the high sorption capacity and the high diffusivity at the disturbed surface of the borehole wall (Borehole Disturbed Zone: BDZ) are assumed for the modelling. This approach is applied for the TDE results considering key features and processes in the REPRO site. Key features and limitations of our modelling in Task 9C are;

- The parameters for modelling such as porosity, distribution coefficient and diffusion coefficient are referred from the Task 9C description and the supplementary data derived from laboratory diffusion and sorption experiments.
- One of the key features of our modelling approaches is the parameter scaling from laboratory data to in situ conditions and the modeling including the BDZ effect. This approach will be applied for the in situ setup considering the specific properties of the rock at the REPRO site.
- Another key feature is the heterogeneity of rock (veined gneiss: VGN) at the REPRO site. The process of drilling for the TDE may cause the disturbed surface of the borehole wall. In addition, the foliation formed by biotite bands oriented in a certain direction may induce anisotropic diffusion. The heterogeneous features of the rock can impact on the diffusion and sorption processes for the TDE. In order to consider the heterogeneity in our modelling, different diffusion coefficients are set for diffusion parallel and perpendicular to foliation.

E2 Methodology and model

E2.1 Conceptual description of features, events and processes of the experiments

The in situ through diffusion experiment (TDE) at REPRO site was carried out between the three parallel boreholes ONK-PP326 (injection), ONK-PP324 (observation), and ONK-PP327 (observation) at about 11 to 13 m depth from the niche wall. The location of PP324 was 115 mm away from PP326 along to the foliation, and PP327 borehole is 150 mm away from the PP326 perpendicular to the foliation. HTO, $^{36}Cl^{-}$, $^{22}Na^{+}$, $^{133}Ba^{2+}$ and $^{134}Cs^{+}$ were chosen as the tracers, and the cocktail containing all tracers was injected into the PP326. Decreasing concentration of the tracers in the injection hole and increasing concentration in the two observation holes were monitored by a liquid scintillation counter and gamma measurement during about 1 500 days of the test duration. However, unexpected artificial events happened during the test. The one of the major events which impacted the TDE was a 40 mL leakage of tracer cocktail from PP326 75 days after beginning the test. The concentrations of the tracers in PP326 dropped at that time. In addition, the experimental section water in PP324 was exchanged to new synthetic groundwater at around 1 000 days. These events were needed to be considered in the modelling for comparison with the TDE experimental results.

The experimental section of the TDE is predominantly surrounded by the rock type VGN (veined gneiss). The veined gneiss has high contents (~30 %) of micas, mainly biotite. The veined gneiss shows a weak to moderate mica banded foliation, but locally also irregular foliation. The orientation of the foliation is almost parallel to the drilling direction (Task 9C description, Andersson et al. 2020). The foliation is oriented along the diffusion direction from PP326 to PP324 and perpendicular to the direction from PP326 to PP327.

In addition to the foliation effects, the effects of the borehole disturbed zone (BDZ) may be important in the TDE setup. The process of drilling in the in situ condition and subsequent sample treatment for laboratory testing results in newly created cracks and microcracks through stress release and disturbance (e.g., Skagius and Neretnieks 1986, Autio et al. 1998, Tullborg and Larson 2006). The effect of the BDZ has been investigated in the in situ LTD experiment conducted at the GTS (Soler et al. 2015, Tachi et al. 2015). These results indicated that the BDZ effect caused high porosity, diffusivity and sorption capacities in near-surface disturbed zones. The BDZ effects may be modelled by considering a layered rock matrix representation featuring cylindrical layers that are coaxial with the drillhole.

Laboratory measurements of matrix diffusion have been performed using small, thin rock samples by through-diffusion and/or in-diffusion tests. Rock samples used for laboratory experiments are typically centimeter scale and are generally taken from drillcores. The process of drilling and subsequent sample shaping for laboratory experiments results in newly created cracks and microcracks through stress release and disturbance (e.g., Skagius and Neretnieks 1986, Autio et al. 1998, Tullborg and Larson 2006). Increased porosity values in laboratory samples at artificially disturbed conditions compared to in situ conditions have been reported (e.g., Ota et al. 2003, Tullborg and Larson 2006, Jokelainen et al. 2013). These differences in porosity may be considered in parameter setting by scaling from laboratory data to in situ conditions.

E2.2 Description of features, events and processes in the conceptual model

Based on the conceptual description of the features, events and processes mentioned above, the conceptual model for radionuclide transport in the TDE setup was developed for a simplified and pragmatic representation. One of the key assumptions for the modelling for the TDE is whether the rock matrix is either homogeneous or heterogeneous with respect to foliation and BDZ. Another key assumption is if the differences in porosity are considered in parameter setting by scaling from laboratory data to in situ conditions. The homogeneous and simplified parameter setting was represented as a simple case by using directly laboratory data. On the other hand, a realistic case was defined, considering the foliation, BDZ and scaled parameters. Figure E-1 shows the concepts and key assumptions in the Simple and Realistic models.

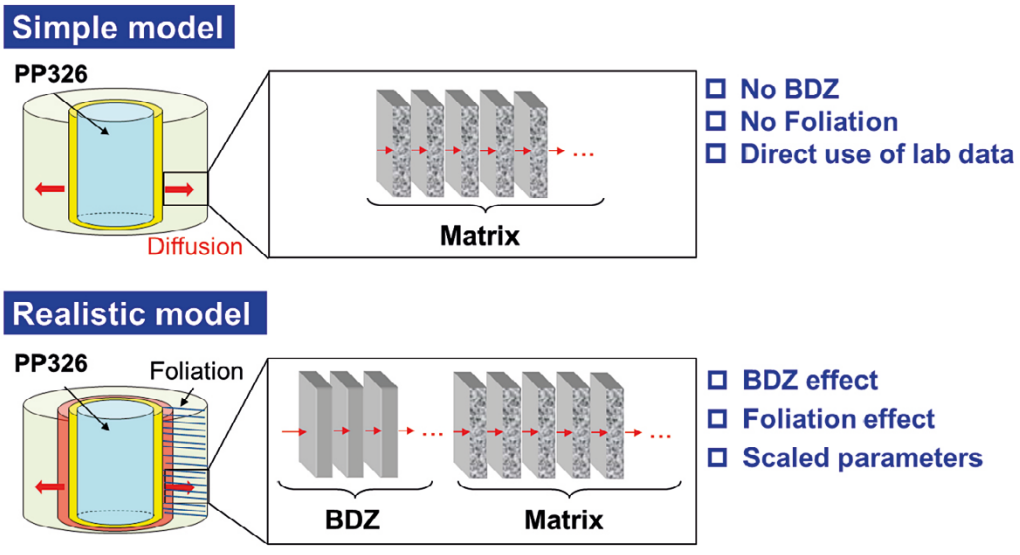

Figure E-1. *Modelling concepts for simulation of the Through-Diffusion Experiment at the REPRO site.*

The Realistic model assumed that the borehole disturbed zone (BDZ) has great impacts on both diffusion and sorption processes. The BDZ effect can be modelled by considering a layered rock matrix representation featuring cylindrical layers that are coaxial with the borehole.

Foliation effect may have strong impact on the effective diffusivity in the rock matrix (Van Loon et al. 2004). Considering the mineralogy with high contents of mica and strong foliation in the rock at REPRO site, these effects may be important in the modelling of the TDE. Our realistic model for the TDE takes into account of the foliation effect on different diffusivity of all tracers along and perpendicular to the foliation.

Fickian matrix diffusion and instantaneous and reversible sorption were assumed for all modelling. However, the parameters for diffusion and sorption were scaled from laboratory to in situ conditions for the Realistic model (Tachi et al. 2015).

E2.3 Model setup

Goldsim software (ver. 10.1; GoldSim Technology Group 2018) was used as the framework for model implementation. Figure E-2 shows the Goldsim model structure for the TDE and the model components for radionuclide transport in a direction perpendicular to the axis of the borehole, from an injection borehole (PP326), through the inner surface in the borehole, to the BDZ and the surrounding rock matrix to the two observation boreholes (PP324 and PP327). In Goldsim software, the CellNet Generator discretises a cylindrical region of space and creates a two-dimensional array of Cell elements, including diffusive mass flux links between them. The BDZ was set to have a thickness of 1 mm.

Matrix diffusion and sorption were modelled assuming homogeneous properties in the matrix. However, the variation of diffusion and sorption properties in the BDZ was considered. Matrix diffusion was expressed by Fickian diffusion. Sorption of radionuclides in the matrix was assumed to be reversible and instantaneous with a linear isotherm.

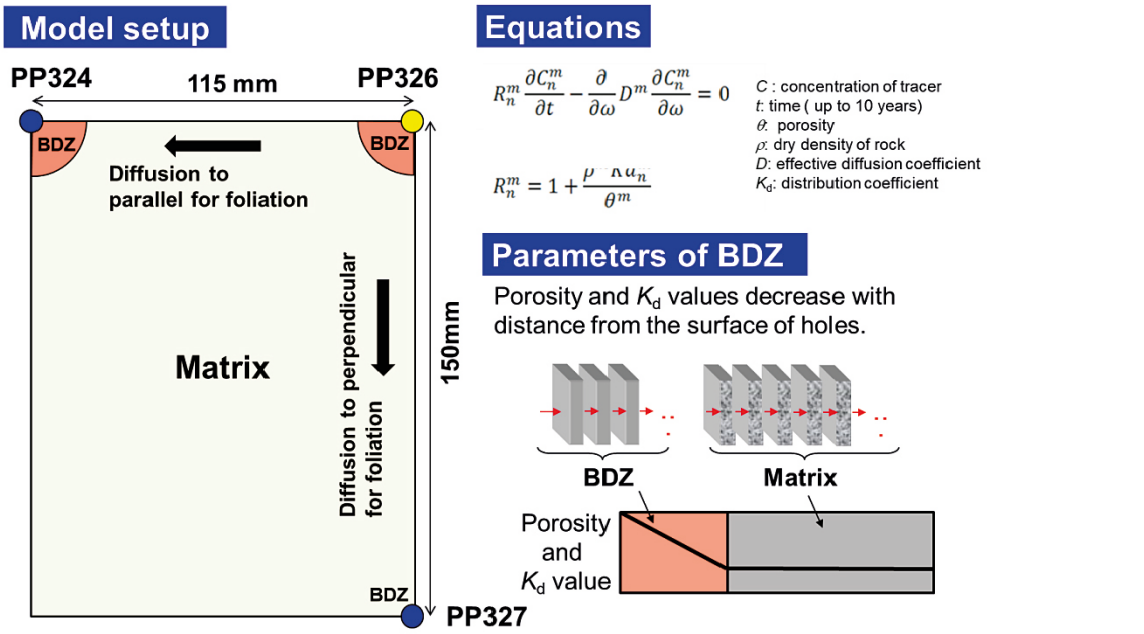

Figure E-2. *Conceptual model and governing equations for our simulations of the Through-Diffusion Experiment (TDE) at the REPRO site.*

E2.4 Input data

The initial concentrations of tracers were set to 785 714 Bq/mL for HTO, 21 825 Bq/mL for Cl^-, 88 889 Bq/mL for Na^+, 8 294 Bq/mL for Cs^+ and 7 619 Bq/mL for Ba^+. Porosity (ε), effective diffusivity (D_e) and distribution coefficient (K_d) are the transport parameters for our models. These parameters were determined based on the dataset derived from laboratory diffusion and sorption experiments, and scaled from laboratory data to in situ conditions, assuming their relationship to rock properties, developed for GTS (Tachi et al. 2015).

The D_e datasets were obtained from the Task 9C description (Andersson et al. 2020, Table 5-5), Task 9A description (Löfgren and Nilsson 2019, Table 2-9), and from diffusion experiments at laboratory (JAEA 2020, Muuri et al. 2017, 2018a, b). The D_e derived from the diffusion experiments has wide variability with more uncertainty than experimental error. The D_e values can be affected by the rock characteristic such as mineral distribution and porosity. The VGN rock at REPRO site is highly foliated as mica-rich mylonite bands distributed and arranged at certain direction. This heterogeneous property can cause anisotropic diffusion. The foliation may be related with the variability of the D_e value. Thus, in order to consider the foliation effect in the model, higher diffusion coefficient for diffusion parallel to foliation was considered, as shown in Table E-1 (a) and (b). However, there are no measured data for D_e of cations (Na^+, Cs^+, Ba^{2+}) perpendicular to foliation for the REPRO rocks. We calculated the values by using the ratio of D_e of HTO perpendicular and parallel to the foliation. Both datasets for diffusion along and perpendicular to the foliation were scaled for the Realistic model. The dataset in Table E-1 (a) was directly used for the Simple model.

The scaled D_e values for the Realistic model were determined based on porosity and diffusion dataset derived from laboratory diffusion experiments. The extrapolating method from the laboratory to the in situ condition takes into account the difference in porosity of VGN between 0.05 ± 0.02 for laboratory (Kuva et al. 2016) and 0.0068 ± 0.08 for in situ conditions (Task 9C description). There have been many attempts to relate the effective diffusivity or the formation factor to the porosity, the most common empirical relationship is a power law correlation, so-called Archie's law (Boving and Grathwohl 2001, Autio et al. 2003, Witthüser et al. 2006), as shown in the following equation,

$$D_e = \mathrm{A} \cdot \varepsilon^m, \qquad \text{(E-1)}$$

where, A is the empirical factor (-) and m is the cementation factor (-). The A value was determined from Archie's law by using the porosity and D_e for the laboratory condition. The m value is 1.58, derived using the dataset obtained for Äspö diorite described in Ohlsson (2000). The D_e values for all tracers in Table E-1 were extrapolated by using the A and m values in Equation (E-1). In addition, the Realistic model assumes a BDZ, where the borehole surface in the in situ test is disturbed by the impact of drilling. For the BDZ, high porosity with gradual linear decline with distance towards the rock matrix was assumed. The corresponding D_e values were calculated with Equation (E-1). The scaled $D_{e,along}$ and $D_{e,perp}$ for BDZ and undisturbed matrix in the Realistic model are summarised in Table E-2.

Table E-1. Effective diffusion coefficient (D_e) for diffusion parallel and perpendicular to the direction of foliation, derived from laboratory experiments and calculation.

(a)	Parallel to foliation		(b)	Perpendicular to foliation	
Traces	**$D_{e,along}$ (m^2/s)**	**References**	**Tracers**	**$D_{e,perp}$ (m^2/s)**	**References**
HTO	3.9×10^{-13}	Andersson et al. 2020	HTO	1.8×10^{-13}	Löfgren and Nilsson 2019
Cl^-	3.4×10^{-13}	Andersson et al. 2020	Cl^-	5.0×10^{-15}	Löfgren and Nilsson 2019
Na^+	3.0×10^{-13}	JAEA 2020	Na^+	1.4×10^{-13}	*Calculation
Cs^+	3.0×10^{-13}	Muuri et al. 2017	Cs^+	1.4×10^{-13}	*Calculation
Ba^{2+}	8.0×10^{-14}	Muuri et al. 2018a	Ba^{2+}	3.8×10^{-14}	*Calculation

$$^{*}D_{e,perp}(\text{cation}) = \frac{D_{e,para}\ (Cation)}{D_{e,para}\ (HTO)} \times D_{e,perp}(HTO)$$

Table E-2. D_e values for the Realistic model, scaled from laboratory to in situ conditions. D_e values in the BDZ decrease from the maximum value at the borehole wall to the values for the matrix (Equation E-1).

Tracers	BDZ (maximum value)		Matrix	
	$D_{e,along}$ (m^2/s)	$D_{e,parp}$ (m^2/s)	$D_{e,along}$ (m^2/s)	$D_{e,parp}$ (m^2/s)
HTO	5.2×10^{-12}	2.5×10^{-12}	2.2×10^{-13}	1.1×10^{-13}
Cl^-	4.6×10^{-12}	6.7×10^{-14}	2.0×10^{-13}	2.9×10^{-15}
Na^+	4.0×10^{-12}	1.9×10^{-12}	1.7×10^{-13}	8.1×10^{-14}
Cs^+	4.0×10^{-11}	1.9×10^{-12}	1.7×10^{-13}	8.1×10^{-14}
Ba^{2+}	1.1×10^{-12}	5.5×10^{-13}	4.6×10^{-14}	2.2×10^{-14}

The K_d values of Na^+, Cs^+ and Ba^{2+} for the REPRO rocks were reported in the Task 9C description, JAEA (2020) and Muuri et al. (2018a, b). Although the K_d value of Na^+ is shown in Task 9C description, the value (0.0013 m^3/kg) is relatively high comparing with Cs^+ and Ba^{2+}, according to our previous research for GTS (Tachi et al. 2015). In addition, the K_d value of Na^+ obtained from a diffusion test on the target of VGN rock is lower than the K_d of the description by two orders of magnitude (JAEA 2020). Thus, this K_d value of Na^+ was selected for the parameters. On the other hand, the sorption data from the Task 9C description and Muuri et al. (2018a) were derived by batch sorption experiments using crushed samples with smaller particle sizes (< 0.3 mm). The major difficulty lies in the transfer of sorption data from crushed rock to intact rock. The crushing process creates new surfaces that significantly increase the specific surface area and the reactive sites that give larger sorption capacities (e.g., Missana et al. 2006, André et al. 2009, Tachi et al. 2015, 2018). The relationship between K_d values and particle size or specific surface area have been widely investigated by batch sorption tests (e.g., Byegård et al. 1998, Crawford 2010). The K_d values seem to increase as the particle size decreases, and a strong correlation between sorption capacity and specific surface area was observed over a range of particle sizes (Byegård et al. 1998). Recent K_d setting for performance assessments (Crawford 2010, Hakanen et al. 2014) used a correction factor which considers the differences in surface areas of crushed rocks used in laboratory sorption measurements and intact rock as in situ conditions.
In the Grimsel LTD project, sorption of cations was compared among laboratory batch sorption and through-diffusion experiments and in situ diffusion experiment, and it was confirmed to be strongly dependent on disturbance due to sample preparation (Tachi et al. 2015). The K_d values for undisturbed granodiorite matrix and disturbed surfaces at the BDZ can be estimated from batch measurement using larger particle sizes (> 1 mm) and smaller particle size (< 0.1 mm), respectively. Although qualitative estimation is still an open question, the K_d values were determined and scaled as follows. The K_d values derived for the REPRO rock with small particle size (< 0.3 mm) shown in Table E-3 were applied directly for the Simple model. In the Realistic model, the K_d values for undisturbed matrix and for the disturbed surface at the BDZ were derived by assuming the K_d dependence on the particle size. For this purpose, the K_d values measured at particle size 0.3 mm were extrapolated to larger particle sizes, 1 mm for BDZ and 3.5 mm for undisturbed matrix, by using the relationship between K_d values and particle size (Soler et al. 2019) measured for Äspö diorite reported in Byegård et al. (1998). The scaled K_d dataset for the Realistic model is shown in Table E-4.

Table E-3. Distribution coefficients (K_d) derived from laboratory sorption experiments.

Tracers	K_d (m^3/kg)	References
Na^+	1.9×10^{-5}	JAEA 2020
Cs^+	0.092	Task 9C description
Ba^{2+}	0.06	Muuri et al. 2018b

Table E-4. K_d values for the Realistic model, scaled from laboratory to in situ conditions.

Tracers	BDZ (maximum value) K_d (m^3/kg)	Matrix K_d (m^3/kg)
Na^+	1.5×10^{-5}	1.3×10^{-5}
Cs^+	3.0×10^{-2}	1.6×10^{-2}
Ba^{2+}	2.6×10^{-2}	1.7×10^{-2}

E3 Results and discussion

E3.1 Comparison between the simple and the realistic models

The simulation results of the Simple model and the Realistic model were compared in Figures E-3 to E-5. The depletion curves in Figure E-3 show reasonable trends of the decays ($Cl^- < HTO < Na^+ < Cs^+ \approx Ba^{2+}$), depending on the retention and diffusion properties of the tracers (Tachi et al. 2015). The concentrations of non-sorbing and weakly sorbing tracers such as HTO, Cl^-, and Na^+ in the Realistic model were higher than those in the Simple model, with a slower decay with time. This result is because that the $D_{e,along}$ and $D_{e,perp}$ of all tracers including in the Realistic model are smaller than those of the Simple model by the scaling approach from laboratory to in situ conditions. On the other hand, the concentration of highly sorbing tracers such as Cs^+ and Ba^{2+} decreases more rapidly in the Realistic model than in the Simple model. This was due to the high K_d and D_e values of Cs^+ and Ba^{2+} in the BDZ region, which caused most of the Cs^+ and Ba^{2+} to be sorbed in that region.

Comparing the breakthrough curves of HTO and Cl^- of the PP324 borehole calculated by the Simple and Realistic models in Figure E-4, concentrations of both HTO and Cl^- of the Simple model were higher than those in the Realistic model. This result is consistent with the result of depletion trend in Figure E-3. On the other hand, the two model breakthrough curves of HTO in the PP327 borehole (Figure E-5) showed larger differences. The concentration of Cl^- in the Realistic model was below 10^{-10} C/C_0. The difference of the breakthrough curves in PP324 and PP327 is attributed to the anisotropic diffusivity (foliation effect). This result indicates that the anisotropic effect of Cl^- diffusion is predicted to be more pronounced than that of HTO.

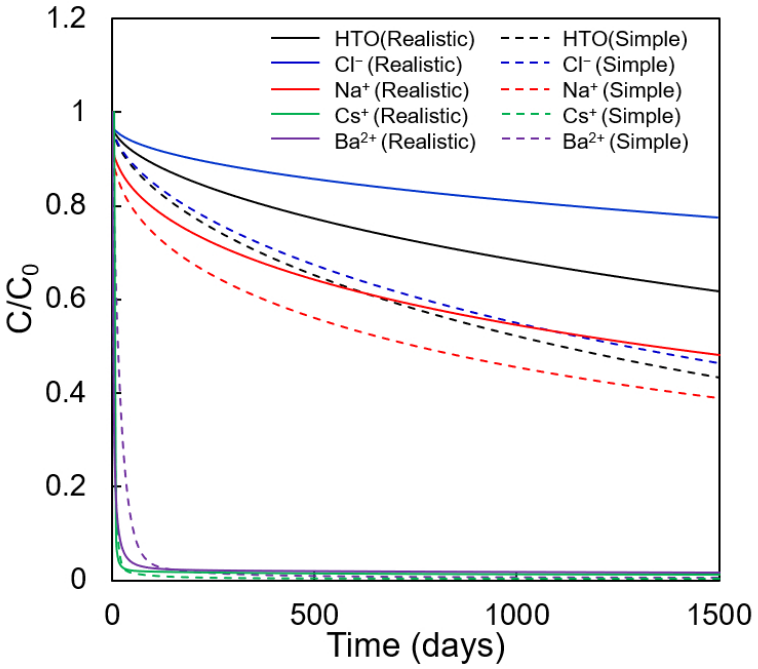

Figure E-3. *Depletion curves of HTO, Cl^-, Na^+, Cs^+ and Ba^{2+} in PP326, calculated by the Simple model (dashed lines) and the Realistic model (solid lines).*

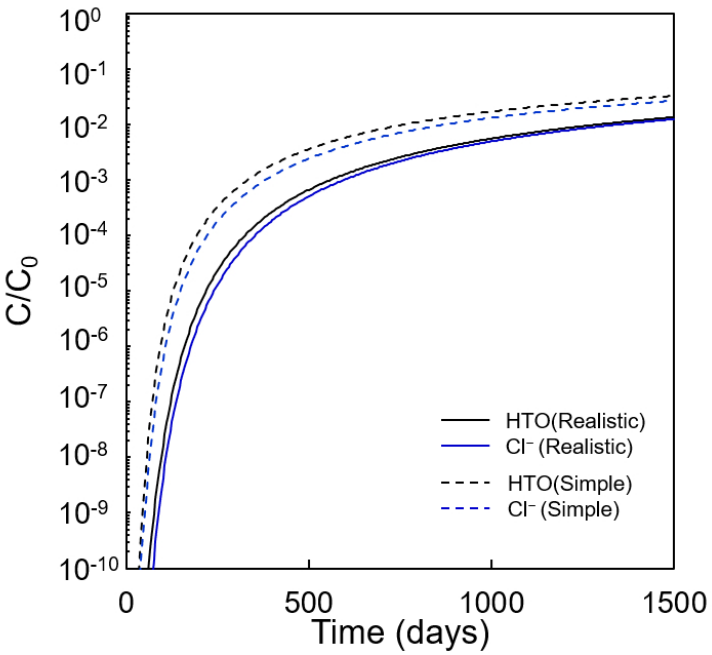

Figure E-4. *Breakthrough curves of HTO and Cl^- in PP324, calculated by the Simple model (dashed lines) and the Realistic model (solid lines).*

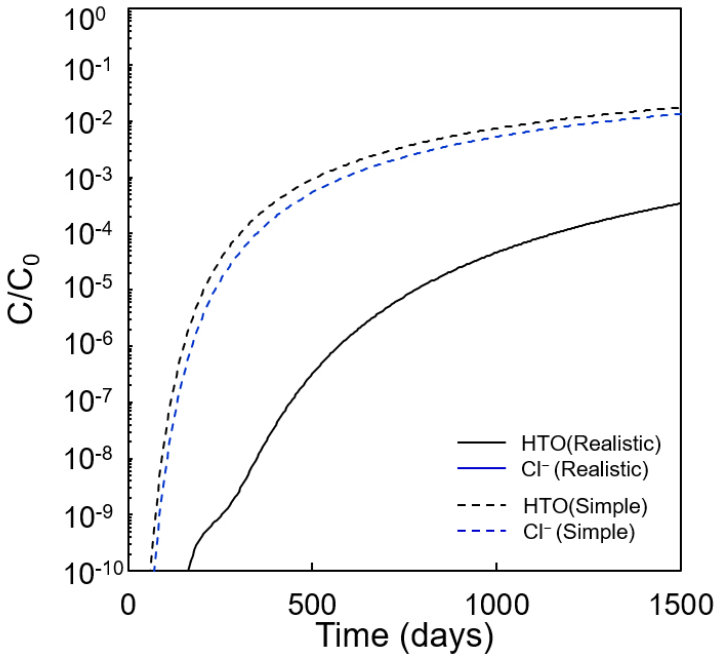

Figure E-5. *Breakthrough curves of HTO and Cl^- in PP327, calculated by the Simple model (dashed lines) and the Realistic model (solid line).C/C_0 for $^{36}Cl^-$ is less than 10^{-10} in the Realistic model.*

E3.2 Comparison between the realistic model and experimental results

The depletion and breakthrough curves obtained from the TDE at REPRO project are shown in Figures E-6 to E-8. In Figures E-6 and E-7, the sudden decrease of the concentration for all tracers happened at 75 days in PP326 and around 1 000 days in PP324. Those decreases were caused of experimental artificial error by the leakage of the injection solution at the line of PP326 and by the refresh of solution at PP324, as mentioned in the Section E2.1. In order to compare the measured data from the TDE and the simulation result from the Realistic model, the artificial errors were simulated in the model. The depletion curves obtained from the TDE in Figure E-6 decayed in order of $^{36}Cl^{-}$ < HTO < $^{22}Na^{+}$ < $^{133}Ba^{2+}$ < $^{134}Cs^{+}$, which were reasonable trends depending on the sorption and diffusion properties of the tracers. In Figures E-7 and E-8, the breakthroughs of HTO and $^{36}Cl^{-}$ were detected in both PP324 and PP327 boreholes, suggesting that the apparent diffusivity of the non-sorbing tracers was higher than that of the sorbing tracers such as $^{22}Na^{+}$, $^{134}Cs^{+}$ and $^{133}Ba^{2+}$. The concentration of $^{36}Cl^{-}$ before 1 000 days for PP324 was lower than that of HTO, suggesting anion exclusion for the diffusivity. The anion exclusion was observed for granodiorite and sedimentary rocks (Tachi et al. 2011, 2015, 2018), and the electrostatic force on the surface of the clay minerals such as biotite may attribute to the effect (Tachi and Yotsuji 2014, Van Loon et al. 2007). However, the concentrations of $^{36}Cl^{-}$ in PP327 and PP324 (after 1 000 days) were very similar to those of HTO. The reason of this result is still under discussion, but advection may have contributed to transport. Comparing the results of PP324 and PP327, concentrations were similar regardless of the distance from the injection hole to PP324 and PP327, suggesting a weak foliation effect on diffusivity.

The simulation results calculated by the Realistic model were compared with the measured results of in situ experiment. This simulation results include the event of the leakage of the solution at PP326 and PP324, showing that the concentrations of all tracers dropped at the leakage days as above mentioned. In Figure E-6, the model predicted a depletion trend ($^{36}Cl^{-}$ < HTO < $^{22}Na^{+}$ < $^{134}Cs^{+}$ < $^{133}Ba^{2+}$) depending on the different diffusion and sorption properties reasonably well. However, the in situ test data and simulation results for both depletion and breakthrough disagreed quantitatively. The different agreement between model and experimental results in the injection (PP326) and observation (PP324, PP327) boreholes might suggest an effect from advection.

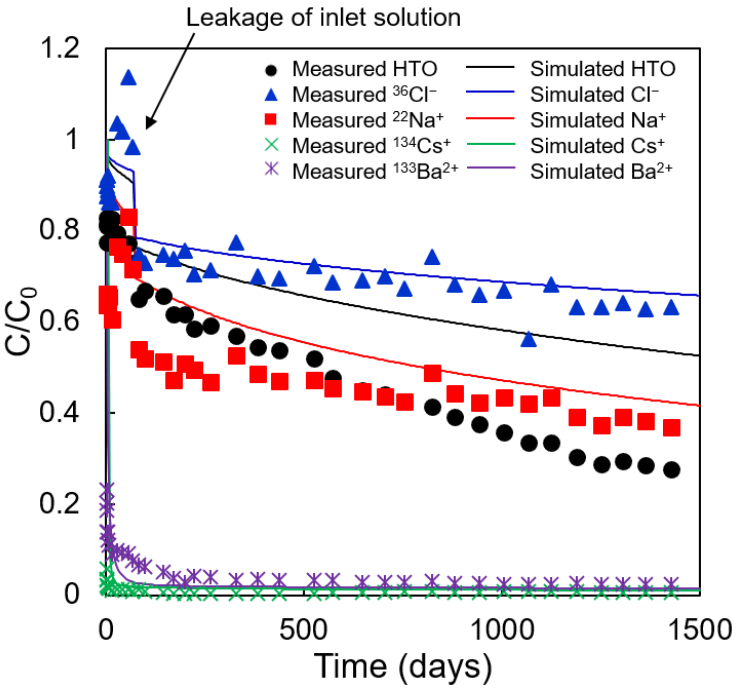

Figure E-6. *Depletion data of HTO, $^{36}Cl^{-}$, $^{22}Na^{+}$, $^{133}Ba^{2+}$ and $^{134}Cs^{+}$ in PP326 from the in situ Through-Diffusion Experiment (symbols), compared with the simulation results by the Realistic model (solid lines).*

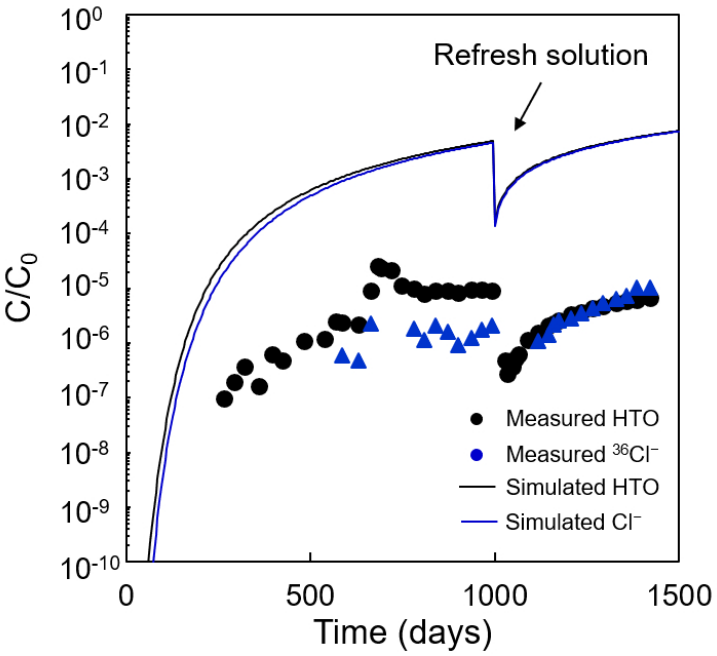

Figure E-7. *Breakthrough data of HTO and $^{36}Cl^-$ in PP324 from the in situ Through-Diffusion Experiment (symbols), compared with the simulation results by the Realistic model (solid lines).*

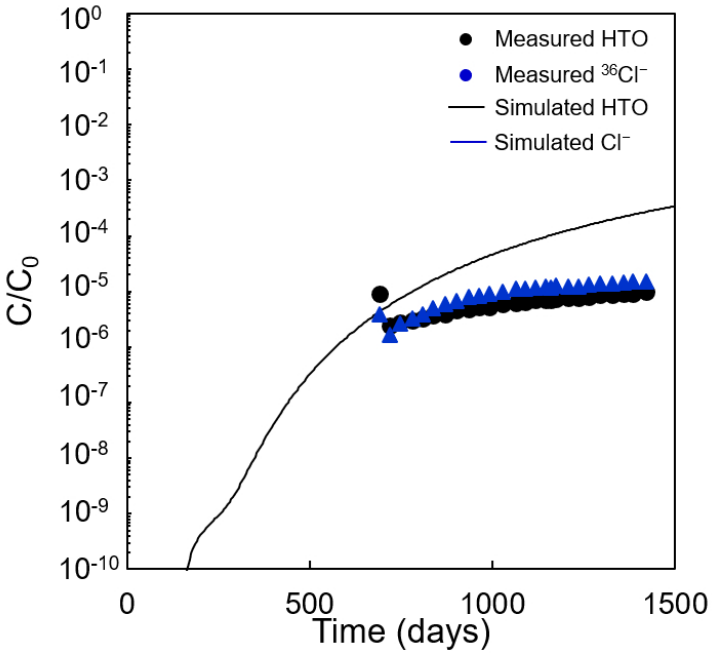

Figure E-8. *Breakthrough data of HTO and $^{36}Cl^-$ in PP327 from the in situ Through-Diffusion Experiment (symbols), compared with the simulation results by the Realistic model (solid line).*

E4 Discussion, conclusions and recommendations

Our modelling approach for the TDE of the REPRO project is based on the combination of the scaling approach from laboratory to in situ condition developed for Grimsel LTD project (Tachi et al. 2015, Soler et al. 2015) and key features of rock properties at REPRO site. One of the key features of our modelling approaches is the scaling of parameters from laboratory data to in situ conditions. Another key feature is the heterogeneity of the rock at the REPRO site, given for instance by the BDZ and foliation effects. By considering these features, verification of the modelling for the TDE was carried out by comparing with the in situ measured data.

The features of REPRO rocks and related features, events and processes of the experiments were modelled using the GoldSim code. By comparing with simulation results from the Simple and Realistic models, the measured depletion and breakthrough curves were found to be consistent with BDZ and foliation effects on the transport of tracers. The Realistic model, including the artificial events of the TDE, could reproduce the trends of the depletion curve ($^{36}Cl^{-}$ < HTO < $^{22}Na^{+}$ < $^{133}Ba^{2+}$ < $^{134}Cs^{+}$). In addition, the breakthrough curves of HTO and $^{36}Cl^{-}$ in PP324 and PP327 could be predicted qualitatively by the simulation. However, the in situ test data and simulation results for both depletion and breakthrough curves disagreed quantitatively. A possible reason could be the existence of advective flow influencing the transport of the tracers. The improvement of the model in a future study should include the effect of advective flow in the parameter setting method.

Appendix F

Computer-aided Fluid Engineering AB (CFE)

Urban Svensson

F1 Introduction

F1.1 Background

From the Task Description (TD) for Task 9C (Andersson et al. 2020) we quote the following sentences: "The task focuses on the realistic modelling of coupled matrix diffusion and sorption in the heterogeneous crystalline rock matrix at depth." , and "The aim is to develop models that in a more realistic way represent retardation in the natural rock matrix at depth." These directions will be followed.

The task is focused on predictive modelling of the ongoing in situ Through-Diffusion Experiment, TDE, which is a part of the REPRO project carried out by Posiva at ONKALO in Olkiluoto, Finland. The experiment was initiated in November 2015 and finalized in the spring of 2020. It is carried out between three parallel drillholes arranged as a right-angled triangle. Drillhole ONK-PP326 is used as the injection hole and drillholes ONK-PP324 and ONK-PP327 as observation holes, see Figure F-1. This facilitates tracer migration along, and across, the rock foliation. The experiment is carried out in 1 m long packed-off sections, at a distance of about 11 to 12 m from the tunnel wall. The distances between the drillhole walls are a little more than one decimetre. Any advective flow between the drillholes is foreseen to be insignificant, as the experiment takes place in a rock volume that locally lacks water-bearing fractures.

A schematic view of the three boreholes is given in Figure F-2. Hole 326 is the injection hole, while holes 324 and 327 are observation holes. The circles inside the boreholes represent dummies; this leaves a 1.25 mm annular slot between the dummy and the drill hole wall. For more details, see the TD. The rock type is veined gneiss with a foliation along a line between boreholes 324 and 326. It has been found that the effective diffusion coefficient is about twice as large along the foliation, as compared to perpendicular to the foliation.

The tracers HTO, Na-22, Cl-36, Ba-133, and Cs-134 have been injected. The decreasing tracer concentrations in the injection hole and (foreseen) increasing tracer concentrations in the observation holes are analysed in the ongoing measurements.

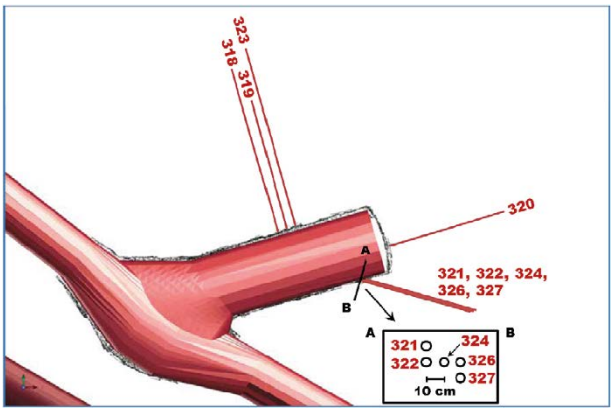

Figure F-1. *REPRO niche ONK-TKU-4219 and TDE drillholes ONK-PP321 to PP327. Reproduced from (Ikonen et al. 2015, Figure 2).*

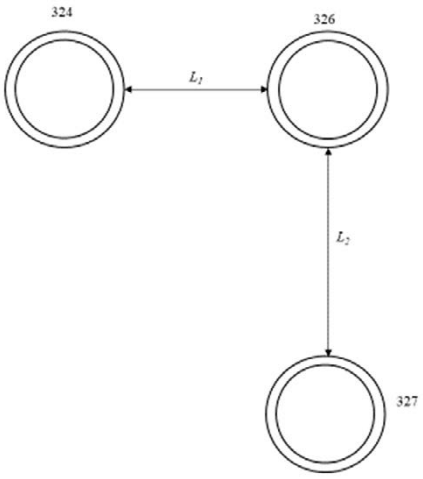

Figure F-2. *Illustration of the three boreholes.*

F1.2 Objectives

As said, the aim of Task 9C is to develop realistic transport models. A special objective of this work is that we want to base the set-up of the models on X-ray microtomography data. The basic models have been presented in two papers (Svensson et al. 2019a, b) and the main objective of this report is to evaluate the models by predictions and back-analysis of experimental data.

F1.3 Scope and limitations

The results to be presented are well within the scope of Task 9C. A limitation of the study is that inverse modelling results are only briefly presented. A full account of the inverse modelling results, or back-analysis, will be presented elsewhere.

F2 Methodology and model

F2.1 Conceptual description of features, events and processes of the experiments

A full description of the field experiment is given by the TD. Here we will only point out some features that are of significance for the model set-up.

- Advection. The experiment was designed not to be influenced by advective transport. During the project some concerns about advection have however been raised. It will here be assumed that advection plays no role for the results of the experiment.
- Large fractures. It is stated in the TD that fractures crossing several of the boreholes are absent. However, fractures with a length scale smaller than, say 10 cm, may be present and strongly influence the experimental results. It will here be assumed that only intergranular fractures (smaller than 100 μm) are present.

F2.2 Description of processes in the conceptual model

In Svensson et al. (2019a) the reactive transport model and its evaluation are described. The basic concept of the model can be described as "when a particle is close to a reactive mineral surface it has a certain probability, P_s, to get sorbed during a certain time, T_s. If sorbed, it will stay so for an average time T_d, before desorbed". In addition to the cell size, Δ, we thus have three model parameters to put numbers to. It is suggested that P_s and T_s are considered as fixed for a particular case while T_d is used as a calibration parameter (varies with type of radionuclide and type of mineral). The model is evaluated by an application to the laboratory experiments by Muuri et al. (2017, 2018a, b). By comparing simulations with the transient diffusion and sorption process, T_d values for C_s (= 2×10^5) and *Ba* (= 7 000) for veined gneiss were found and used in the Task 9C simulations. For *Na* no value is calibrated and the employed value, 500, is simply guessed from the fact that K_d for *Na* is about one order of magnitude lower than for *Ba* (from the LTDE experiment, Widestrand et al. 2010). Another key result from the paper is that surface sorption was important in the simulations. This result was brought over to the Task 9C simulations.

F2.3 Model setup

As stated, we would like to base our model on X-ray data. There is however a fundamental problem with this approach; the X-ray data sets are on the cm scale, while the TDE is on the dm scale. With a certain degree of approximation, it is however possible to follow this approach, as will be demonstrated.

As a first case, the situation outlined in Figure F-3 will be simulated as a 2D transient case. Both the diffusion equation (DE) and a particle tracking method (ParTracK, PTK) will be used. The code DarcyTools (Svensson and Ferry 2014) is used for all simulations to be presented.

A way to simplify the computational domain is suggested in Figure F-4. A number of "approximate symmetry lines" are drawn. The lines are approximate for several reasons like foliation, different distances between boreholes, etc. It is then possible to simulate the injection hole and one observation hole at the time, see Figure F-5. How good the approximation is can be judged by comparing with the full 2D solution described above.

This domain is still too large for utilizing the X-ray data. However, the domain shown in Figure F-6 is of the right size. Once again, we evaluate how good the approximation is by comparing with the full 2D solution.

F2.4 Input data

The X-ray data to be used are given by the file VGN323_grain_map_67.9µm_254x254x187.txt. (Input data in Task 9C) This veined gneiss grain map has a resolution of 67.9 µm. It is not from the boreholes considered in the TDE, but still from the REPRO site. The borehole (323) is shown in Figure F-3. The computational domain will be generated from this grain map, based on the methods introduced in Svensson et al. (2019b).

F2.5 Alternative models and sensitivity cases

In addition to matrix diffusion, it was found in the model simulations that sorption on the borehole walls is an important process. Predictions will for this reason be presented with/without this process included.

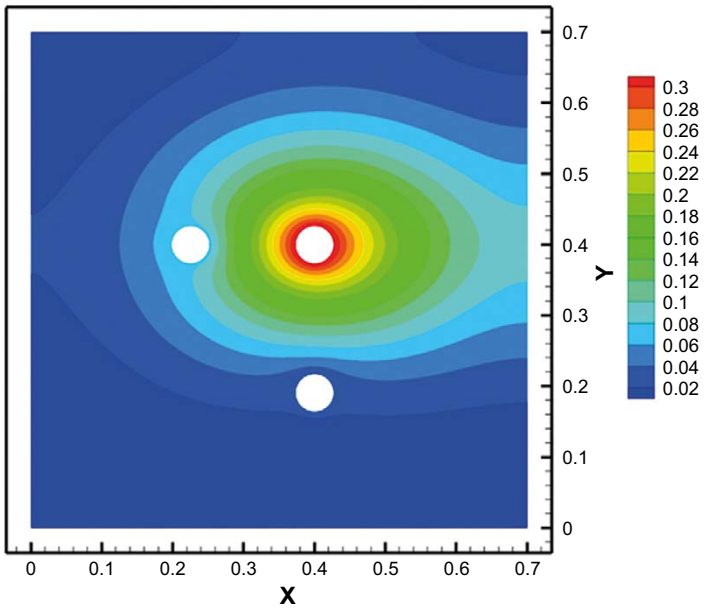

Figure F-3. *Outline of a case called "full 2D". Contours show tracer distribution after 10 years. Coordinates in [m]. Concentrations normalized with the initial concentration.*

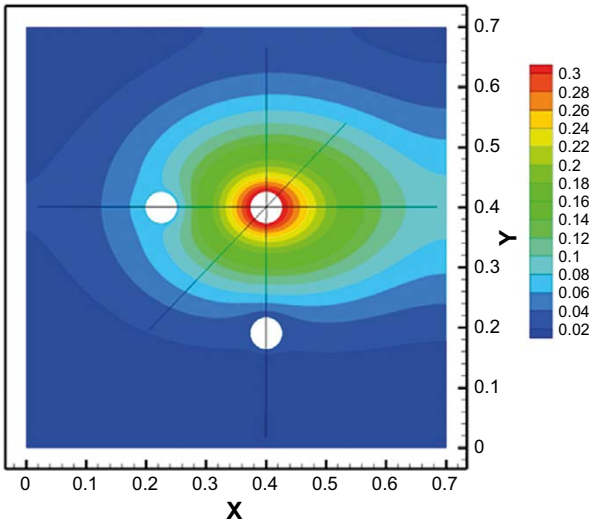

Figure F-4. *Approximate symmetry lines in the full 2D case. Contours show tracer distribution after 10 years. Coordinates in [m]. Concentrations normalized with the initial concentration.*

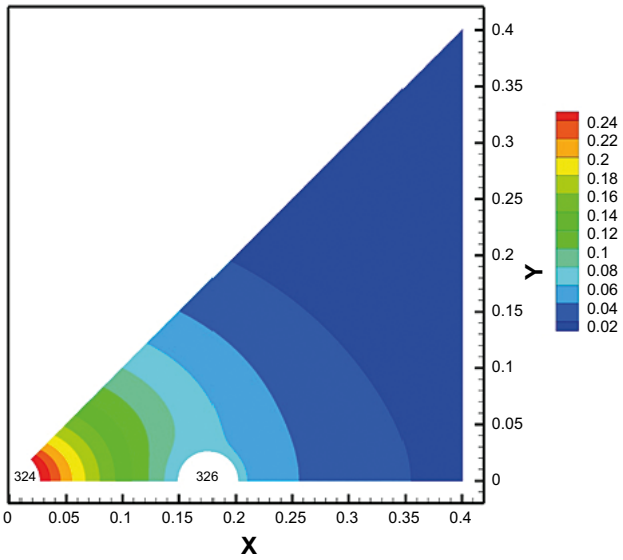

Figure F-5. *A simplified domain that can be used for two boreholes at the time. Contours show tracer distribution after 10 years. Coordinates in [m]. Concentrations normalized with the initial concentration.*

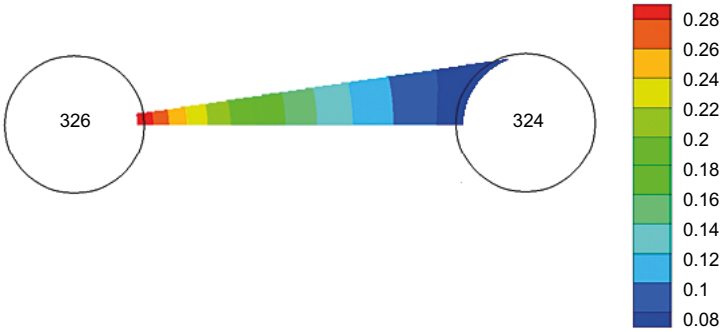

Figure F-6. *A computational domain that can utilize X-ray data. Contours show tracer distribution after 10 years. Concentrations normalized with the initial concentration.*

F3 Results and discussion

F3.1 Model formulation, conservative tracers

This section will start with a discussion of the computational grid, which may seem to be misplaced in a result section. However, one objective is to find a way to utilize X-ray data and the grid issue is hence a part of the results.

Let us start with the full 2D situation outlined in Figure F-3. The tracer distribution shown is in fact the distribution given by the diffusion equation. In this set up the porosity was set to 0.6 %, the diffusion coefficient along the foliation was set to 4×10^{-13} m^2/s and to 2×10^{-13} m^2/s perpendicular to the foliation. A uniform cell size of 0.5 mm was used. The same case was next simulated with the particle tracking method. The particle density distribution is shown in Figure F-7. The two methods are in very good agreement when it comes to the concentration development in the three boreholes, see Figure F-8.

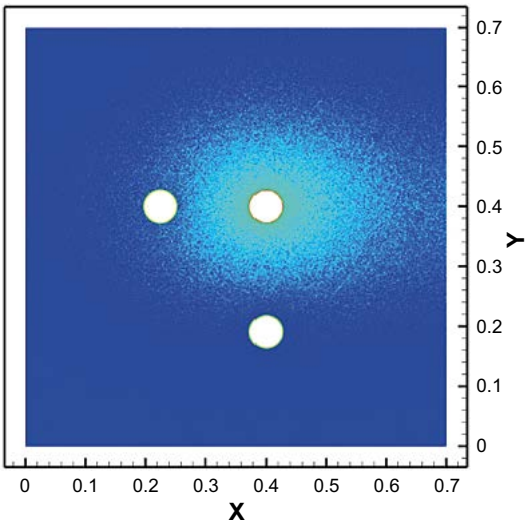

Figure F-7. *The full 2D case. Particle density after 10 years. Coordinates in [m].*

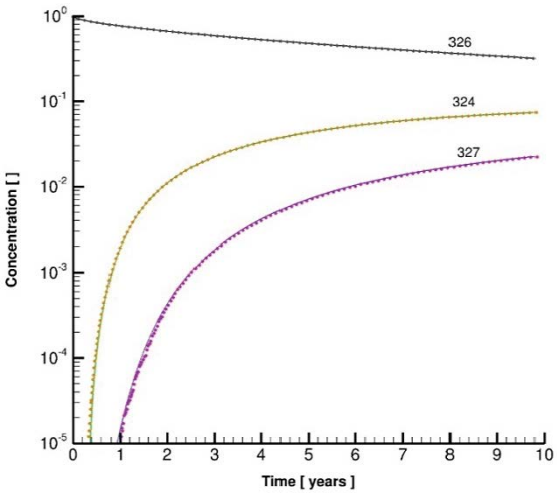

Figure F-8. *Case full 2D. Comparison of normalized concentration development in the three boreholes. Solid lines represent the diffusion equation and dots the particle tracking solution.*

Next, we test if a smaller domain can be used; the 45° sector shown in Figure F-5, where also the solution of the diffusion equation is given. With this set up we can only consider one observation hole at the time, taking note of the two diffusion coefficients. We compare the results with the full 2D case in Figure F-9. A fair agreement is found. For the injection hole (326) we get two curves as we simulate two cases. The full 2D solution is the average of these, which is expected considering the two diffusion coefficients. So, we conclude that the 45° sector is a good approximation of the full 2D simulation.

A smaller domain is however required if a model based on X-ray data should be formulated. Considering the resolution in the X-ray data and the cell size in the numerical model, it is found that a domain like the one showed in Figure F-6 is adequate. We hence need to evaluate how good this approximation is. This is done as above, i.e. we simulate the development under 10 years and compare with the full 2D solution. The result is shown in Figure F-10.

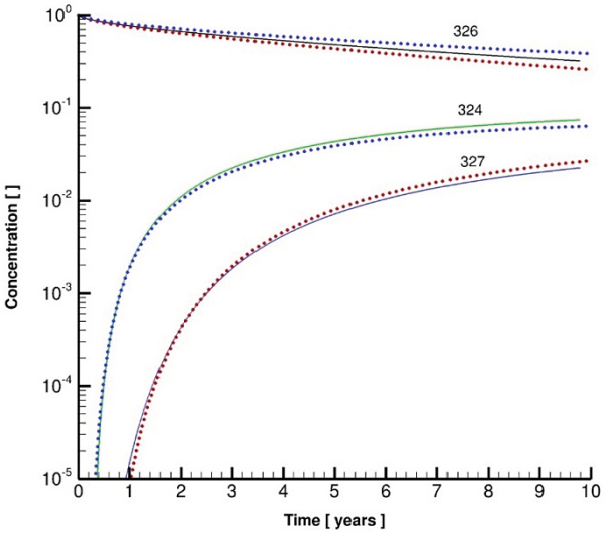

Figure F-9. *The 45° sector case. Solid lines represent the full 2D case, while dots give the 45° sector solution. All based on the diffusion equation.*

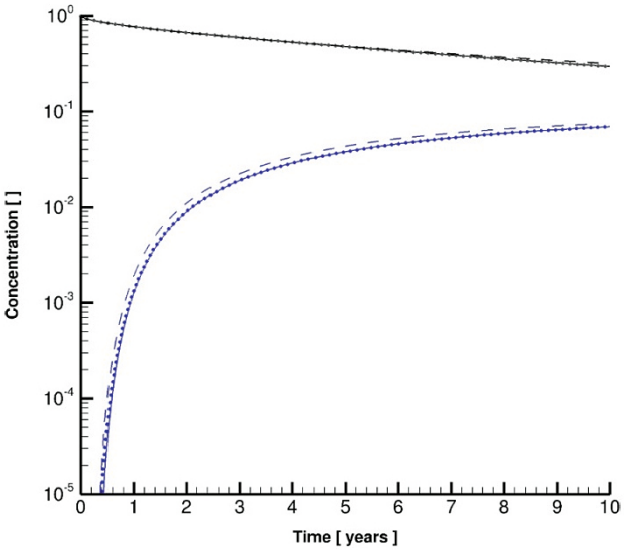

Figure F-10. *The 2D domain, given in Figure F-6. Concentration development in boreholes 326 and 324. Solid lines represent the solution based on the diffusion equation, dots the particle tracking solution and the dashed line the full 2D solution.*

The grain map given by the X-ray data is shown in Figure F-11. As seen, it is a small volume ($17.25 \times 17.25 \times 12.70$ mm). This box is put in a" test bench" in order to evaluate how a computational domain with a realistic effective diffusion coefficient, D_e, and a mean porosity, ε, can be generated. Here we follow the procedures outlined in Svensson et al. (2019b) and choose, the "intergranular approach". A fracture network specification that gives $D_e = 2.9 \times 10^{-13}$ m^2/s and $\varepsilon = 0.71$ % is found, by solving a steady state diffusion equation. The intergranular fracture specification is given by Table F-1.

We are now ready to formulate the X-ray based model. An outline is shown in Figure F-12. The injection hole and one observation hole at the time can be simulated (the distance between the boreholes is relevant for 324). The grain map covers a domain of $17.25 \times 17.25 \times 12.70$ mm and is for this reason repeated several times in the x and z directions. In the y direction the domain is 17.25 mm and no repetition is needed. The cell size is 67.9 µm and hence the same as in the grain map; this in order to avoid averaging. The intergranular fracture network has 30 million fractures and the computational grid has 60 million cells.

A number of properties are calculated and represented in the grid (porosities, diffusion coefficients, mineral types, etc). As one example, the porosity field is shown in Figure F-13. For each grid cell that is in contact with a grain, the grain type is stored. This will be utilized when reactive transport is dealt with.

A transport simulation has also been carried out, using the particle tracking method. 10^5 particles were injected in borehole 326 and tracked for 10 years. The result is shown in Figure F-14, where also the curves for the full 2D simulation are included. We conclude that a fair agreement is found which means that the X-ray based model is relevant as an approximation. If desired, the X-ray model may of course be fine-tuned in order to get a closer agreement with the full 2D solution.

Table F-1. Properties of the fracture network from the tuning to the experimental data.

Property	Value
Length interval	50 – 100 µm
Diffusivity	10^{-10} m^2/s
Aperture	2.0 µm
Intensity	30 m^{-3}
Power law exponent	−2.6
Fracture normal vector orientation	Poisson

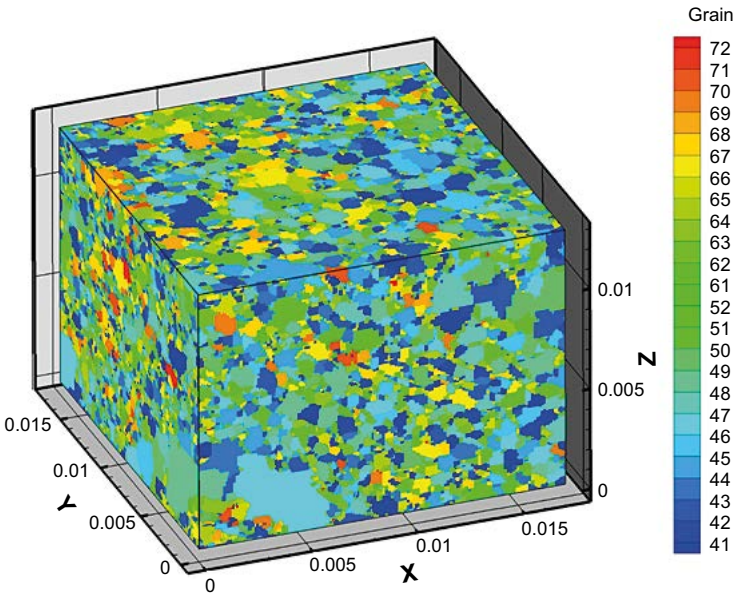

Figure F-11. *The grain map. The grain indexes give different mineral types. Coordinates in [m].*

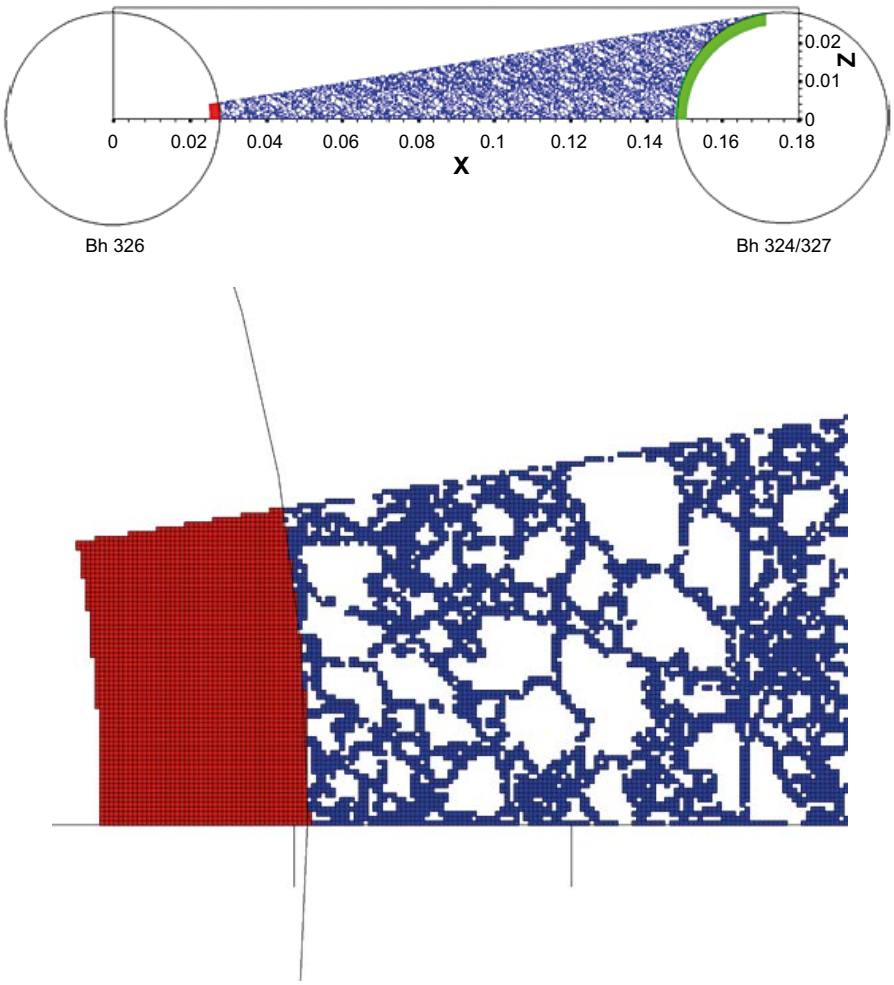

Figure F-12. *The 3D X-ray based grid. Computational grid in a 2D section (top) with an enlarged view close to borehole 326 (bottom). Coordinates in [m].*

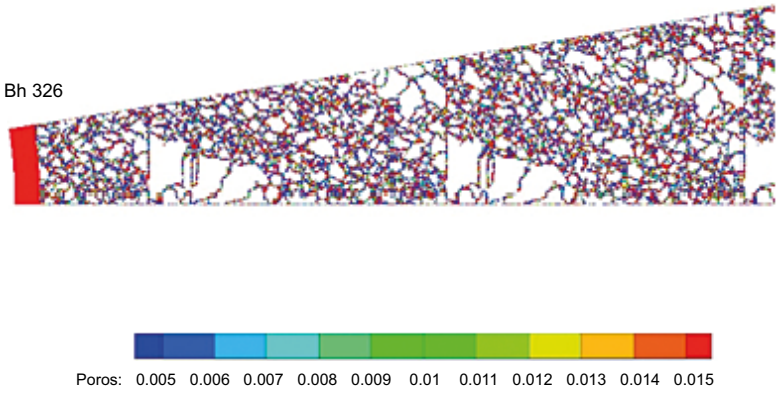

Figure F-13. *The 3D X-ray based grid. Porosity distribution close to borehole 326.*

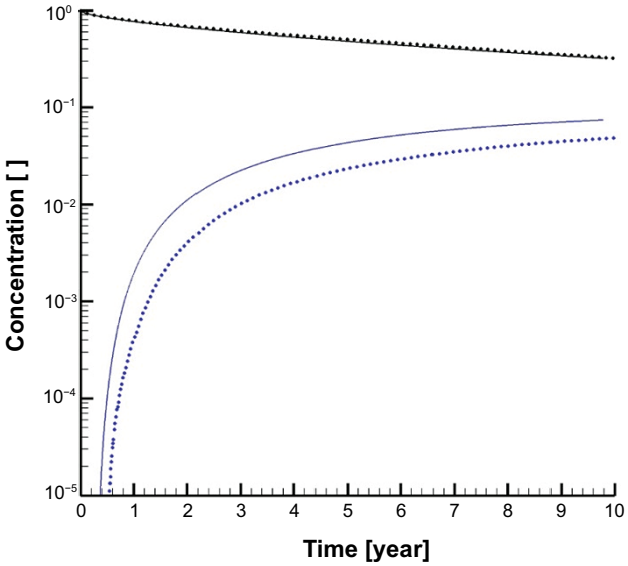

Figure F-14. *The 3D X-ray based case. Comparison between the results for the X-ray grid (dots) and the full 2D case (lines).*

F3.2 Model formulation, reactive tracers

The results reported for a conservative tracer were obtained in the summer of 2017. It was then expected that the X-ray grid in Figure F-12 should be used also for reactive tracers. However, during the winter 2017/18 an extensive development and validation of the reactive particle tracking method was carried out. From this work, it was clear that the reactive tracers would only penetrate the rock matrix by a few centimetres, at the most. The distance between the boreholes is around ten centimetres and it could hence be concluded that the reactive tracers would not reach boreholes 324 and 327 within ten years. For this reason, another approach was chosen for the reactive tracers.

The domain and grid outlined in Figure F-15 is used for *Na, Ba* and *Cs*. Due to the smaller domain size a higher resolution could be achieved and a grain map with the corresponding resolution was employed. The X-ray file VGN323_2018_grain_map_27.16µm_635x635x469.txt (Input data in Task 9C) is for veined gneiss and has a resolution of 27.16 µm. The computational grid has the same resolution in the matrix, but uses an expansion in the slot between the borehole and the dummy. In the *z*-direction (along the borehole) the domain dimension is 5 mm. Considering that the grain size is typically 0.5 mm, it is expected that this is an adequate dimension along the borehole. The grid has 48 million cells and the micro-DFN around 8 million fractures. Global properties for this set-up were evaluated by a steady state through diffusion test. It was found that the effective diffusion coefficient, D_e, was 3.2×10^{-13} m^2/s and the porosity 0.58 %. Foliation was introduced by multiplying D_e with a factor that varied with the angle between the x and y direction, see Figure F-15. This factor generated a D_e that was twice as large in the y-direction, as compared to the x-direction; still keeping the mean value 3.2×10^{-13} m^2/s.

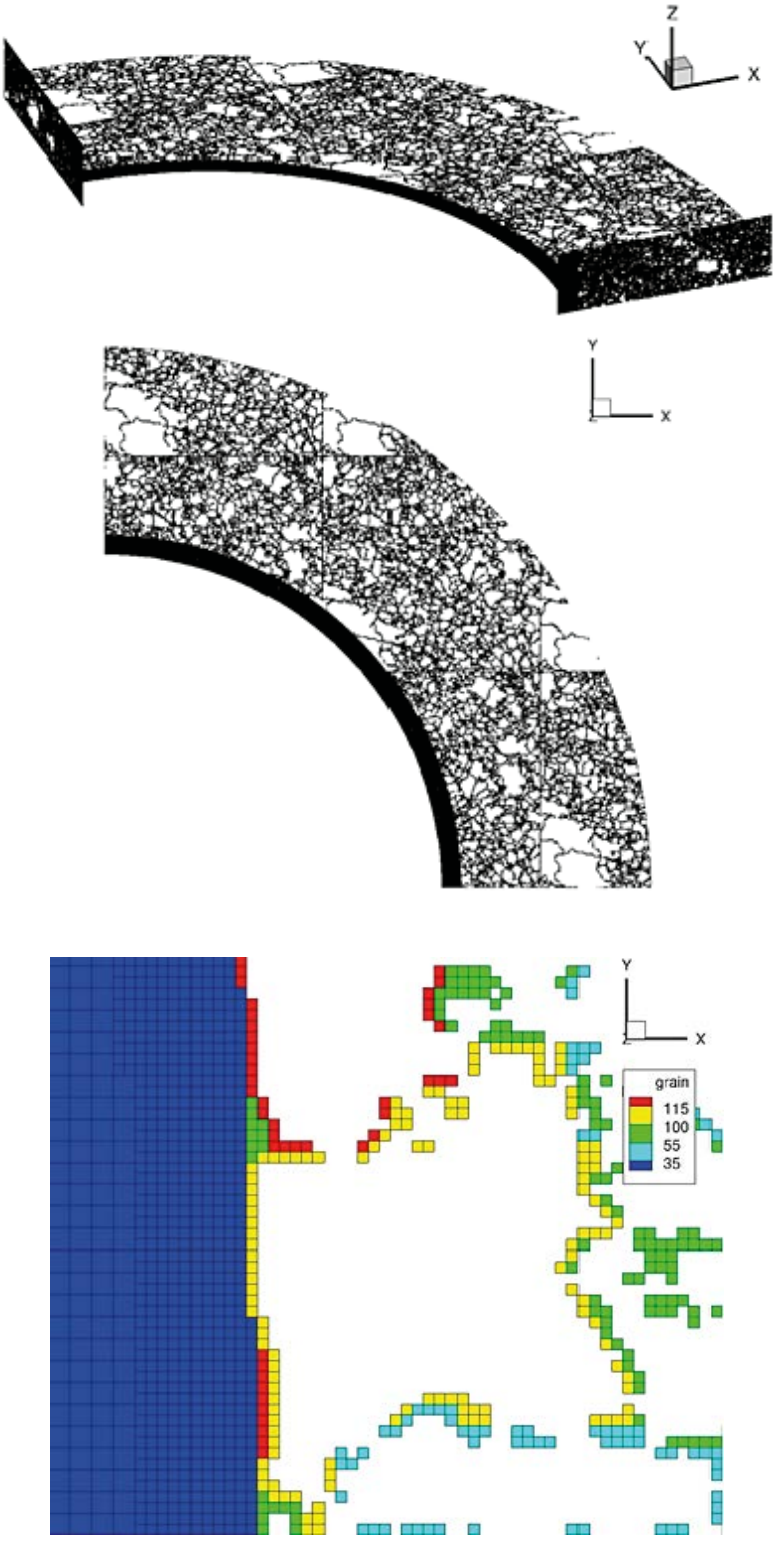

Figure F-15. *Computational grid for sorbing tracers. A perspective view (top), the xy-plane (middle) and an enlargement showing the near borehole grid (bottom). The colours for grain type are as follows: quarts (light blue), mica (green), plagioclase (yellow) and K-feldspar (red). Borehole marked as dark blue in the bottom figure.*

F3.3 The central prediction

The main result of the simulations is the decrease of the tracers in the injection hole. The concentration as a function of time is denoted $C(t)$ and the initial concentration is denoted C_0. In the Figures F-16 to F-18 the normalized concentration, $C(t)/C_0$, for *Na, Ba* and *Cs* is given for 10 years. As seen two curves are found in each figure. The solid line gives the expected behaviour while the broken line gives a form of sensitivity test; the surface sorption is excluded in this case. Excluding surface sorption was achieved by specifying that reactive mineral surfaces are absent for the 50 µm rock closest to the slot in the borehole. It is clear that the simulations are very sensitive to how surface sorption is handled. Particle distributions after ten years are illustrated in Figures F-16 to F-18. The grid covers a distance of 15 mm into the rock and it seems that this is enough even for the least sorbing tracer *Na.*

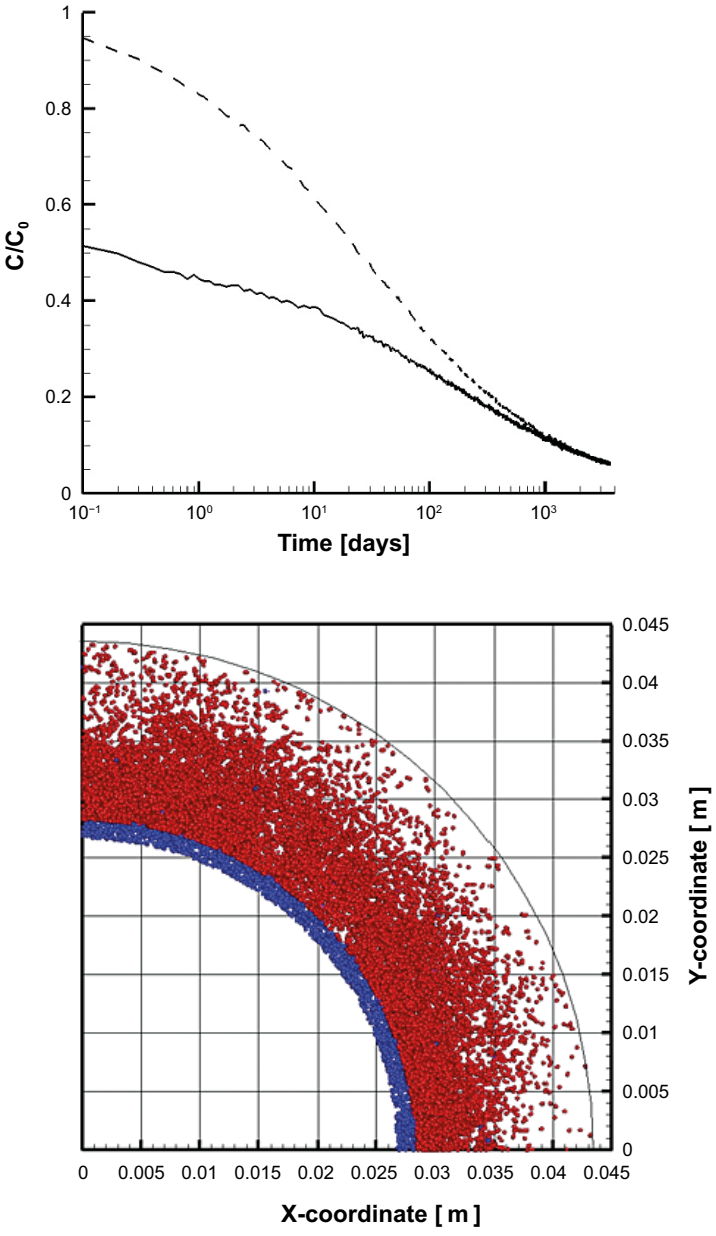

Figure F-16. *Na. The decrease of concentration in the injection hole (top) and the particle distribution after 10 years. Broken line in the top figure illustrates a case where surface sorption is excluded. Particles marked red are sorbed while blue are "free to move".*

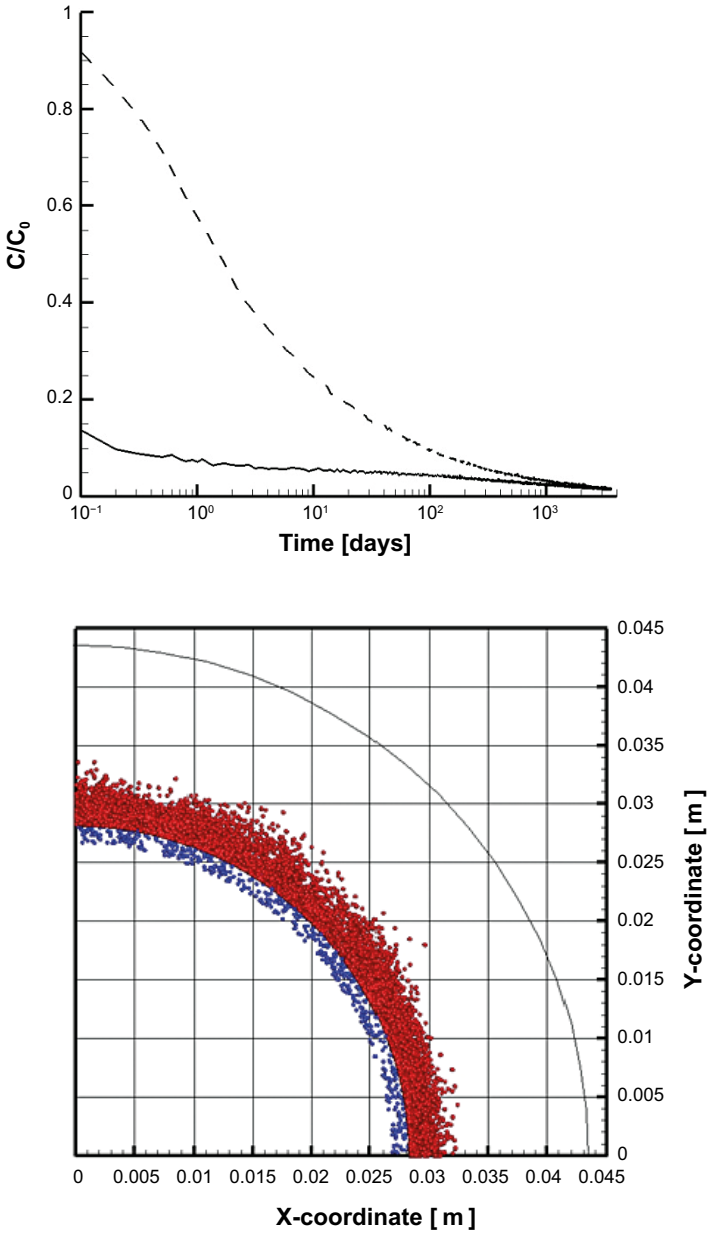

Figure F-17. *Ba. The decrease of concentration in the injection hole (top) and the particle distribution after 10 years. Broken line in the top figure illustrates a case where surface sorption is excluded. Particles marked red are sorbed while blue are "free to move".*

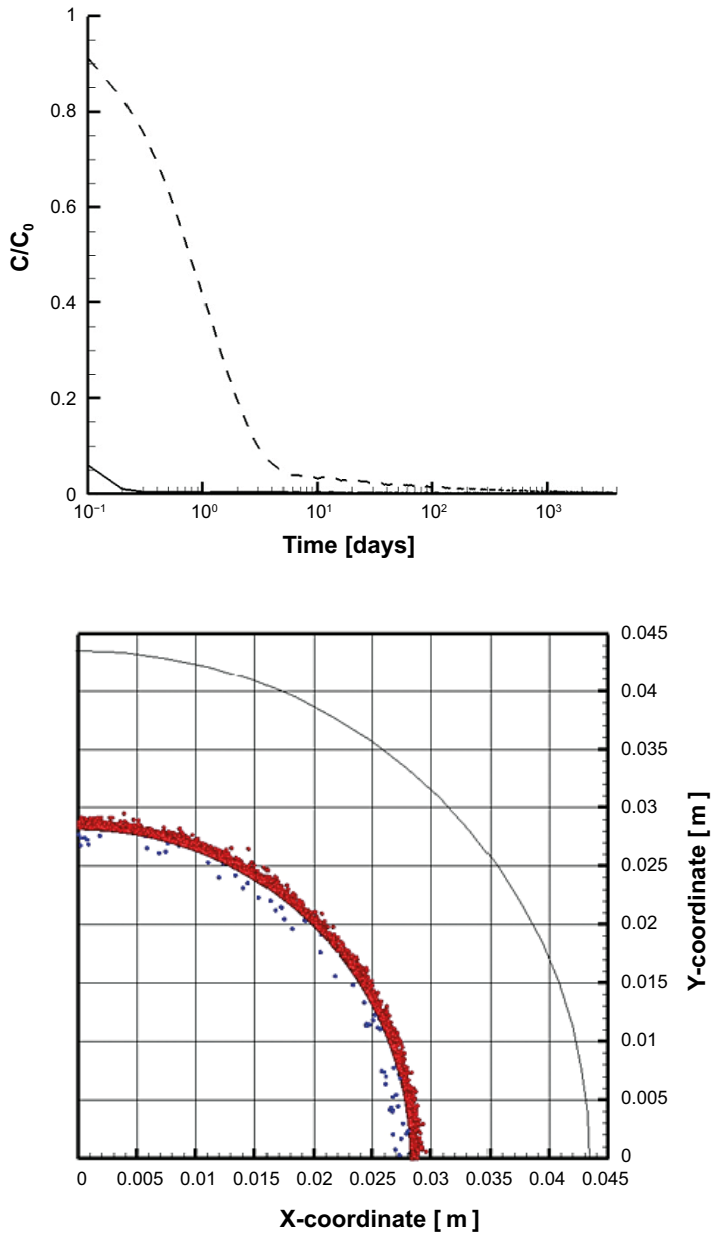

Figure F-18. *Cs. The decrease of concentration in the injection hole (top) and the particle distribution after 10 years. Broken line in the top figure illustrates a case where surface sorption is excluded. Particles marked red are sorbed while blue are "free to move".*

F3.4 Back-analysis

Predictions were carried out during 2018 and the results from the field experiment were presented in October 2018. After this an extensive back-analysis was carried out. Here we will give a brief account of this inverse modelling of the field experiment.

The back analysis started with an evaluation of the most appropriate grid; the result is shown in Figures F-19 and F-20. Also, the micro-DFN was fined tuned to best fit the data. It was found that a global diffusion coefficient of 5.7×10^{-13} m^2/s and a mean porosity of 0.57 % worked well. This was achieved by the specification of the micro-DFN given in Table F-2.

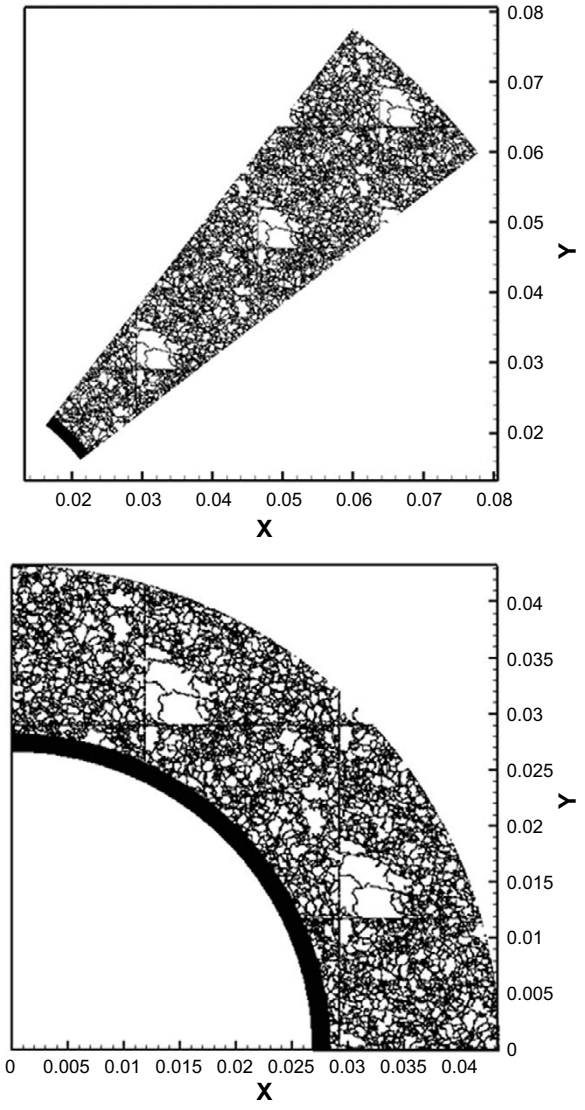

Figure F-19. *Back analysis of the field experiment. Computational grid used for conservative tracers (HTO and Na-22) (top) and reactive tracers (Ba-133 and Cs-134) (bottom). Cell size is 27.16 µm. The black part (too fine grid to be seen) gives the injection volume in the borehole ONK-PP326. Coordinates in [m].*

Table F-2. Properties of the fracture network from the tuning to the experimental data.

Property	Value
Length interval	50 – 100 µm
Diffusivity	8×10^{-10} m^2/s
Aperture	1.2 µm
Intensity	100 m^{-3}
Power law exponent	−2.6
Fracture normal vector orientation	Poisson

The above discussed parameter T_d (time before desorption) was used as a calibration parameter. It was found that Na-22 was best simulated as a conservative tracer ($T_d = 0$), for Ba-133 T_d was set to 1 200 and for Cs-134 a value of 12 000 was found to best simulate experimental data.

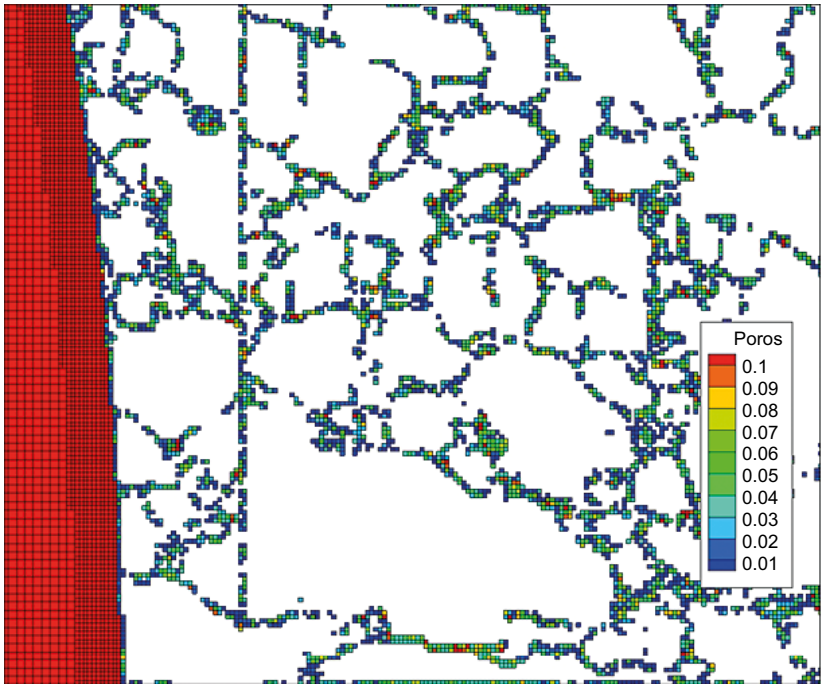

Figure F-20. *Back analysis of the field experiment. Computational grid and porosity field.*

The comparison with experimental data is given in Figures F-21 to F-24. Data were collected in two ways, from samples and from on-line measurements. Both data sets are included in the comparisons for Na-22, Ba-133 and Cs-134. As mentioned, Na-22 was best simulated as a conservative tracer. However, an even better fit to data was achieved by reducing the diffusivity of the micro fractures with a factor of two, see Figure F-22. This also illustrates the sensitivity to the specification of the microDFN. For Ba-133 and Cs-134 the agreement with data is considered to be good, see Figures F-23 and F-24.

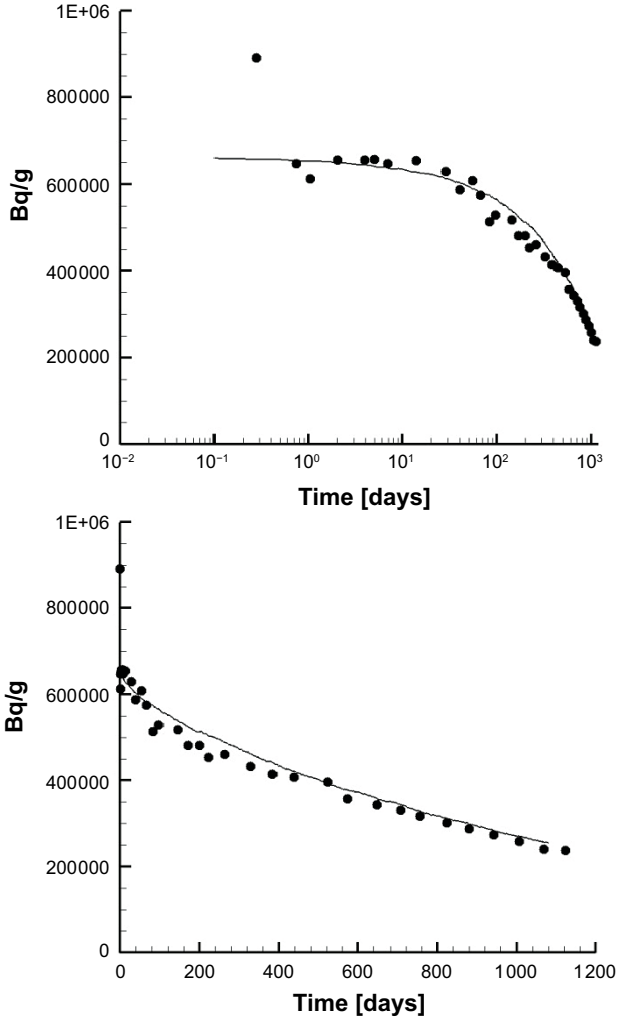

Figure F-21. *Back analysis of the field experiment. A comparison of measured (symbols) and simulated (solid line) concentration decrease of HTO.*

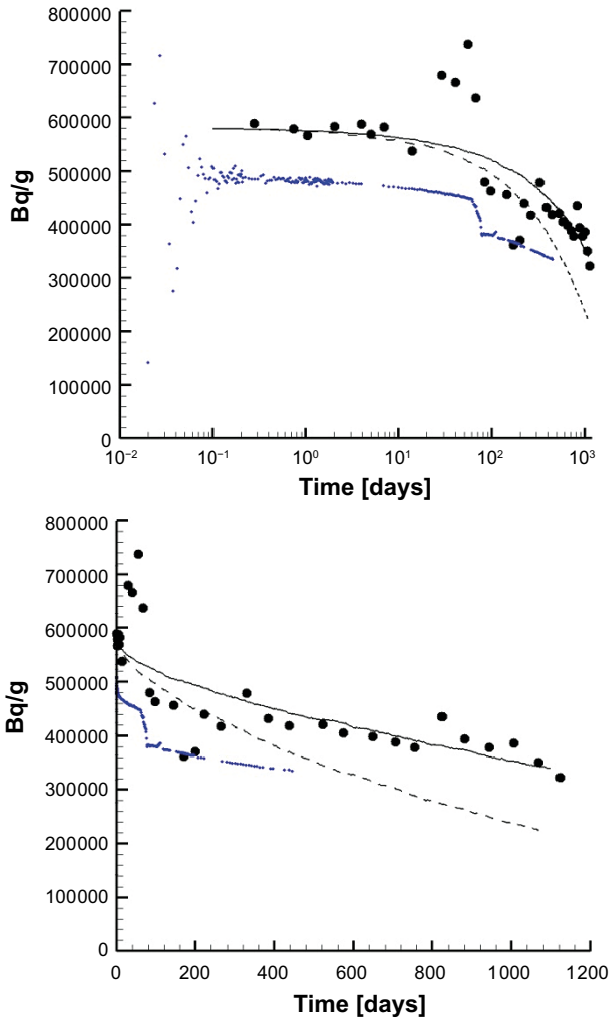

Figure F-22. *Back analysis of the field experiment. A comparison of measured (symbols) and simulated (solid line) concentration decrease of Na-22. Blue small dots give the data from the on-line measurements (black dots are from samples). Dashed line illustrates a simulation with* $T_d = 0$ *and* $D_f = 8 \times 10^{-10}$ m^2/s, *while the solid line results from* $T_d = 0$ *and* $D_f = 4 \times 10^{-10}$ m^2/s.

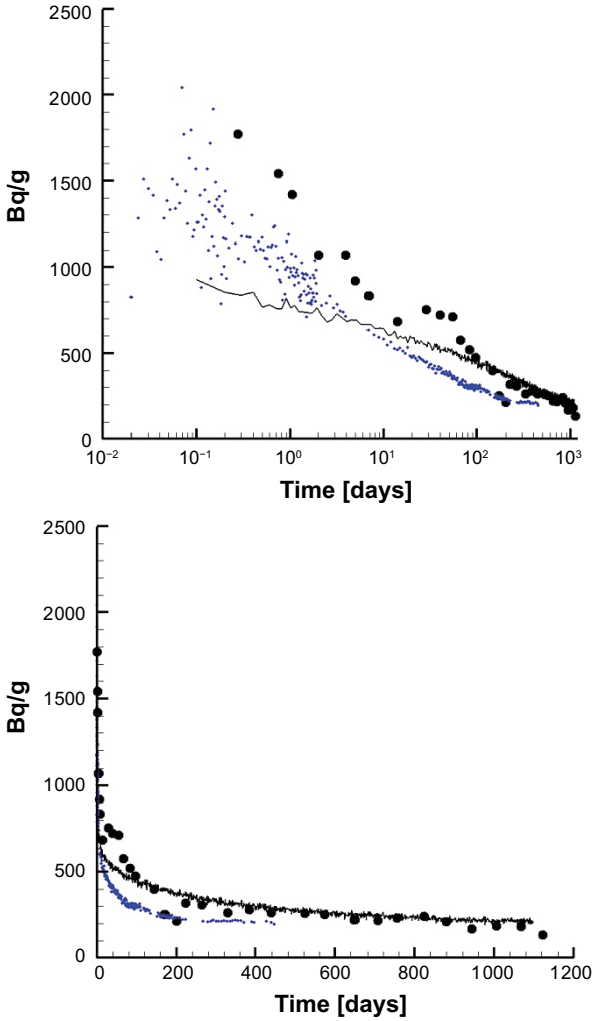

Figure F-23. *Back analysis of the field experiment. A comparison of measured (symbols) and simulated (solid line) concentration decrease of Ba-133. Blue small dots give the data from the on-line measurements (black dots are from samples).*

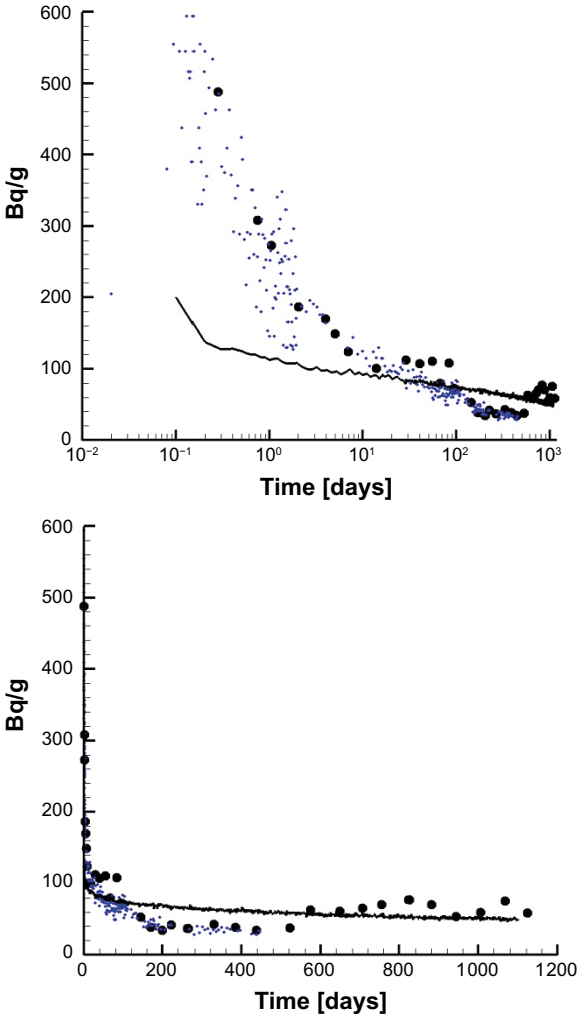

Figure F-24. *Back analysis of the field experiment. A comparison of measured (symbols) and simulated (solid line) concentration decrease of Cs-134. Blue small dots give the data from the on-line measurements (black dots are from samples).*

F4 Discussion and conclusions

The discussion chapter will be started by a list of some uncertainties that may influence the simulation results.

- Large fractures. It is stated in the TD that fractures crossing several of the boreholes are absent. However, fractures with a length scale smaller than, say 10 cm, may be present and strongly influence the experimental results.
- Foliation. In this report two different diffusion coefficients have been used to simulate the effect of foliation. Is that the only thing that needs to be done? It may be the case that fractures have different length and aperture along and perpendicular to the foliation.
- Advection. Task 9C was not expected to be influenced by advective transport, but some concerns have been raised during the project.
- Borehole "wall effects". Surface sorption has been discussed in this report. However, "the borehole deformation zone (BDZ)" may imply that other effects, like a higher porosity, may be present and significant.

In the TD the ultimate aim of Task 9 is stated as "develop models that in a more realistic way represent retardation in the natural rock matrix at depth". The work reported here (this report and Svensson et al. 2019a, b) has certainly followed this aim, as new methods and techniques have been developed and evaluated. A common feature of the developments is the use of X-ray data. Using X-ray data as a starting point necessitates developments of new approaches and techniques.

Some specific achievements and results:

- A new reactive transport model has been formulated and evaluated.
- New grid techniques, suitable for X-ray data, have been developed in order to describe the diffusion available pore space.
- Computational techniques to calculate grain properties directly from X-ray data files have been demonstrated (Svensson et al. 2019b).
- For conservative tracers the requested results for Task 9C have been obtained in various ways (advection-diffusion, particle tracking, different grids, etc).
- For sorbing tracers, the reported results for Task 9C are limited to the decrease of concentration in the injection hole. The TD asked for break-through curves in observation holes, but it was here concluded that this would not happen.
- The sensitivity to surface sorption on the borehole wall in the injection borehole has been tested.

Based on this list one may conclude that a promising development has been initiated and more testing and applications should be carried out.

Arkitektkopia AB, Bromma, 2021

SKB is responsible for managing spent nuclear fuel and radioactive waste produced by the Swedish nuclear power plants such that man and the environment are protected in the near and distant future.

skb.se